DISS. ETH NO. 27334

INVESTIGATION OF NEW AEROSOL PARTICLE FORMATION IN POLAR REGIONS

ANDREA BACCARINI

DISS. ETH NO. 27334

INVESTIGATION OF NEW AEROSOL PARTICLE FORMATION IN POLAR REGIONS

A thesis submitted to attain the degree of

DOCTOR OF SCIENCES of ETH ZURICH

(Dr. sc. ETH Zurich)

presented by

ANDREA BACCARINI

M.Sc., Faculty of Physics, University of Trento

born on 31.03.1990

citizen of
Italy

accepted on the recommendation of

Prof. Dr. Urs Baltensperger (examiner)
Prof. Dr. Ruth Signorell (co-examiner)
Prof. Dr. Hans-Christen Hansson (co-examiner)
Prof. Dr. Julia Schmale (co-examiner)
Dr. Josef Dommen (co-examiner)

2021

CONTENTS

SUMMARY

Aerosol-cloud interactions are one of the least understood drivers of radiative forcing on Earth. In the atmosphere, clouds can form only when aerosols are present, because a surface is needed for water vapour to condense on and create a droplet. Particles, on which cloud droplets form, are known as cloud condensation nuclei (CCN), and the ability to serve as a CCN depends both on the aerosol size and chemical composition. Aerosols in the atmosphere are produced by a variety of sources, which can be both natural and anthropogenic. Additionally, there are several different atmospheric processes that can alter aerosols' chemical and physical properties and remove them from the atmosphere. Both the distribution and the occurrence of aerosol sources and processes are characterized by a high degree of spatial and temporal variability, leading to very heterogeneous aerosol properties in the atmosphere. This inherent complexity is one of the reasons why aerosol-cloud interactions are still poorly understood despite several decades of research in this field.

The second reason is that the cloud albedo, which depends on the number of droplets, varies non-linearly with the CCN concentration. In particular, it is much more sensitive to changes in the CCN number when their absolute concentration is low. Therefore, observations of aerosol-cloud interactions with high aerosol loading, which is the case for most of present-day measurements, can hardly provide information about cloud albedo sensitivity in a low aerosol concentration environment. However, the preindustrial atmosphere was characterized by lower aerosol abundance compared to today due to the much lower anthropogenic emissions. Without a proper understanding of aerosol-cloud interactions in a pristine world, it is not possible to constrain the preindustrial cloud albedo, which defines the baseline to calculate the present-day aerosol forcing and largely contribute to the overall forcing uncertainty.

New particle formation (NPF) is the process by which aerosols are formed from nucleation of gaseous precursors. NPF is an important source of CCN worldwide. Models estimate that NPF accounts for 38% to 66% of present-day CCN and for 45% to 84% in the preindustrial time. However, there are still many unknowns about the relevance of different NPF mechanisms and the concentrations of gaseous precursors that nucleate new aerosols, particularly in remote and pristine regions. Measurements in these locations are important because they can provide information about natural aerosol sources in a preindustrial-like environment. Additionally, a better understanding of natural aerosol sources is valuable to assess how these will change in a warming climate and improve the accuracy of future climate predictions.

This Thesis focuses on the investigation of NPF in remote polar regions and its relevance as a source of CCNs. NPF was contrasted with other aerosol sources, mainly sea spray, to better understand their relative contribution to the CCN budget. This Thesis also characterizes the spatial and temporal distribution of some trace gases, which are relevant for secondary aerosol formation. Namely, sulfuric acid, iodic acid and methanesulfonic acid (MSA). The effects of environmental conditions in controlling the occurrence of NPF and the concentration of the aforementioned trace gases were also investigated. Measurements were conducted during two different expeditions: the Antarctic Circumnavigation Expedition (ACE) in the Southern Ocean from Decem-

ber 2016 to March 2017 and the Arctic Ocean 2018 (AO18) expedition in the central Arctic Ocean during August and September 2018.

In the Austral summer, the Antarctic circumpolar vortex prevents the transport of anthropogenic aerosols over the Southern Ocean. Therefore, this region is an ideal place to investigate preindustrial-like aerosol sources and processes. Based on previous studies in the region, the main nucleating species is thought to be sulfuric acid, an oxidation product of dimethyl sulfide (DMS), which is produced by phytoplankton in the ocean.

During ACE, it was confirmed that new particle formation in the marine boundary layer is mainly driven by sulfuric acid but occurs very sporadically and does not contribute to the local CCN budget. Sea spray emissions account for a consistent fraction of the CCN number, with a contribution varying between 10% and more than 50% at 0.15% supersaturation. This variability depends both on the location and the environmental conditions (*e.g.* wind speed and sea state). The remaining fraction of the CCN number probably comes from NPF in the free troposphere. Measurements revealed also a high concentration of MSA both in the particle and in the gas phase around the coast of Antarctica. MSA is another oxidation product of DMS and the ocean around the Antarctic coast is characterized by one of the highest DMS concentrations in the world. Here, global climate models tend to underestimate the CCN concentration, because of a missing or wrongly parametrised aerosol source or process. By comparing gaseous and particulate MSA, it was possible to show that most of the MSA is probably formed via heterogeneous oxidation of DMS. This process is missing in many global climate models and may be related with their tendency to underestimate the CCN number concentration around the coast of Antarctica.

The central Arctic Ocean is also a pristine place during summer with a very small influence from anthropogenic activities. Here, natural aerosol sources are weak because of sea ice which inhibits formation of sea spray and low DMS concentration. The CCN number concentration is usually so small that the formation of clouds is limited. Hence, small changes in the CCN concentration can have a significant effect on the formation of clouds and their albedo.

Observations performed during AO18 have shown that no NPF occurs over the central Arctic Ocean during summer, but it becomes very frequent at the beginning of autumn when new sea ice starts to form. Direct measurements of the nucleating clusters revealed that nucleation is driven by iodic acid, which increases substantially during autumn. These observations answer a question which remained unresolved for almost 30 years. In fact, NPF has been observed since the first aerosol measurements in the region in 1991, but no conclusive answers on the nucleation mechanism were provided so far. Iodic acid is produced from the iodine radical, which can be formed from the photolysis of different iodine containing molecules. The exact precursor is not known nor is its source. However, both microalgae living below the sea ice or heterogeneous reactions on snow or frozen surfaces can emit iodine compounds. These are the two most likely sources of iodine in the central Arctic Ocean. It was also shown that the iodic acid concentration is tightly connected to some environmental variables: these are the boundary layer height, deposition velocity, condensation sink and occurrence of fog. A simple model was developed using these parameters to derive an iodine emission factor, which can be used in regional or global climate models to simulate iodic acid over the central Arctic Ocean. Moreover, it was shown that iodic acid is also vital for the growth of the newly formed particles, contributing to most of the growth in the majority of observed cases. Particles only grew up to $20 - 30$

nm maximum, which is too small to activate as a CCN under typical supersaturations for low-level clouds or fog in the Arctic. However, direct measurements of cloud residuals revealed that such small particles can also activate into cloud droplets when the concentration of larger particles is sufficiently small. This is an extreme case, which can only occur in very clean environments where the formation of clouds is limited by the availability of CCN. Yet, it is an important indication that iodine NPF in the central Arctic Ocean can have a significant effect on cloud formation and their radiative effect.

This Thesis provides new insights on natural aerosol sources and processes in two different pristine environments: the Southern Ocean and the central Arctic Ocean. During summer over the Southern Ocean, sea spray was found to be the only important boundary layer source of aerosols, yet it could only explain a minority fraction of the total CCN number. The remaining fraction was attributed to entrainment of particles nucleated in the free troposphere. Measurements also revealed a large concentration of MSA around the coast of Antarctica, which is probably produced via heterogeneous oxidation of DMS. This process could be important to grow aerosol particles and reduce the critical supersaturation required to activate them in clouds. In addition, the mechanism behind NPF over the central Arctic Ocean was elucidated for the first time, revealing the role of iodic acid, which was responsible for all the observed events. It was found that iodic acid increases sharply towards the end of summer with a direct effect on the occurrence of NPF, which becomes frequent during autumn. NPF represents an important source of aerosols over the Arctic pack-ice and it was found that newly formed particles can activate as CCN even if they are smaller than 30 nm, when the concentration of larger aerosols is sufficiently low. These findings contribute to a better understanding of aerosol particles in the preindustrial atmosphere and are valuable to improve the representation of natural aerosols in regional and global climate models. They can be used to reduce the radiative forcing uncertainty and to improve the accuracy of future climate predictions.

SOMMARIO

Le interazioni tra aerosol atmosferico e nuvole sono uno dei fattori meno compresi della forzante radiativa terrestre. Nell'atmosfera, le nuvole possono formarsi solo in presenza di aerosol, infatti è necessaria una superficie esterna sulla quale il vapore aqueo possa condensare e formare una gocciolina. Le particelle che formano le goccioline nelle nuvole sono note come nuclei di condensazione. La capacità di fungere da nucleo di condensazione dipende dalla dimensione dell'aerosol e dalla sua composizione chimica. Gli aerosol, in atmosfera, possono essere prodotti da diversi tipi di sorgenti, sia di origine naturale che antropogenica. Inoltre, esistono vari processi atmosferici in grado di rimuovere il particolato dall'atmosfera o alterarne le proprietà chimiche e fisiche. Sia le sorgenti che i diversi processi atmosferici sono caratterizzati da un alto livello di variabilità spaziale e temporale, che si riflette in una distribuzione altamente eterogenea del particolato atmosferico e delle sue proprietà. Questa complessità intrinseca è uno dei motivi per cui le interazioni tra aerosol atmosferico e nuvole sono tuttora poco comprese, nonostante diversi decenni di ricerca in questo campo.

La comprensione delle interazioni tra particolato e nuvole è resa complessa anche dal fatto che l'albedo delle nubi dipende dalla concentrazione dei nuclei di condensazione in maniera non lineare. In particolare, l'albedo è molto piú sensibile al numero di nuclei di condensazione disponibili quando la loro concentrazione è bassa. Pertanto, misure in un ambiente ricco di aerosol, come la maggior parte delle osservazioni condotte nel nostro tempo, difficilmente riescono a fornire informazioni utili per valutare la sensitività dell'albedo rispetto a basse concentrazioni di nuclei di condensazione. Tuttavia, l'era preindustriale era caratterizzata da una concentrazione di aerosol molto inferiore rispetto a quella attuale, per via delle ridotte emissioni di natura antropogenica. Senza una corretta comprensione delle interazioni tra particelle e nuvole in un mondo incontaminato, non è possibile definire quale fosse l'albedo delle nuvole in epoca preindustriale. Questa albedo definisce il valore di riferimento per calcolare l'attuale forzante radiativa dovuta all'aerosol atmosferico e l'incertezza associata contribuisce all'incertezza della forzante radiativa complessiva in maniera preponderante.

In atmosfera, nuove particelle, dette secondarie, si possono formare a seguito della nucleazione di precursori gassosi. Questo tipo di processo è un'importante sorgente di nuclei di condensazione sulla terra. Alcuni modelli stimano che le particelle cosí formate in atmosfera rappresentino tra il 38% e il 66% dell'attuale concentrazione di nuclei di condensazione. Si stima che nell'era preindustriale questo contributo fosse maggiore e compreso tra il 45% e l'84% della concentrazione totale di nuclei di condensazionee. Tuttavia, ci sono ancora molte incognite sulla rilevanza dei diversi meccanismi di formazione di nuove particelle e sulla concentrazione dei loro precursori gassosi, in particolare nelle regioni piú remote e incontaminate. Le misurazioni in questi luoghi sono importanti perché forniscono informazioni sulle sorgenti di aerosol naturali, che sono rappresentative dell'era preindustriale. Inoltre, una migliore conoscenza delle sorgenti naturali di aerosol è preziosa per valutare come queste si modificheranno all'aumentare della temperatura terrestre e per migliorare l'accuratezza delle previsioni climatiche.

Questa tesi si focalizza sullo studio della formazione di nuove particelle atmosferiche nelle remote regioni polari e sulla sua rilevanza come sorgente di nuclei di condensazione. La nucleazione di nuove particelle è stata paragonata ad altre sorgenti di aerosol atmosferico, principalmente aerosol marino (*sea spray*), per comprenderne meglio il contributo in termini della concentrazione totale dei nuclei di condensazione. Inoltre, si è studiata anche la distribuzione spaziale e temporale di alcuni gas in traccia, rilevanti per la formazione di aerosol secondari. Vale a dire, acido solforico, acido iodico e acido metansolfonico. Infine, si é analizzato l'effetto delle condizioni ambientali e delle concentrazioni dei suddetti gas in traccia sulla formazione dell'aerosol secondario. Le misurazioni sono state condotte durante due diverse spedizioni: l'Antarctic Circumnavigation Expedition (ACE) nell'Oceano Antartico da dicembre 2016 a marzo 2017 e la spedizione Arctic Ocean 2018 (AO18) nell'Oceano Artico centrale durante agosto e settembre 2018.

Durante l'estate australe, il vortice circumpolare antartico impedisce il trasporto di aerosol antropogenici sull'Oceano Antartico. Pertanto, questa regione è il luogo ideale per studiare i processi e le sorgenti di aerosol atmosferico simili all'epoca preindustriale. Sulla base di studi precedenti condotti in questa regione, si pensa che il principale gas in traccia responsabile della nucleazione di nuove particelle sia l'acido solforico, una molecola formata dall'ossidazione del dimetilsolfuro (DMS), che viene prodotto nell'oceano dal fitoplancton.

Durante la spedizione ACE, le misurazioni hanno confermato che la formazione di nuove particelle nello strato limite marino è principalmente causata dall'acido solforico, tuttavia avviene in modo molto sporadico e non contribuisce significativamente al bilancio locale di nuclei di condensazione. Le emissioni di spray marino rappresentano una frazione consistente del numero di nuclei di condensazione, con un contributo che varia tra il 10% e più del 50% a $0,15\%$ di supersaturazione. Questa variabilità dipende sia dalla regione che dalle condizioni ambientali (*e.g.* velocità del vento e stato del mare). La frazione rimanente del numero di nuclei di condensazione è da attribuirsi probabilmente alla formazione di nuove particelle nella troposfera libera. Le misurazioni hanno rilevato anche un'alta concentrazione di acido metansolfonico sia nelle particelle che nella fase gassosa intorno alla costa dell'Antartide. L'acido metansolfonico è un altro prodotto di ossidazione del DMS e l'oceano intorno alla costa antartica è caratterizzato da una delle più alte concentrazioni del DMS al mondo. I modelli climatici globali tendono a sottostimare la concentrazione dei nuclei di condensazione in questa regione, questo è dovuto alla mancata rappresentazione di una sorgente di aerosol o alla sbagliata rappresentazione di un processo atmosferico. Confrontando la concentrazione di acido metansolfonico in fase gassosa e nelle particelle, è stato possibile mostrare che questo composto si forma molto probabilmente attraverso l'ossidazione eterogenea del DMS. L'ossidazione eterogenea del DMS è un processo assente in molti modelli climatici globali e potrebbe essere connesso alla loro tendenza a sottostimare la concentrazione di nuclei di condensazione intorno alla costa dell'Antartide.

Anche l'Oceano Artico centrale è un luogo incontaminato durante l'estate, con un'influenza molto piccola delle attività antropiche. Qui le sorgenti naturali di aerosol sono deboli a causa del ghiaccio marino che inibisce la formazione di spray marino e che limita la concentrazione di dimetilsolfuro. La concentrazione di nuclei di condensazione è solitamente cosí bassa che la formazione di nuvole è fortemente limitata. Quindi, piccole variazioni nella concentrazione dei nuclei di condensazione possono avere un effetto significativo sulla formazione di nubi e sulla loro albedo.

Le osservazioni effettuate durante la spedizione AO18 hanno mostrato che durante l'estate sull'Oceano Artico centrale non si verifica nessun evento di nucleazione, tuttavia questa diventa molto frequente all'inizio dell'autunno, quando comincia a formarsi nuovo ghiaccio marino. Misure dirette dei cluster di nucleazione hanno rivelato che questo processo è causato dall'acido iodico, il quale aumenta sostanzialmente durante l'autunno. Queste osservazioni rispondono ad una domanda rimasta irrisolta per quasi 30 anni. Infatti, la formazione di nuove particelle è stata osservata fin dalle prime misure di aerosol nella regione nel 1991, ma fino ad ora non era stato possibile identificare il meccanismo responsabile della nucleazione di queste particelle. L'acido iodico è prodotto dal radicale ioduro, che può formarsi dalla fotolisi di diverse molecole contenenti iodio. L'esatto precursore non è noto, né lo è la sua origine. Tuttavia, sia le microalghe che vivono sotto il ghiaccio marino che le reazioni chimiche che avvengono sulla neve o sulle superfici ghiacciate possono emettere composti di iodio. Queste rappresentano le due sorgenti più probabili di iodio nell'Oceano Artico centrale. É stato anche dimostrato che la concentrazione di acido iodico è strettamente connessa ad alcune variabili ambientali quali l'altezza dello strato limite, la velocità di deposizione, le perdite per condensazione e la presenza di nebbia. É stato sviluppato un semplice modello basato su questi parametri per stimare l'emissione di iodio. Questa informazione può essere utilizzata nei modelli climatici regionali o globali per simulare la concentrazione di acido iodico nell'Oceano Artico centrale. Inoltre, è stato dimostrato che l'acido iodico è vitale anche per la crescita delle particelle di nuova formazione, contribuendo in maniera sostanziale alla crescita nella maggior parte dei casi osservati. Si è osservato anche che le particelle crescono in genere soltanto fino ad un massimo di $20 - 30$ nm in diametro. Questo valore è troppo piccolo affinché le particelle possano attivarsi come nuclei di condensazione con le tipiche supersaturazioni raggiunte nelle nuvole di bassa quota o nella nebbia dell'Artico. Tuttavia, misure dirette dei residui delle goccioline di nube hanno rivelato che anche queste piccole particelle possono attivarsi come goccioline se la concentrazione di particelle più grandi è sufficientemente bassa. Quello descritto è un caso estremo, che può verificarsi solo in ambienti molto puliti dove la formazione di nubi è limitata dalla disponibilità di nuclei di condensazione. Eppure, è un'indicazione importante che nell'Oceano Artico centrale la formazione di nuove particelle guidata dallo iodio può avere un effetto significativo sulla formazione di nubi e sul loro effetto radiativo.

Questa tesi contribuisce ad ampliare la conoscenza delle sorgenti e dei processi legati all'aerosol atmosferico in due ambienti incontaminati: l'Oceano Antartico e l'Oceano Artico centrale. Durante l'estate sull'Oceano Antartico, la nebulizzazione di aerosol marino è risultata essere l'unica sorgente di particelle importante all'interno dello strato limite. Tuttavia, questa sorgente rappresenta soltanto una frazione minoritaria del numero totale di nuclei di condensazione. La frazione rimanente è da attribuirsi al trasporto di particelle nucleate nella troposfera libera. Le misure hanno anche rilevato una grande concentrazione di acido metansolfonico intorno alla costa dell'Antartide, prodotto probabilmente attraverso l'ossidazione eterogenea del DMS. Questo processo di ossidazione potrebbe essere importante per la crescita delle particelle di aerosol, riducendo quindi la supersaturazione minima necessaria per attivarle come goccioline di nube. Inoltre, per la prima volta é stato chiarito il meccanismo alla base della formazione di nuove particelle nell'Oceano Artico centrale, rivelando il ruolo dell'acido iodico, responsabile di tutti gli eventi osservati. Si è scoperto infatti che la concentrazione di acido iodico aumenta notevolmente verso la fine dell'estate con un effetto diretto sulla formazione di nuove particelle, evento che diventa frequente

durante l'autunno. La nucleazione di aerosol atmosferico rappresenta un'importante fonte di aerosol sul ghiaccio artico e si è scoperto che le particelle secondarie formatesi possono attivarsi come nuclei di condensazione nonostante la taglia minore di 30 nm se la concentrazione di aerosol più grandi è sufficientemente bassa. Questi risultati migliorano la nostra comprensione delle particelle presenti nell'atmosfera preindustriale e sono importanti per poter rappresentare piú accuratamente gli aerosol naturali nei modelli climatici regionali e globali. Possono infatti essere utilizzati per ridurre l'incertezza associata al budget radiativo terrestre e quindi migliorare l'accuratezza delle previsioni climatiche future.

1 INTRODUCTION

1.1 ATMOSPHERIC AEROSOLS

Aerosols are fine solid or liquid particles suspended in a gas, with a size ranging from few nanometres to several tens of micrometres, also commonly termed aerosol particles or particulate matter (PM). Aerosols are ubiquitous in the atmosphere and have multifaceted effects on the Earth system: they directly affect climate by scattering and absorption of solar radiation and indirectly by acting as cloud condensation nuclei (CCN)[1]. Because they control the formation and properties of clouds they are also important for the hydrological cycle[2]. They can also have adverse effects on human health[3] and even act as a vehicle for virus transmission[4]. Despite of several decades of aerosol research our understanding of aerosol particles is still limited and important challenges need to be addressed by the scientific community in the near future[5]. One of these challenges is to provide a quantitative description of aerosols and their interactions in the Earth system. This is a demanding task because of the inherent complexity of aerosol particles: they are produced and modified by a variety of sources and processes leading to different compositions and physicochemical properties, which are heterogeneously distributed both in time and in space. This introduction will first provide a short summary of aerosol properties and their role in the climate system, followed by a more detailed part on polar regions and the role of aerosols therein. Finally, the motivations and the outline of the thesis will be provided.

1.1.1 Aerosol sources and processes

Aerosols are said to be primary if they are directly emitted to the atmosphere or secondary when generated via gas-to-particle conversion. Primary aerosol are usually formed via mechanical processes, including (1) mineral dust from wind resuspension and erosion, (2) volcanic dust, (3) sea spray from breaking waves, (4) bioaerosols generated by plants and animals from wind or other processes, (5) blowing snow from the wind stress over sea-ice and snow covered regions, (6) non-exhaust particles from traffic, like tire debris and resuspended dust, and (7) other aerosol particles related with various anthropogenic activities (construction works, mining operations, etc.)[1,6–9]. Incomplete combustion also generates an important fraction of the primary aerosol population through the formation of organic, black carbon and metal particles[1].

Secondary aerosols are formed in the atmosphere via the conversion of molecules from the gas to the condensed phase, which can happen either via direct nucleation or by condensation on pre-existing particles. Only vapours with a sufficiently low volatility will partition to the condensed phase undergoing a phase transition. These low-volatility vapours are usually produced by oxidation of more volatile species like SO_2 or volatile organic compounds (VOCs). Oxidation occurs either via chemical reactions with atmospheric oxidants in the gas phase (*i.e.* O_3, OH and NO_3) or heterogeneously with condensed phase reactions (*i.e.* in water droplets or pre-existing aerosols).

The oxidation of organic molecules proceeds via the formation of functional groups producing oxygenated molecules which are more polar and less volatile and can partition to the condensed phase[1]. Secondary organic aerosol constitutes about half of the total secondary aerosol mass with the rest being composed by sulfate, nitrate and ammonium[10].

NPF occurs in the atmosphere when gas molecules condense on each other forming a small molecular cluster, the so-called *critical nucleus*, which can either grow by condensation to larger sizes and form an aerosol particle or evaporate back into the gas phase. This process is called new particle formation or aerosol nucleation and is responsible for a large fraction of the total aerosol number concentration, with model predictions between 38% and 66% of CCN by number from NPF[11,12]. Sulfuric acid is the main responsible for NPF, because of its low vapour pressure and widespread presence in the lower troposphere. However, in the BL, sulfuric acid concentrations are generally too low for binary homogeneous nucleation and a third compound (or class of compounds) is required to stabilize the critical nucleus. Field and laboratory studies have found that, under typical atmospheric conditions, ternary sulfuric acid NPF happens via the formation of hydrogen bonding with ammonia, amines and organic acids[13–17]. NPF can also occur without the presence of sulfuric acid and be driven by other compounds such as highly oxygenated organic molecules (HOMs)[18,19] and iodine oxides[20,21] but it occurs more rarely and it is generally confined to specific locations.

Primary and secondary aerosols are defined as natural or anthropogenic depending on the source that generates them. This thesis work is focused on the investigation of natural sources of secondary aerosols in polar regions. Aerosol particles in the atmosphere are not only produced from a variety of sources but also removed by different processes. Sinks and sources are equally important in determining the actual atmospheric concentrations of aerosols. As an example, freshly nucleated aerosol particles are formed in great numbers, orders of magnitude higher compared to primary sources, however they also have a high diffusivity and are quickly lost via coagulation with pre-existing aerosol particles. The survival of newly formed particles is driven by their condensational growth into the Aitken mode size range (typically between 10 and 100 nm) where their lifetime can increase by one to three order of magnitudes, going from minutes to days[1].

Aitken mode particles reside in the atmosphere from days to weeks depending on the environmental conditions, these particles can also grow further in size by condensation of semi-volatile compounds or by aqueous phase processing (*e.g.* SO_2 uptake) when activated as CCN. Because of their small sizes, Aitken mode particles require high water vapour supersaturations (SS) to be activated in clouds. However, when activated they can quickly grow into larger sizes, reaching the so-called accumulation mode (roughly between 100 nm and 1 μm). An empirical evidence of aqueous phase processing shaping the aerosol size distribution is the presence of a characteristic dip, the Hoppel minimum, frequently measured in ambient particle size distributions (PSD) over the oceans. This minimum separates the Aitken from the accumulation mode and corresponds to the smallest size of particles which were activated in clouds and grown to larger sizes via condensation of water, droplet coalescence and uptake of soluble material. Hence, the amount of material within the droplets also increases leading to larger aerosol particles after evaporation of the droplets, a very common fate for cloud droplets[22,23]. Accumulation mode particles also have a long lifetime in the order of days to weeks, with the main loss process being wet deposition (*rainout*

for particles activated in clouds and *washout* for interstitial aerosols or particles below the clouds).

Finally, a coarse mode also exists which is composed of super-micron particles that generally have a primary origin. These particles are mainly removed via dry deposition (*i.e.* sedimentation) and are characterized by a shorter lifetime compared to the accumulation and Aitken mode size range.

In essence, the presence of distinct aerosol modes is driven by the convolution of sources, loss and transformation (*e.g.* condensational growth) processes, which result in particles accumulating in characteristics size ranges. Figure 1.1 summarizes the description of this section with an illustrative PSD, showing the different aerosol modes, the main loss terms and the formation of new particles via aerosol nucleation.

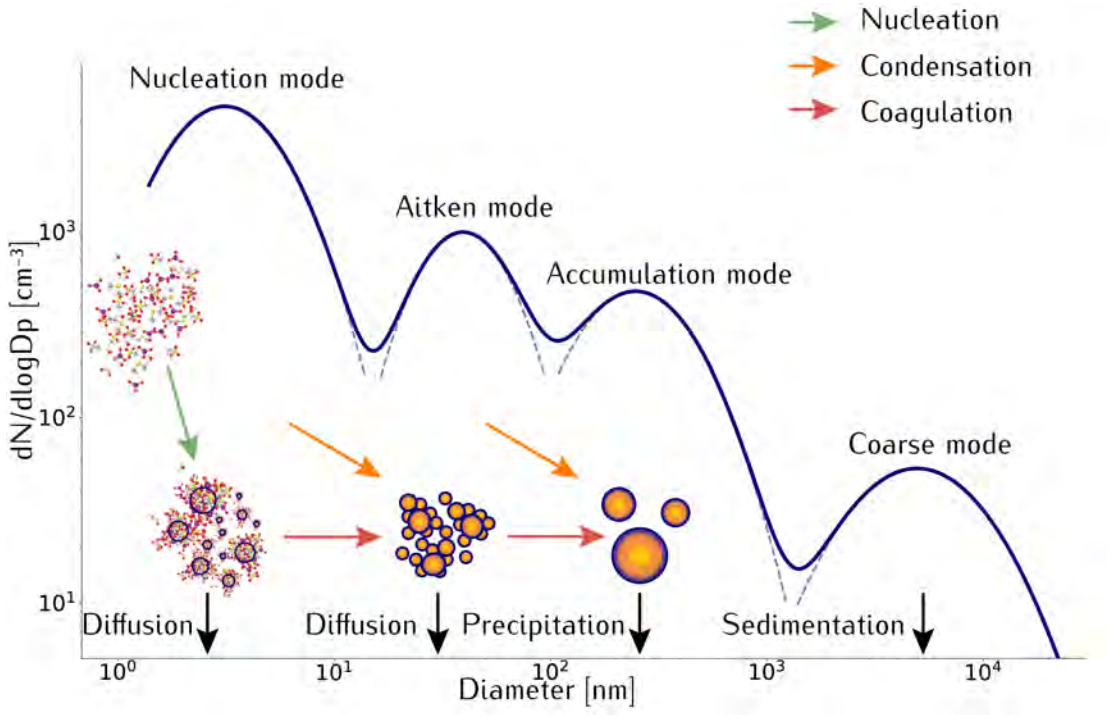

Figure 1.1: Illustrative particle size distribution with the four different characteristic aerosol modes, the black arrows indicate the predominant loss processes associated to each mode. A simple sketch illustrating the new particle formation process is also reported with gas molecules nucleating into small clusters (green arrow) and then growing into larger sizes via condensation (orange arrow) and coagulation (red arrow).

1.1.2 Aerosol effects on climate

The air temperature on Earth is increasing and current estimates attribute a 1.0 °C of global warming to human activities for the 1850 – 2017 period, with a 1σ confidence interval from 0.8 °C to 1.2 °C[24]. This 1.0 °C warming is responsible for important changes in the Earth system, affecting both natural ecosystems and human activities: there is a widespread shrinking of the cryosphere, while desertification is expanding, both with consequences, for example, for water resources. The frequency of extreme meteorological events (*e.g.* heat waves, floods and tropical cyclones) is increasing and the global mean sea level is rising, affecting coastal communities. Finally the oceans are taking up more CO_2, which results in increased acidity and reduction in the oxygen

content, impacting marine ecosystems[24,25]. This is just a selected minority of effects caused by a warming climate with the full list being much longer and still largely uncertain. According to models, the warming will continue, reaching 1.5 °C to 2.0 °C in the next few decades with even larger effects on the Earth system[24].

It is clear that the most effective way to slow down the climate warming is to substantially decrease anthropogenic greenhouse gas (GHG) emissions. Figure 1.2 shows the measured temperature record from 1960 to 2017 and the predicted increase until 2100, based on three different emission scenarios (net zero CO_2 emissions achieved in 2055 with and without reduction of non-CO_2 forcing after 2030 and net zero CO_2 emissions achieved in 2040). As intuitively expected, stronger emission reductions will be more effective in reducing global warming, however, the time by which Earth's temperature will be 1.5 °C higher is highly uncertain.

The contribution of individual drivers to the anthropogenic climate warming is defined in terms of the radiative forcing (RF), which is the change in the net radiative flux at the top of the atmosphere (expressed in W m^{-2}), with respect to a certain time period[26]. CO_2 and other GHGs are the dominant drivers of anthropogenic global warming, contributing to the largest RF, however, the uncertainty is dominated by aerosols as shown in Figure 1.3.

Aerosols scatter and absorb solar radiation (aerosol radiation interaction effect), they are also essential for cloud formation because they act as CCN or ice nucleating particles (INP) and can influence various cloud properties such as albedo and lifetime (aerosol-cloud interactions). Overall aerosols have a net cooling effect. Anthropogenic activity during the past centuries led to an increase of both primary and secondary aerosols together with GHGs, offsetting a fraction of the warming generated by the latter. As a consequence, both the aerosol radiation interaction effect and aerosol-cloud interactions have to be properly understood and accurately represented in Earth system models in order to calculate the total anthropogenic forcing on the Earth radiative balance. However, the present knowledge on aerosols and in particular on aerosol-cloud interaction is still limited and results in the single largest uncertainty among all climate forcing drivers[26], as shown in Figure 1.3.

Another important source of uncertainty stems from the impossibility to directly measure the concentration and properties of aerosols in the pre-industrial (PI) atmosphere (1750 is commonly used as the reference for PI times). This is an important difference compared to GHGs which can be more easily reconstructed from climate archives (*i.e.* ice cores, tree rings and sediments). The PI aerosol state is the baseline against which the present day (PD) forcing is calculated, hence, uncertainties in the PI aerosols reflect directly on the calculated forcing uncertainty. More importantly, the radiative forcing associated to aerosol-cloud interactions scales non-linearly with the aerosol loading and is much more sensitive to low aerosol numbers in pristine environments compared to higher aerosol loadings in the polluted PD atmosphere[29,30]. Therefore, a deeper understanding of natural aerosols, their sources and processes can have a much larger effect in reducing the aerosol forcing uncertainty compared to measurements of anthropogenic aerosols. The value of remote marine measurements in reducing the aerosol forcing uncertainty has been illustrated recently by Regayre *et al.*[31], which showed that a small set of measurements in the Southern Ocean can constrain the model uncertainty as much as thousands of measurements in the Northern Hemisphere.

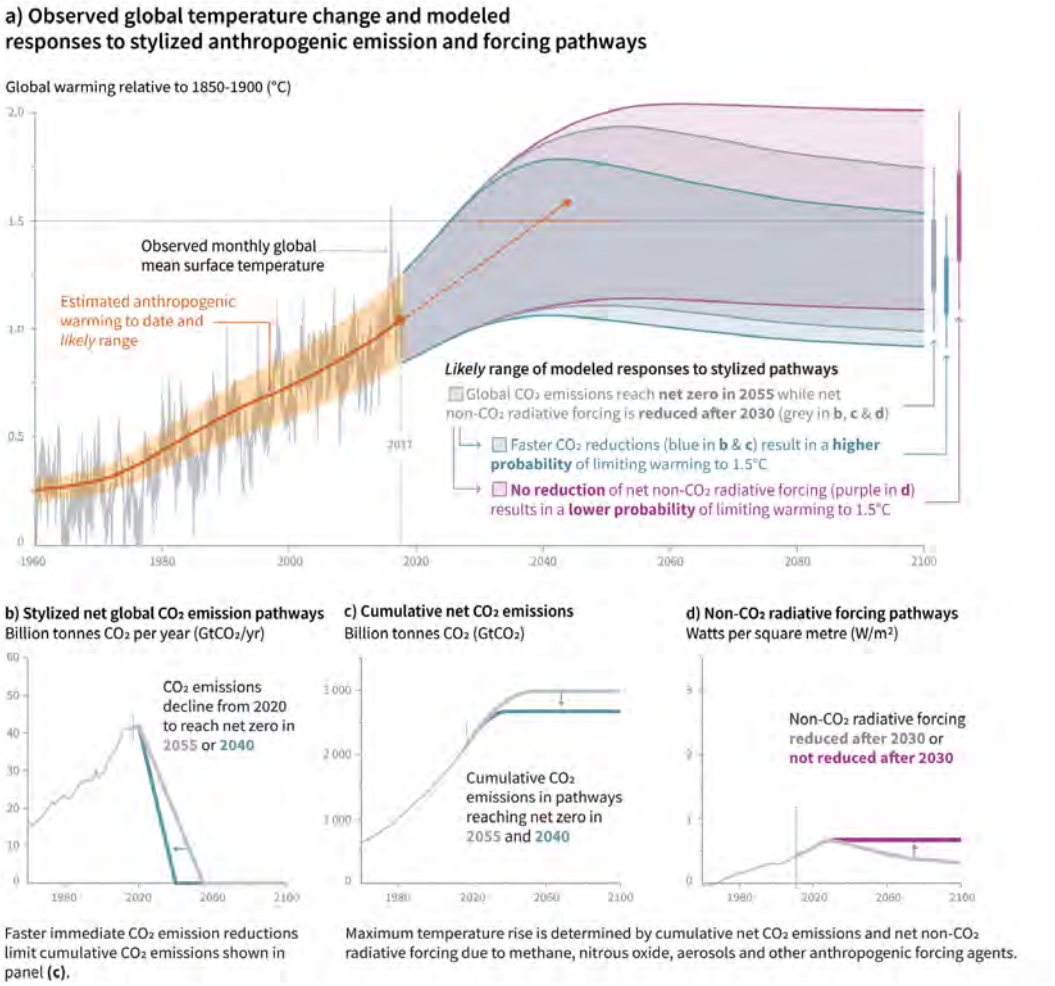

Figure 1.2: **a**: Observed monthly global mean surface temperature (GMST, grey line up to 2017, from the HadCRUT4, GISTEMP, Cowtan–Way, and NOAA datasets) change and estimated anthropogenic global warming (solid orange line up to 2017, with orange shading indicating assessed likely range). Orange dashed arrow and horizontal orange error bar show the central estimate and likely range, respectively, of the time at which 1.5 °C is reached if the current rate of warming continues. The grey plume on the right of panel **a** shows the likely range of warming responses, computed with a simple climate model, to a stylized pathway (hypothetical future) in which net emissions (grey line in panels **b** and **c**) decline in a straight line from 2020 to reach net zero in 2055 and the net non-CO_2 radiative forcing (grey line in panel **d**) increases to 2030 and then declines. The blue plume in panel **a)** shows the response to faster CO_2 emissions reductions (blue line in panel **b**), reaching net zero in 2040, reducing cumulative CO2 emissions (panel **c**). The purple plume shows the response to net CO2 emissions declining to zero in 2055, with net non-CO_2 forcing remaining constant after 2030. The vertical error bars on the right of panel **a)** show the likely ranges (thin lines) and central terciles (33rd – 66th percentiles, thick lines) of the estimated distribution of warming in 2100 under these three stylized pathways. Vertical dotted error bars in panels **b**, **c** and **d** show the likely range of historical annual and cumulative global net CO_2 emissions in 2017 (data from the Global Carbon Project) and of net non-CO_2 radiative forcing in 2011 from AR5, respectively. Vertical axes in panels **c** and **d** are scaled to represent approximately equal effects on GMST. Both the image and caption are taken from Masson-Delmotte *et al.*[24].

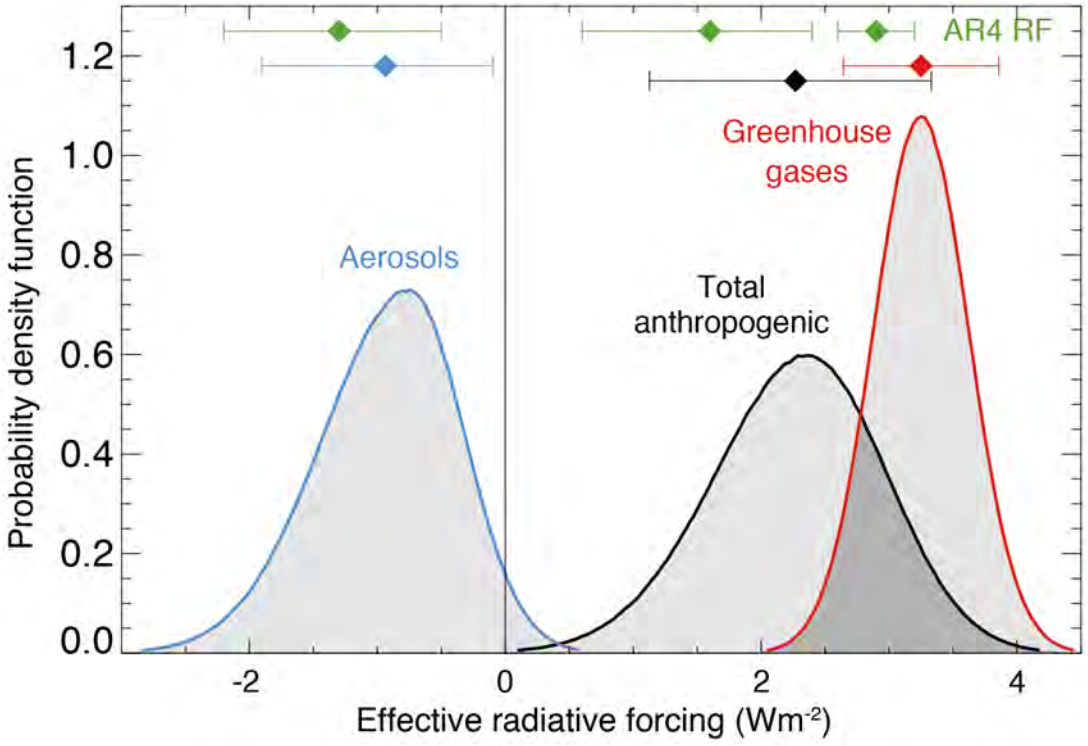

Figure 1.3: Probability density function (PDF) of the effective radiative forcing (ERF, which is the RF after accounting for rapid adjustments in the atmosphere) due to total GHG, aerosol forcing and total anthropogenic forcing. The GHG consists of well mixed GHG, ozone and stratospheric water vapour. The combination of the individual RF agents to derive total forcing over the Industrial Era are done by Monte Carlo simulations and based on the method in Boucher *et al.*[27]. Lines at the top of the figure compare the best estimates and uncertainty ranges (5 to 95% confidence range) with RF estimates from Solomon *et al.*[28]. The figure and the caption are from Stocker *et al.*[26], the caption was adapted for clarity reason, the reader is referred to chapter 8 of Stocker *et al.*[26] for more details.

1.2 CLIMATE CHANGE IN POLAR REGIONS

The Intergovernmental Panel on Climate Change (IPCC) recently produced a special report on the effect of climate changes on the oceans and the cryosphere[25] combining a large corpus of evidence to show that these remote places are severely affected by human-caused climate change, probably more than any other place on Earth. In particular, the Arctic has been warming at a rate that is two to three times higher than the global average (Arctic amplification)[32–35] with dramatic consequences on sea ice extent which is decreasing at a rate of about 13% per decade (referred to the September ice-minimum). The magnitude of these sea ice losses is unprecedented in the last 1000 years of history[25,36] and is altering Arctic marine ecosystems with changes in the net primary production and phytoplankton bloom occurrence and extent. The amplified warming is affecting also the terrestrial Arctic biome with increased forest fire occurrence and permafrost degradation[24,25].

Although the mechanisms behind Arctic amplification are still poorly understood, there is an agreement concerning the main drivers, which are for example the reduced albedo due to decreased sea ice coverage, a higher total water vapour concentration and changes in summer cloudiness[25,37]. However, the relative importance of each individual effect is still debated as well as all the potential feedback mechanisms. There-

fore, models largely struggle in reproducing Arctic temperature and predictions on the rate and magnitude of future warming are largely uncertain. An example for the mismatch between predictions and observation is the consistent overestimation of the observed sea ice coverage by the forecasts of sea ice extent[38].

Antarctica, on the other hand, has been characterized by less pronounced warming and a higher degree of regional variability. It is believed that the Southern Ocean (SO) is playing an important regulatory role for the Antarctic climate, taking up a significant fraction of the heat[39]. In fact, the uptake of heat by the SO is asymmetrically high compared to the global ocean average (45% to 62% of the global ocean heat uptake despite occupying only 25% of the total ocean surface[25]). In general, the SO acts as a short-term regulator of Earth's climate via heat uptake and exchange of water vapour with the atmosphere. However, it is not clear how these exchanges will evolve in a warming climate and also what will be the effect on the emissions of aerosol precursors (*e.g.* dimethylsulfide, DMS) or primary particles directly (*i.e.* westerly winds around Antarctica have been increasing over the past decade and this can have a direct effect on seaspray aerosol fluxes[40])[25].

To conclude, there is a variety of interconnected processes that regulate and control changes in polar regions and their response to global climate warming. However, a proper understanding is missing calling out for detailed process based studies, ideally based on a strong interdisciplinary approach to investigate the coupling between the cryosphere, the atmosphere and the oceans.

1.2.1 Aerosols and new particle formation in the Southern Ocean

During summer in the Southern Ocean the transport of anthropogenic aerosols is inhibited by the Antarctic Circumpolar Vortex, which acts as a barrier for airmass transport from mid to high latitudes. Local sources of aerosol are therefore prevalent in the Southern Ocean, and measurements here can be used to characterize natural sources of marine aerosols with very limited anthropogenic influence[41–43]. Undisturbed measurements of natural aerosols can be used to constrain the PI aerosol baseline which is the main source of uncertainty in global climate models[29,31].

Major sources of aerosols in the Southern Ocean are sea spray, which includes both sea salt and marine organics, and secondary aerosols formed from the oxidation of DMS, a volatile organic compound produced by phytoplankton in the sea water. The contribution of sea spray to the total CCN number varies largely depending on the region and the environmental conditions (mainly wind speed and sea state), previous measurements reported values varying from 10% to 100%[42,44,45]. The DMS-derived CCN fraction is often dominant[42] and mainly composed by non-sea-salt sulphate and methanesulfonate[45,46]. In this case, DMS is oxidized into sulfuric acid which nucleates either with water alone, if temperature is sufficiently low, or more often with a third stabilizing compound, mainly ammonia[13,15,47]. To act as a CCN, nucleated particles have to grow in size and this happens via condensation of low-volatility species, mainly sulfuric acid and methanesulfonic acid (MSA), another oxidation product of DMS. If a particle activates in a cloud it will grow even more via aqueous uptake of SO_2 and to a lesser extent MSA[1,48]. This process does not produce new CCNs but reduces the supersaturation required to re-activate the particle after dissipation of the cloud, which is common in the marine environment[22].

There have been several studies investigating aerosol properties in the Southern Ocean (see for example Figure 1 and Table 1 in Schmale *et al.*[42]). However, NPF

is still poorly understood in the region, despite the relevance of this process for the CCN budget[49,50]. In particular, there have been very few reported observations of NPF in the Southern Ocean[51,52] and this contrasts with measurements in Antarctica, which reported frequent occurrence of NPF during summer with air masses originating from the Southern Ocean[15,53–55]. Modelling works suggested that NPF may be occurring preferentially in the free troposphere, where temperature is lower and conditions more favourable[56,57]. This hypothesis seems to be supported by some field studies which reported a higher concentration of newly formed particles above the boundary layer[47,58]. However, there are no observations of these particles growing into a relevant size for CCN activation (*e.g.* above 70 nm) and, with the average sulfuric acid concentrations in the SO (between 10^6 and 10^7 molecule cm^{-3})[15,47,59], it would take several days to grow a newly formed particle to 70 nm or larger sizes[60]. Additionally, models tend to strongly underestimate the CCN concentration around the coast of Antarctica when compared against measurements[42,50], indicating that an aerosol source may be missing.

Therefore, aerosol measurements investigating the role of NPF as a CCN source in the SO and the distribution of relevant trace gases (*e.g.* sulfuric acid, MSA and iodic acid) are required to fill this knowledge gap. These data would be valuable to better understand natural sources of aerosol in a pre-industrial like marine environments, which could be better constrained in global climate models reducing the aerosol radiative forcing uncertainty.

THE ANTARCTIC CIRCUMNAVIGATION EXPEDITION The Antarctic circumnavigation expedition (ACE), organized by the Swiss Polar Institute, took place from December 2016 to March 2017 sailing around Antarctica across the Southern Ocean on board of the Russian icebreaker *Akademik Tryoshnikov*. This expedition was characterized by a strong interdisciplinary approach with 22 different projects investigating a very broad spectrum of topics. A map of the expedition is reported in Figure 1.4.

This thesis includes results from *the Study of Preindustrial-like Aerosol and their Climate Effect* (ACE-SPACE) project (Chapters XX and YY [insert ref.]), which was centred around investigations of aerosol-cloud interactions in preindustrial-like conditions.

1.2.2 Aerosols and new particle formation in the central Arctic Ocean

In the Arctic, clouds play a critical role for the surface radiative budget influencing, for example, the thickness and extent of sea ice[61,62]. It is also thought that clouds could exert a negative feedback on the Arctic system, slowing down the warming[37]. However, models are not able to accurately represent clouds, especially when CCN concentrations are low[63,64]. In the summertime Arctic, particle concentrations are typically very low over the pack ice and clouds are often limited by the availability of CCNs[65,66]. Under this *CCN-limited* cloud regime, a small increase of the CCN concentration can lead to a pronounced increase of surface warming due to the augmented liquid water content and the associated long-wave radiation change[65]. Therefore, understanding the sources and evolution of aerosols in the central Arctic Ocean is crucial to model the formation and the properties of clouds.

Studies in the central Arctic Ocean are limited due to the remoteness of the site and the thick pack ice through which ships have to navigate in order to reach this region. Previous observations in the region have reported a variety of different particle sources, including typical primary and secondary marine aerosols but also long-range

transport of continental emissions[67–70]. The mechanism behind the formation of new particles in the region has been particularly controversial. In fact, NPF has been observed since the first aerosol measurements in the region in 1991[71,72] but the origin of nucleating particles was not identified. In particular, sulfuric acid nucleation was ruled out because estimated concentrations could not explain the observed nucleation rates[73,74]. A mechanism based on the fragmentation of large primary particles into thousands of nanoparticles was also proposed but so far there has been no experimental evidence that such a process could occur[75]. Additionally, a model study showed that NPF was essential to reproduce the observed PSD in the central Arctic Ocean but an artificially high nucleation rate had to be used for the simulations[76].

A direct molecular characterization of the nucleating vapours is the preferred way to elucidate the nucleating mechanism in the central Arctic Ocean and understand the source of these newly formed particles. The knowledge of this mechanism would also help improving the representation of Arctic aerosol sources in climate models and constrain the contribution of NPF to the Arctic CCN budget.

THE ARCTIC OCEAN 2018 EXPEDITION The Arctic Ocean 2018 (AO18) expedition, organized by the Swedish Polar Research Secretariat, took place in August and September 2018 on board the Swedish icebreaker Oden. The expedition was structured in three phases: a first part of transit from Svalbard up to the central Arctic Ocean, a second, longest phase, of ice drifting with the ship moored to an ice floe and a final return stage. This expedition was more focused on the investigation of aerosol sources and processes in the central Arctic Ocean with a broad range of different techniques and complementary approaches. A map of the expedition is shown in Figure 1.4.

The *Microbiology–Ocean–Cloud-Coupling in the High Arctic* (MOCCHA) project, whose results are presented in this thesis, was focused on investigating the sources of CCNs, including NPF, with online characterization of both total, interstitial and activated aerosol particles inside and outside of clouds.

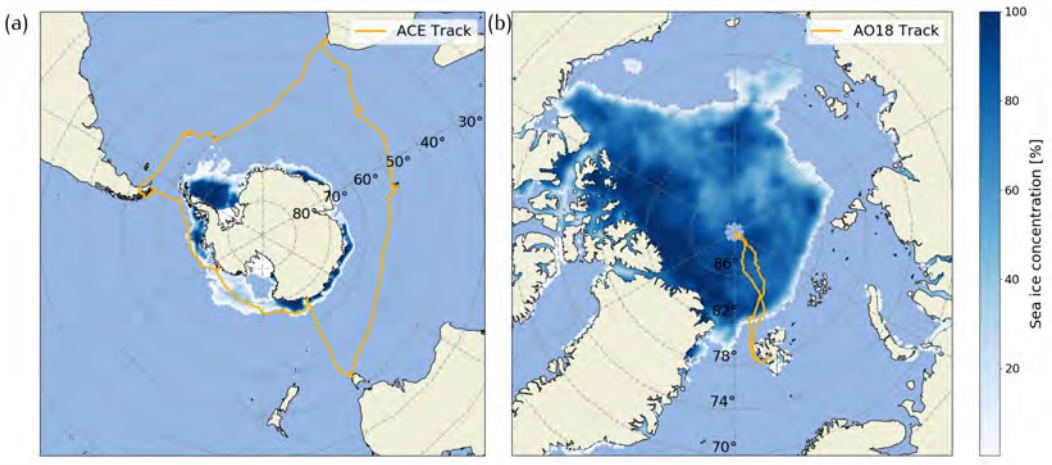

Figure 1.4: Expedition maps: **(a)** map of the ACE and **(b)** map of the AO18 expedition. On both maps the fractional sea ice concentration is also reported. The sea ice concentration shown in panel (a) is the average for January 2017 while panel (b) shows the concentration retrieved for 15 September 2018[77].

1.3 RESEARCH QUESTIONS AND THESIS OUTLINE

The overarching theme of this thesis is to characterize new particle formation processes in polar regions in terms of sources, physico-chemical properties and relevance for the CCN budget. The main research questions are:

- What are the mechanisms and the gas species responsible for NPF in polar regions and which are the sources of these gaseous precursors?
- How often is NPF happening and what are the main drivers regulating its occurrence?
- What is the contribution of NPF to the CCN budget and how significant is this process in controlling the formation of clouds and their properties?

These questions were addressed by means of direct in-situ measurements during two expeditions at the two different poles as previously described. In particular, a large suite of instruments was deployed during both campaigns to measure the full spectrum of aerosol properties with a subset specifically targeted to investigate NPF processes and to measure the chemical composition, physical properties and concentration of nucleating vapours and newly formed particles.

Chapter 2 provides a short description of the theoretical framework behind nucleation, particle growth and CCN activation.

Chapter 3 describes the instruments, the measurement set-up and the methodology applied to process and analyse the data collected during the two expeditions. In particular, a considerable part of the chapter is focused on the description of the calibration of a mass spectrometer, which was used to measure nucleating vapours during both expeditions. Furthermore, a novel approach to identify ship exhaust pollution and separate it from the ambient signal is presented.

Chapter 4 presents an overview of the ACE-SPACE project, describing the overarching research goals of the expedition and the first results. In particular, micro-physical aerosol properties across the Southern Ocean are described in conjunction with model predictions and remote sensing observations.

Chapter 5 describes more in detail NPF during the ACE expedition. A characterization of trace gases that are relevant for nucleation (*i.e.* sulfuric acid, iodic acid and methanesulfonic acid) and their distribution across the SO is provided with considerations about potential sources and processes regulating their concentration. Furthermore, the occurrence of NPF events and their significance for the CCN budget in the SO is discussed.

Chapter 6 presents the results from the AO18 expedition, describing nucleating vapours and NPF occurrence over the Arctic pack ice. It analyses the temporal variability and in particular the changes associated with the transition from summer into autumn and the formation of new sea ice. Additionally, the connection from new particle to cloud condensation nuclei formation is explored by means of direct measurements of cloud residuals.

In the Conclusions (Chapter 7) the results of the thesis are summarized and their implications are discussed in a broader context. Limitations of this study will also be discussed together with recommendation for further research.

2 THE PHYSICAL BASIS

2.1 NEW PARTICLE FORMATION

Aerosol nucleation can be described as the clustering of gaseous molecules to form small aerosol particles in the nm-size range. In the atmosphere most of these newly formed particles are lost via coagulation but a small fraction will survive growing to larger sizes where they can eventually act as CCN and influence Earth's climate. Globally, NPF is an important process which accounts for about half of the CCNs produced worldwide according to models[11,12].

The theory of nucleation essentially describes any phase transition from a phase α to a phase β that is characterized by an energy barrier, preventing phase β to form even when the latter is the thermodynamically stable phase. For atmospheric applications, nucleation theory is typically applied to describe transition from the gas to the condensed phase (either solid or liquid) or from the liquid to the solid phase (*i.e.* ice formation). The condensation of vapours is the relevant process to describe NPF and the kinetic gas theory is also more developed compared to liquids. Here, only vapour nucleation will be described as it is the relevant process studied in this thesis.

Nucleation is said to be *homogeneous* when only vapour molecules are included and *heterogeneous* if a third body, like a surface, is involved. Moreover, if only one species is condensing the nucleation process is called *homomolecular*, otherwise it is defined as *heteromolecular*. This classification results in four types of different nucleation processes[1]. Under real atmospheric conditions nucleation is generally *heteromolecular* and often *heterogeneous* but the theory behind these processes is complex and in this section only the classical theory of homogeneous nucleation will be described.

A vapour A needs to be supersaturated with respect to its condensed phase in order to homogeneously nucleate. However, even in supersaturated conditions an energy barrier prevents the condensed phase to form and the vapour phase would persist in a metastable phase. This energy barrier can be explained by surface-free energy considerations (*i.e.* the Kelvin effect). The degree of supersaturation can be defined as the saturation ratio S:

$$S = \frac{p_A}{p_A^s(T)}, \tag{2.1}$$

where p_A is the vapour pressure of gas A and $p_A^s(T)$ is the gas saturation vapour pressure in equilibrium with its condensed phase at temperature T. A higher supersaturation leads to a lower energy barrier which would make the nucleation process more favourable. Homogeneous nucleation is a stochastic process with the continuous formation and destruction of molecular clusters by condensation and evaporation of gas molecules. There is a critical size for these clusters after which they become stable and can grow spontaneously, forming larger particles. This critical size corresponds to the maximum of the energy barrier and is the the so-called *critical nucleus*.

Homogeneous nucleation can be described based on thermodynamic equilibrium considerations, and in particular in terms of the variations of the Gibbs free energy (G) of the system[78]:

$$G = N_\alpha \mu_\alpha + N_\beta \mu_\beta, \tag{2.2}$$

with α and β being the vapour and condensed phase, respectively, N the number of molecules and μ the chemical potential. The change in the Gibbs free energy when a new cluster is formed is:

$$dG = \mu_\alpha dN_\alpha + \mu_\beta dN_\beta + \sigma dA \tag{2.3}$$

$$= \left(8\pi\sigma r - \frac{4\pi r^2 \Delta\mu\, \rho_\beta}{m}\right) dr \tag{2.4}$$

with σ being the surface tension of the cluster, $A = 4\pi r^2$ the cluster surface, m and ρ_β the cluster mass and density, respectively[1]. The change in chemical potential, $\Delta\mu = \mu_\alpha - \mu_\beta = kT\ \ln(S)$, is positive since the condensed phase is the thermodynamically stable phase when $S > 1$. Equation 2.4 can be integrated, giving:

$$\Delta G(r) = G(r) - G(0) = 4\pi\sigma r^2 - \frac{4\pi\Delta\mu\, \rho_\beta}{3m} r^3, \tag{2.5}$$

with the first and the second term on the right hand side of the equation representing the contribution of the surface tension and of the chemical potential, respectively. The equilibrium is obtained when $dG(r)/dr = 0$, that is when the radius of the cluster equals a critical size r_{crit}:

$$r_{\text{crit}} = \frac{2\sigma m}{\rho_\beta \Delta\mu}. \tag{2.6}$$

Figure 2.1 shows the Gibbs free energy as a function of the cluster size for three different thermodynamic conditions: (1) $S < 1$ that is homogeneous nucleation does not occur because the vapour phase is the thermodynamically stable configuration, (2) $1 < S < S^{\max}$ that is the situation described above with new particle formation being hindered by the presence of an energy barrier and (3) $S > S^{\max}$ when no energy barrier exists and each cluster freely grows into a new particle.

At the equilibrium, for $S > 1$, clusters will be distributed following a Boltzmann distribution:

$$N_i^{eq} = N_1 \exp(-\Delta G_i / kT), \tag{2.7}$$

with i being the number of molecules in the cluster. From the cluster distribution it is possible to derive a nucleation rate (J), which is the net number of clusters growing above the critical size per unit time as a function of temperature, saturation ratio and molecular properties:

$$J = C \exp(-\Delta G_{\text{crit}} / kT), \quad \Delta G_{\text{crit}} = \frac{4\pi}{3} \sigma r_{\text{crit}}^2. \tag{2.8}$$

C is a pre-exponential factor, which also depends on the properties of the condensing species and on the saturation ratio, for further details the reader is referred to Seinfeld *et al.*[1].

The theory described so far is useful as an illustrative example to describe the underlying physics behind the nucleation process. However, the classical nucleation theory

1 One of the main assumptions of the classical nucleation theory is the attribution of bulk properties to the critical cluster.

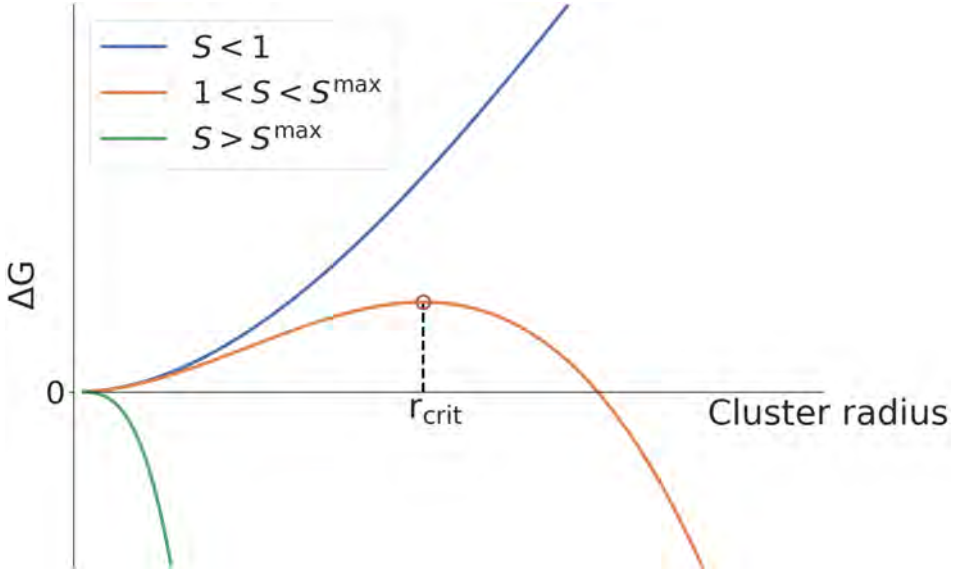

Figure 2.1: Free energy diagram for a nucleation process as a function of the cluster size for three different saturation ratio regimes.

has some important shortcomings (*e.g.* bulk properties are used to describe the critical cluster properties) which can lead to substantial differences between the predicted and observed nucleation rates. Therefore, results from the classical theory should be interpreted more on a qualitative basis. They can be useful to understand the effect of various parameters, mainly T and S, on the formation of the critical cluster and on the nucleation rates, but they should not be extrapolated directly to the real atmosphere. More practical approaches to model nucleation processes in the real atmosphere are based on numerical solutions of the general dynamic equation[79,80]. However, a description of these methods falls outside the scope of this thesis.

2.2 AEROSOL GROWTH

Newly formed nanometre-size particles have a high diffusivity and can be quickly lost by coagulation with pre-existing aerosol surfaces. Their only possibility to survive is to grow to a larger size, where their lifetime would be significantly longer. Figure 2.2a shows that the coagulation coefficient steeply decreases as a function of particle size. Under typical atmospheric conditions, growth occurs via condensation of gaseous compounds that are sufficiently low in volatility to partition into the condensed phase. In general, the mass flux of gas molecules from a species i towards a particle is driven by the difference between the vapour pressure of i (p_i) and the equilibrium vapour pressure above the particle surface ($p_{eq,i}$):

$$\frac{dm}{dt} = \frac{2\pi d_p D_i M_i}{RT} f(Kn, \alpha)(p_i - p_{eq,i}). \tag{2.9}$$

This equation explains the change in mass over time of a particle having a diameter d_p, caused by condensation of species i with molecular weight M_i. The factor $f(Kn, \alpha)$ is a correction term to account for non-continuum effects, it depends on the Knudsen number (Kn) and the accommodation coefficient α and becomes important when the mean free path of the gas molecule is comparable to the particle size.

Generally, the equilibrium vapour pressure over the particle surface depends both on the particle size (Kelvin effect) and its chemical composition (Raoult law). However, for compounds with sufficiently low volatility compounds like sulfuric acid and HOMs, $p_{eq,i}$ can be considered negligible and condensation can be treated kinetically in terms of collisions between the gas molecules and the particle. In particular, the collision rate between vapour molecules and an aerosol particle is:

$$k = \underbrace{\frac{4}{3} Kn\, df(Kn, \alpha)}_{\gamma} \underbrace{\frac{\pi}{4}(d_p + d_v)^2 + (c_p^2 + c_v^2)^{1/2}[C_v]}_{k_{kin}}, \tag{2.10}$$

with d_v being the diameter of the vapour molecule, c_p and c_v the thermal speed of the particle and the gas molecule, respectively, and $[C_v]$ the concentration of the gas species. The first term of the equation, γ, represents a correction for the transition regime and the second term, k_{kin}, is the collision rate constant in the kinetic regime. The collision rate can be converted into a particle growth rate (GR) assuming that the molecular volume can be approximated with its bulk phase properties[81] (*i.e.* $V_v = m_v/\rho_v$, with ρ_v being the vapour condensed phase density and m_v its molecular mass):

$$\mathrm{GR} = \frac{d\, d_p}{dt} = \frac{\gamma}{2\rho_v}\left(1 + \frac{d_v}{d_p}\right)^2 \left(\frac{8kT}{\pi}\right)^{1/2} \left(\frac{1}{m_p} + \frac{1}{m_v}\right)^{1/2} m_v[C_v], \tag{2.11}$$

where m_p is the mass of the particle.

Equation 2.11 can be used to estimate the contribution of a compound of interest to the growth of an aerosol population when the gas molecule concentration is known. However, when dealing with strongly polar molecules, like sulfuric acid, which tend to form stable hydrates under atmospheric conditions it is important to use the properties of the hydrated molecule in Equation 2.11.

It is difficult to measure a hydrated molecule in its native form without disturbing it. Therefore, it is common to infer the hydration from theoretical calculations. For example, quantum chemical calculations predict that at 80% RH each sulfuric acid molecule would be prevalently bound to three water molecules[82], with this ratio the density of the sulfuric acid-water solution can be inferred from bulk phase data[83]. Figure 2.2b shows the effect of hydration on the sulfuric acid growth rate as a function of particle size.

The collision rate can also be enhanced by attractive van der Waals forces between gas molecules and particles when the latter are sufficiently small[84]. Stolzenburg *et al.*[60] recently found that this effect is important for sulfuric acid growth of sub-10 nm particles at atmospherically relevant conditions and should be considered in the analysis of atmospheric growth rates when sulfuric acid is included. As a reference, Figure 2.2b reports the van der Waals enhancement factor as parametrized by Stolzenburg *et al.*[60].

2.3 CLOUD CONDENSATION NUCLEI

Formation of cloud droplets is also a nucleation process and the theory described in Section 2.1 can be directly applied to describe the homogeneous nucleation of water

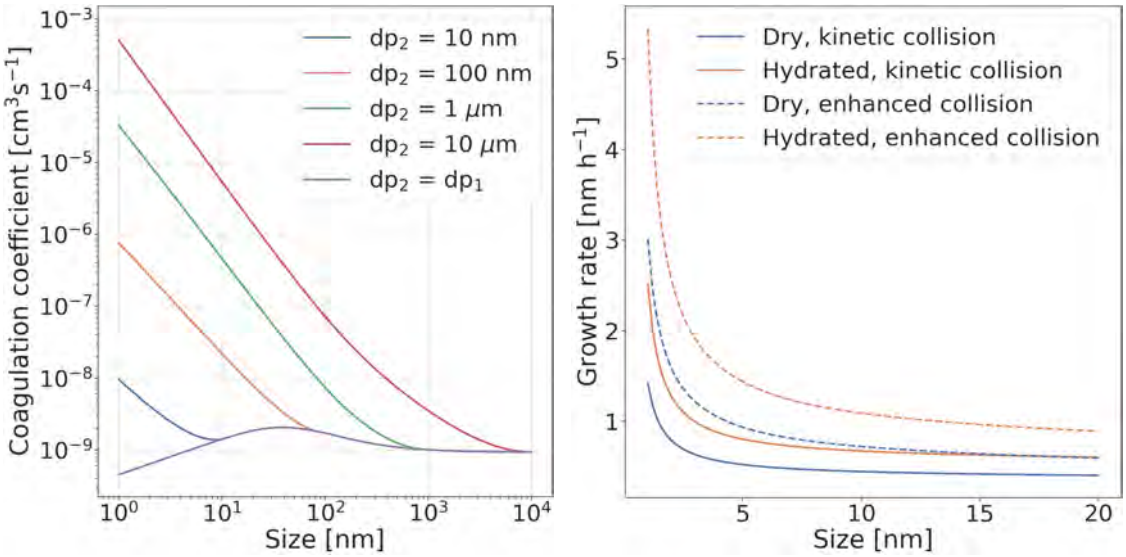

Figure 2.2: Coagulation and growth. **(a)** shows the coagulation coefficient between two different particles with diameters dp_1, given by the x-axis, and dp_2, represented by the different lines in the graph. The purple line on the bottom of the graph represents the self coagulation coefficient for two particles having the same size. The coagulation coefficient was calculated using the Fuchs equation[1]. **(b)** Particle growth rate due to sulfuric acid condensation as a function of particle size. The calculation was performed considering a single sulfuric acid molecule and a hydrate with 3 water molecules assuming kinetic condensation, the enhancement due to van der Waals forces is shown with the dotted lines. The calculation was performed at 273 K considering a sulfuric acid concentration of 1×10^7 molecules cm^{-3}.

molecules. In particular Equation 2.6 can be written in terms of the critical saturation ratio:

$$\ln(S_{\text{crit}}) = \frac{2\sigma_w m}{\rho k T r_{\text{crit}}}, \tag{2.12}$$

where the definition of the chemical potential was used, $\Delta\mu = kT \ln(S)$. This equation is known as the Kelvin equation and describes the equilibrium saturation ratio as a function of the droplet radius, which is always larger than the corresponding equilibrium saturation ratio over a flat surface. The classical nucleation theory can be used to infer the rate of formation of pure water droplets under atmospherically relevant conditions: at a water vapour saturation ratio of 2 at 293 K the water droplet formation rates would be about 10^{-54} droplets cm^{-3} s^{-1}[1], this means that about 10^{46} years would be required to form one droplet in a centimetre cube (as a reference the Earth is about 4.5×10^9 years old). Yet, most of the Earth surface is covered in clouds that usually form at much lower saturation ratios (the majority of clouds in the atmosphere is characterized by $S < 1.1$[85]). This is possible because atmospheric droplets form heterogeneously by condensation on aerosol particles: virtually all cloud droplets contain a dissolved solute which reduces the equilibrium vapour pressure lowering the energetic barrier for nucleation. This effect can be described by the modified Raoult's law:

$$p_w(T, x_w) = p_w^s(T)\gamma_w x_w, \tag{2.13}$$

with x_w being the mole fraction of water and γ_w the water activity coefficient. The Raoult's law (Eq.2.13) can be combined with the Kelvin equation (Eq.2.12) to give the equilibrium vapour pressure over a solution droplet:

$$\frac{p_w(d_d)}{p_w^s} = \gamma_w x_w \frac{4\sigma_w v_w}{\rho R T d_d}, \tag{2.14}$$

with d_d being the droplet diameter and v_w the partial molar volume of water. The water activity coefficient can be made explicit to obtain the Köhler equation[1]:

$$\ln\left(\frac{p_w(d_d)}{p_w^s}\right) = \underbrace{\frac{4M_w\sigma_w}{RT\rho_w d_d}}_{\text{Kelvin term}} - \underbrace{\frac{6n_s M_w}{\pi\rho_w d_d^3}}_{\text{Raoult term}}, \tag{2.15}$$

where M_w is the molar mass of water and n_s is the number of solute moles. The combined effect of the Raoult and the Kelvin terms, with the former dominating at small droplet diameters and the latter at larger sizes, give the very well known equilibrium curve for water droplets in the atmosphere, which is reported in Figure 2.3. This curve has a maximum corresponding to a critical droplet diameter ($d_{d,\,\text{crit}}$). Droplets smaller than this critical value are in a stable equilibrium and can follow ambient variations of relative humidity adjusting their size. On the other hand, droplets above this critical diameter are in an unstable configuration and small fluctuations in the ambient RH can make them growing to very large sizes, orders of magnitude larger than the original aerosol particle on which the droplet was formed. From a meteorological point of view $d_{d,\,\text{crit}}$ also defines the threshold above which droplets are effectively considered as cloud droplets.

According to the Köhler equation, the activation of an aerosol particle into a cloud droplet depends both on the size and the chemical composition of the aerosol (the size effect is also shown in Figure 2.3). Therefore, in a real case scenario, larger and more hygroscopic particles are the first to activate and as soon as they are activated they can grow spontaneously taking up a significant amount of water vapour and reducing the supersaturation inside the cloud, hence preventing other particles to activate. This effect is what generally limits the peak supersaturation inside a cloud, apart from strong convective systems with very high updraught velocities which can sustain the SS. However, in pristine locations where the aerosol concentration is very low, SS can reach relatively high values even with moderate updraught velocities because the water vapour in excess is not immediately depleted by droplet formation[21,56,66].

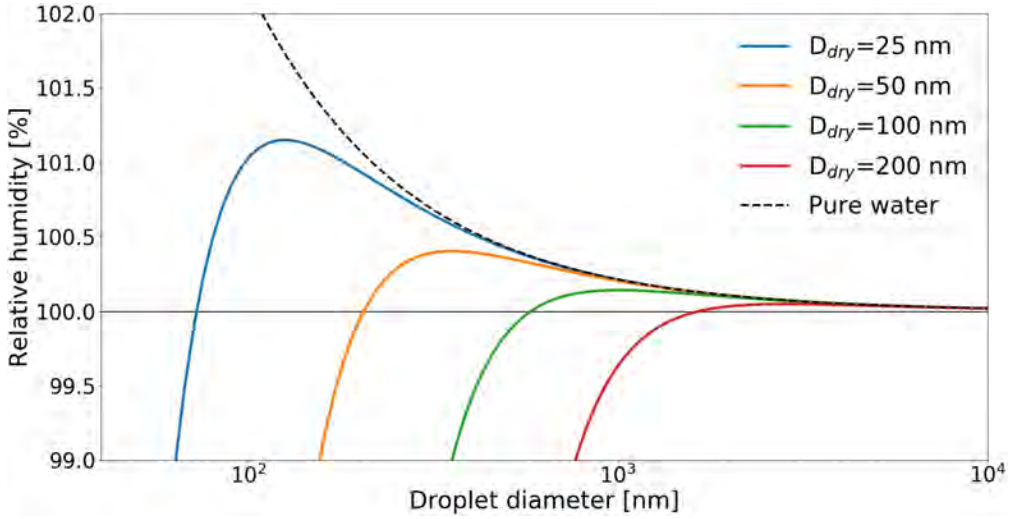

Figure 2.3: Formation of a cloud droplet. The figure shows the equilibrium RH for water droplets forming on ammonium sulphate aerosol particles with different dry diameters. For comparison also the Kelvin term (dashed black line) is reported.

3 METHODS

In this chapter the main instruments used for this thesis work are introduced and their calibration as well as the data handling procedures are described. In particular, in Section 3.1.1 the Atmospheric Pressure Interface Time-of-Flight Mass Spectrometer (APi-ToF, Tofwerk AG)[86] and its variant coupled with a chemical ionization inlet (CI-APi-ToF)[87] are described. This is a fundamental instrument for the research presented in this work because it can characterize in real-time the chemical composition of the nucleating molecules and clusters, providing a clear understanding of the chemical processes behind new particle formation (NPF). Moreover, in Section 3.1.3, a short description of the instruments that were used to measure the number concentration and size distribution of aerosol particles is provided. Section 3.2 describes the measurement set-up and the inlet lines used during both campaigns. Section 3.3 focuses on the description of one of the most critical aspects for atmospheric measurements on research vessels, *i.e.* the contamination from the ship exhaust, and two different methods that were developed to identify and separate data affected by self-pollution are illustrated. Finally, the motivation and a short description on the importance of providing data and possibly also data analysis codes in open repositories for a better accessibility and reproducibility of experimental results are provided.

3.1 INSTRUMENTATION

3.1.1 Gas phase instruments

APi-ToF

The APi-ToF is a time-of-flight (ToF) mass spectrometer with a dedicated atmospheric pressure interface (APi) which can be used to sample atmospheric ions directly into the analyser. Figure 3.1 shows a simple scheme of the instrument. The APi consists of the first three chambers where ions are focused by means of two quadrupoles and an ion lens assembly, while neutral gas molecules are pumped out. A combination of a scroll pump and a 3-stage molecular turbo pump are used to obtain incrementally higher vacuum in the various sections of the instrument. After the APi, the ions enter into the ToF region where they are accelerated further and detected by a microchannel plate detector. The mass to charge ratio of the ions is determined based on their time of flight inside the analyser. The flow inside the instrument is regulated by a critical orifice in front of the APi. For this study an 0.3 mm orifice was used, which generated a flow of about 0.8 lpm. The mass resolution (R) of the instrument, defined as the mass to charge ratio over the peak width at half maximum, is principally determined by the size of the ToF analyser and to a minor extent by the tuning of the instrument. For the work presented in this thesis we used the *H-ToF* version of the analyzer manufactured by Tofwerk AG, which has a typical resolution of $4000 - 5000$ Th/Th. The mass resolving accuracy of the APi-ToF is generally better than 10 ppm and the ion transmission efficiency within the instrument around 1%.

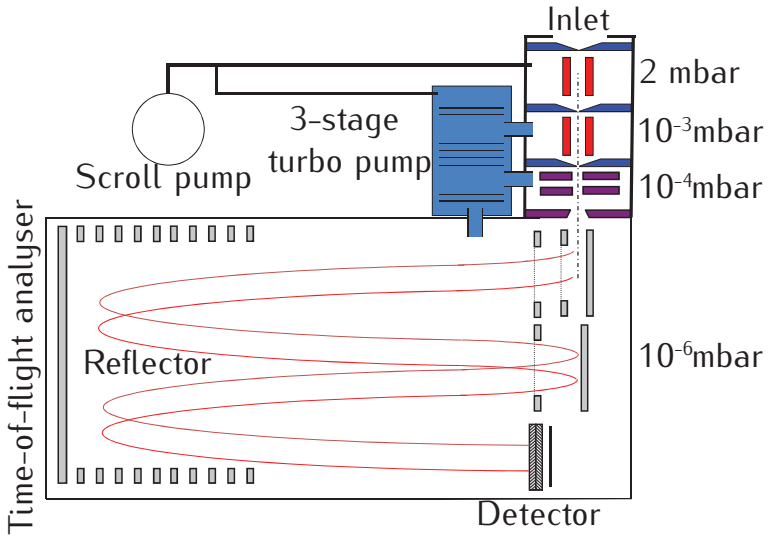

Figure 3.1: A simplified schematic of the APi-ToF adapted from Junninen *et al.*[86]. The two quadrupoles in the APi are represented with the vertical red bars, while the horizontal purple bars show the ion optics section. The red lines indicate a typical ion trajectory within the ToF analyser. The pressure inside each instrument section is reported on the right side of the schematic.

Mass spectra are acquired at a high rate (usually between 10 and 20 kHz) and averaged on the analogue to digital converter (ADC) before being sent to the computer, a typical ADC averaging time is around 1 s. The raw data were analysed using TofTools, a Matlab package developed by the University of Helsinki[86].

Figure 3.2 shows a negative-ion mass spectrum representative of a clean summer Arctic atmosphere. Reading and interpreting ambient mass spectra is generally complicated due to the large variety of different compounds present in the atmosphere. A very useful tool to visualize mass spectra and identify different classes of compounds is the mass defect (MD) plot, where the MD of each molecule is plotted against its mass. The MD is defined as the difference between the exact mass of a molecule and its nominal unit mass (*e.g.* hydrogen has an exact mass of 1.0078250 and its mass defect is 0.007825, iodine's exact mass is 126.90447 and its mass defect is -0.09553). In an MD plot, classes of molecules that share a similar structure would appear along lines or bands depending on the molecular composition. This is particularly evident during NPF events, where the nucleating clusters originate from the sequential addition of one or more molecules (*e.g.* sulfuric or iodic acid). Figure 3.3 shows an MD plot during an iodine new particle formation event: the large negative MD of the iodine atom makes all the clusters closely align on a negative slope in the MD plot.

CI-APi-ToF

The APi-ToF can be coupled with different types of inlets to characterize neutral molecules in the atmosphere[88]. For the measurements presented in this thesis a nitrate chemical ionization (CI) inlet[87,89] was used, which is suited to measure strong acids and highly oxygenated species. The working principle of this inlet is relatively simple: nitric acid is added to a sheath flow of clean air and ionized with a soft x-ray lamp. Nitrate ions are then guided inside the sample flow by means of a static electric field, ionizing trace gases in the ambient air via the following reactions:

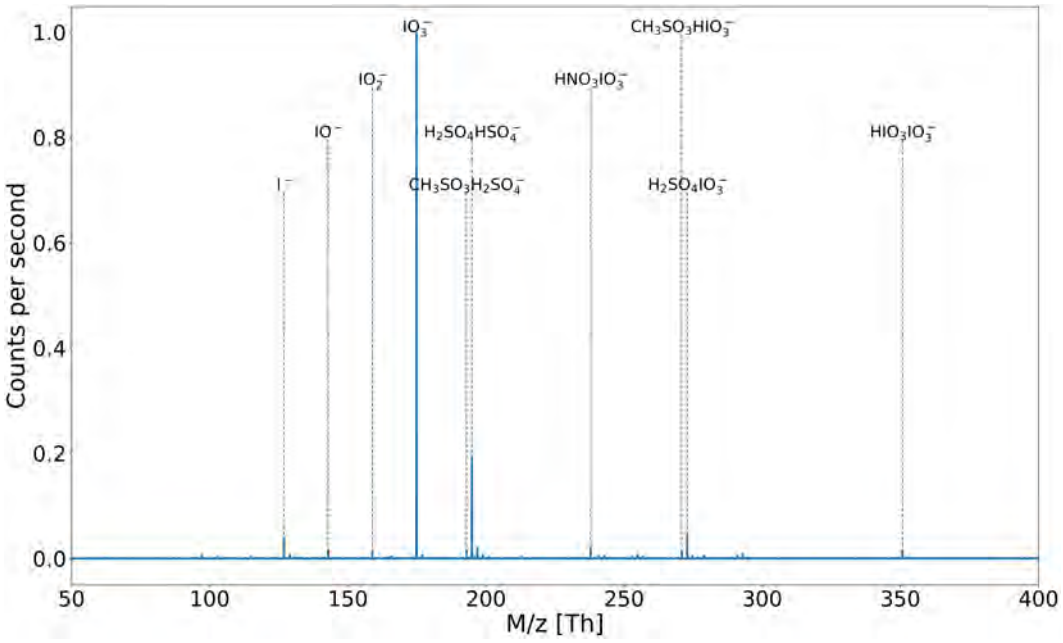

Figure 3.2: An example of a summertime mass spectrum measured during AO18 showing the chemical composition of negatively charged natural ions. The chemical composition of the ten most prominent peaks is reported. The mass spectrum is clearly dominated by iodine containing compounds.

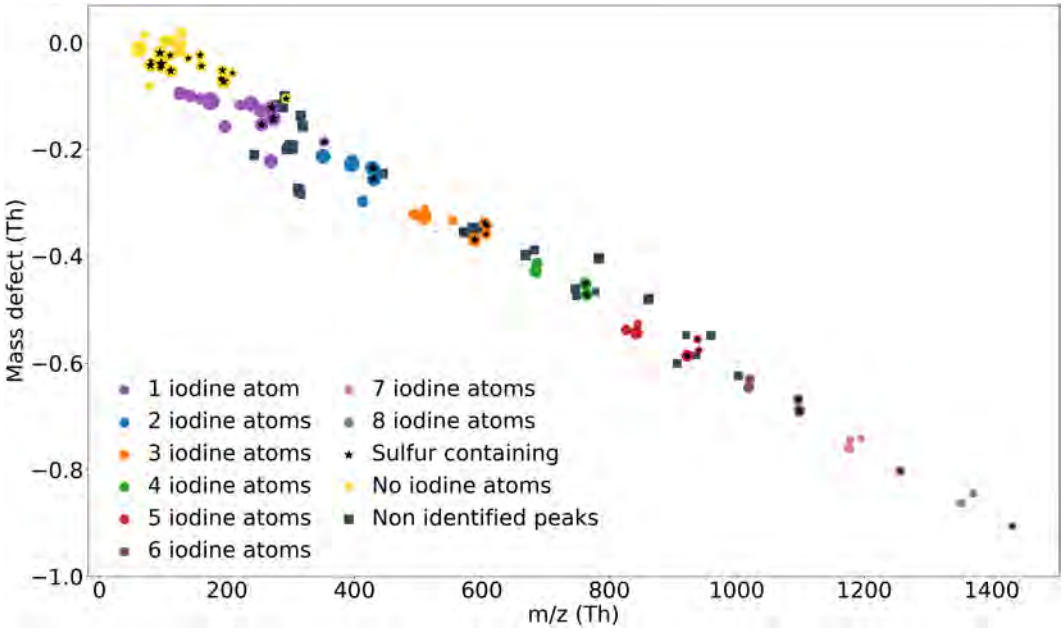

Figure 3.3: Mass defect plot of negative ions measured during an iodine NPF event in the Arctic. The size of each marker is scaled proportionally to the logarithm of the concentration of the respective peak and colour coded by the number of iodine atoms.

$$(HNO_3)_nNO_3^- + HX \longrightarrow (HNO_3)_n + HNO_3 + X^- \quad \text{(R3.1)}$$

$$(HNO_3)_nNO_3^- + HX \longrightarrow (HNO_3)_n + HXNO_3^-, \quad \text{(R3.2)}$$

where HX is any species with sufficiently low proton affinity to be ionized by the nitrate ion (*e.g* iodic or sulfuric acid). The reaction time is short, $\sim$ 200 ms, and for those species with a proton affinity lower than nitric acid the ionization can be assumed to proceed at the kinetic limit (each collision leads to a stable cluster or deprotonated acid molecule). Figure 3.4 shows a schematic of the inlet. The concentration of a species HX is calculated as:

$$[HX] = C \frac{X^- + HXNO_3^-}{\sum_{n=0}^{2} (HNO_3)_n NO_3^-}, \tag{3.1}$$

with C being a calibration factor which can be experimentally determined. The instrument is typically calibrated by injecting a known amount of sulfuric acid which can be produced in different ways, as described in Section 3.1.2. Under the assumption that each collision leads to a stable cluster or deprotonated acid molecule, the sensitivity of the instrument can be assumed to be constant and the same calibration factor C can be applied to estimate the concentration of different molecules in the atmosphere. This is the case for sulfuric, iodic and methanesulfonic acid[87,89], the three key molecules investigated in this thesis.

As already mentioned, the CI inlet is generally operated with an electric field that drives the nitrate ions inside the sample flow. However, for a part of ACE the inlet was operated without any voltage due to a technical issue. In this case the reagent ions are mixed with the sample flow because of diffusion and some turbulence in the inlet. Therefore, a different sensitivity compared to the normally operated CI inlet could be expected. However, as shown in Section 3.1.2, it was found that this difference was smaller than the calibration uncertainty. Therefore, a single calibration constant was used for the entire ACE campaign.

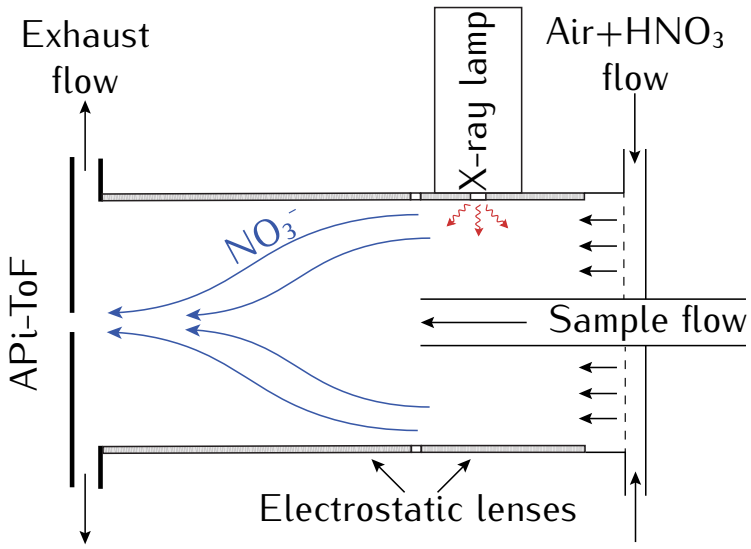

Figure 3.4: Schematic of the CI inlet (not to scale): a flow of clean air and nitric acid is added coaxially to the sample flow and ionized by a soft x-ray lamp. The ions are then driven towards the sample flow with two electrostatic lenses (the blue lines represent the ion trajectory) and react with the neutral molecules present in the ambient air. A fraction of the flow enters then into the APi-TOF through a small pinhole and the ions therein are measured by the mass spectrometer.

3.1.2 Sulfuric acid calibration

Two different methods were used to generate a known amount of sulfuric acid and calibrate the CI-APi-ToF: a series of smog chamber experiments and a sulfuric acid generator. In both cases sulfuric acid was produced from the oxidation of sulfur dioxide which proceeds as follows:

$$SO_2 + OH + M \longrightarrow HSO_3 + M \quad \text{(R3.3)}$$
$$HSO_3 + O_2 \longrightarrow SO_3 + HO_2 \quad \text{(R3.4)}$$
$$SO_3 + 2\,H_2O \longrightarrow H_2SO_4 + H_2O, \quad \text{(R3.5)}$$

with the first reaction being the limiting step, proceeding at a rate[90]

$$k_{OH+SO_2} = 1.3 \times 10^{-12}\,\mathrm{cm^{-3}\,s^{-1}\,molecule^{-1}}. \quad (3.2)$$

Calibration using the PSI smog chamber

The PSI smog chamber (SC) is made of a $27m^3$ flexible Teflon bag inside a wooden enclosure where temperature can be controlled. Photochemistry can be initiated inside the chamber using 4 xenon arc lamps and a set of 80 UV-A light tubes, for further details on the SC characteristics the reader is referred to Paulsen *et al.*[91]. Experiments were conducted at a temperature of $(20 \pm 2)\,^{\circ}\mathrm{C}$ and a relative humidity (RH) between 20% and 40% and carried out injecting SO_2 at a mixing ratio between 0 and 15 ppb, ozone between 0 and 250 ppb and trimethylbenzene (TMB) between 0 and 10 ppb. TMB was introduced in the chamber as a tracer to estimate the OH concentration, as further described below. Figure 3.5 shows a typical sulfuric acid experiment run. Initially lights are off and the sulfuric acid concentration is low, then lights are turned on (first vertical dashed line) and sulfuric acid rapidly increases, the same happens to the temperature because of the heat produced by the lights. Shortly after, also the particle concentration increases because of nucleation. This decreases the sulfuric acid concentration because of an increased loss rate to the particles. About 15 minutes after the beginning of the run the lights are turned off, interrupting the production of both sulfuric acid and new particles.

The sulfuric acid concentration inside the chamber can be described by a simple kinetic model:

$$\frac{d[H_2SO_4]}{dt} = k_{OH\,+\,SO_2}[OH][SO_2] - (W + CS)[H_2SO_4], \quad (3.3)$$

with W being the sulfuric acid wall loss rate and CS the condensation sink. The CS represents the sulfuric acid loss term to the particles and can be calculated from the particle number size distribution following Dal Maso *et al.*[92]:

$$CS = 2\pi D \sum_i \beta_i d_{pi} N_i, \quad (3.4)$$

$$\text{where} \quad \beta = \frac{1 + Kn}{1 + (\frac{4}{3\alpha} + 0.337)Kn + \frac{4}{3\alpha}Kn^2}, \quad (3.5)$$

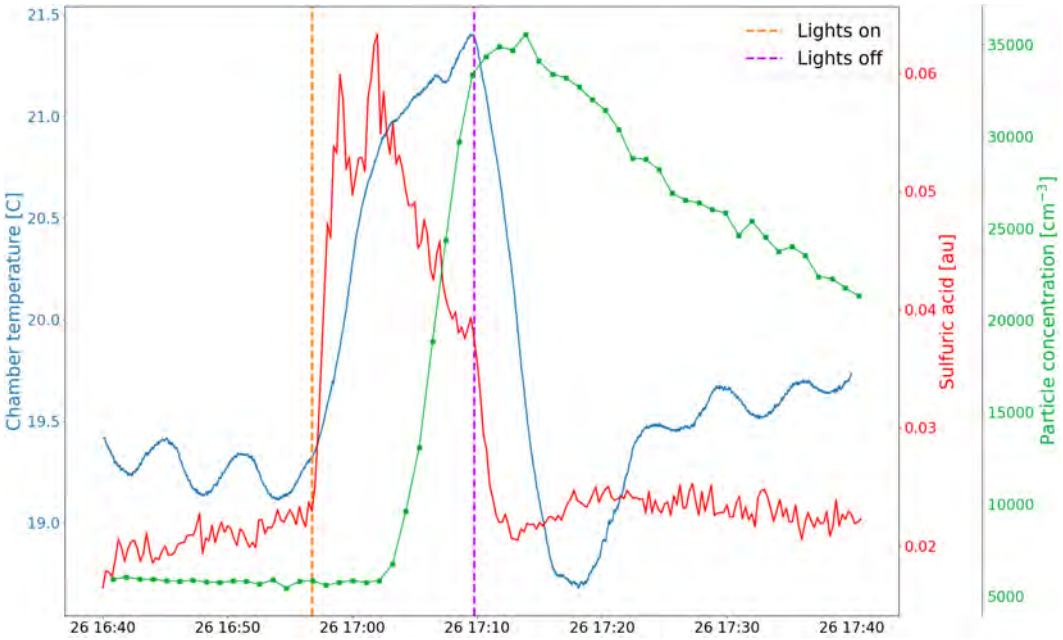

Figure 3.5: Example of a sulfuric acid production experiment in the smog chamber. The temperature of the chamber is reported in blue, sulfuric acid in red and the particle number concentration in green. The two vertical dashed lines indicate when lights were turned on and off.

with D being the sulfuric acid diffusion coefficient[93], d_{pi} and N_i the diameter and number concentration of particles in size-bin i, respectively, Kn the Knudsen number and α the sticking coefficient of sulfuric acid (a value of one was used for this work[94]).

At steady state the concentration of sulfuric acid inside the chamber can be calculated:

$$[H_2SO_4] = \frac{k_{OH\ +\ SO_2}[OH][SO_2]}{W + CS}. \tag{3.6}$$

The wall loss rate is estimated from the sulfuric acid decay, as described below.

OH CALCULATION OH is produced from the photolysis of ozone and its concentration estimated from the TMB decay:

$$\frac{d[TMB]}{dt} = k_{TMB+OH}[OH] \rightarrow [TMB] = [TMB_0]e^{-k_{TMB+OH}[OH]t}, \tag{3.7}$$

$$k_{TMB+OH} = (5.73 \pm 0.53) \times 10^{-11}\,\mathrm{cm^{-3}\,s^{-1}\,molecule^{-1}}, \tag{3.8}$$

where the reaction rate constant k_{TMB+OH} is taken from Kramp *et al.*[95].

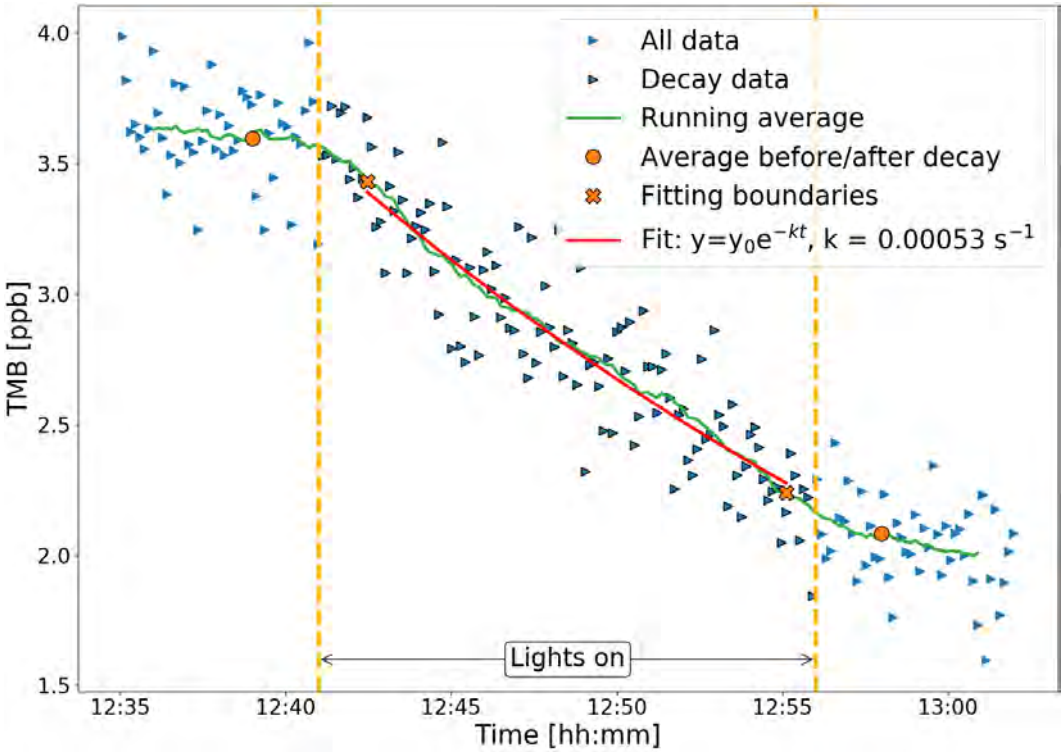

(a)

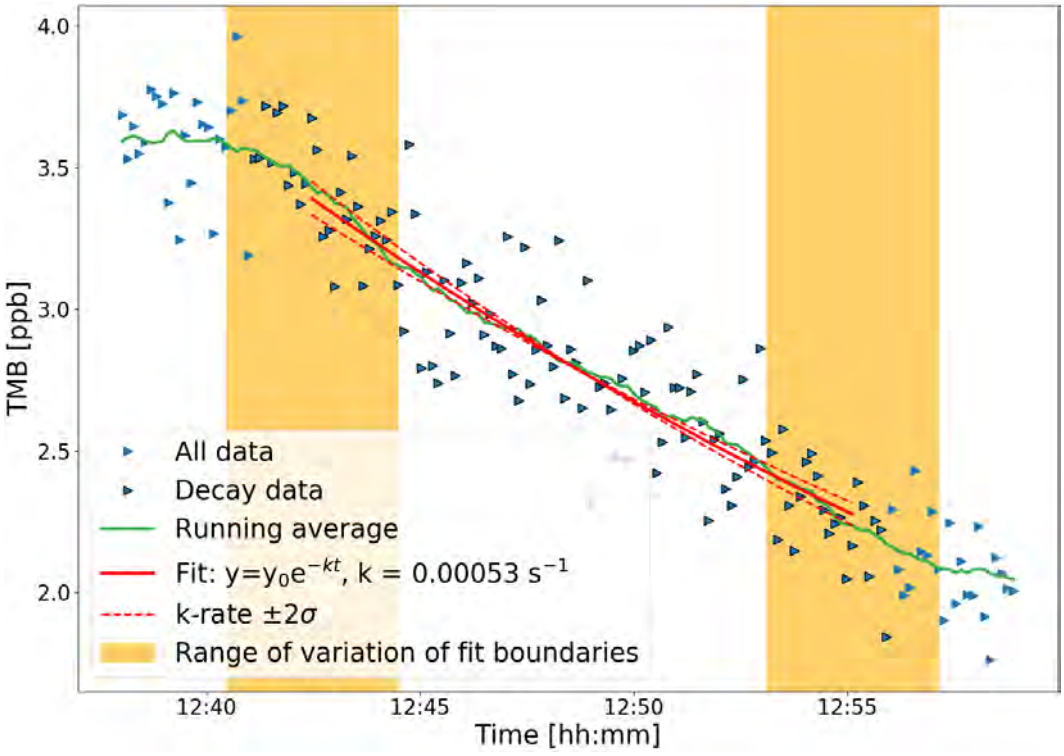

(b)

Figure 3.6: Example of a TMB decay from which OH is calculated: **(a)** decay rate estimation, the orange circles show the average TMB concentration before and after the decay whereas the orange crosses correspond to the fitting boundaries, blue triangles are the original TMB data and the green solid line is the smoothed TMB time series. The red line is the result of the decay fit. **(b)** same as in (a) but in this case the effect of varying the fit boundaries on the final decay rate calculation is shown. The orange areas indicate the ± 2 minutes region where the fit boundaries were varied and the dashed red lines the corresponding fit curves when the decay rate is varied by two standard deviations.

The TMB decay was fit with an exponential function in order to estimate the OH concentration. However the TMB decrease its often very small and the choice of the fitting boundaries can become arbitrary. Therefore, a standardized procedure was created to remove ambiguities in the choice of the data:

- the initial, TMB_i, and final, TMB_f, concentrations were determined by averaging a 5 minute interval before and after lights were turned on;
- the TMB data were smoothed using a 25 data points convolution window;
- the period where the smoothed TMB time series is between $0.9(TMB_i - TMB_f)$ and $0.1(TMB_i - TMB_f)$ was select for the decay fit.

The decay rate was calculated from the logarithm of the TMB concentration using an ordinary least squares regression. Figure 3.6a displays this procedure based on a TMB decay example.

Moreover, the effect of the choice of interval on the decay rate estimation was analysed by varying the fit boundaries. In particular, the decay rate was calculated for different segments of the data considering all possible combinations within ± 2 minutes from the interval boundaries chosen before. The standard deviation of this decay rate distribution was then calculated and an error equal to 2 standard deviations was associated to the final OH value. Figure 3.6b shows the range of variations of the fit boundaries for a TMB decay example and the resulting uncertainty on the final decay rate. The relative error for all the experiments was on average below 10% with a couple of notable exceptions exceeding 40%. These corresponded to decay runs with a very small change in the absolute TMB concentration.

WALL LOSS RATE CALCULATION The sulfuric acid decay at the end of each run is the combined effect of losses to the particles and to the walls of the chamber, as described by Equation 3.3. The CS is calculated using Equation 3.4 and the total sulfuric acid loss rate can be estimated with an exponential fit of the sulfuric acid decay after each stage. Also in this case an ordinary least squares regression was used to fit the logarithm of the data used and obtain the sulfuric acid decay rate. Finally, the wall loss rate is estimated from an ordinary least squares regression of the total sulfuric acid loss rate against the CS as reported in Figure 3.7.

SULFURIC ACID CONCENTRATION CALCULATION After estimating the wall loss rate and the OH concentration the sulfuric acid concentration was calculated using Equation 3.6 for all the individual experiments and compared to the CI-APi-ToF measurements. Equation 3.6 applies only to steady-state conditions, therefore for each stage the periods with a stable sulfuric acid signal were selected. The main reason for deviations from the steady-state during a single experiment is a change in the CS, which increases as a consequence of new particles being formed inside the chamber. Moreover, the CI-APi-ToF was characterized by a sulfuric acid background, which probably came from the CI inlet itself and was not produced inside the chamber. This was corrected for by averaging the data before and after each run and subtracting this value from the average sulfuric acid signal during the experiment. Figure 3.8 shows a sequence of experiments highlighting the periods used for the sulfuric acid average and background calculation as well as the condensation sink time series.

The final calibration result is reported in Figure 3.9, where the ordinate shows the sulfuric acid concentration calculated from Equation 3.6 and the abscissa the aver-

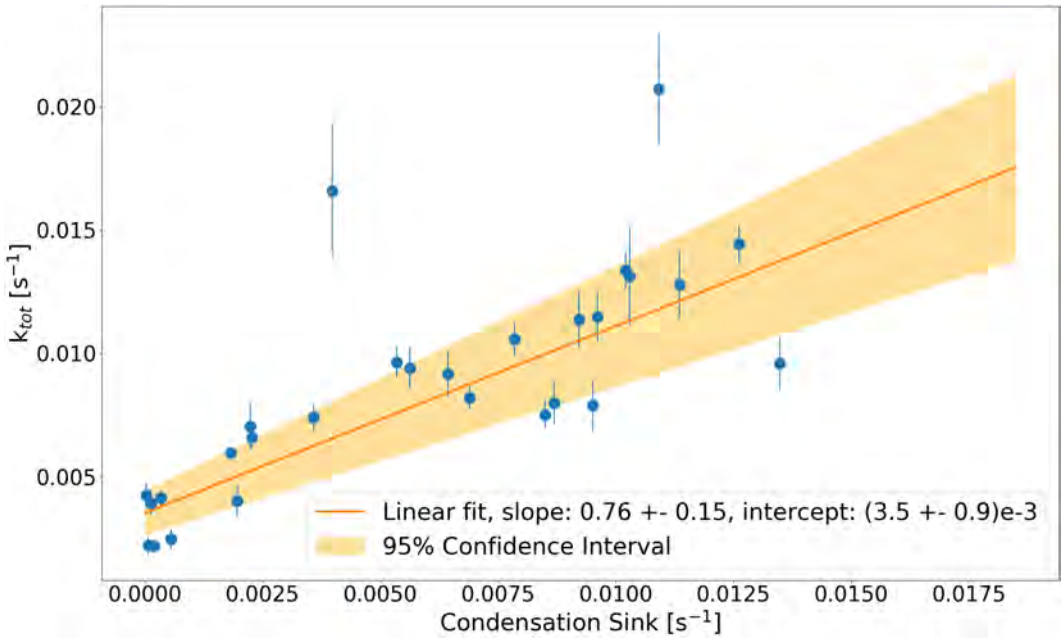

Figure 3.7: Sulfuric acid wall loss rate. We used a weighted least squares regression to estimate the wall loss rate, the errors on the fit parameters correspond to a 95% confidence interval. The error bars are derived from the standard error of the fit for each individual sulfuric acid decay rate experiment.

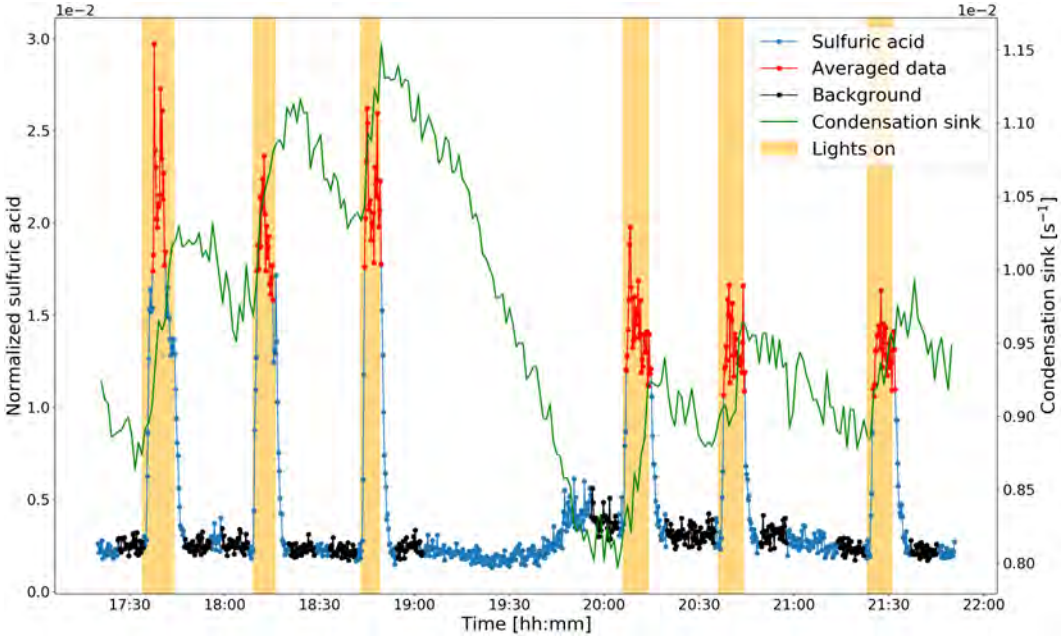

Figure 3.8: Sequence of sulfuric acid experiments. In blue the full time series of the normalized sulfuric acid concentration measured with the CI-APi-ToF, in black the data used to estimate the background and in red the values used for the averaging. The condensation sink (in green) and the periods when the lights were turned on are also reported.

age of the measured sulfuric acid signal normalized by the reagent ion concentration. The uncertainty of the calculated sulfuric acid concentration was obtained by standard error propagation from Equation 3.6, whereas the uncertainty on the CI-APi-ToF measurements was calculated as the standard error of the mean. A weighted least

squares regression was applied to estimate the calibration constant C as described in Equation 3.1. The CI inlet is usually operated with an electric field to force the reagent ions into the sample flow. During the calibration the instrument was run also without the electric field in order to simulate the CI-APi-ToF operating conditions during ACE. The results presented in Figure 3.9 clearly show that there is no systematic difference between the two operating modes of the inlet. Therefore a single calibration value was used:

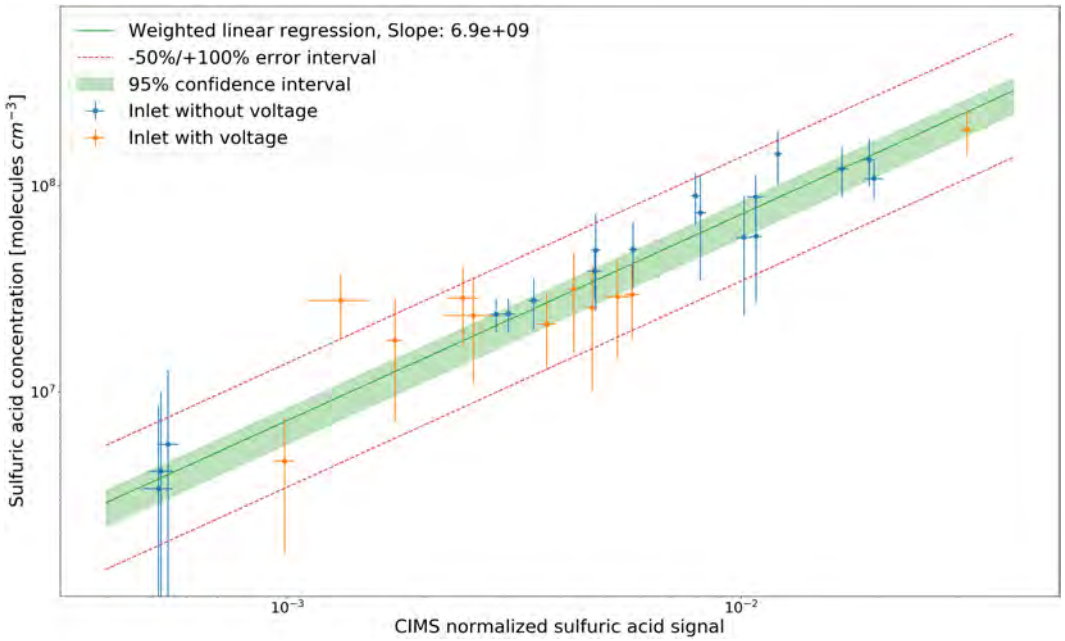

Figure 3.9: Sulfuric acid calibration with smog chamber experiments. Each data point represents a different experiment with the CI-APi-ToF normalized sulfuric acid signal on the x-axis and the corresponding concentration of sulfuric acid inside the chamber on the y-axis. Error bars on the x-axis are equal to the standard error of the mean whereas errors on the y-axis are equal to the propagated uncertainty via Equation 3.6. Orange and blue markers indicate measurements where the CI inlet was operated with and without voltage, respectively.

$$C_{ACE} = 6.9 \times 10^9 [-50\% + 100\%] \,\text{molecule}\,\text{cm}^{-3}, \tag{3.9}$$

where the calibration coefficient was already corrected for diffusional losses of sulfuric acid in the inlet line. An uncertainty of $[-50\% + 100\%]$ was associated with the calibration factor, which is a standard estimate for sulfuric acid measurements in the field. This estimate is larger than the linear regression confidence interval and accounts for the intrinsic variability of field conditions, which are difficult to quantify.

Calibration with a sulfuric acid generator

The calibration with a sulfuric acid generator is simpler compared to the smog chamber experiments and follows the work of Kürten *et al.*[96]. In essence, a mixture of synthetic air, SO_2 and water vapour is passed through a quartz tube where a UV mercury lamp (184.9 nm) photolyses H_2O to produce OH. OH reacts then with SO_2 following Reactions R3.3-R3.5 to produce sulfuric acid. The sulfuric acid concentration is varied by changing the amount of water vapour, which controls the OH production. The SO_2 mixing ratio was kept constant at about 2 ppm. Figure 3.10 shows the calibration res-

ults: for sulfuric acid concentrations larger than 1×10^7 molecule cm^{-3} the calibration results are well within the experimental uncertainty. However, at lower concentrations data are affected by a non-linearity issue as clearly evident from the relative residuals plot. This effect at low water vapour concentrations has been reported already[96] and it is probably related to a less accurate quantification of the real amount of water vapour in the system and to O_2 photolysis, which becomes a relevant source of OH under these conditions. The AO18 calibration constant is reported in table 3.1 together with the value obtained for the ACE campaign, which is provided for comparison.

Table 3.1: Sulfuric acid calibration constants.

	Calibration constant [molecule cm^{-3}]	Uncertainty range [molecule cm^{-3}]
ACE	6.9×10^9	$[3.5 - 13.8] \times 10^9$
AO18	2.4×10^9	$[1.2 - 4.8] \times 10^9$

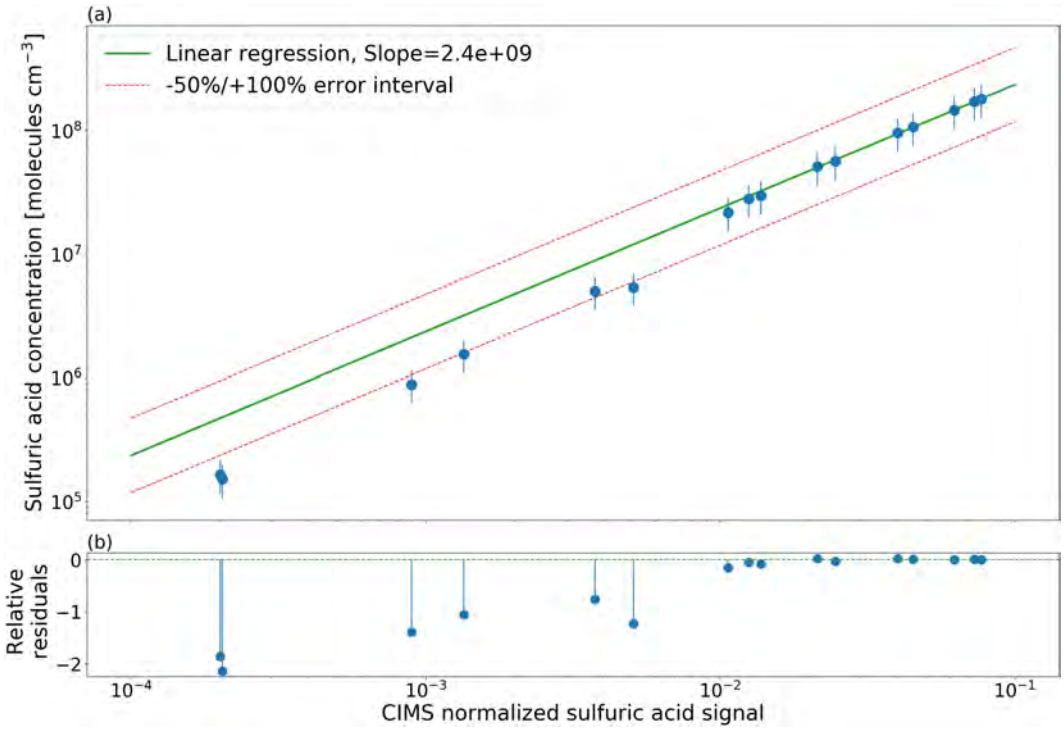

Figure 3.10: Sulfuric acid calibration with generator. **(a)** calibration experiment results, the x-axis gives the CI-APi-ToF normalized sulfuric acid signal and the y-axis the concentration produced with the sulfuric acid generator. Error bars reflect the uncertainty of the OH production estimation from H_2O photolysis. **(b)** plot of the relative residuals. The deviation from linearity at low sulfuric acid concentration is a known effect and is explained in the main text.

3.1.3 Particle phase instruments

A suite of different instruments to characterize aerosol physical properties, mainly size and number concentration, was deployed during both AO18 and ACE. In particular, multiple condensation particle counters (CPC) were used to measure the total particle number concentration[97–99], a differential and a scanning mobility particle sizer, DMPS

and SMPS, respectively, to measure the particle size distribution[100–102] and a neutral and air ion spectrometer (NAIS) to measure the particle and ion size distribution below 40 nm[103–105]. Additionally, a cloud condensation nuclei counter (CCNC) was used to measure the CCN concentration at different supersaturations[106,107]. These are instruments that are routinely operated on similar research expeditions and they have already been described extensively in the literature referenced above. Therefore, no description of their working principles is provided here.

To assure data quality, the data were intercompared amongst each other with a specific focus on the NAIS. The reason for this is that the NAIS was widely used during this thesis work, more than any other particle instruments, for its ability to measure particles and ions as small as 2 nm and 0.8 nm, respectively. The high detection efficiency of the NAIS comes at a price: the instrument does not detect the particles individually like a CPC but measures the current generated by these particles when they are collected on a series of electrodes[103]. Therefore, the overall accuracy is worse than for a DMA-based particle sizer and the measurements are also affected by electronic background noise, which is particularly evident at low particle number concentration (roughly below 100 particles cm^{-3}). Figure 3.11 shows a comparison between the integrated concentration of the NAIS and an ultrafine CPC (UCPC) for all data collected during AO18. The UCPC data were averaged to match the NAIS time resolution (90 s) and the particle concentration above 40 nm was subtracted in order to match the measurement size range of the NAIS. The Figure clearly shows the effect of the electronic background noise with a deviation from the 1 : 1 line below $\sim$ 100 particles cm^{-3}. Moreover, there is a subset of the data, characterized by a relatively high wind speed, which deviates from the overall data distribution by more than a factor 2. Figure 3.12 shows an example for one of these *high wind speed events* with the NAIS particle number concentration measurement being about 3 times larger than the UCPC. This problem regularly occurred on AO18 but not during ACE, despite the latter expedition being characterized by higher wind speeds. The reason for this discrepancy at high wind speed is not completely understood but it could be related with the shattering of ice crystals inside the inlet from snow drifting, which would also explain why this problem did not occur during ACE. Therefore, all the periods characterized by a high discrepancy between the UCPC and the NAIS integrated concentration (about 7% of the measurements), were removed and only the fit to the remaining data is shown in Figure 3.11. The slope of the linear regression indicates that the NAIS measured about 1.5 times more particles than the UCPC. This value is in line with previous studies, which also reported similarly higher concentrations from NAIS measurements[103,108]. The intercept of 26 particles cm^{-3} is instead a measure of the electronic background that affects the NAIS measurements.

For an independent evaluation of the NAIS performance the integrated concentration between 20 nm and 40 nm was compared against the DMPS. 20 nm was chosen as the lower cut-off because the DMPS has a lower transmission efficiency for smaller particles. In this case the data were averaged to 9 minutes in order to match the DMPS time resolution and the *high wind speed periods* were removed. The comparison, shown in Figure 3.13, reveals a larger slope of 2.3. This difference is probably due to the fact that the inlet to the DMPS was longer and therefore characterized by larger diffusion losses (we corrected the data for the inlet transmission efficiency but this correction is based on theoretical calculations and not 100% accurate). Moreover, since the concentration range is small (only 1% of the data points is above 500 particles cm^{-3}), the data at low concentrations, which are more affected by the electronic background noise,

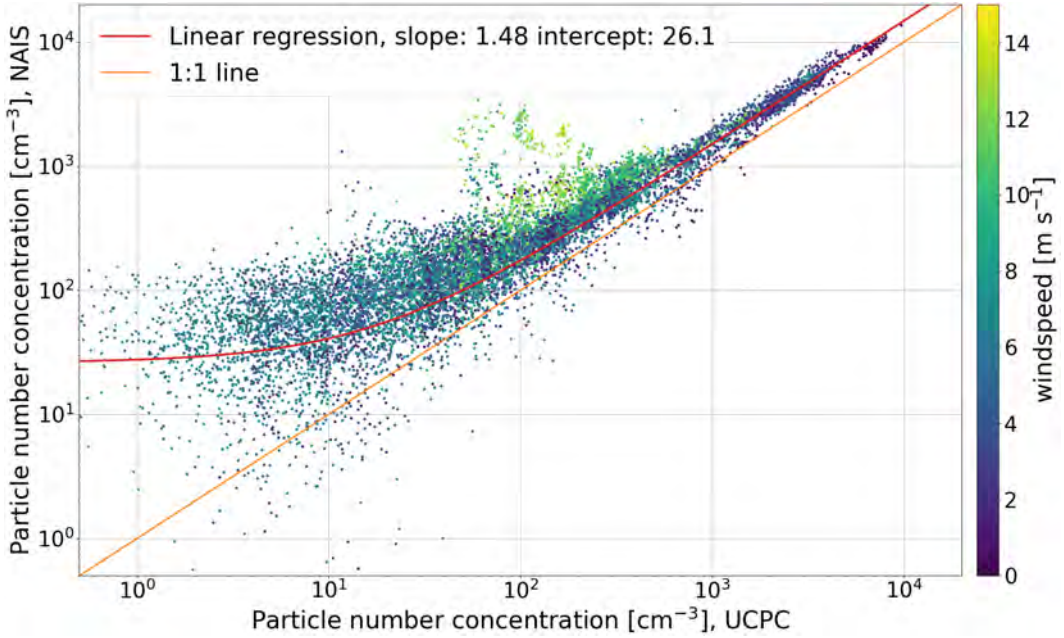

Figure 3.11: Intercomparison of particle number concentration measurements from the UCPC and the NAIS during AO18. NAIS particle size distribution measurements were integrated from 3 nm to 40 nm and the concentration of particles larger than 40 nm (measured with the DMPS) was subtracted from the UCPC data in order to make the two datasets comparable. Data are colour-coded by wind speed. A linear regression was used to investigate the relationship between NAIS and UCPC data. The linear regression line shown here does not include *high wind speed events*.

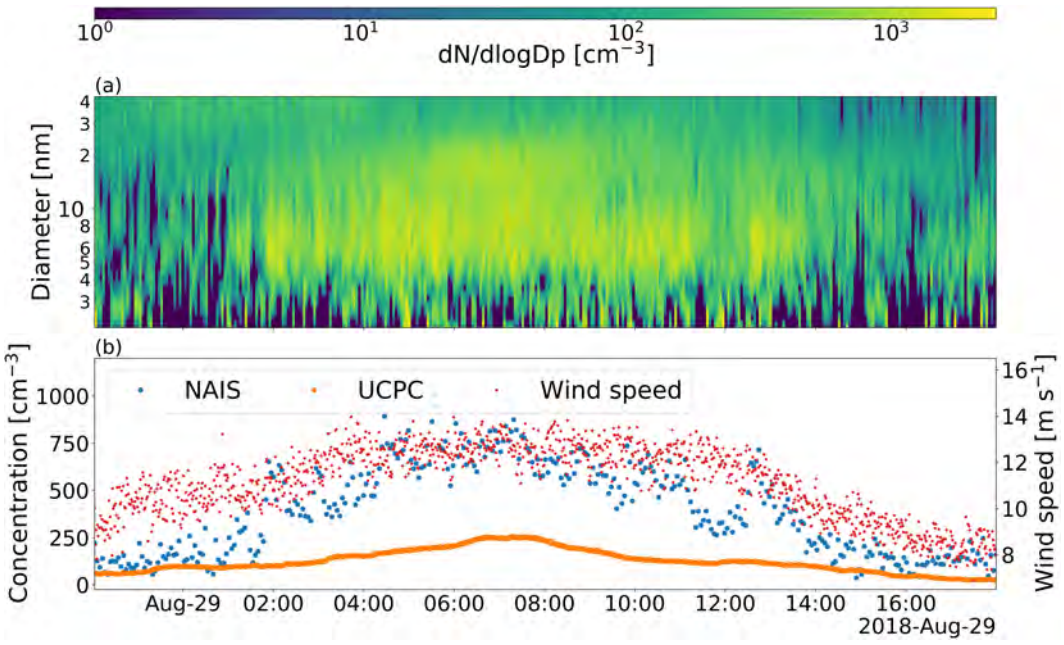

Figure 3.12: High wind speed event during AO18: **(a)** neutral particle size distribution measurement from the NAIS. **(b)** Particle number concentration measured with the UCPC and the NAIS (left axis) and wind speed (right axis).

have a stronger effect on the linear regression result. For example, if the regression of NAIS vs UCPC data (shown in Figure 3.11) was limited to measurements with a concentration below 500 particles cm^{-3}, then the resulting slope would increase to around 2.

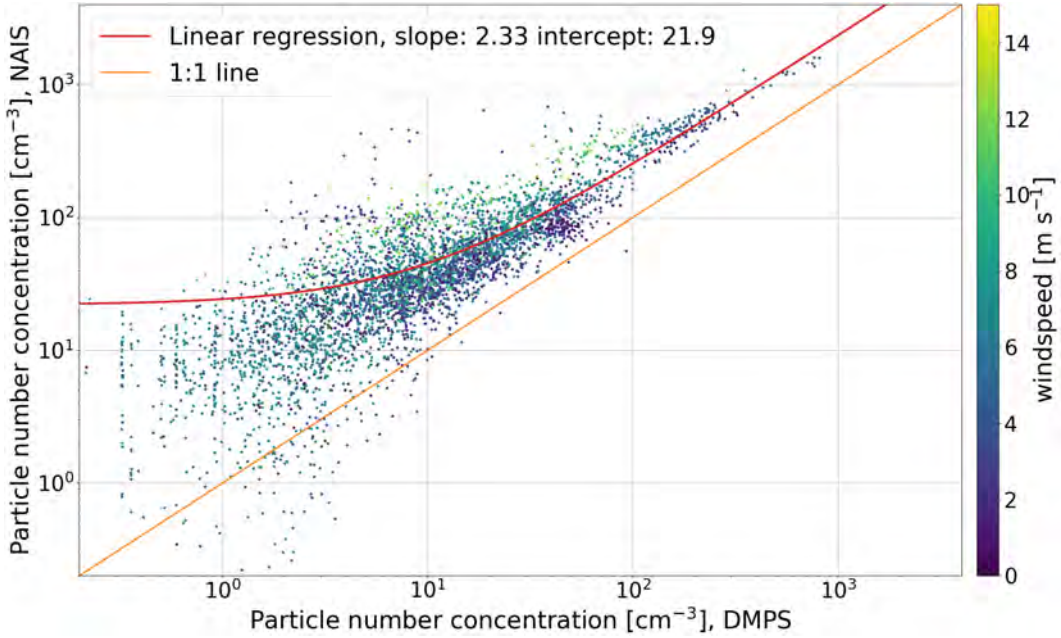

Figure 3.13: Intercomparison of particle number concentration measurements from the DMPS and the NAIS during AO18. DMPS and NAIS particle size distribution measurements were integrated from 20 nm to 40 nm in order to make the two datasets comparable. Data are colour-coded by wind speed. A linear regression was used to investigate the relationship between NAIS and DMPS data.

Apart from the issue at high wind speed, the overall NAIS data quality is good and matches intercomparison results from previous studies[103,108]. When using NAIS data for quantitative analysis (*i.e.* formation rate calculation) it is important to be aware that the integrated total particle number concentration may be overestimated but for any other application the NAIS provides reliable data with very high detection efficiency and time resolution.

MERGED PARTICLE SIZE DISTRIBUTION It is useful to combine the PSD measured with the NAIS and that measured with a DMPS or an SMPS in order to create a single PSD spanning particle diameters from 2 nm up to several hundreds of nm. There does not seem to be a standard procedure to combine different PSD measurements, despite the fact that combined PSDs are common in the literature. A simple approach to obtain a continuous PSD with minimum modifications of the original datasets was developed. This was created for AO18 but it can be easily generalized to any other dataset:

- Identification of an optimal common size range interval for the averaging, for AO18 we used 17 nm to 40 nm. The choice of the lower bound was motivated by the poor detection efficiency of the DMPS for particles below $15 - 20$ nm due to increased diffusional losses. Differently from the previous DMPS-NAIS intercomparison analysis, 17 nm was chosen as the lower bound instead of 20 nm to increase the number of DMPS size bins for the averaging. In fact, the DMPS has a coarse size resolution with only 5 bins in the range $20 - 40$ nn, which would be practically reduced to 4 considering that a null weight is given to the smallest DMPS size bin in the averaging, as explained below.

- Time averaging of the NAIS data to match the original DMPS time resolution.

- Interpolation of the DMPS PSDs with a 3rd order spline function over the NAIS diameter bins. The interpolating function was chosen in order to get a smooth result considering the coarse size resolution of the DMPS, however, this is not a critical aspect and even a simpler linear interpolation can be used.

- Weighted averaging of NAIS and DMPS PSDs over the common diameter grid. We used a linear distribution of weights going from zero at 17 nm to one at 40 nm for the DMPS and the opposite for the NAIS (one at 17 nm and zero at 40 nm). In this way the NAIS measurements have a higher weight at smaller sizes and the DMPS at larger sizes.

Figure 3.14 shows an example from AO18 with the individual NAIS and DMPS size distribution measurements and the resulting merged PSD.

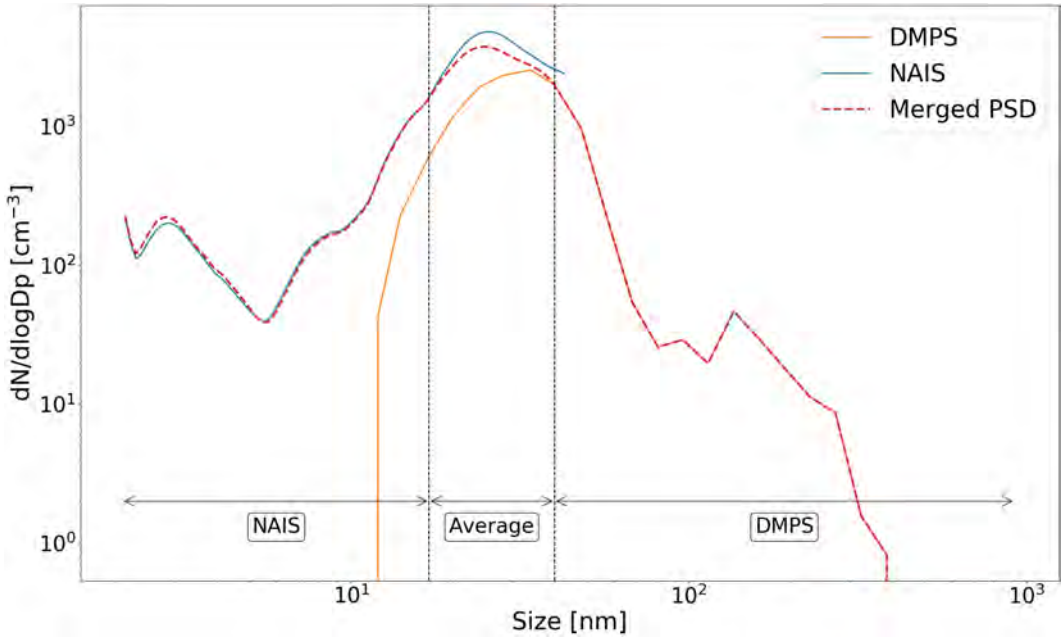

Figure 3.14: Example of a merged PSD including the original NAIS and DMPS data. The vertical dashed lines indicate the size range interval where the averaging was performed.

3.2 MEASUREMENT SET-UP

During both expeditions, measurements were performed using a dedicated container, the so-called *Swiss lab*, which was equipped with several different instruments to characterize aerosol and trace gas properties. The ambient air is sucked inside the container by means of one or more inlet and then distributed to the various instruments. The temperature inside the container is kept constant at about 293 K, more than 20 K warmer than the average outside temperature during both ACE and AO18. Therefore, when the ambient air enters into the container it becomes warmer and dryer and the dry aerosol properties can be measured (during ACE an additional silica gel dryer was also used). It is important to measure dry properties for comparability reason but also because cloud residuals can be characterized during in-cloud sampling. Figure 3.15a shows the instrumental set-up used during ACE and Figure 3.15b the one used during

AO18. The set-up during this second campaign was more complicated (a second container, the *Triple lab*, was used in addition to the *Swiss lab)*, with more instruments and various inlets to specifically differentiate between activated and non-activated aerosol particles inside clouds. In particular, in addition to the whole-air inlet, which was used also during ACE and samples the entire aerosol population (activated and non-activated fraction), an interstitial inlet with a cut-off of 1 μm was used to measure only the non-activated fraction and a counterflow virtual impactor inlet (CVI) was used to measure the cloud residuals[109].

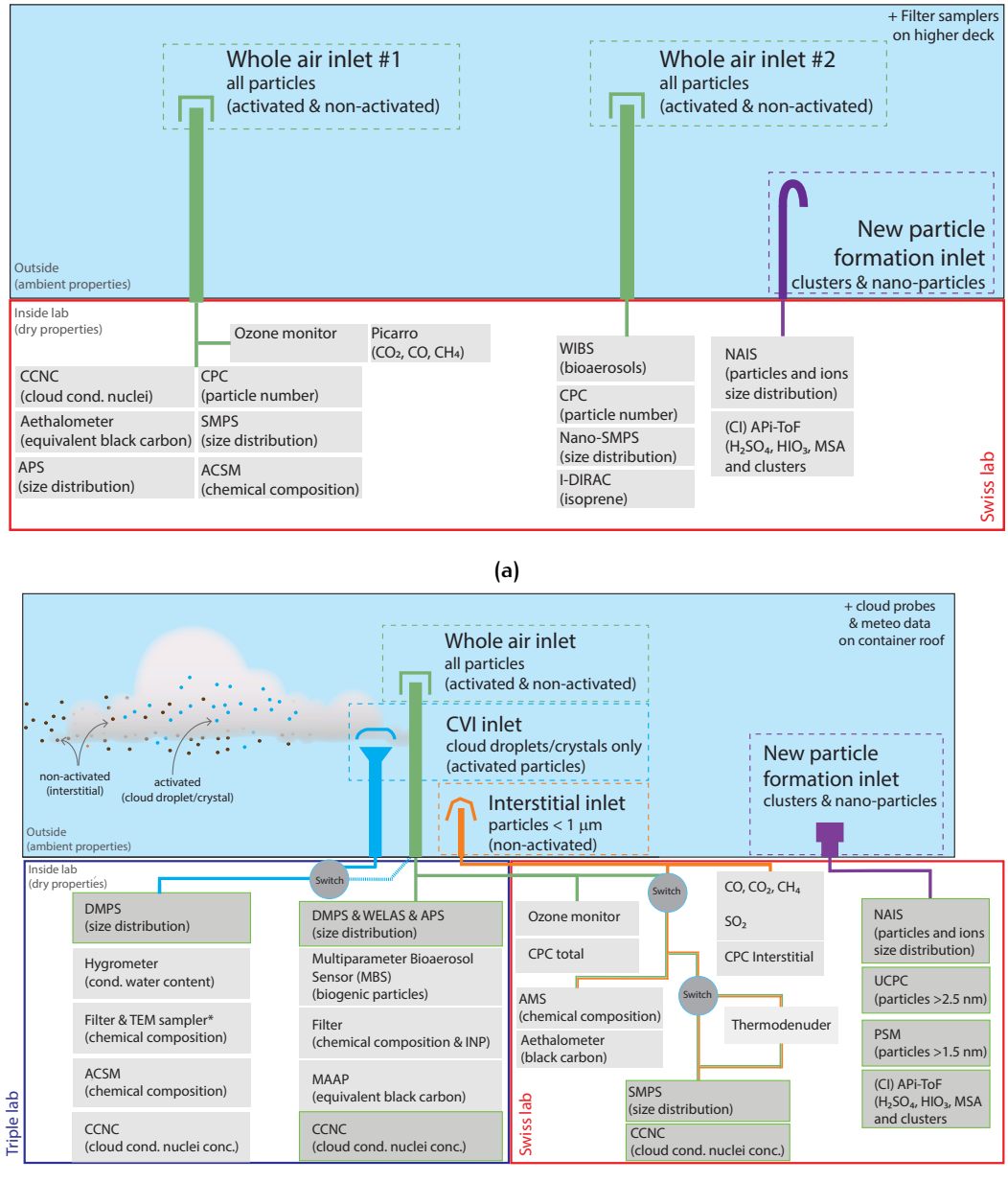

Figure 3.15: Instrumental set-up used during **(a)** the ACE expedition and **(b)** the AO18 expedition. The name of each instrument and a short description of the measured quantity is reported. For AO18 (panel b), the instruments that were directly used during this thesis work are highlighted with a green border and darker background, this was not necessary for ACE (panel a) as all the instruments were used. The graphic is adapted from Paul Zieger.

A critical aspect of every aerosol measurement set-up is the design of the inlet lines, for which a high transmission must be ensured in order to collect reliable data. Aerosols can be lost via three main mechanisms: diffusion, impaction and sedimentation[110]. Diffusion is effective in removing small particles which have a high diffusivity, whereas impaction and sedimentation remove mainly larger particles. The best way to reduce to aerosol losses is to use short and straight inlet lines, however this is generally not possible because of the number of different instruments, with very different characteristics and dimensions, which need to be arranged in a limited space. Therefore, compromises are necessary when planning the instrument positioning and designing the inlet lines, this task usually represents a major effort in the preparation phase of an expedition. For both ACE and AO18, it turned out that a dedicated inlet for the NPF instruments was the best solution to reduce the aerosol residence time inside the lines and minimize diffusional losses. The inlet used during ACE was sampling vertically through the roof of the container, it was roughly 2 m long with a sample flow rate of 70 lpm. For *AO*18, it was decided to modify the inlet in order to further reduce the losses, in particular an horizontal inlet was used, which was about 1 m long with a total flow rate of 113 lpm. Figure 3.16 shows the estimated aerosol transmission corresponding to the NAIS line for the two different campaigns (only diffusional losses are taken into account in this case)[110]. The improvement from ACE to AO18 is clear with a transmission that is about 50% higher for the smaller particles. In the same figure also the CI-APi-ToF sulfuric acid transmission efficiency is shown (the sulfuric acid monomer mobility diameter is estimated to be around 0.8 nm, based on its diffusion coefficient[93]). In this case, the difference between ACE and AO18 is smaller and it is because losses are dominated by the last part of the inlet which goes to the CI-APi-ToF only (the initial part is in common with the NAIS) and is characterized by a lower flow rate ($\sim$ 10 lpm). As a reference, Figure 3.16 also shows the transmission efficiency for the SMPS inlet line used during AO18, which was not optimized for NPF measurements. It is evident that losses for particles smaller than 20 nm are substantial and that it would have not been possible to characterize NPF processes with the SMPS inlet.

3.3 POLLUTION IDENTIFICATION

Research vessels are unique platforms to characterize gases and aerosol in pristine and remote locations, however, in most of the cases they are powered by large engines running on fossil fuel emitting very high concentrations of both aerosol and gaseous compounds[111,112]. Emissions from the ship exhaust and other human related activities (*e.g.* helicopter flights, painting, cooking etc...) must be identified and separated from the background natural aerosols and gases. This is particularly critical in pristine locations, as investigated in this thesis, which are generally characterized by a very low aerosol concentration, orders of magnitude lower compared to the plume of a ship engine. As an example Figure 3.17 shows the average size distribution measured from AO18 in clean and polluted conditions with the NAIS; the inset shows the different particle number concentration distribution for the same two conditions by means of a violinplot.

The problem of pollution identification during measurements on research vessels is highly important, however there are no established procedures to deal with it. Several different methodologies have been applied in previous works, from very simple

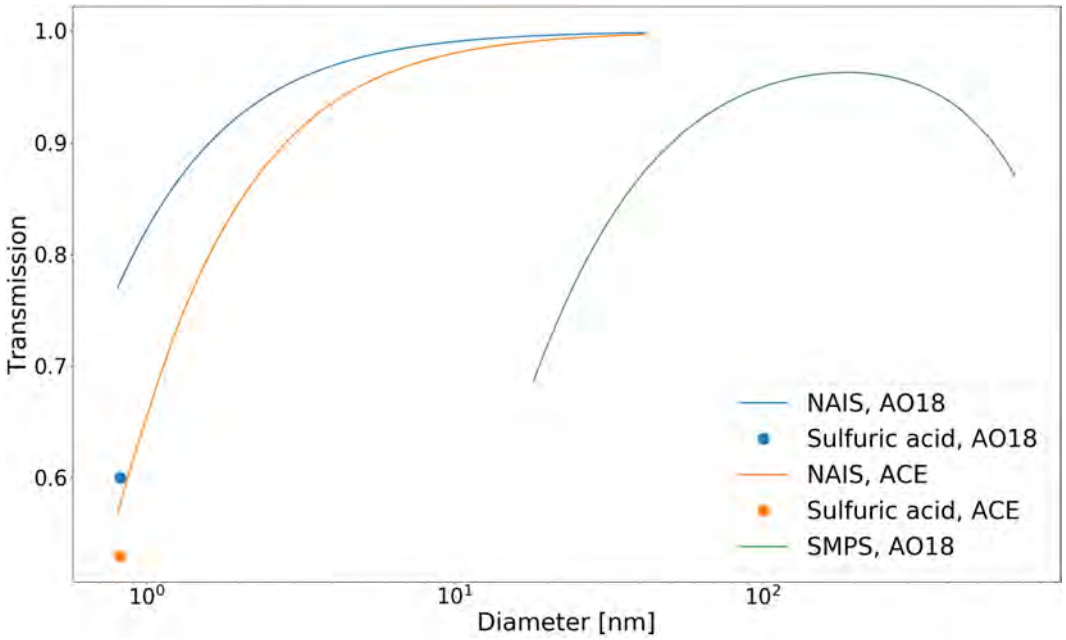

Figure 3.16: Transmission efficiency estimation for different inlets. The NAIS and sulfuric acid transmission was estimated considering only diffusional losses[110], whereas for the SMPS line all losses were included.

approaches based only on wind direction or total particle number concentration[113] to more elaborated algorithms using a larger set of measurements to identify pollution[114,115].

Here, two different methods to identify pollution were developed, both based on the concept that pollution is characterized by much faster temporal variations compared to the underlying natural processes. In the first case, the instantaneous particle number and CO_2 concentration were compared with a smoothed time series of the same two variables. If the difference exceeded a predefined threshold then the data were marked as polluted. This threshold is not unique and requires adjustments by investigation of the data on a case by case basis. Other proxies were also used to validate this mask, such as black carbon and wind direction[107]. This filtering technique proved to be effective and was applied to the ACE dataset removing about 50% of the data. For AO18 this method was further generalized to reduce the level of subjectivity in the threshold identification. In particular, the derivative of the particle number concentration signal as a function of the corresponding total particle number was investigated (Figure 3.18). As the Figure shows, the data cluster along two bands with different slopes in a log-log scale, *i.e.* they can be described by two different power laws in a first order approximation. The data are colour-coded by the equivalent black carbon concentration in order to highlight the polluted data, which are also characterized by a higher derivative and particle number concentration, as expected. Figure 3.18 shows very clearly that discriminating pollution based on a fixed derivative value or particle number concentration threshold is not a good method as it would either remove good data or include pollution. Instead, a simple yet powerful approach to separate these two bands is to use a threshold on the derivative value defined by a power law function of the total particle number concentration. To do so, we identified an appropriate power law function, $y = ax^b$, $a = 0.2\,s^{-1}$, $b = 0.53$, and used it to normalize the derivative values; Figure 3.19 shows the result. Because the cluster of clean data is now orthogonal to the y-axis, it is easy to verify that these data are log-normally distrib-

uted (panel **b** in Figure 3.19) with a long tail that is composed of the polluted part of the dataset. The clean data distribution was fitted with a log-normal function while constraining and adjusting the upper bound of the fit to obtain the best match with the underlying distribution. In this way, we found a value of 1.12 to be a good threshold and used it to separate clean from polluted data after the power law normalization described above. It is important to note that both the threshold and the power law coefficients are not universal but depend on the instrument transfer function and the time resolution of the data, however the general approach can be extended to similar datasets.

This data filtering procedure provides a systematic approach to identify most of the pollution, however some adjustments were required. In particular, it was decided to take a conservative approach and removed all closest neighbours of polluted data and any point within a 30 minutes window when more than 2/3 of the data were already marked as pollution. Finally, with a visual inspection of the time series while using other pollution proxies for an independent verification (*e.g.* CO_2, black carbon, the PSD and wind direction), it was ensured that the data were cleaned properly.

It is compelling that the absolute value of the particle number concentration derivative for all ambient data from AO18 can be described, to a good extent, by a simple power law as a function of the total number concentration. We exploited this relationship for pollution identification but we do not have a clear understanding of the reason why such a trend emerges so clearly from the data. This is a topic that may deserve further investigations.

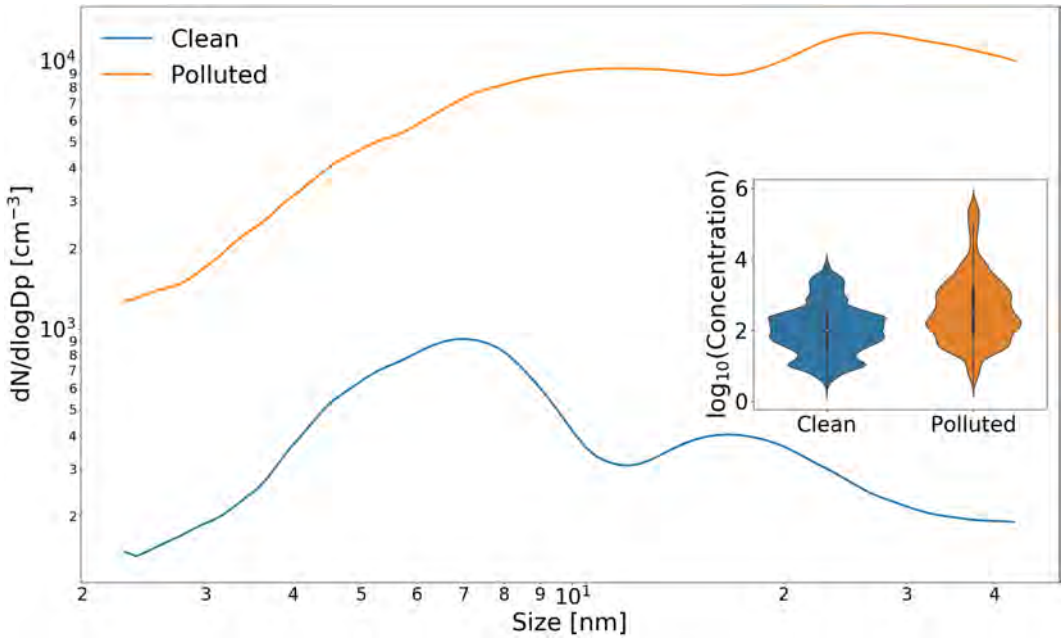

Figure 3.17: Average PSD measured with the NAIS during AO18 for clean and polluted conditions. The inset shows the different particle number concentration distributions under clean and polluted conditions by means of a violinplot. The violinplot shows the data distribution by means of a kernel density estimate.

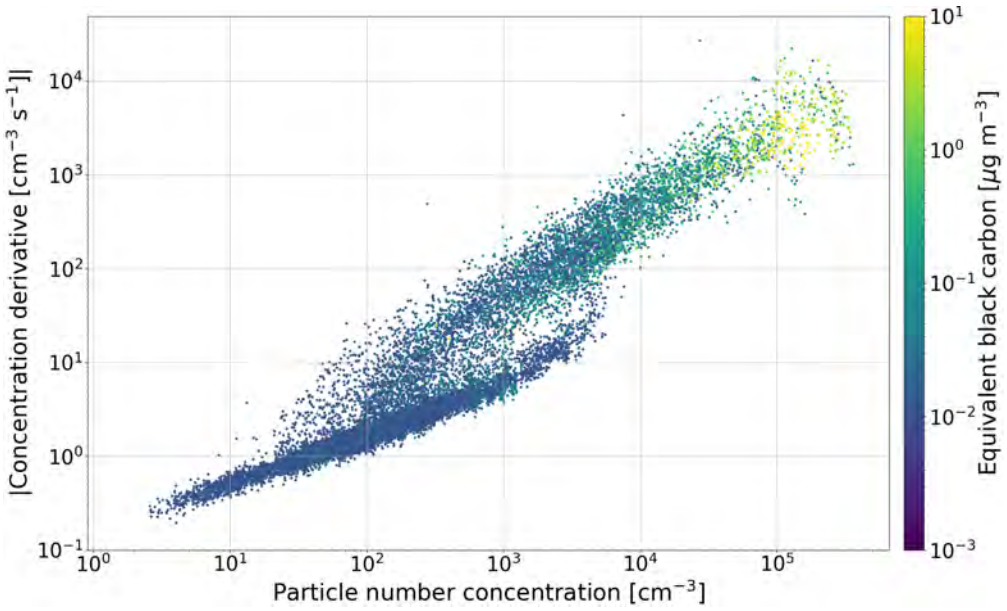

Figure 3.18: Absolute value of the particle number concentration derivative as a function of the total particle number concentration. The derivative was calculated on the original 1−second time resolution and then averaged to 1 minute. Data are colour-coded with the corresponding equivalent black carbon concentration.

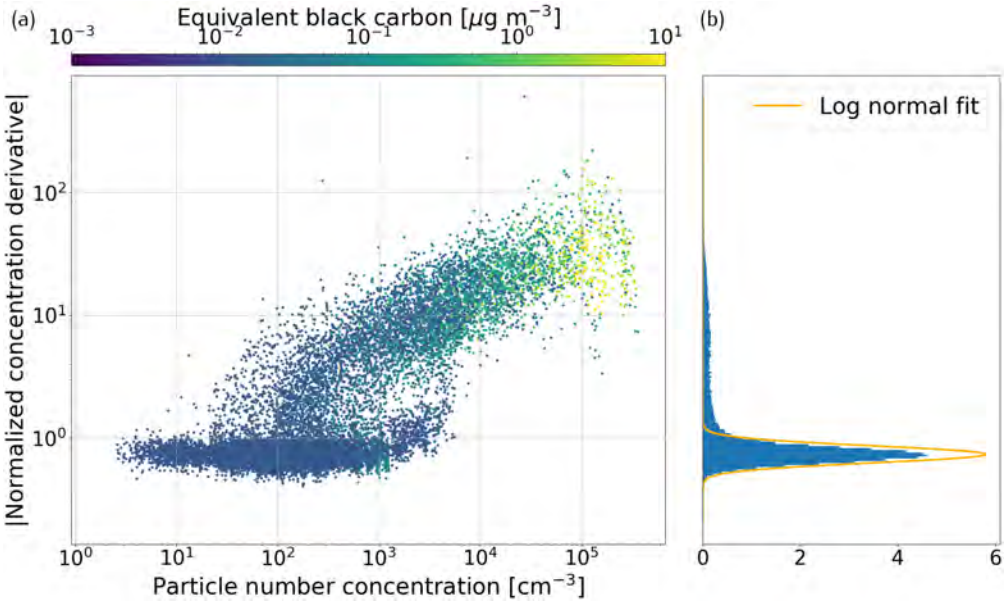

Figure 3.19: **(a)** Normalized absolute value of the particle number derivative as a function of the total particle number concentration. The normalization function is a power law: $y = ax^b$, $a = 0.2\,s^{-1}$, $b = 0.53$. Data are colour-coded with the corresponding equivalent black carbon concentration. **(b)** Distribution plot of the normalized derivative data with a log-normal fit on top; the fit was constrained to the main distribution mode.

3.4 OPEN DATA AND REPRODUCIBILITY

According to a survey by *Nature*, 90% of the scientists worldwide are worried about reproducibility of scientific results[116]. In the Earth and environmental sciences group more than 60% of the interviewed scientists experienced failure in reproducing pre-

viously published results. Similar survey results are not uncommon. The general awareness for the lack of reproducibility has increased and many research units are now establishing procedures to improve the situation[117]. One of the most effective actions to tackle this problem is to promote transparency and open science, which includes making data, results and all related materials publicly available. For field campaigns in polar or other remote regions promoting open science is even more important because repeating the measurements can be very complicated and expensive. This element is recognized also by state administrations and funding agencies that are now requesting explicitly to deposit data on public repositories. As an example, the 8 state members of the Arctic council recently signed a legally binding agreement to facilitate research in the Arctic, supporting, among the other things, full ad open access to scientific data and metadata[118].

Earth scientists recognise the importance of open science, with more than 80% of the scientists highlighting that open data is important for advancing research[119]. However, another survey points out that about 32% of Earth scientists do not make data available and 28% only upload them as supplementary material in the publications without proper documentation[120]. There are several barriers that hinder researchers to make their data fully available, among them the difficulty to structure the data in a clear way is apparently the most important[120].

This author believes that findable, accessible, interoperable and resuable (FAIR) open data is the way forward not only to improve reproducibility but also to accelerate scientific research and foster interdisciplinary collaborations. For this reason a considerable amount of time was invested to produce FAIR data with a complete documentation. All the data presented in this work are available on public repositories and uniquely identifiable with a DOI[21,121–143], most of the scripts that were used to analyse the data are available on GitHub or will be made available at a later stage.

4 OVERVIEW OF THE ANTARCTIC CIRCUMNAVIGATION EXPEDITION: STUDY OF PREINDUSTRIAL-LIKE AEROSOLS AND THEIR CLIMATE EFFECTS (ACE-SPACE)

Julia Schmale[1], Andrea Baccarini[1], Iris Thurnherr[2], Silvia Henning[3], Avichay Efraim[4], Leighton Regayre[5], Conor Bolas[6], Markus Hartmann[3], André Welti[3,†], Katrianne Lehtipalo[1,7,8], Franziska Aemisegger[2], Christian Tatzelt[3], Sebastian Landwehr[1], Robin L. Modini[1], Fiona Tummon[2,9], Jill Johnson[5], Neil Harris[10], Martin Schnaiter[11], Alessandro Toffoli[12], Marzieh Derkani[12], Nicolas Bukowiecki[1,‡], Frank Stratmann[3], Josef Dommen[1], Urs Baltensperger[1], Heini Wernli[2], Daniel Rosenfeld[4], Martin Gysel-Beer[1] and Ken Carslaw[5].

[1] *Laboratory of Atmospheric Chemistry, Paul Scherrer Institute, Villigen, Switzerland*
[2] *ETH, Institute for Atmospheric and Climate Science, Zurich, Switzerland*
[3] *Leibniz Institute for Tropospheric Research, Leipzig, Germany*
[4] *The Hebrew University of Jerusalem, Jerusalem, Israel*
[5] *University of Leeds, Leeds, United Kingdom*
[6] *University of Cambridge, Cambridge, United Kingdom*
[7] *Finnish Meteorological Institute, Helsinki, Finland*
[8] *Institute for Atmospheric and Earth System Research and Department of Physics, Faculty of Science, University of Helsinki, Helsinki, Finland*
[9] *MeteoSwiss, Payerne, Switzerland*
[10] *Centre for Environmental and Agricultural Informatics, Cranfield University, Cranfield, United Kingdom*
[11] *Karlsruhe Institute of Technology, Institute of Meteorology and Climate Research, Germany*
[12] *Department of Infrastructure Engineering, The University of Melbourne, Australia*
[†] *now at Finnish Meteorological Institute, Helsinki, Finland*
[‡] *now at Atmospheric Sciences, Department of Environmental Sciences, University of Basel, Basel, Switzerland*

Published in: **Bulletin of the American Meteorological Society 100, 11 (2019): 2260-2283, DOI:10.1175/BAMS-D-18-0187.1 (2019)**

Contribution: Designing, preparation and characterization of the measurement set-up, data acquisition, analysis of new particle formation and trace gas data, scientific discussion, contribution to manuscript writing and comments.

4.1 ABSTRACT

Uncertainty in radiative forcing caused by aerosol–cloud interactions is about twice as large as for CO_2 and remains the least well understood anthropogenic contribution to climate change. A major cause of uncertainty is the poorly quantified state of aerosols in the pristine preindustrial atmosphere, which defines the baseline against which anthropogenic effects are calculated. The Southern Ocean is one of the few remaining near-pristine aerosol environments on Earth, but there are very few measurements to help evaluate models. The Antarctic Circumnavigation Expedition: Study of Preindustrial-like Aerosols and their Climate Effects (ACE-SPACE) took place between December 2016 and March 2017 and covered the entire Southern Ocean region (Indian, Pacific, and Atlantic Oceans; length of ship track $> 33,000$ km) including previously unexplored areas. In situ measurements covered aerosol characteristics [*e.g.*, chemical composition, size distributions, and cloud condensation nuclei (CCN) number concentrations], trace gases, and meteorological variables. Remote sensing observations of cloud properties, the physical and microbial ocean state, and back trajectory analyses are used to interpret the in situ data. The contribution of sea spray to CCN in the westerly wind belt can be larger than 50%. The abundance of methanesulfonic acid indicates local and regional microbial influence on CCN abundance in Antarctic coastal waters and in the open ocean. We use the in situ data to evaluate simulated CCN concentrations from a global aerosol model. The extensive, available ACE-SPACE dataset provides an unprecedented opportunity to evaluate models and to reduce the uncertainty in radiative forcing associated with the natural processes of aerosol emission, formation, transport, and processing occurring over the pristine Southern Ocean.

4.2 INTRODUCTION

The World Climate Research Programme highlights the fact that "limited understanding of clouds is the major source of uncertainty in climate sensitivity, but it also contributes substantially to persistent biases in modeled circulation systems"[144]. Investigating aerosol–cloud interactions over the Southern Ocean is a crucial step toward improving these shortcomings for two reasons. The first reason is that the Southern Ocean is the largest continuous region on Earth in which climate models exhibit a strong positive bias of surface solar radiation of between 10 and 20 W m^{-2}[145]. The bias has implications for the representation of sea surface temperature, sea ice, storm tracks, and atmospheric energy transport in climate models[146–148].

A major reason for this bias is the poor representation of the persistent layer of shallow clouds in climate models, which do not reflect enough solar radiation[149,150]. Stratocumulus clouds over the Southern Ocean are often mixed-phased and contain supercooled droplets[151]. In mixed-phased clouds liquid droplets and ice crystals coexist. Ice crystals form on ice nucleating particles (INP) at temperatures higher than the homogeneous freezing point of water (at$<$ –36°C), while liquid droplets form on cloud condensation nuclei (CCN). Models often produce too many ice crystals in mixed-phased clouds that consume the liquid droplets and precipitate the cloud[148]. Models are hence very sensitive to INPs as demonstrated by Vergara-Temprado *et al.*[152], who show that the short lifetime of clouds in the cold sectors of extratropical cyclones in the model is caused by inadequate representation of natural INP and cloud microphysical processes.

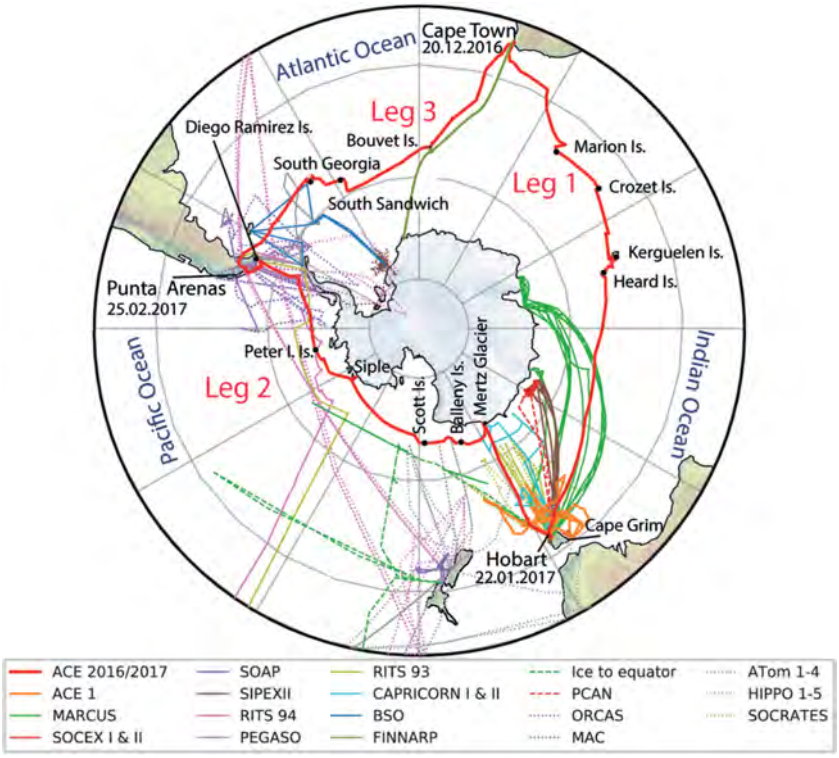

Figure 4.1: Tracks of Southern Ocean campaigns with aerosol measurement components between the 1970s and 2018. Harbor departure dates and island (Is.) stops of the ACE 2016/17 cruise (red line) are indicated. Ship tracks are represented by full lines, and flight tracks by dashed lines. See Table 4.1 for campaign information.

The second reason why the study of Southern Ocean clouds is important is because the region still exhibits preindustrial-like aerosol properties in austral summer due to its remoteness[41]. Currently, the lack of a well-defined baseline for preindustrial aerosol–cloud interactions introduces large uncertainty in estimates of anthropogenic radiative forcing caused by cloud albedo adjustments due to human activity[29]. Hence, studying aerosol and cloud properties and behavior under preindustrial-like aerosol conditions is essential to reduce this uncertainty.

Fundamental questions related to the sources and processes of particles that influence cloud albedo remain open despite the number of field studies targeted at understanding gaseous chemistry, aerosol processes, and clouds in the region since the 1970s (Figure 4.1, Table 4.1). The remoteness of the Southern Ocean and the large and heterogeneous area it covers pose a challenge to performing in situ measurements. In situ measurements are needed to study processes that cannot be observed by satellite, such as condensation of semi-volatile species on aerosol particles or heterogeneous chemistry (cloud processing), but need to be included in models to properly represent the surface energy budget. Among these processes is also sea spray formation, the Southern Ocean being the stormiest ocean in the world[153]. The formation of secondary aerosol from biogenic gaseous emissions is another important process because the Southern Ocean is one of the most biologically active in the world[49]. Entrainment of free tropospheric air into the marine boundary layer can also influence the aerosol budget and cloud properties[44]. Understanding these processes will allow us to better simulate the CCN and INP budget over the Southern Ocean. CCN and INP are fundamental ingredients to cloud formation in addition to atmospheric dynamic processes[154].

This paper presents an overview and first results from the Antarctic Circumnavigation Expedition: Study of Preindustrial-like Aerosol Climate Effects (ACE-SPACE) project. In this project we combined in situ measurements of aerosols and trace gases, satellite observations of cloud droplet number concentrations, and global model simulations to constrain anthropogenic radiative forcing from aerosol cloud interactions.

4.3 ACE-SPACE STUDY DESIGN

Measurements were conducted from December 2016 to March 2017 aboard the R/V *Akademik Tryoshnikov* between 34° and 78°S for 90 days while the ship moved from Cape Town, South Africa, through the Indian Ocean to Hobart, Australia (leg 1), via the Pacific Ocean to Punta Arenas, Chile (leg 2), and through the Atlantic Ocean back to Cape Town (leg 3, Figure 4.1). Given the constant movement of the ship except for short stays (12–60 h) at islands and the Antarctic coast, the focus of ACE-SPACE was the continuous measurements of a range of aerosol and trace gas characteristics (Table 4.2) relevant for aerosol–cloud interactions. The in situ measurements are also used to validate satellite observations of cloud droplet number concentrations (N_d) and to constrain the uncertainty of aerosol parameters in the Global Model of Aerosol Processes[170] and hence the uncertainty in aerosol radiative forcing in the United Kingdom Chemistry and Aerosol (UKCA) model. Other projects on board measured complementary variables such as wave properties, marine microbial activity and precipitation (variables used for this work are listed in Table 4.2, an overview of all projects is provided at http://spi-ace-expedition.ch/).

Specific objectives

Measurements were designed for three principal objectives:

i to capture the summertime spatial variability of the aerosol characteristics around Antarctica and the Southern Ocean;

ii to provide an in situ reference, meaning spectra of CCN number concentrations, for remotely sensed cloud droplet number concentration N_d; and

iii to facilitate improved representations of preindustrial-like aerosol properties in global climate models to reevaluate the radiative forcing from aerosol–cloud interactions.

Regarding (i), the Southern Ocean is one of the regions where we know very little about aerosol properties[41]. Geographically, most efforts have focused on specific sectors of the Southern Ocean, for example, south of Tasmania or around the Drake Passage, in the last three decades (Table 4.1). ACE-SPACE offered the first opportunity to study aerosol properties in the Indian, Pacific, and Atlantic Oceans in the same season. This allows comparison of aerosol properties over the open ocean in the westerly wind belt, close to the coast of Antarctica in the microbially active polynya region, and in the vicinity of sub-Antarctic islands. Polynya are large open water areas in otherwise sea-ice-covered regions. Expected differences include the relative importance of sea spray aerosol (SSA; including sea salt and organic compounds) and marine biogenic emissions for the CCN number concentration[45,155], the potential contribution of locally confined emissions from land-based animal colonies[171], and occasional influence

Table 4.1: List of studies related to aerosol-cloud interactions in the Southern Ocean.

Name	Year	Location	Objective	Reference	Platform type
Cape Grim	Since 1976	40°38′S, 144°43′E	Long-term monitoring of atmospheric constituents	Ayers *et al.*[155]	Station
BSO	Oct 1992 - Jan 1993	51°-76°S	British Southern Ocean cruise influence of biogenic emissions on CCN	O'Dowd *et al.*[156]	Vessel
RITS 93	Mar 1993	53°-70°S	Radiatively Important Trace Species, atmospheric chemistry	Bates *et al.*[157]	Vessel
RITS 94	Dec 1994	53°-70°S	Radiatively Important Trace Species, atmospheric chemistry	Bates *et al.*[157]	Vessel
SOCEX I and II	Jul 1993, Jan - Feb 1995	40°-43°S	Southern Ocean Cloud Experiments seasonality, cloud microphysics	Boers *et al.*[158], Boers *et al.*[159]	Vessel
ACE I	Nov - Dec 1995	40°-55°S	Aerosol Characterization Experiment, atmospheric chemical processes, cloud microphysics	Bates *et al.*[160]	Vessel
FINNARP	Nov - Dec 2004	34°-70°S	Finnish Antarctic Research Program, ultrafine aerosol characterization	Vana *et al.*[161]	Vessel
HIPPO	Five flights between 2009 and 2011	43°-67°S	HIAPER Pole to Pole Observations, atmospheric chemical processes, cloud microphysics	Wofsy[162]	Aircraft
SOAP	Feb - Mar 2012	41°-47°S	Surface Ocean Aerosol Production	Law *et al.*[163]	Vessel
SIPEX II	Sep - Nov 2012	42°-66°S	Sea Ice Physics and Ecosystem Experiment, aerosol microphysics and chemistry, waves	Humphries *et al.*[164], Kohout *et al.*[165]	Vessel
PEGASO	Jan - Feb 2015	53°-60°S	Plankton-derived Emissions of trace Gases and Aerosols in the Southern Ocean, air–sea interactions of trace gases and aerosols	Dall'Osto *et al.*[52], Fossum *et al.*[45]	Vessel
MAC	Nov - Dec 2015	72°-78°S	Microphysics of Antarctic Clouds	O'Shea *et al.*[166]	Aircraft/ station
ORCAS	Jan - Mar 2016	35°-75°S	O_2/N_2 Ratio and CO_2 Airborne Southern Ocean Study, air–sea gas exchange, cloud microphysics	Stephens *et al.*[167]	Aircraft (vessel)
CAPRICORN I and II	Mar 2015, Mar - Apr 2016	43°-48°S, 43°-53°S	Clouds, Aerosols, Precipitation, Radiation and Atmospheric Composition	Protat *et al.*[168], Mace *et al.*[169]	Vessel
ACE 2016/17	Dec 2016 - Mar 2017	34°-78°S	Antarctic Circumnavigation Expedition, preindustrial-like aerosol cloud interaction	This study	Vessel
ATom	Feb 2017 flight from New Zealand to Chile	45°-66°S	Atmospheric Tomography Mission, atmospheric chemistry	ATom	Aircraft
Ice to Equator	Apr - Jun 2016	0°-65°S	Monitoring ocean change and variability along 170°W	Ice to equator	Vessel
PCAN	Jan - Mar 2017		Polar Cell Aerosol Nucleation	PCAN	Vessel
SOCRATES	Jan - Feb 2018	43°-67°S	Southern Ocean Clouds, Radiation, Aerosol Transport Experimental Study	SOCRATES	Aircraft, vessel
MARCUS	Oct 2017 - Apr 2018	43°-67°S	Measurements of Aerosols, Radiation, and Clouds over the Southern Ocean	MARCUS	Vessel

Table 4.2: Instrumentation and measured variables on board R/V Akademik Tryoshnikov. All data will be available on the ACE database (https://zenodo.org/communities/spi-ace/). Datasets will be available within 2019. Some have restricted access until the end of 2019; thereafter, they are fully accessible. Particle sizes are given as diameters. Abbreviations are condensation particle counter (CPC), neutral cluster and air ion spectrometer (NAIS), scanning mobility particle sizer (SMPS), aerodynamic particle sizer (APS), wideband integrated bioaerosol sensor (WIBS), chemical ionization atmospheric pressure interface time of flight mass spectrometer (CI-APi-TOF), aerosol chemical speciation monitor (ACSM), cloud condensation nuclei counter (CCNC), cloud condensation nuclei (CCN), high-volume filter sampler (HVS), low-volume filter sampler (LVS), ice nucleating particles (INP), custom-built online gas chromotograph (iDIRAC), Automated Weather Station (AWS), and wave monitoring system II (WaMoSII).

Observation type	Instrument name	Measured variables	Time resolution (acquisition)
Particle microphysics	CPC (TSI models 3022, 3772, 3010D)	Particle number concentration with different lower cutoff (7, 10, 20 nm)	10 s
	NAIS	Particle number size distribution (2–40 nm), ion size distribution (0.8–40 nm)	3.5 min
	SMPS	Particle number size distribution (11–400 nm)	5 min
	APS	Particle number size distribution (0.5–19 μm)	5 min
	WIBS-4	Particle number size distribution (0.5–12.5 μm), fluorescent particle number concentration and size	1 s
Real-time chemical composition of ions, clusters, particles	CI-APi-TOF	Chemical composition of ions or neutral clusters	1 min
	ACSM	Submicron particulate organics, ammonium, nitrate, sulfate, chloride	30 min
	Aethalometer	Equivalent black carbon (eBC) mass concentration of total PM	1 s
Hygroscopicity	CCNC	CCN number concentrations (at 0.15%, 0.2%, 0.3%, 0.5%, 0.7% supersaturation)	1 s
Filter-based chemical composition of particles	HVS	PM_{10} organic carbon (OC), elemental carbon (EC), water soluble organic carbon (WSOC), major ions (e.g., Na^+, Cl^-), methanesulfonic acid	24 h
	LVS	PM_{10} INP number concentrations	8 h
Optical particle properties	Microtops	Aerosol optical depth (AOD)	Event based
Trace gases	Ozone monitor (model 2BT)	O_3 mixing ratio	10 s
	Picarro 2401	CO_2, CO, CH_4, H_2O mixing ratios	1 s
	iDIRAC	isoprene mixing ratio	10 min
Meteorology	Ship-based Vaisala AWS420 including ceilometer	Wind speed, wind direction, relative humidity, temperature, pressure, cloud-base height, radiation	30 s
Waves	WaMoSII	Wave height, velocity, phase, period	20 min

from outgassing volcanoes[172]. Figure 4.2 schematically illustrates the various elements and processes that can contribute to the particle population. Based on previous cruises in the Southern Ocean, the contribution of SSA to CCN can be highly variable between 10% and 100%[44,45]. This implies that in the absence of anthropogenic influence the oxidation products from marine emissions of dimethylsulfide (DMS), that is, non-sea-salt sulfate (nss-SO_4) and methanesulfonic acid (MSA, Figure 4.2) can be responsible for very large fractions of the CCN population. DMS can contribute to CCN through two different pathways (e.g., Korhonen *et al.*[56]): 1) DMS oxidation to sulfuric acid and formation of new particles, which can either happen in the marine boundary layer (MBL) or in the free troposphere, and 2) condensation of DMS oxidation products (*i.e.*, MSA and H_2SO_4) onto preexisting smaller particles, which subsequently grow into the CCN size range[173,174].

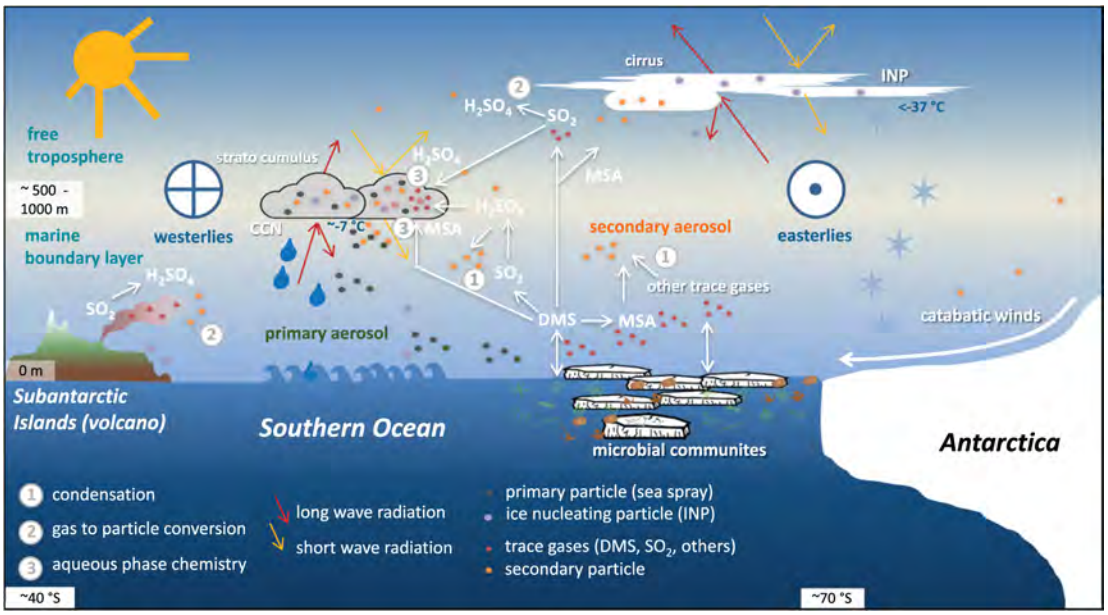

Figure 4.2: Schematic of summertime aerosol processes over the Southern Ocean. Individual processes are described in the text. Latitudes, heights, and temperatures are only indicative.

With regard to the second objective, satellite observations of N_d are most relevant for globally assessing the response of clouds to CCN. The relationship between surface-measured CCN and Nd determines the climatic effects of the CCN from the ocean surface. Increasing Nd for the same cloud liquid water path increases cloud albedo (the Twomey effect[175]). Increasing N_d for a given cloud geometrical thickness decreases precipitation[176]. Since precipitation tends to break cloud cover of marine stratocumulus[177–179], added CCN increase cloud cover. Rosenfeld *et al.*[180] have shown that increasing N_d for a given cloud geometrical thickness also increases the liquid water path. The combination of the effects (increased cloud albedo, cloud cover, and liquid water path) means a dramatic increase of the cloud radiative effect[180]. Since N_d has such a major impact on the energy budget, it is necessary to accurately determine its driving factors. The CCN number concentration as a function of supersaturation and the base updraft determine the peak supersaturation at cloud base[181]. However, documenting the cause and effect relationships between surface-measured CCN and N_d is very challenging due to the uncertainty in base updraft and the variable strength of the connection between the CCN near the surface and at cloud base. Therefore,

addressing this question by the combined satellite and ship measurements is of major importance. For methodological reasons (see Appendix B), we focus on liquid clouds. However, it is important to note that understanding mixed-phased clouds over the Southern Ocean is highly important for the regional energy balance[169].

With respect to the third objective, much progress has been made in understanding the causes of uncertainty in state variables related to aerosol radiative forcing, such as cloud-active aerosol concentrations, precipitation, and top-of-atmosphere radiative fluxes. However, a well-constrained representation of the present-day atmosphere (influenced by anthropogenic aerosols) is insufficient to reduce uncertainty in aerosol forcing over the industrial period[182]. Processes known to cause much of the uncertainty in the preindustrial time need further investigation. These include sea spray and DMS emission fluxes, particle formation rates, and particle size distributions[29,183]. A modeling study by Hamilton *et al.*[41] showed that in austral summer the Southern Ocean is among the most pristine locations on Earth, with more than 29 days month^{-1} in which the aerosol population is not directly influenced by human activity. Hence, measurements taken in this region are ideally suited to constraining preindustrial-like aerosol concentrations. Furthermore, key measurements taken during the ACE-SPACE (sea spray particle concentrations, nss-SO_4 concentrations, newly formed particle concentrations, and particle size distributions) can be used to constrain the most uncertain model processes that cause aerosol radiative forcing uncertainty in climate models.

In situ measurements and remote sensing

Table 4.2 gives details of the in situ instrument suite that we installed on the research vessel in a laboratory container with inlets sampling approximately 16 m above mean sea level (MSL). The link to the database is given in the table caption. More details regarding sampling line loss assessment, identification of ship exhaust periods, and instruments are provided in Appendix A. Cloud droplet number concentrations were retrieved from MODIS cloud products (see Appendix B).

Modeling tools

With the back trajectories calculated using the Lagrangian analysis tool LAGRANTO[184,185] based on wind fields from the operational analysis data of the European Centre for Medium-Range Weather Forecasts (ECMWF), we determined the airmass history for interpretation of the in situ results. In the supplementary material we provide an animation of airmass trajectories for every hour of the expedition.

Measurements are compared to output from version 8.4 of the UKCA model, which is a whole-atmosphere chemistry and aerosol model embedded within the HadGEM3 host model[186]. Within the UKCA model the evolution of particle size distribution and size-resolved chemical composition of aerosols in seven size and composition modes are calculated using the Global Model of Aerosol Processes model (GLOMAP-model[170]). Here we compare measurements to the mean output from perturbed parameter ensembles of the UKCA model[187]. In these ensembles multiple uncertain aerosol and physical atmosphere parameters were perturbed simultaneously to produce a set of model variants that spans the model behaviour and can be used to quantify the value of measurements as constraints on model uncertainty. More details on both models are given in Appendix C.

4.4 ENVIRONMENTAL CONDITIONS DURING THE CRUISE

Figure 4.3a shows the climatological wind speed from the ERA-Interim dataset[188] at 10 m altitude for December–March from January 1979 to February 2017. The actual wind conditions encountered during ACE-SPACE are overlain. To check the comparability of the ECMWF product and the measured wind, we correlated the hourly values for the expedition at 30 m height and found a correlation coefficient of $R^2 = 0.83$ and a slope of 1.12 (with higher measured values). For details, see Appendix C.

The temporal and spatial variability of wind speeds encountered during the expedition is much larger than reflected by the 38-yr climatology. Individual sections, especially in the westerly wind belt between 70° and 130°E (leg 1) and 30°W and 10°E (leg 3), as well as most of leg 2, were calmer than expected from climatology. One contributing factor might be the avoidance of storms by the expedition. However, the median wind speeds of legs 1 and 3 are similar to the climatological mean.

Especially within the high wind belt, frontal systems are frequently expected[189], which can impact the aerosol population, for example, through precipitation. During leg 1, warm-air advection dominated (60% of all instances), whereas cold-air advection was more frequent during legs 2 and 3 with 80% and 85% of the time, respectively.

Sea ice conditions were mostly relevant during leg 2, because the other legs passed well north of the main sea ice regions (Figure 4.3b). Compared to climatology[190,191], there was significantly less ice in the Amundsen Sea (around 120°W near the Siple region), but more near the Mertz area (approximately 150°E). In fact, the spring–summer season 2016/17 showed unusual warming of the Southern Ocean by up to 1°C compared to the 2010–15 average (https://data.giss.nasa.gov/gistemp/maps/), which might have had some impact on sea spray production and biological activity.

The Southern Ocean is known for its high waves, caused by strong surface winds and large fetch[153]. Figure 4.3b compares the measured significant wave height H_s with the corrected December–March climatological significant H_s from 2001 to 2018 from the joint CNES/NASA satellite oceanography mission series Jason-1 and Jason-2[192]. The former was launched in December 2001 and decommissioned in July 2013, while the latter is an ongoing follow-on mission launched in June 2008. Averages are computed in grid points of 0.5° resolution. The open-ocean legs 1 and 3 are characterized by similar H_s with a measured median of 5.5 m and an interquartile range (IQR) between 4 and 7 m. The climatological mean suggests H_s around 4.5 m and is hence slightly lower than that encountered during ACE-SPACE. Leg 2, south of the westerly wind belt, saw a median H_s of 2.5 m. The breaking of waves is the main driver behind sea spray production. During breaking, which is induced when H_s is larger than one-seventh of the wavelength, air bubbles are entrained into the water that subsequently rise to the surface and either eject jet droplets or spray from collapsing cavities[193].

In addition to the physical conditions described above, we present in Figures 4.3c and 4.3d the MODIS-retrieved concentration of chlorophyll-a during February 2017 and the climatological mean between 2002 and 2016 based on MODIS Aqua observations[194]. Generally, we encountered the expected pattern of blooms, meaning lower activity in the leg 1 region and more intense blooms during leg 2. A direct comparison for leg 2 is difficult due to the cloud coverage (white areas in Figure 4.3d). Leg 3 saw less activity than the climatological mean, likely because it was relatively late in the season (March). Chlorophyll-a is a direct indication for the presence of phytoplankton but cannot be used to directly infer the amount of DMS released into the atmosphere, which can subsequently be oxidized to H_2SO_4 or MSA Figure 4.2. We show the con-

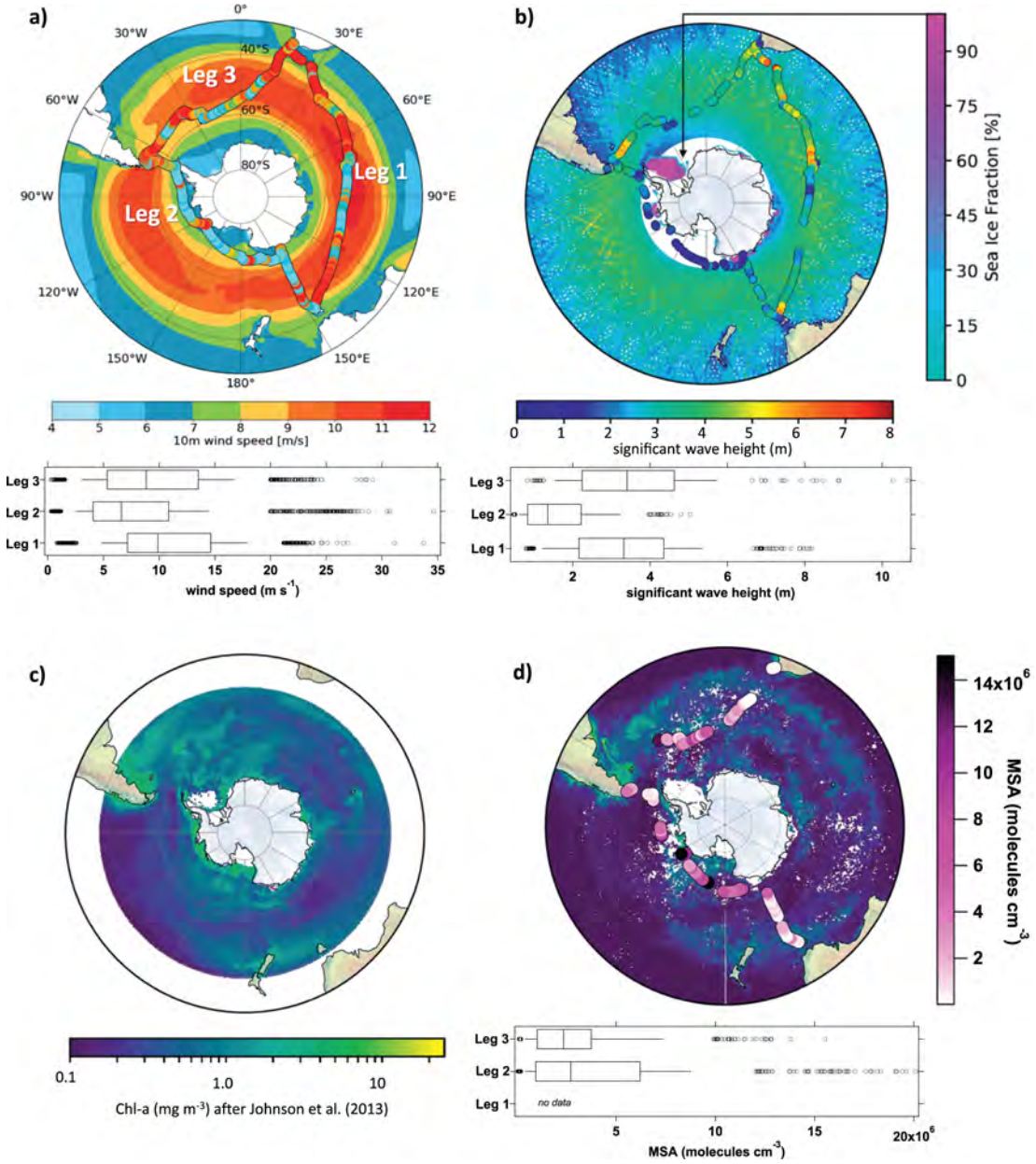

Figure 4.3: Climatological mean values for December–March of **(a)** 10−m wind speed, **(b)** wave height and sea ice extent, and **(c)** chlorophyll-a (Chl-a). Wind speeds are based on the 1979–2017 ERA-Interim climatology. The measured wind speed during the cruise is plotted along the track, and box-and-whisker plots at the bottom of the panel summarize each leg. They denote the mean, interquartile range, 10th and 90th percentiles, and data points in the outer 2.5th percentiles. The significant wave height is based on radar altimeter data from the CNES/NASA oceanography mission series Jason−1 and Jason−2 for the years 2001–18. Measurements from the cruise are overlain and box plots are provided. Additionally, sea ice extent from MODIS is shown for 31 January 2017 (color scale on the right). In (c) the MODIS chlorophyll-a climatology covers DJFM between 2002 and 2016. **(d)** The chlorophyll-a concentrations for February 2017 [MODIS, same color scale as in (c)] and MSA in situ concentrations including boxplot.

centration of gaseous MSA in Figure 4.3d. The highest localized concentrations were found during leg 2 in the polynya near the Siple region and leg 3 southwest of the Sandwich Islands. Note that high atmospheric MSA concentrations are not necessar-

ily expected in the same location of high marine chlorophyll-a or DMS concentrations because of atmospheric transport and transformation processes. The atmospheric lifetime of DMS (MSA) in the Southern Ocean is estimated to vary between 2 and 5 days (2–6 days), calculated as the ratio of the mean atmospheric burden by the sum of loss processes[173]. We find enhanced MSA concentrations in the immediate vicinity of regions with elevated chlorophyll-a concentrations and along trajectories that travelled above such regions.

Transport of anthropogenic emissions to the Southern Ocean is another environmental condition that we need to consider to understand in how far our observations during ACE-SPACE are preindustrial-like. Figure 4.4 shows the concentrations of equivalent black carbon (eBC) and CO as a function of latitude and indicates the location of the visited ports. Elevated concentrations of these two tracers can represent anthropogenic emission influence. Concentrations for both tracers reach their background levels south of 55°S: 19.2 ng m^{-3} eBC and 23.2 ppb CO. For comparison, eBC concentrations at the high alpine observatory Jungfraujoch 3,500 m MSL in the Swiss Alps, which represent the remote European atmosphere, are generally > 50 ng m^{-3} during not specifically polluted conditions[195].

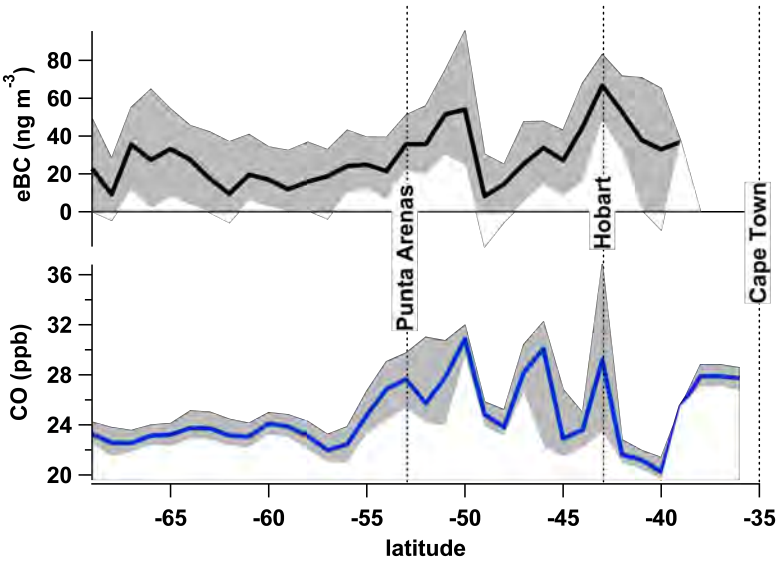

Figure 4.4: Concentrations of the anthropogenic tracers eBC and CO as functions of latitude. Solid lines indicate the median values, and the shaded area the interquartile range. The dotted vertical lines indicate the latitudinal locations of the ports visited.

4.5 PARTICLE NUMBER, CLOUD CONDENSATION NUCLEI AND ICE NUCLEATING PARTICLE CONCENTRATION

Aerosol properties varied substantially over the Southern Ocean, and each leg exhibited distinct characteristics (Table 4.3). Total particle number concentrations with a lower cutoff diameter of 7 nm N_7 ranged between 10 and $> 1,000$ cm^{-3} (Figure 4.5). For reference, over the summer Arctic Ocean concentrations vary in a broader range between 1 and $< 4,000$ cm^{-3}, however with a smaller median concentration (measured with the same instrument during the Arctic Ocean 2018 expedition). Concentrations in urban areas are usually between 10^4 and 10^5 cm^{-3} [*e.g.* Wang *et al.*[196] for Beijing and

Pikridas *et al.*[197] for Paris]. Leg 1 saw the highest median concentration with 470 cm^{-3}, followed by leg 3 with 350 cm^{-3} and leg 2 with 280 cm^{-3}. Importantly, CCN activating at a supersaturation of 0.2% ($CCN_{0.2}$) do not follow the same pattern. Median concentrations are nearly the same for legs 1 and 2 (114 and 111 cm^{-3}) and slightly lower for leg 3 (90 cm^{-3}). These values are significantly higher than in the Arctic and slightly lower than at Mace Head[107]. Figure 4.6 provides the $CCN_{0.2}$ concentration (Figure 4.6b) and the activation ratio (Figure 4.6c), defined as the CCN concentration divided by the total particle number concentration N_7 along the track. The activation is higher in leg 2 and can be explained with larger particles (see Figure 4.6a) and possibly also differences in chemical composition.

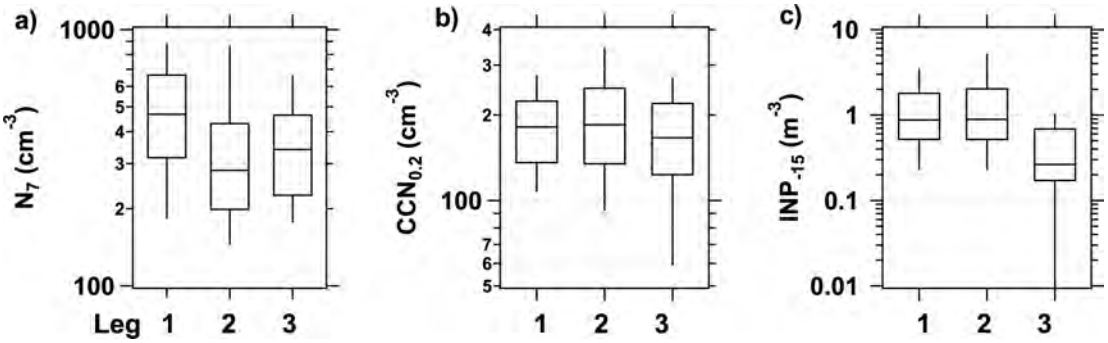

Figure 4.5: Number concentrations of different particle types: **(a)** total particle number concentrations > 7 nm (N_7), **(b)** $CCN_{0.2}$, and **(c)** INP at −15°C for each leg. The box-and-whisker plots show the median, interquartile range, and 10th and 90th percentiles.

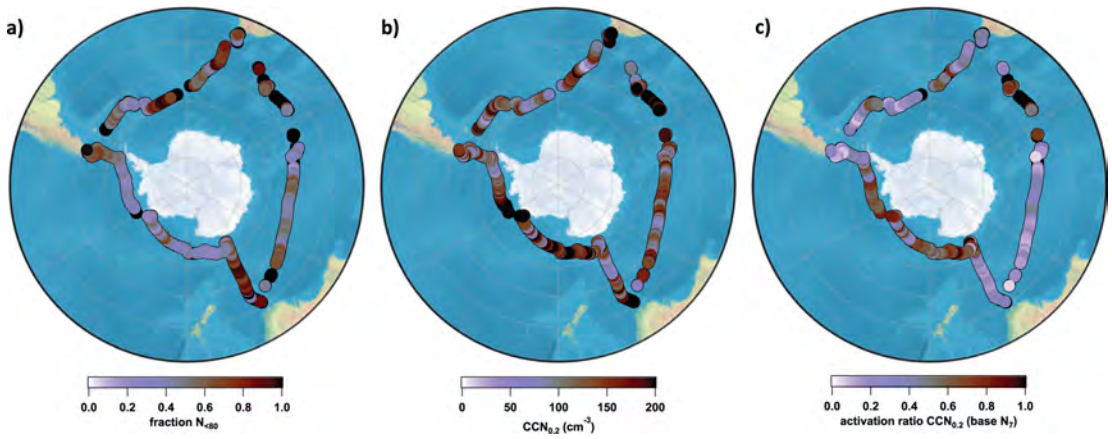

Figure 4.6: Aerosol characteristics along the ship track: **(a)** fraction of particles with diameters lower than 80 nm compared to particles greater than 7 nm, **(b)** $CCN_{0.2}$ concentration, and **(c)** ratio of $CCN_{0.2}$ over N_7.

Concentrations of INP at –15°C (INP_{-15}; Figure 4.5) ranged between the detection limit (0.1 m^{-3}) and 54 m^{-3} accounting for all measured values. The detection limit is 0.1–0.2 m^{-3} depending on the sampled volume of air. The median values per leg are < 1 m^{-3}, with leg 3 having the smallest INP concentrations. For reference, INP concentrations at Mace Head in Ireland are also around 1 m^{-3} during clean conditions[198]. Legs 1 and 2 show very similar distributions of INP number concentrations even though they represent two very different environments. Comparing our results to the survey from Bigg[199] of INP_{-15} concentrations between 80°E and 140°W, we find concentrations lower by two orders of magnitude. Newer data from McCluskey

Table 4.3: Key aerosol and trace gas properties per leg. Numbers are medians and interquartile ranges (IQR) are given in brackets. N_7 refers to all particles larger than 7nm measured by the condensation particle counter, $N < 80$ refers to the number of particles with a diameter smaller than 80 nm, $CCN_{0.2}$ is CCN that activates at 0.2% supersaturation, and INP_{-15} is INP that produces ice crystals at –15°C.

Property	**Leg** 1	**Leg** 2	**Leg** 3
N_7 (cm^{-3})	470 [320, 665]	280 [200, 430]	350 [225, 460]
SSA concentration (cm^{-3})	151 [73, 253]	28 [11, 72]	89 [41, 174]
SSA mode contribution to total integrated size distribution (%)	10 [7, 15]	9 [5, 14]	10 [5, 16]
$CCN_{0.2}$ (cm^{-3})	114 [80, 140]	111 [80, 150]	90 [65, 125]
Activation ratio $CCN_{0.2}$ (cm^{-3}) **based on N_7** (%)	25 [15, 39]	51 [27, 65]	37 [19, 48]
SSA mode contribution to CCN(%)	SS = 0.15% 32 [23, 55] SS = 1.0% 16 [10, 22]	SS = 0.15% 19 [11, 32] SS = 1.0% 11 [6, 16]	SS = 0.15% 30 [18, 51] SS = 1.0% 16 [9, 25]
Hoppel minimum diameter [range] (nm)	48 [44, 53]	74 [70, 78]	68 [51, 82]
Contribution of $N < 80$ (%)	51 [42, 64]	47 [36, 63]	55 [39, 71]
INP–15 (m^{-3})	0.87 [0.52, 1.79]	0.89 [0.52, 2.02]	0.26 [0.17, 0.69]
First cloud level (m)	590 [330, 918]	500 [225, 855]	610 [291, 927]
ECMWF boundary layer height (m)	851 [648, 1252]	660 [340, 913]	807 [592, 1127]
MSA gaseous (molecules cm^{-3})	–	2.7×10^6 $[1.0 \times 10^6,\ 6.2 \times 10^6]$	2.4×106 $[1.0 \times 10^6,\ 3.7 \times 10^6]$
H_2SO_4 gaseous (molecules cm^{-3})	–	2.6×10^6 $[1.7 \times 10^6,\ 3.7 \times 10^6]$	2.1×10^6 $[1.3 \times 10^6,\ 3.7 \times 10^6]$
Particulate MSA $(\mu g\ m^{-3})$	0.13 [0.08, 0.18]	0.17 [0.08, 0.23]	0.08 [0.06, 0.10]
Particulate sodium $(\mu g\ m^{-3})$	3.94 [2.88, 5.41]	1.75 [1.03, 2.88]	2.74 [2.02, 4.28]
Particulate chloride $(\mu g\ m^{-3})$	6.40 [4.80, 9.05]	2.60 [1.67, 4.87]	4.59 [3.28, 7.41]
Temperature $(°C)$	6.1 [4.5, 10.2]	–0.1 [–0.9, 3.1]	3.2 [1.3, 9.5]
Wind speed $(m\ s^{-1})$	9.88 [7.14, 14.63]	6.62 [4.07, 10.86]	8.85 [5.34, 13.51]
Significant wave height (m)	3.3 [2.2, 4.3]	1.4 [0.8, 2.2]	3.4 [2.2, 4.6]

et al.[200] between Tasmania and 53°S from the CAPRICORN campaign (Table 4.1) compare well with ours. Their measurements had an approximate limit of detection of 1 m^{-3} for INP_{-15}. The discrepancies between the recent measurements and in the 1970s are currently under investigation.

4.6 PARTICLE SIZE, HYGROSCOPICITY AND AIRMASS ORIGIN

To interpret the CCN concentrations, particle size and hygroscopicity (water affinity), airmass history, and cloud processing information are needed. We show aggregated data of leg 2 (Figure 4.7) as an example for the type of information that can be extracted from the ACE-SPACE dataset that includes the particle size distribution, an estimate of the cloud supersaturation and the particle hygroscopicity. Figure 4.7a shows k-means-based clusters of particle size distributions (run with 1,000 iterations). The figure also shows the airmass history associated with each cluster (Figures 4.7b-d). For each hour of leg 2 in which a certain cluster occurred, we released 21 trajectories at different levels below 850 hPa. This pressure level roughly represents the MBL height. We counted the number of trajectories per cluster that passed through bins of 0.5° latitude and 10−hPa altitude. Figures 4.7b-d hence provide a longitudinally integrated information about the statistical distribution of the airmass origin during the previous 5 days. They allow for interpretation of particle processing rather than emission sources.

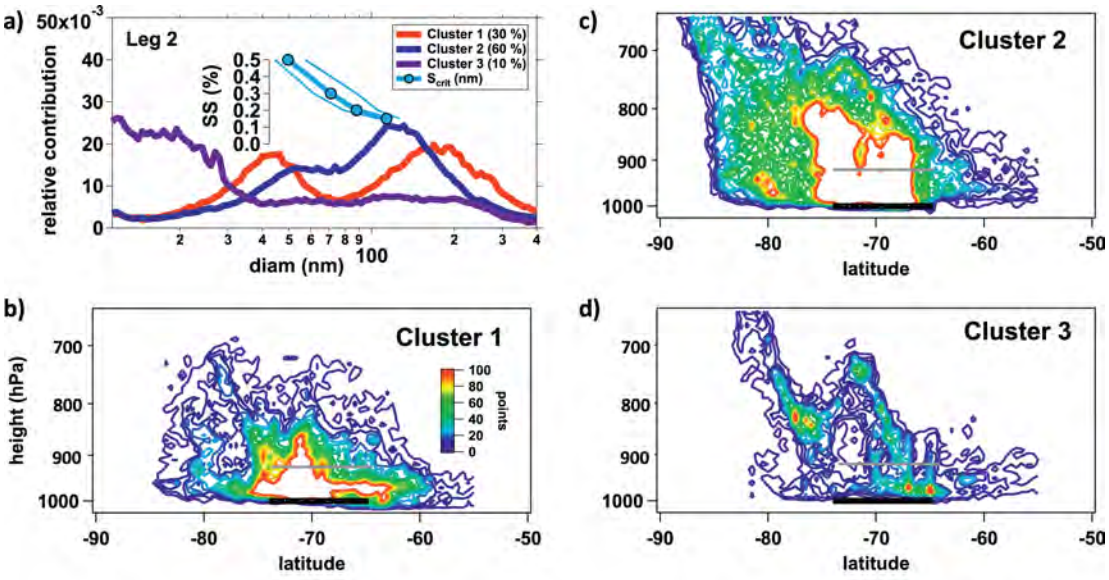

Figure 4.7: Clustered particle size distributions of leg 2 and 5-day airmass back trajectories. **(a)** Normalized size distribution clusters. The inset shows the supersaturation median and interquartile range as a function of the critical diameter for leg 2. **(b)–(d)** Contour plots of back trajectories for clusters 1, 2, and 3, respectively, are plotted as the zonal sum (crossings) as a function of latitude and altitude. The black line indicates the latitude band of the ship track, and the gray line the approximate average cloud-base level.

The aerosol size distribution for cluster 1 features a pronounced Hoppel minimum[201], a signature of cloud processing. It can reflect the scavenging of smaller Aitken mode

particles into cloud droplets, which subsequently accrue mass through the aqueous phase oxidation of volatile gases such as SO_2 (originating from DMS oxidation) into less volatile H_2SO_4, leaving larger accumulation mode particles behind if the cloud evaporates. The Hoppel minimum diameter ranges between 70 and 78 nm, which is distinctly larger than the Hoppel minimum diameters of the other legs (Table 4.3), see also Figure 4.6a for the small fraction of particles with a diameter smaller than 80 nm N$<$ 80 during leg 2. Such a difference can reflect both varying cloud supersaturations across the Southern Ocean regions and different particle chemical composition, and hence different particle hygroscopicity. Higher hygroscopicity will move the Hoppel minimum to lower diameters for a fixed supersaturation, while higher supersaturations for the same particle hygroscopicity has the same effect on the Hoppel minimum. The median and interquartile range of the critical particle diameter, above which they act as CCN at different supersaturations during leg 2 are shown as an inset in Figure 4.7. Comparing the location of the Hoppel minimum with the supersaturation–activation curve suggests that cloud peak supersaturation was on average 0.28% during leg 2.

The back trajectories indicate that particles of the cluster 1 size distribution are associated with MBL and lower tropospheric airmasses that move along the latitudes of the cruise track. The altitude range of the trajectories is consistent with the MBL height predicted by ECMWF (about 660 m or roughly 930 hPa), which is similar to the height of the lowest cloud level measured by the ship-based ceilometer (500 m, Table 4.3). The fact that clouds are mostly within the MBL supports the hypothesis that cloud processing shapes the particle size distribution at the surface.

The airmass history for cluster 2 is different. A much stronger signature comes from more southerly latitudes and higher altitudes, indicating that particles might have arrived with airmasses that traveled over Antarctica and the polynya region. Cluster 2 represents the most common size distribution of the leg (60% of the time) and is associated with the cold sector of frontal systems. There is also evidence of a Hoppel minimum, which appears to be obscured by Aitken mode particles growing into the pronounced accumulation mode by other processes than exclusively cloud processing. The Aitken mode likely represents different stages of particle growth linked to the availability of condensable matter, for example, from marine biological emissions (Figure 4.3d), while the accumulation mode is likely a result of cloud processing and sea spray emission.

Cluster 3, which occurs 10% of the time, represents nucleation mode particles that were formed from gas to particle conversion. Few particles of larger sizes are present in this cluster, indicating a relatively low condensation sink for condensable species. This cluster corresponds almost entirely to two pronounced new particle formation episodes that happened in the vicinity of the Mertz glacier (Figure 4.1). This is reflected by the distribution of back trajectories (Figure 4.7d) which are much less spread in latitude and altitude compared to the other clusters. Trajectories show a clear MBL influence with a contribution from free tropospheric airmasses that traveled over Antarctica. Measurements of the ion size distribution down to 0.8 nm (not reported here as it will be used for a specific paper focused on new particle formation) point out that nucleation happened locally. Therefore, we can exclude a contribution of downward transported particles formed in the free troposphere. Previous research in the Southern Ocean has shown that nucleation mode particles can be entrained from aloft[202] and down-mixed after cold-frontal passages[203]. Observations of new particle formation around the Antarctic coast are very sparse and a clear understanding of the

processes involved is still missing. In a single case ultrafine particles were linked to air-masses arriving from Antarctica, that is, northward air motion over sea ice[51] but most other studies report open-ocean influence which drives coastal new particle formation (NPF)[15,53], consistent with our observations. In particular, Jokinen *et al.*[15] reported for the first-time molecular-level characterization of NPF in Antarctica showing that sulfuric acid–ammonia ion induced nucleation is the predominant NPF mechanism in Queen Maud Land (Aboa station).

4.7 THE ROLE OF SEA SPRAY FOR CCN

Sea spray formation is a key process that influences the aerosol properties significantly in some regions of the Southern Ocean. Bubbles that burst at the ocean surface as a result from air entrained into the water through wave breaking[193] are the most important mechanism to generate sea spray. Sea spray droplets evaporate once in the air and leave behind aerosol particles that consist of a mixture of sea salt and organic particles, the latter are enriched in the sea surface micro layer[204]. Wind, which drives wave formation, is one of the key factors for sea spray aerosol (SSA) generation. This is particularly important in the Southern Ocean, where wind–wave interactions are a dominant feature[153]. We use the term SSA to refer to sea salt and primary organic aerosol stemming from the ocean.

We applied the three mode fitting algorithm after Modini *et al.*[205] to the joint SMPS and APS size distributions to derive an estimate of sea spray contribution to the total particle concentration and CCN at all supersaturations. The mode diameter of the fitted SSA size distribution was constrained to lie within ±20% of 180 nm to be consistent with the breaking-wave size distribution measurements of Prather *et al.*[206], yielding a correlation coefficient of 0.75 between fitted SSA and filter-based Na^+ mass concentrations. We estimate that the uncertainty in the 15-min median fitted-SSA number concentrations is ±50% based on a sensitivity analysis to the choice of constrained mode diameter over the range 140–300 nm. SSA was similarly important for the total particle number concentration of the integrated joint particle size distribution in legs 1 and 3 with a median contribution of 10%, followed by leg 2 with 5% median contribution (Table 4.3). The SSA contribution to CCN for supersaturations up to 0.3% was up to 100% in extreme cases (< 2.3% of all 15-min-averaged data points), for higher supersaturations, contributions of 80% were not exceeded. Generally, the contribution of SSA to CCN across all supersaturation is highest for leg 1, followed by leg 3, and then leg 2. Table 4.3 provides the contribution of SSA to CCN at 0.15 and 1.0% supersaturation for each leg. The results are in agreement with the wind speed and wave observations that suggest higher SSA production during legs 1 and 3 (Figures 4.3a,b). Chemical information from the 24-h particulate matter with a diameter < 10 μm (PM_{10}) filter samples confirms this observation: the average sodium chloride mass of leg 1 is 1.3 and 2.1 times higher than in legs 3 and 2, respectively. Our SSA contribution estimate is similar to recent measurement-based calculations of SSA mode contributions south of 60°S using also the fitting method after Modini *et al.*[205]. Quinn *et al.*[44] found an average SSA contribution of 15% to the total particle number concentration and between 20% and 40% to CCN for supersaturations between 1% and 0.1%, respectively. Our average SSA contributions are 11% to N7 and 16% to $CCN_{1.0}$ and 35% to $CCN_{0.15}$. Note that Quinn *et al.*[44] estimates are based on a smaller sector of the Southern Ocean from the RITS93 and 94 campaigns (Table 4.1, Figure 4.1). Leg 2

of ACE-SPACE was frequently characterized by airmasses from Antarctica, hence the contribution of SSA is expected to be lower there (10% were observed). In addition, the ocean was partly covered by sea ice (Figure 4.3b) and the median wind speed (6 m s^{-1}) was lower than during leg 1 (10 m s^{-1}) and Leg 3 (8 m s^{-1}; Figure 4.3a).

4.8 COASTAL ANTARCTIC CCN: UNRESOLVED FORMATION MECHANISMS

The fraction of particles serving as CCN was higher near the coast of Antarctica (Figure 4.6c), in agreement with results from the large accumulation mode over coastal waters. We hypothesize that this mode compared to the rest of the cruise could be a result of two factors: 1) mass acquisition through multiple cycles of cloud processing and/or 2) the comparatively higher availability of condensable gases originating from marine microbial activity. With respect to the first factor, SO_2 (a DMS oxidation product) can either be oxidized to sulfuric acid in the gas phase or through aqueous phase reactions in cloud droplets (Figure 4.2), whereby heterogeneous oxidation is the faster reaction[173]. The pronounced Hoppel minimum suggests that particulate sulfate formation takes place in the droplets. In this case, the marine emissions grow CCN so that lower supersaturations are sufficient to form droplets. The larger accumulation mode particles in leg 2 might result from multiple processing cycles of dissipating and condensing clouds. Being close to Antarctica on leg 2, we observed more cold and dry air outbreaks than on the other legs. The entrainment of dry air might cause clouds to dissipate more often before they precipitate their CCN. In fact, katabatic winds have been demonstrated to sublimate a significant fraction of falling snow[207]. And, over the Antarctic Peninsula, bursts of CCN have been observed after cloud evaporation[208].

Regarding the second factor, airmasses associated with leg 2 accumulation mode clusters traveled over chlorophyll-rich regions (Figures 4.3c,d and 4.7b,c) from where DMS might be emitted and oxidized into MSA and SO_2. Here again, the faster oxidation path of DMS to MSA is via heterogeneous reactions[173]. The 75th-percentile concentration of gaseous MSA was significantly higher during leg 2 compared to leg 3 (Table 4.3 and Figure 4.3d); observations are not available from leg 1. Gaseous sulfuric acid (median) was also slightly higher in leg 2 compared to leg 3 (Table 4.3). The formation rates of MSA and sulfuric acid from DMS are a function of temperature, with colder temperatures favoring the formation of MSA Seinfeld *et al.*[1]. This is consistent with the colder temperatures near Antarctica and the higher 75th-percentile ratio of MSA to H_2SO_4 in leg 2 compared to leg 3.

As speculated, both gases (H_2SO_4 and MSA) could grow the particles either through direct condensation in the gas phase or via heterogeneous chemistry inside the clouds. For a quantitative analysis of this process, in situ measurements of size-resolved MSA partitioning, in-cloud chemical evolution of particles, and cloud formation and dissipation cycles are needed.

The enhanced concentrations of trace gases, particularly MSA, are reflected in the contribution of particulate MSA to the particle population. It is 2.5 times higher in leg 2 compared to legs 1 and 3 based on the PM_{10} filter analysis. The chemical composition of particles is important because it influences their hygroscopicity and potential to become a CCN. Hygroscopicity can be expressed by the kappa value[209] that relates a particle's dry diameter with the critical supersaturation at which it can activate as

droplet. The higher the kappa value the more readily a particle can become CCN. The bulk kappa value for leg 2 has been calculated following the kappa–Köhler equation[209]. It is 0.59 and reflects the contribution of various compounds. Kappa values of MSA have rarely been reported in the literature. We use the hygroscopic growth factor at RH = 90% of 1.57 reported by Johnson *et al.*[210] and calculate a kappa value of 0.32 based on a water activity of 0.9 [see Eq. (2) in Petters *et al.*[209]]. A pure sea salt contribution to CCN would result in kappa $\simeq 1.1$[211] and pure sulfuric acid contribution in $\simeq 0.70$[107]. Similar observations of decreased hygroscopicity, compared to sea salt or sulfuric acid, with higher particulate MSA fraction have been made at the Antarctic coastal station AboaAsmi *et al.*[212].

Considering that CCN concentrations in leg 2, which were not SSA dominated, are at least as high as in the open-ocean legs, it seems that a combination of multiple cloud processing cycles and increased availability of DMS oxidation products led to particle sizes large enough to act as CCN. This counteracts the lower particle hygroscopicity through MSA addition and reduces the importance of sea spray. While previous studies have shown that N_d are associated with elevated chlorophyll-a concentrations[49], the actual mechanisms leading to this correlation remained unclear.[49] used the particulate sulfate concentration and organic mass fraction obtained from model simulations to explain more than 50% of the spatial N_d variability (retrieved from satellite observations) and estimated that marine biological activity may be responsible for a doubling of N_d in summer. Proposed explanations include that marine surfactants enhance the SSA fraction of aerosols between 50 and 200 nm[206], which are most relevant for the CCN number concentration. With regard to leg 2, this seems unlikely to be a major contributing factor due to the small influence of SSA that we estimate. A further suggestion was that ocean-derived particulate organics have surfactant characteristics that can reduce the surface tension and hence lower the critical diameter[213,214]. Our clustered size distributions show that the Hoppel minimum occurs at larger diameters closer to Antarctica. Quinn *et al.*[44] predicted that SSA contributes a significant proportion of the Southern Ocean MBL CCN budget, between 30% and 40%, at supersaturations smaller than 0.3%. This means that they ascribed roughly 40% of CCN to surface sources while the origin and formation mechanisms of the remainder, that is, accumulation mode, remained unresolved.

From our data, it appears likely that accumulation mode particles grew through cloud processing; a mechanism that is potentially enhanced due to cloud formation and dissipation cycles in combination with the increased availability of condensable gases, that is, MSA and H_2SO_4. However, the question remains as to which pathways lead to the addition of MSA and H_2SO_4 to the particle mass.

4.9 COMPARISON OF REMOTE SENSING AND IN SITU OBSERVATIONS OF CLOUD CONDENSATION NUCLEI

Even though our in situ observations are representative of what would be expected from climatological conditions, they only cover a limited amount of time (summer) and space (cruise track). Using satellite observations to retrieve N_d to the extent that they reflect the actual CCN number concentration enables the community to create a dataset that reflects spatial and multiannual variability (see Appendix B for details). Such a dataset is important to improve our estimates of radiative forcing from pristine

aerosol–cloud interactions. We identified 73 satellite overpasses of the ACE-SPACE ship track with valid CCN measurements from the ship, when only shallow (up to 800 m) liquid clouds were sampled. For each case we have calculated N_d, the updraft and the supersaturation at cloud base and matched the CCN concentration at the same supersaturation from a CCN spectrum measured on the ship 2 h before and after the satellite overpass (Figure 4.8). It shows that generally the N_{d90} (the 90th percentile) concentration observed by MODIS is smaller than the measured CCN at the determined cloud-base supersaturation. Most points fall within the triangle below the 1 : 1 line of satellite versus ship-based measured CCN—the cloud-base-retrieved CCN is mostly lower than ship measured CCN. This means that for most of the cases the source of CCN is associated to the surface rather than to entrainment of particles from the free troposphere. A dominant free-tropospheric source would incur cloud-base N_{d90} mostly larger than the ship measured CCN.

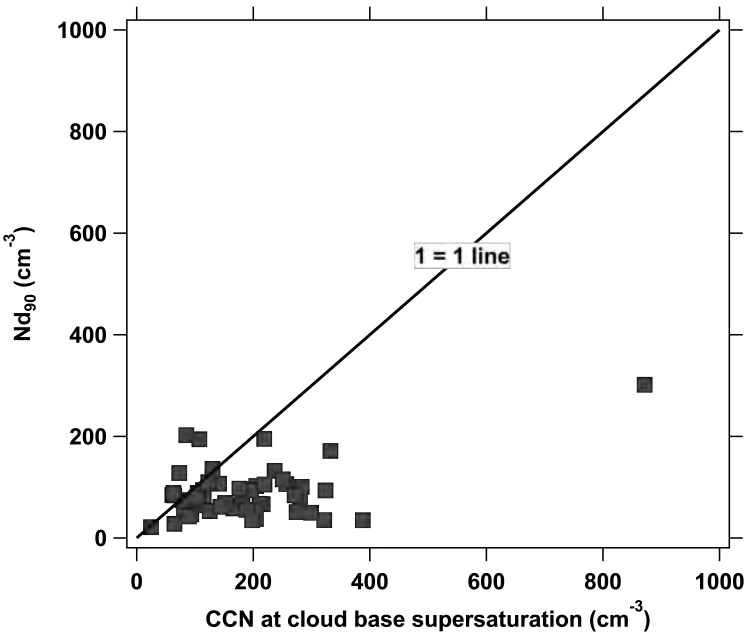

Figure 4.8: Satellite-retrieved cloud droplet concentrations N_{d90} vs ship-measured CCN number concentrations interpolated to the same cloud-base supersaturation for clouds with a geometrical depth of up to 800 m and within 150 km of the ship.

The result here is contrary to previous studies of the same methodology[215], that included tropical and midlatitude terrestrial locations and some oceanic trade wind cumulus. The satellite-retrieved N_{d90} showed good agreement with the surface measured CCN, probably due to the strong coupling of these convective clouds with the surface. The fundamental difference is that the clouds in the Southern Oceans were mostly stratocumulus and stratus, which are often decoupled from the ocean surface.

Therefore, an obvious next step in the research is analyzing the relationships between the satellite-retrieved and ship-measured CCN based on the coupling state of the clouds.

4.10 COMPARISON OF MODEL AND MEASUREMENT RESULTS

On average, the GLOMAP model underestimates $CCN_{0.2}$ number concentrations by roughly 50% in 80% of the grid boxes covering the ship track (Figure 4.9). The regions

of highest underestimation are close to the coast of Antarctica during leg 2, close to South Africa and around 45°E during leg 1. These regions coincide with the highest concentrations of gaseous MSA (for leg 1 this remains speculation since we do not have measurements but it is backed up by particulate MSA observations). This preliminary model–measurement comparison suggests that the model may be missing an important source of high-latitude CCN. Another possibility is that the degree of cloud processing in the model may be too low in these regions, since our analysis indicates that repeated cloud processing increases the particle number concentration in the CCN size range.

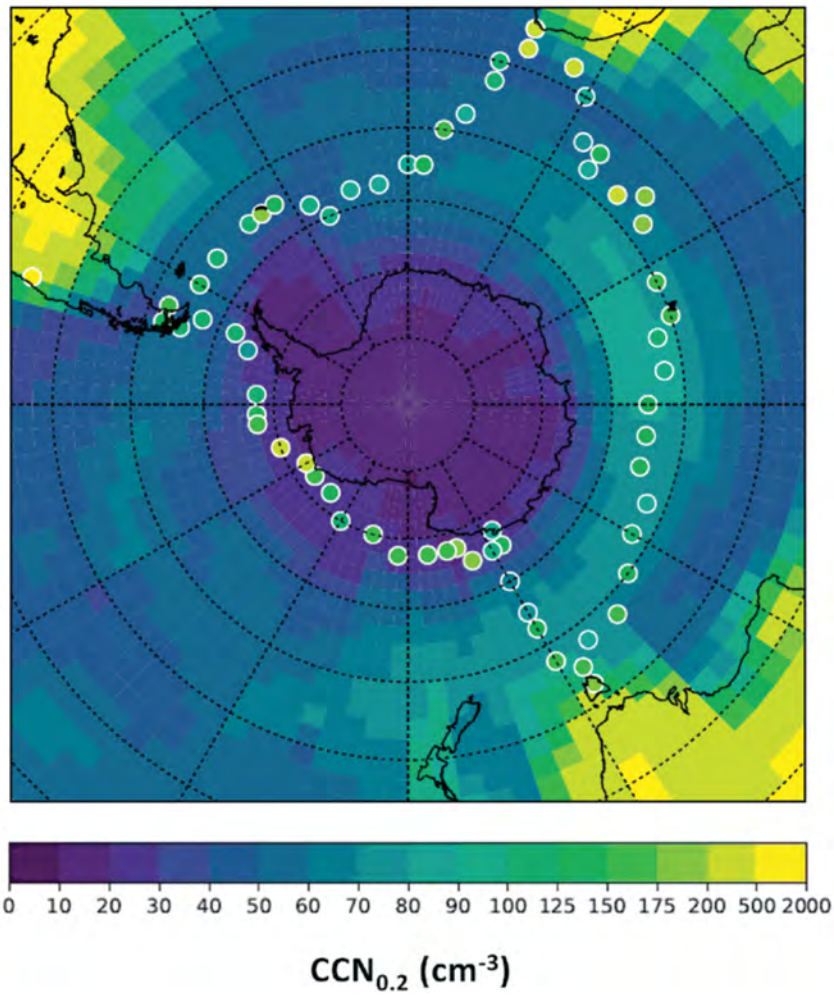

Figure 4.9: Comparison of the global aerosol model GLOMAP simulation of monthly mean $CCN_{0.2}$ with ACE-SPACE in situ measurements.

Modeled $CCN_{0.2}$ concentrations are also underestimated by at least 10% in places where MSA concentrations are low. There are multiple parameters in the model that could cause this underestimation. For example, sea spray and DMS emission fluxes from the ocean surface layer may be too low in the model. Alternatively, a dry deposition that is too vigorous could remove aerosols too quickly from the atmosphere. Aerosol removal through excessive precipitation could also cause the $CCN_{0.2}$ bias, and several parameters affect aerosol size distributions, cloud droplet activation and aerosol removal rates by precipitation.

In this analysis we compared the model mean output (from a sample of 1 million model variants[216]) with measured values. The degree to which individual model vari-

ants and their associated parameter values agree with measurements will be evaluated in a future study. A thorough model–observation comparison requires rigorous statistical techniques that account for multiple sources of uncertainty such as observation representativeness errors[217], which are beyond the scope of this article.

4.11 SUMMARY AND OUTLOOK

The first results from ACE-SPACE highlight that the Southern Ocean is a region with highly heterogeneous aerosol properties. The areas around the strong westerly wind belt are characterized by significant sea spray contributions to the total particle and CCN number concentrations in the MBL. Future work will link detailed wave and wind observations to sea spray production.

In the Ross and Amundsen Sea polynyas (leg 2), biogenic emissions appear to play an important role for CCN abundance. There are a number of open questions associated with this observation. First, even though this particular region was probed during a phytoplankton bloom period, it was not the only region with microbial activity but showed the clearest link to high CCN concentrations. Hence, either DMS production from dimethylsulfoniopropionate in the water and/or DMS fluxes into the atmosphere were enhanced. Second, the major pathway of how MSA is added to the particle phase remains to be identified. There are two possibilities: it can condense from the gas into the particle phase, or it can be added during cloud processing. The latter process would be consistent with the reduced efficiency of wet removal because of droplet evaporation or snowflake sublimation in the cold and dry airmasses from Antarctica.

Our results also indicate that the absence of MSA-related processes in the aerosol model could explain the underestimation of CCN concentration, particularly in high aerosol-MSA regions. Given that the number of CCN influence N_d, this is an important issue to solve, especially close to the coast of Antarctica where clouds could impact the surface snow mass balance by influencing both the surface energy budget and precipitation. Further studies are planned that more closely investigate the linkages between CCN number concentrations and model simulations that take DMS emissions fluxes and particle phase MSA into account.

A comparison of satellite-retrieved N_{d90} and ship-based measurements of CCN shows a clear underestimation of CCN from remote sensing, even for coupled cloud cases. This is a strong indication of the importance of surface sources as opposed to the free troposphere for particle origin. Further investigation is underway to understand the cause of the discrepancy between the remote sensing and in situ measurements.

We did not find direct evidence for new particle formation as an important source of CCN. However, some nucleation events were observed and a nucleation mode was present in the clustered particle size distributions. A dedicated study will investigate the gases involved in these events and the fate of the nucleation mode in the atmosphere.

Our ice nucleating particle findings suggest that concentrations are lower than in Northern Hemisphere marine airmasses and that concentrations decreased from summer toward fall with only small differences between open-ocean and coastal Antarctic samples. The ACE-SPACE INP concentrations are also consistent with findings of a recent study in the Southern Ocean[200], but much lower than results from several decades ago[199]. More detailed studies including information on potential island effects, long-range transport and fluorescent and microbial particles are underway.

The ACE-SPACE project is motivated by the idea of constraining uncertainty in anthropogenic radiative forcing from aerosol–cloud interactions through measurement of preindustrial-like aerosol–cloud interactions. We have shown that the in situ data are suitable for constraining the aerosol model for preindustrial-like conditions. After a detailed model–measurement comparison, we will use the aerosol model to further constrain uncertainties of global radiative forcing from aerosol–cloud interactions.

ACKNOWLEDGEMENTS

ACE-SPACE, JS, IT, AT, SH, and MD received funding from EPFL, the Swiss Polar Institute, and Ferring Pharmaceuticals. ACE-SPACE was carried out with additional support from the European FP7 project BACCHUS (Grant Agreement 49603445). SL received funding from the Swiss Data Science Center project c17 − 02. AB received funding from the Swiss National Science Foundation (Grant 200021_169090). FT was supported by the Swiss National Science Foundation (Grant 20*F*121_138017). The U.K. Natural Environment Research Council sponsored the iDirac development (NE/K016377/1) and the Doctoral Training Partnership for CB. CT received funding from DFG within the SPP 1158 (Grant STR 453/12 − 1). KC is currently a Royal Society Wolfson Merit Award holder. LR, JSJ, and KC acknowledge funding from NERC under Grants AEROS, ACID-PRUF, GASSP, and A-CURE (NE/*G*006172/1, NE/*I*020059/1, NE/*J*024252/1, and NE/*P*013406/1), and were also supported by the U.K.–China Research and Innovation Partnership Fund through the Met Office Climate Science for Service Partnership China as part of the Newton Fund. This work used the ARCHER U.K. National Supercomputing Service and JASMIN super-data-cluster, via the Center for Environmental Data Analysis. ARCHER project allocation n02-FREEPPE and the Leadership Project allocation n02-CCPPE were used to create the perturbed parameter ensemble. KL was funded by the European Commission's Horizon 2020 programme (MSCA-IF project Nano-CAVa, 656994). MG received funding from the ERC under Grant ERC-CoG-615922-BLACARAT. We thank MeteoSwiss for providing access to operational ECMWF data.

APPENDIX A: IN SITU MEASUREMENTS

The two air-sampling inlets were built after the Global Atmosphere Watch recommendations and as operated on the Jungfraujoch, Switzerland[218]. They sample particles up to 40 μm in diameter under wind conditions of up to 20 m s^{-1}. Particle number concentrations were obtained from CPCs with different lower cutoff diameters: TSI 3022, 7 nm; TSI 3772, 10 nm; TSI 3010D, 20 nm. The NAIS instrument was used to measure particle number size distributions from 2 to 40 nm. A home-built SMPS[102] sized particles between 11 and 400 nm, an APS 3321 between 500 nm and 19 μm, and a WIBS−4 between 0.5 and 12.5 μm. All sizes are given as diameters. The WIBS determines also the number and size of fluorescent particles, and the NAIS determines in addition the ion size distribution between 0.8 and 40 nm and was used in conjunction with the atmospheric pressure interface time-of-flight mass spectrometer (APi-TOF[86]) capable of measuring the atmospheric ion composition or the composition of neutral clusters when using an upstream chemical ionization unit (CI-APi-TOF, nitrate-based in our case). Note that data are preliminary, and updated versions can be found

on https://zenodo.org/communities/spi-ace as soon as available. The bulk chemical composition of the submicron aerosol was determined with a time-of-flight aerosol chemical speciation monitor (ACSM; Ng *et al.*[219]; Fröhlich *et al.*[220]), which quantifies the mass concentration of nonrefractory aerosol (defined as evaporating at 600°C), meaning that relative variations of sea salt concentrations can be determined but not well quantified. The major ion composition of particulate matter with a diameter < 10 μm (PM_{10}) is based on ion chromatography from 24−h filters. The CCN number concentration was measured by a CCNC[106], while the INP concentrations were determined based on 8−h filters processed with the droplet freezing array INDA (Ice Nucleation Droplet Array) after Conen *et al.*[221] and Budke *et al.*[222]. Trace gases (O_3, CH_4, CO, CO_2) were measured with a PICARRO G2401 to identify different types of airmasses as well as marine biogenic emissions. Atmospheric isoprene concentrations were determined by the custom-built portable gas chromatograph iDirac[223]. Equivalent black carbon, trace gases data such as CO and CO_2, and the 10−s variability of particle number concentrations were used to identify the influence of ship exhaust. Identified exhaust periods are not included here and constitute about 50% of the total data. Size-dependent particle losses in the inlet lines were determined experimentally after the cruise and data are corrected accordingly. Losses were < 10% for submicron particles and about 15% for supermicron particles.

The cloud base was measured by a Vaisala Ceilometer CL31 that was part of the automated ship-based weather station.

APPENDIX B: REMOTE SENSING

We obtained cloud droplet number concentrations from MODIS products[224] and cloud-base updraught. The methodology of Zhu *et al.*[225] was used to maximize the relationships between N_d and CCN. The retrieval was focused on the brightest 10% of the clouds in the area of interest, in which the clouds were closest to adiabatic, as assumed in the N_d retrieval algorithm. The cloud-base updraught was obtained from the cloud-top radiative cooling rate, which was shown by Zheng *et al.*[226] to be linearly related to cloud-base updraught. The cloud-base maximum supersaturation S was calculated by:

$$S = C(T_b, P_b) W_b^{3/4} N_d^{-1/2}, \tag{4.1}$$

where C is a coefficient that is based on cloud-base temperature T_b, cloud-base updraught W_b, and pressure P_b[227]. By definition, N_d is the then number of CCN at supersaturation S.

APPENDIX C: MODELLING

BACK TRAJECTORY MODELLING Ten-day air parcel backward trajectories were calculated with the Lagrangian analysis tool LAGRANTO[184,185] using the three-dimensional wind fields from the 3-hourly global operational analysis data of the European Centre for Medium-Range Weather Forecasts (ECMWF). The ECMWF analysis fields were interpolated on a regular horizontal grid of 0.5° horizontal resolution on each of the 137 vertical model levels. In total 56 trajectories were launched every hour from the surface to 500 hPa in steps of 10 hPa with a higher resolution of 1–5 hPa in the lowermost

20 hPa. Additionally, the sea surface temperature (SST) from ECMWF operational analyses was interpolated along the track, and compared to the measured in situ air temperature T_a. If SST $> T_a$, we classified the local airmass as being part of the cold sector of a frontal system, and if SST $< T_a$ as part of the warm sector.

For the intercomparison of measured wind speed and ECMWF operational output that provides wind speed at 10-m neutral stability we converted it to friction velocity with the wind-speed-dependent drag coefficient from the COARE 3.5 bulk flux model[228]. The ERA-Interim output of surface sensible and latent heat flux where used together with the friction velocity to estimate the Monin–Obukhov length scale, which was used with the stability functions provided in Fairall *et al.*[229] to relate the ERA-Interim $10-$m wind speed to the measured $30-$m wind speed. According to Schmidt *et al.*[230], ERA-Interim, the reanalysis product based on ECMWF, is the most accurate product to represent temporal variability of winds.

MODELLING WITH GLOMAP The GLOMAP-mode model, used in the UKCA, simulates new particle formation, aerosol coagulation, gas-to-particle transfer, cloud processing of aerosols, and both dry and wet deposition of gases and aerosols. In our model setup, 2.5° latitude × 3.75° longitude, GLOMAP resolves five aerosol components -sulfate, organic carbon, black carbon, sea salt, and dust- into seven modes: soluble modes in nucleation, Aitken, accumulation, and coarse size ranges and insoluble modes in all but the nucleation size range. Within each particle size mode, chemical components are assumed to be internally mixed and particles follow the lognormal number–size distribution. Particles form through binary homogeneous nucleation[231] throughout the atmosphere and through organically mediated nucleation[232] in the planetary boundary layer. Particles grow following microphysical processes such as condensation of gas species and coagulation between particles. They are moved from one mode to another when the mean modal size becomes larger than a prescribed threshold, or when insoluble particles are aged to become soluble. Aerosols are removed from the atmosphere through gravitational settling, turbulent mixing, nucleation into cloud drops (followed by autoconversion to rain), and impact by precipitating rain drops[233].

Soluble particles grow according to the relative atmospheric humidity using composition-dependent hygroscopicity factors (k; kappa) in accordance with the Köhler theory. The activation of aerosols into cloud droplets is calculated using distributions of subgrid vertical velocities[234] and the removal of cloud droplets is calculated by the host model. The SOCRATES radiation code[235] is used within HadGEM3-UKCA to calculate the radiative effects of aerosols.

Sea spray aerosols are emitted into the atmosphere using the Gong[236] surface-wind-speed-dependent parametrisation. Surface ocean dimethylsulfide concentrations are prescribed using the Kettle *et al.*[237] dataset and are emitted into the atmosphere using a surface-wind-speed-dependent parametrisation[238]. Primary marine organic aerosols are not explicitly in our simulations.

Horizontal winds above around 2 km were nudged toward ERA-Interim for the year 2006 in the model, not the year measurements were collected. Therefore, simulated and measured wind speeds are only weakly correlated ($R^2 = 0.13$). However, simulated $CCN_{0.2}$ concentrations and wind speeds are uncorrelated over the locations where measurements were collected. Wind speeds have compensating effects on aerosol and CCN concentrations[40]. Higher wind speeds increase the emission flux of sea spray aerosols and aerosol precursors (DMS), but are also associated with larger waves that

increase the removal rate of near-surface aerosols, at least on the scales simulated by global climate models. The lack of CCN dependence on 10-m wind speeds suggests our model–measurement comparison results will not be affected by the meteorological year used in the model.

5 LOW-VOLATILITY VAPORS AND NEW PARTICLE FORMATION OVER THE SOUTHERN OCEAN DURING THE ANTARCTIC CIRCUMNAVIGATION EXPEDITION

Andrea Baccarini[1,2], Josef Dommen[1], Katrianne Lehtipalo[3,4], Silvia Henning[5], Robin L. Modini[1], Martin Gysel-Beer[1], Urs Baltensperger[1] and Julia Schmale[2].

[1] *Laboratory of Atmospheric Chemistry, Paul Scherrer Institute, Villigen, Switzerland*
[2] *School of Architecture, Civil and Environmental Engineering, École Polytechnique Fédérale de Lausanne, Switzerland*
[3] *Finnish Meteorological Institute, Helsinki, Finland*
[4] *Institute for Atmospheric and Earth System Research/Physics, University of Helsinki, Helsinki, Finland*
[5] *Institute for Tropospheric Research, Experimental Aerosol and Cloud Microphysics, Leipzig, Germany*

Submitted to: **Journal of Geophysical Research: Atmospheres**

5.1 ABSTRACT

During summer, the Southern Ocean is largely unaffected by anthropogenic emissions, which makes this region an ideal place to investigate marine natural aerosol sources and processes. A better understanding of natural aerosol is key to constrain the preindustrial aerosol state and reduce the aerosol radiative forcing uncertainty in global climate models. We report the concentrations of gaseous sulfuric acid, iodic acid, and methanesulfonic acid (MSA) together with a characterization of new particle formation (NPF) events over a large stretch of the Southern Ocean. Measurements were conducted on board the Russian icebreaker *Akademik Tryoshnikov* from January to March 2017. Iodic acid is characterized by a particular diurnal cycle with reduced concentration around noon, suggesting a lower formation yield when solar irradiance is higher. Gaseous MSA does not have a diurnal cycle and measured concentrations in gas and condensed phase are compatible with this species being primarily produced via heterogeneous oxidation of dimethyl sulfide and subsequent partitioning into the gas phase. We also found that NPF in the boundary layer is mainly driven by sulfuric acid but it occurred very rarely over the vast geographical area probed and did not contribute to the CCN budget in a directly observable manner. Despite the near absence of NPF events in the boundary layer, Aitken mode particles were frequently measured, supporting the hypothesis of a free tropospheric source. Iodic acid and MSA were not

found to participate in nucleation, however, MSA may contribute to aerosol growth via heterogeneous formation in the aqueous phase.

5.2 INTRODUCTION

Aerosols have a major impact on our climate[26]. They scatter and absorb solar radiation and are part of cloud formation processes as cloud condensation nuclei (CCN) or ice nucleating particles (INP). The combination of aerosol-radiation and aerosol-cloud interactions contributes the largest fraction of uncertainty to the overall radiative forcing budget[26]. The present day (PD) aerosol forcing is calculated against a preindustrial (PI) baseline, which is poorly constrained because direct measurements of PI aerosols are impossible. Additionally, the radiative forcing due to aerosol-cloud interactions (RF_{aci}) is non-linearly dependent on the total aerosol number concentration and is much more sensitive to changes in low concentration regimes, which are more representative of the the PI time[29,30]. Therefore, the highly uncertain global level and distribution of PI aerosols has a disproportionately large effect on the PD RF_{aci} uncertainty. One way to constrain this uncertainty is to better characterize natural sources of aerosols, which were predominant during the PI time. However, there are very few places on Earth that may still resemble PI-like conditions with minimum anthropogenic influence. Among these locations, the Southern Ocean is probably the region with the highest number of PI-like days during summer[41]. Recently, Regayre *et al.*[31] demonstrated that a small set of measurements over the Southern Ocean can be as effective as a two orders of magnitude larger and more heterogeneous set of data from the Northern Hemisphere in reducing the RF_{aci} in a global climate model. This highlights the value of measurements in pristine and remote locations.

The contribution of anthropogenic activities to the aerosol population over the Southern Ocean is small and generally limited to the more northerly sector[42,43]. This implies that natural emissions constitute the overwhelming share of the aerosol population with sea spray and new particle formation from marine emissions presumably being the two main aerosol sources. Other minor sources are volcanic emissions[172], emissions from sea birds and other animals[171] and blowing snow from ice covered regions[7]. The concentration of sea spray aerosol is mainly driven by wind speed and sea state and can vary largely across the Southern Ocean[42,44]. Previous measurements reported a contribution between 10% and 100% to the CCN concentration, depending also on supersaturation[42,44,45]. NPF occurs via the nucleation of low-volatility vapors to form small particles, which eventually grow by condensation of the same or other gaseous compounds. Over the Southern Ocean, NPF is thought to happen mainly via sulfuric acid[12,239,240], which is formed from the oxidation of dimethyl sulfide (DMS), a biogenic compound produced in the water by phytoplankton. During the austral summer the concentration of DMS in the water of the Southern Ocean is the highest of the planet[241], with high fluxes into the atmosphere and potentially producing high concentrations of sulfuric acid. However, under typical boundary layer conditions the concentration of sulfuric acid is too low to form particles alone, and another molecule, such as ammonia, is required to stabilize the nucleating clusters[13]. Jokinen *et al.*[15] reported the first molecular characterization of NPF from Aboa station (73.0364 °S, 13.4109 °W) in Antarctica, showing that new particles are formed via nucleation of sulfuric acid and ammonia. Sources of ammonia over the Southern Ocean are related to animals, mainly bird or seal colonies, which are known to be strong local sources of

ammonia[171,242,243]. Another potentially important compound for NPF in this region is iodine, which is known to form new particles via iodic acid nucleation[20,21,244] and concentrations can be very high in Antarctica. Iodine monoxide concentrations larger than 20 ppt have been reported in coastal Antarctica[245,246].

There are multiple studies investigating new particle formation in Antarctica[15,53,54,247] but observations of NPF over the Southern Ocean have been rare and concentrated around the sea ice region[51,52,248]. Some field studies have observed a higher concentration of recently formed particles in the free troposphere[47,58,239,249,250] and proposed that NPF may be happening predominantly in the free troposphere in the outflow of clouds. Here, formation rates can be higher because of the lower temperatures and smaller condensation sink. Newly formed particles can then be entrained in the boundary layer following for example the passage of cold fronts[251,252]. These results are also supported by modelling studies showing that typical marine boundary layer conditions are unfavourable for NPF[56,57,240,253,254]. However, global climate models also tend to underestimate both the Aitken mode aerosol concentration[174] and the CCN number[42,50,255] over the Southern Ocean, pointing towards a missing aerosol source or an inaccurate process representation (*e.g.*, too strong deposition velocity) in the models. The underestimation of Aitken mode particles is particularly relevant because NPF is believed to be the largest source of particles in this size range[1,256,257]. The reason for this discrepancy is still not known and additional process based measurements over the Southern Ocean are required to better understand the sources and distribution of aerosols.

An important process that is often overlooked is DMS oxidation, which is generally implemented in models without considering heterogeneous chemistry. This is particularly relevant for methanesulfonic acid (MSA), an oxidation product of DMS, which can be more efficiently produced in the aqueous phase than in the gas phase[48,173] and grow the mass of aerosols activated in cloud droplets (cloud processing). MSA constitutes a large fraction of the secondary aerosol mass over the Southern Ocean, up to 50% compared to the non-sea-salt sulfate aerosol mass[258,259], but its contribution to the CCN budget has not been quantified so far.

In this work, measurements of low-volatility vapors and the observations of NPF events during the Antarctic Circumnavigation Expedition (ACE) will be presented. In particular, we measured the concentration of sulfuric acid, MSA and iodic acid together with naturally charged ions and newly formed aerosol particles. In the Methods (section 5.3) we provide details on the expedition, the instruments used and the methodology adopted to treat the data. The results and discussion (section 5.4) is divided into three parts. The first part provides a broad overview of the results with a focus on sulfuric acid, iodic acid and MSA distribution over the Southern Ocean. In the second part we provide a detailed analysis on sources and processes controlling the MSA concentration, both in the gas and in the condensed phase. The third part is centered around NPF with a presentation of the events detected during ACE, a characterization of the nucleating vapors and a description of the most relevant drivers for the formation of new particles. The conclusions (section 5.5) summarizes our results and put them into perspective.

5.3 METHODS

The Antarctic Circumnavigation Expedition took place between December 2016 and March 2017, sailing around Antarctica across the Southern Ocean on board of the Russian icebreaker *Akademik Tryoshnikov*. The expedition was divided into 3 legs:

1. Leg 1: from Cape Town (South Africa) to Hobart (Tasmania) [20 December 2016 - 19 January 2017]

2. Leg 2: from Hobart (Tasmania) to Punta Arenas (Chile) [22 January 2017 - 22 February 2017]

3. Leg 3: from Punta Arenas (Chile) to Cape Town (South Africa) [26 February 2017 - 19 March 2017],

with several stops around islands and other points of interest during the cruise. A detailed description of the voyage is reported in Schmale *et al.*[42] and in the cruise report[260].

We measured sulfuric acid, MSA and iodic acid using a nitrate chemical ionization Atmospheric Pressure Interface Time-of-Flight Mass Spectrometer (CI-APi-ToF)[87]. The same instrument, an APi-ToF, was also used without the chemical ionization inlet to characterize the chemical composition of naturally charged ions[86]. The concentration and size distribution of newly formed and Aitken mode particles were obtained using a Neutral cluster and Air Ion Spectrometer (NAIS)[103]. The particle size distribution (PSD) was measured using a Scanning Mobility Particle Sizer (SMPS) and an Aerodynamic Particle Sizer (APS), together covering a size range from 11 nm to 19 μm. The PSDs obtained from these two different instruments were combined using a mode-fitting technique similar to Modini *et al.*[205]. The results of the mode-fitting procedure were used to estimate the aerosol number concentration in the different modes and to calculate the condensation sink following Dal Maso *et al.*[92].

Aerosols and gases were sampled from three different inlets mounted on a container, which was located on the second deck of the ship at a height of about 15 m above the ocean surface. Two of the inlets (the ones used for standard aerosol and trace gas measurements) consisted of heated 2 m long vertical tubes of 2.54 cm outer diameter and a specifically designed top-cover for isokinetic sampling of particles up to 40 μm in diameter, following the Global Atmosphere Watch recommendations for aerosol sampling[218]. A third inlet was specifically designed for short residence time of the sampled air to improve detection of low-volatility vapors and newly formed particles. This inlet was a simple 1.5 m long tube of 5 cm inner diameter and a U-shaped bend at the end to prevent rain from entering. It was not heated. The (CI)-APi-ToF and the NAIS were sampling behind this third inlet and were operated only during Leg 2 and Leg 3. A more detailed description of the measurement set-up is provided in the Methods, Chapter 3 of this Thesis, and in the cruise report[260].

The CI-APi-ToF was calibrated for sulfuric acid at the end of the campaign with a series of experiments at the Paul Scherrer Institute (PSI) smog chamber[91], yielding a calibration constant of:

$$C_{ACE} = 6.9 \times 10^9 [-50\% + 100\%] \text{ molecule cm}^{-3},$$

with the calibration uncertainty being indicated in the square brackets. The same calibration constant was used to quantify MSA and iodic acid based on the assumption

that the ionization proceeds at the kinetic limit for species that have a lower proton affinity than nitric acid as in these cases. A description of the CI-APi-ToF and its calibration is reported in the the Methods, Chapter 3 of this Thesis.

The nitrate CI-APi-ToF is designed to work with a constant addition of nitric acid to the sheath flow in order to produce the reagent ions which are used to ionize the sample air. During ACE, the instrument was operated without an active addition of nitric acid due to a technical problem which was identified only at the end of the expedition. Still the background concentration of nitric acid, desorbing from the walls of the inlet lines, was enough to produce a sufficiently high reagent ion concentration like in a regularly operated nitrate CI-APi-ToF. This was confirmed by the sulfuric acid calibration, which is comparable with previously reported values[87,96]. However, the nitric acid concentration was probably not high enough to take up all the charges produced by the photoionizer. Therefore, reactions with other ions like O_2^- and CO_3^- also occurred inside the nitrate CI-APi-ToF inlet. These other reactions led to the production of SO_5^- and HSO_4^- from ambient SO_2, which interfered with the detection of ambient sulfuric acid. A detailed characterization of this issue was performed with experiments at the PSI smog chamber and at the CLOUD chamber at CERN and is described in the Appendix A. Unfortunately, because the background production of HSO_4^- was not constant and depended strongly on the instrument settings, such as the inlet flow and voltages, it was not possible to correct for it within a reasonable uncertainty. Therefore, all sulfuric acid values reported in this work are uncorrected and should be considered as upper limit estimates.

Gases and aerosol particles generated by the ship exhaust and other campaign related activities (*e.g.* helicopter flights) were identified and separated from the background measurement data. As described in Schmale *et al.*[42], data were filtered using a method based on particle number, black carbon and CO_2 concentrations leading to a removal of about 50% of the data for the entire expedition. However, there are also species that are not produced by the ship exhaust, like MSA and iodic acid. Figure 5.1 shows sulfuric acid, MSA and iodic acid data in clean and polluted conditions by means of violin plots, together with box and whiskers for a concise statistic summary. A violin plot represents the distribution of the data using a kernel density estimate[261]. As expected, sulfuric acid was clearly affected by the ship exhaust with much higher concentrations during polluted conditions, whereas iodic acid was not.

A special situation is found for MSA which showed a cluster of high values (larger than 10^8 molecules cm^{-3}) during a polluted period. However, this was a single event where pollution and high MSA occurred coincidentally, but without the pollution causing the high concentration. The event was investigated but it remains unknown why MSA concentrations were so high, because no clear relationship with any external variable was identified. Data from this event were not considered for further analysis because their validity is uncertain.

Even if MSA and iodic acid are not directly emitted by the ship exhaust they could still be affected by the higher aerosol concentration within the exhaust plume which acts as a condensation sink and can reduce the concentration of low-volatility vapors. This effect is not evident from the data distribution shown in Figure 5.1, however, there are periods where emissions from the ship reduce the concentration of gaseous MSA and iodic acid. Figure S5.1 shows an example of this: during pollution (gray shadowing) there are clear spikes in the sulfuric acid and SO_5^- signal (which is produced from SO_2) and in some cases dips in the MSA and iodic acid traces. However, these dips are not always present and generally less pronounced than the pollution spikes, explain-

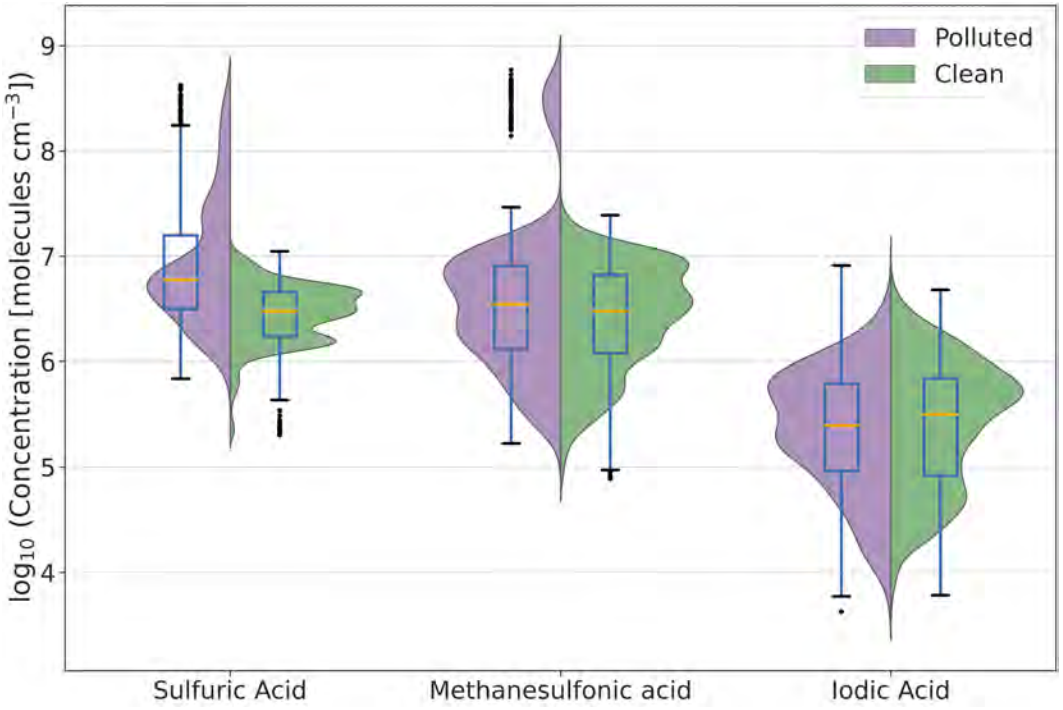

Figure 5.1: Violin, and box and whiskers plots of sulfuric acid, MSA and iodic acid divided into clean and polluted conditions. Here, polluted means that the measurements were affected by the exhaust of the research vessel. Polluted periods were identified according to the pollution mask developed by Schmale *et al.*[42]. The box extends from the first quartile (Q1) to the third quartile (Q3) with a line indicating the median. The whiskers are set to 1.5×[Q3-Q1].

ing why the overall data distribution seems to be unaffected by pollution. Therefore, given that the effect of pollution on reducing the concentration of MSA and iodic acid is minor, both polluted and clean data were included in the following analysis (except for the single high-concentration event of MSA mentioned above).

We identified NPF events based on the analysis of the particle and ion size distribution below 10 nm from the NAIS, after excluding the influence from ship exhaust. In particular, only periods with an increase of the sub-10 nm particle concentration larger than a factor of 3 compared to the baseline were considered as NPF events. The sub-10 nm particle concentration baseline was calculated using a 2 hour average before and after each potential event. We also excluded cases where the increase in the sub-10 nm concentration could be attributed to a tail of the Aitken mode based on a visual inspection of the PSD.

5.4 RESULTS AND DISCUSSION

5.4.1 Overview of ACE Results

Figure 5.2 shows an overview map with the expedition track, 6-hour averages of sulfuric acid, MSA and iodic acid concentration measurements and the location of NPF events, which will be described in Section 5.4.3. The same set of data is also reported in Figures 5.3.a and 5.3.b together with the air temperature as hourly averages. Gaps in the data indicate either instrumental problems or periods when the instrument was

operated as an APi-ToF. The time is given in the UTC time-zone here and in the rest of this manuscript, unless specified differently. Additionally, in Figure 5.4 the distribution of the data divided into two latitudinal ranges (above and below 60 °S) is reported. These two latitudinal bands can be classified as Antarctic and Subantarctic regions[262].

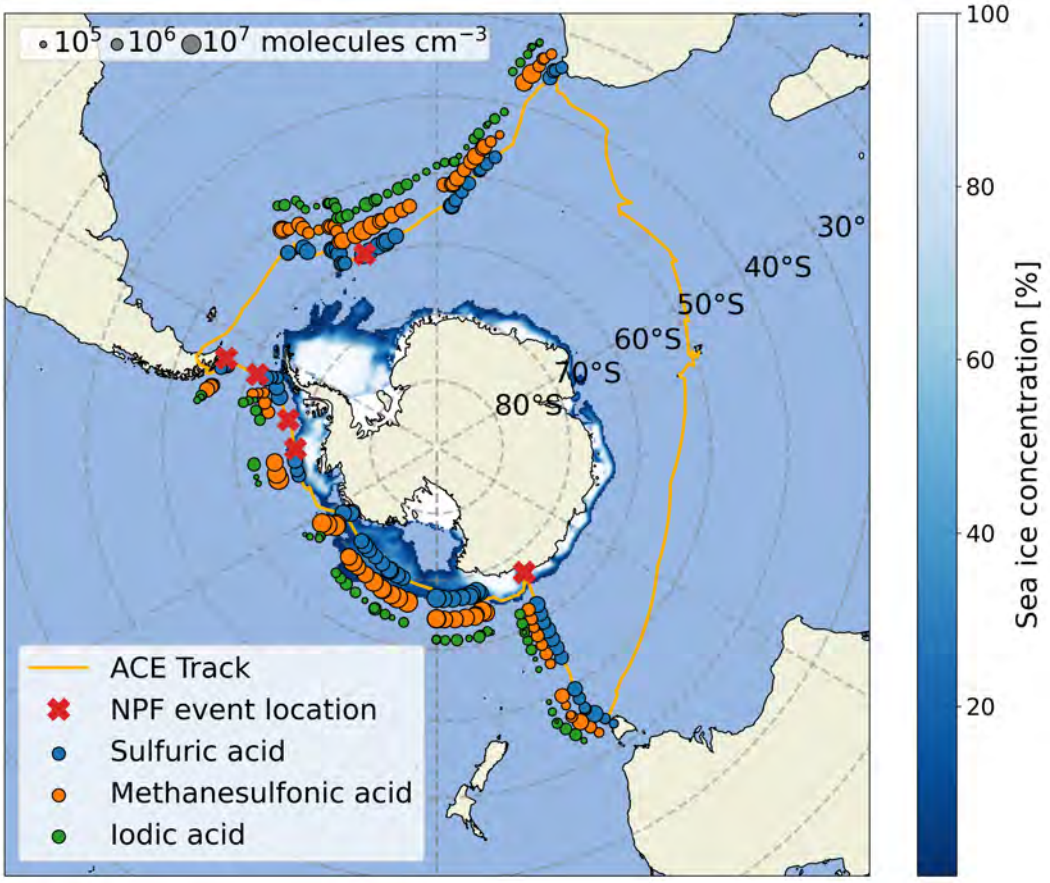

Figure 5.2: Map showing the track of the expedition and concentrations of sulfuric acid, MSA and iodic acid. Each marker represents a 6-hour median value with the size being proportional to the concentration on a logarithmic scale. The location of the new particle formation (NPF) events is also reported together with the sea ice concentration (fraction of covered surface) retrieved for January 2017[77]. The MSA and iodic acid data were shifted on the map for better visualization. There are no data available for Leg 1 because the CI-APi-ToF and the NAIS were not operated.

Figure 5.5 illustrates the day and night time data distributions of the trace gases under consideration by means of violin, and box and whiskers plots. The separation between day and night is based on the solar irradiance (SIR) data (night is when SIR is null and day when SIR is larger than 10 Wm^{-2}). Additionally, Figure 5.6 depicts the diurnal cycles of the data, which were binned according to the local time. We identified the local noon based on the maximum height of the sun above the horizon and the data were shifted accordingly before the diurnal averaging. This procedure was necessary to avoid artefacts due to the eastward movement of the ship, which caused a continuous shift of the local time with respect to UTC. Moreover, the different latitudes at which the measurements were performed had an effect on the day duration, which can affect the width of the diurnal profiles. To investigate this effect, we also calculated the diurnal profiles separately for measurements above and below 60 °S as reported in Figure S5.2. It is evident that the latitudinal variation does not strongly

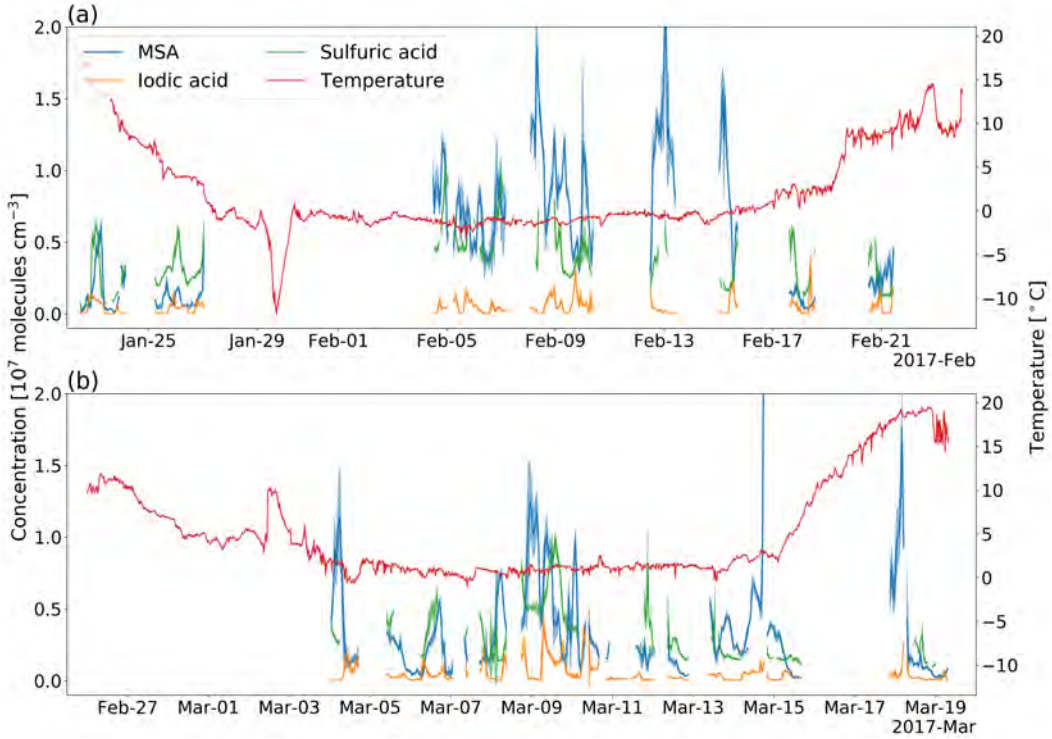

Figure 5.3: Time series of sulfuric acid, MSA and iodic acid (left axis). Solid lines represent hourly mean values and the shaded envelopes around these lines represent ± 1 standard deviation. Temperature is shown on the right axis. **(a)** Leg 2 data and **(b)** Leg 3 data.

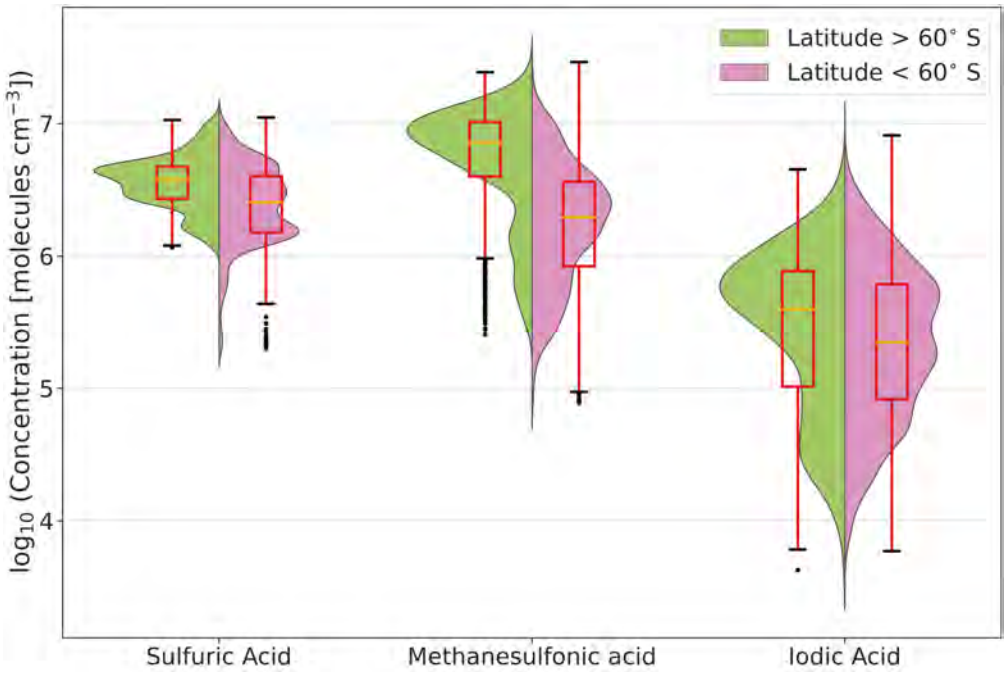

Figure 5.4: Violin, and box and whiskers plots of sulfuric acid, MSA and iodic acid separated by latitude. Measurements south and north of 60 °S are representative of Antarctic and Subantarctic conditions, respectively. The box extends from the first quartile (Q1) to the third quartile (Q3) with a line indicating the median. The whiskers are set to 1.5×[Q3-Q1].

determine the diurnal evolution of the investigated species but it has an effect on their absolute values (MSA and to a smaller extent also sulfuric acid are higher in more southerly latitudes). The fact that latitude does not have a noticeable effect on the diurnal distribution of the data can probably be explained by solar irradiance being lower at higher latitudes and compensating for the longer duration of the days (Fig. S5.2d).

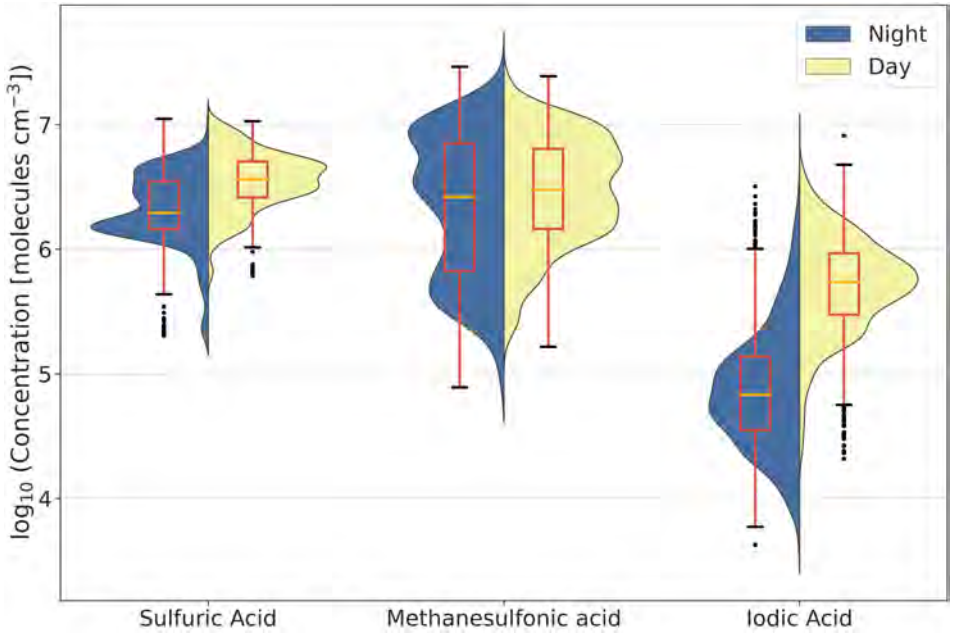

Figure 5.5: Violin, and box and whiskers plots of sulfuric acid, MSA and iodic acid separated by day and night. The separation was done based on the solar irradiance (SIR) value, with night being SIR $= 0$ Wm^{-2} and day SIR > 10 Wm^{-2}. The box extends from the first quartile (Q1) to the third quartile (Q3) with a line indicating the median. The whiskers are set to 1.5×[Q3-Q1].

The main results, which can be inferred from these overview figures regarding the spatial and temporal distribution of gaseous sulfuric acid, MSA and iodic acid over the Southern Ocean, are:

Sulfuric acid is the only species showing a clear diurnal cycle with higher concentration during midday. This result is consistent with sulfuric acid being predominantly produced via photo-oxidation of SO_2 and is in line with previous measurements in several marine environments[263–265] and in Antarctica[59,266]. On the other hand, its night time values are surprisingly high; this could be an indication of a night time production mechanism as previously suggested[264,266] or more likely an indication of the instrumental background sulfuric acid production problem described above. Nevertheless, it is safe to assume that the sulfuric acid increase during day time hours is not driven by the background production because SO_2 does not have a diurnal cycle as confirmed by the SO_5^- measurements (Fig. S5.3). Finally, the sulfuric acid concentration was higher in the region around Antarctica, which is a more biologically productive region characterized by higher DMS concentration in the water[241]. However, also the SO_5^- signal was higher in this region, which may indicate a larger sulfuric acid instrumental background. Therefore, these variations must be interpreted with caution.

MSA does not show any diurnal cycle and the distribution of the data is very similar between day and night, the only difference being the presence of a lower concentration

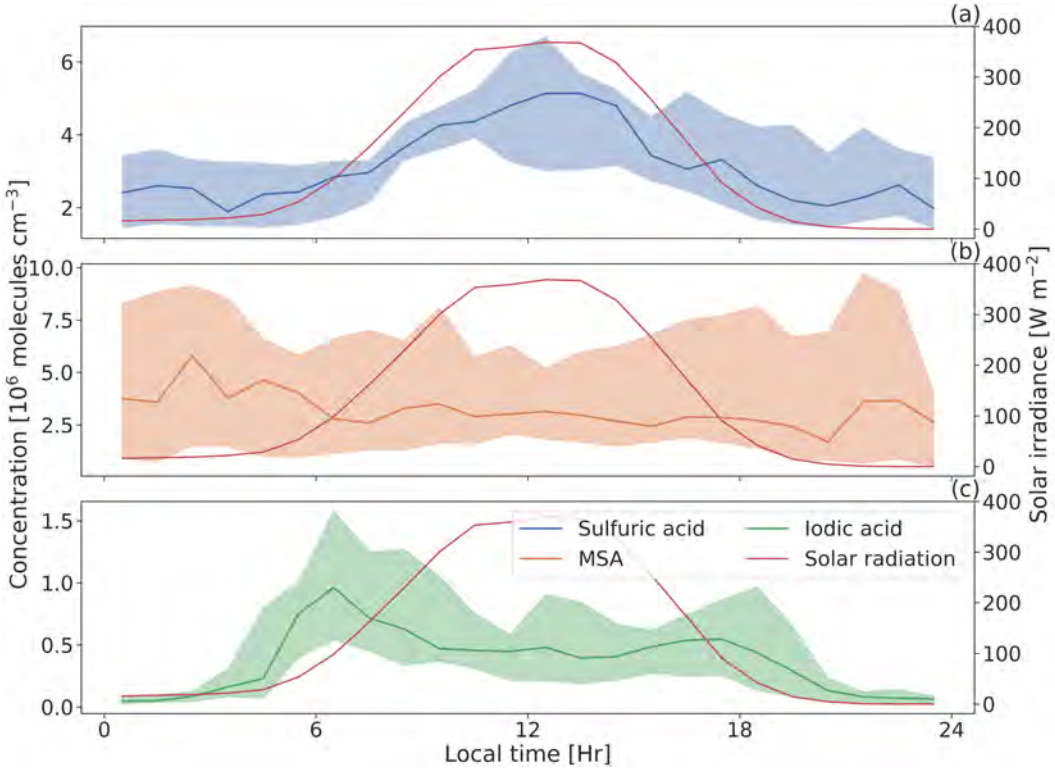

Figure 5.6: Diurnal profiles of **(a)** sulfuric acid, **(b)** MSA and **(c)** iodic acid. The thick line represents the median and the shaded area the interquartile range. Data were binned using local time determined by the sun height above the horizon. The red line is the solar irradiance median with values on the right axis.

mode during night time (Fig. 5.5). While previous observations already reported that gaseous MSA has a weak to non-existent diurnal cycle[263,264], this study is the first to show it on a large regional scale. The absence of a clear MSA diurnal cycle suggests that photochemical production from DMS oxidation is only of minor importance, in line with recent modelling work, which proposed that the largest fraction of MSA is produced in the aqueous phase[48,173]. Condensed phase MSA could then be followed by partitioning to the gas phase. The MSA concentration is also higher close to Antarctica, like sulfuric acid, with a distribution peaking at around 10^7 molecules cm^{-3} and the median being about 3.7 times higher compared to the Subantarctic region (Figure 5.4). As described, the region around Antarctica is characterized by higher DMS concentrations which could probably explain the higher MSA concentration. Additionally, higher latitudes correspond to lower temperatures, which increase the MSA production yield from DMS oxidation compared to SO_2 production[267]. We will provide a more detailed analysis of MSA variability and its sources over the Southern Ocean in section 5.4.2.

Iodic acid is characterized by a peculiar diurnal cycle peaking at dawn and dusk with a minimum around noon and very low concentration during night time (the median is below 10^5 molecules cm^{-3}). This indicates the presence of a photochemical source and no production during night. Although the formation mechanism of iodic acid is still not well understood, it is known that iodic acid is formed from the iodine radical, which is photochemically produced from precursor molecules like I_2, HOI or CH_2I_2[244,268,269] and this is consistent with the observations reported here. Figure 5.7 shows the iodic acid concentration binned by SIR to illustrate the effect of solar ra-

diation. This plot shows that the highest iodic acid concentration is measured when SIR is between 20 and 80 Wm^{-2} and decreases for higher values up to 1000 Wm^{-2}. The diminished concentration around noon (high SIR) does not have any obvious explanation and it has not been reported before. Two possible hypotheses are (1) that a precursor of iodic acid is reacted away by the OH and/or the HO_2 radicals, which have higher concentrations during noon, or (2) that iodic acid or one of its precursors are photolabile and are photolysed during the day. Without a proper understanding of iodic acid formation it is not possible to discriminate between the aforementioned processes. However, Gómez Martín *et al.*[269] proposed that iodic acid may be formed from IO or I_2O_3, where both molecules are photolabile in the near-UV[268,270] and a reduced concentration of IO during midday has also been predicted[271,272]. Therefore, photolysis is probably the reason for the reduced iodic acid concentration at higher SIR values. This phenomenon may have consequences on the latitudinal and seasonal distribution of iodic acid and its contribution to NPF. He *et al.*[244] demonstrated that iodic acid does not require the presence of OH to form; ozone and the iodine radical are sufficient. The amount of solar radiation reaching the surface is generally enough to photolyse I_2 even when the atmospheric optical depth is high (*e.g.* the sun is low over the horizon), meaning that the most favourable conditions for iodic acid formation may be at high latitudes or during early morning/late afternoon. This observation is consistent with recent studies in the Arctic reporting iodic acid NPF in spring and autumn[21,273]. Regarding the latitudinal distribution in the Southern Ocean, iodic acid does not show any evident geographical pattern and the data distribution is similar in the Antarctic and Subantarctic regions. It is interesting to note that iodic acid was not enhanced around the coast of Antarctica, despite previous studies showing exceptionally high concentrations of other iodine oxides near coastal Antarctica[245,246]. This difference is not necessarily a discrepancy considering that different iodine oxides, measured in different years and locations, are compared. However, this is a topic that deserves further attention considering the importance of iodic acid for NPF in other locations[20,21,273].

5.4.2 Sources and processes controlling MSA concentration

In the previous section we tentatively explained the absence of a diurnal cycle in the concentration of gaseous MSA by the fact that DMS photoxidation is likely not the dominant source of MSA over the Southern Ocean. However, the lifetime of gaseous MSA should also be considered because the atmospheric concentration is controlled by both sources and sinks. MSA is a stable molecule which does not react further under typical tropospheric conditions[267]. Therefore, its major sinks are condensation to pre-existing aerosol surfaces and dry deposition to the ocean. Previous studies have treated MSA condensation similar to sulfuric acid, assuming kinetic condensation with different accommodation coefficients[94,265,274,275] varying from about 0.2 to 1 and obtaining a typical lifetime of 40 minutes or lower[265,276]. If the same approach were used for the ACE data then the median and interquartile (IQR) range of the MSA lifetime for an accommodation coefficient of 0.2 would be 55 (39 ; 79) minutes, and 23 (16 ; 30) minutes for an accommodation coefficient of 1. In both cases, the lifetime is relatively short and a decrease in the concentration of MSA during night time would be expected if photooxidation were the dominant source, which was generally not observed. We estimated the lifetime of gaseous MSA against dry deposition to the ocean to be around 23 hours during ACE, which is much longer than the estimated condensation

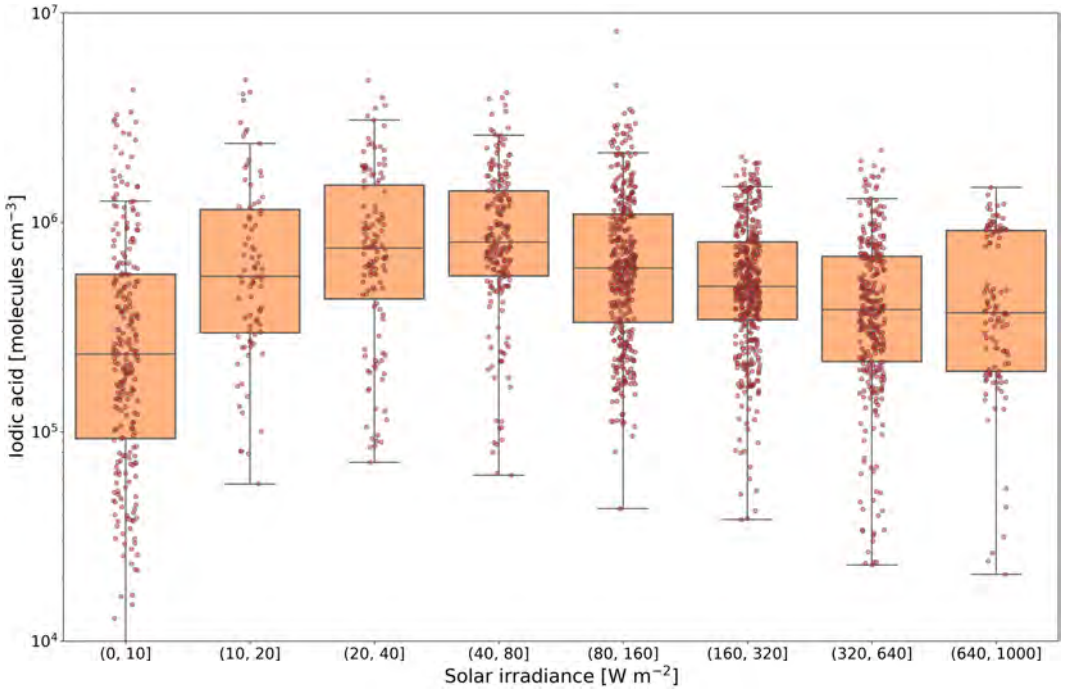

Figure 5.7: Iodic acid box and whiskers plots as a function of solar irradiance (SIR). Data were binned into different SIR classes as indicated by the axis label. The original data are shown with the small semi-transparent circles. The box extends from the first quartile (Q1) to the third quartile (Q3) with a line indicating the median. The whiskers are set to 1.5×[Q3-Q1].

timescales. We calculated dry deposition lifetime by assuming an average boundary layer height of 800 m as reported by Schmale *et al.*[42] and a deposition velocity of 1 cm s^{-1}, which is the typical value for nitric acid over the ocean[1]. Nitric acid and MSA should have a similar deposition velocity as they are equally soluble in water[1].

A possible source of gasous MSA which could explain the absence of a diurnal cycle is evaporation of MSA from the condensed phase. Previous studies already hypothesized that MSA may evaporate from particles, especially at low relative humidity (RH)[263,265]. More recently, Hodshire *et al.*[174] provided a parametrization of MSA equilibrium vapor pressure using the Extended Aerosol Inorganics Model (E-AIM; http://www. aim.env.uea.ac.uk/aim/aim.php, last access: 22 April 2021)[277] and showed that MSA could behave both as a non-volatile or semi-volatile species depending on the environmental conditions (temperature and relative humidity) and aerosol acidity. This is an important result, which can be used to represent more accurately the partitioning of MSA between the gas and the particle phase. However, in the work of Hodshire *et al.*[174] only the MSA to ammonia ratio was used to evaluate the role of particle acidity without considering the role of other compounds.

The gaseous MSA concentration during ACE follows a trend similar to previous studies[263,265,278,279] with higher values at lower RH and temperature. Figure 5.8 shows the gaseous MSA concentration as a function of relative humidity with data separated between day and night for two different parts of the ACE transect. We isolated these two different periods to reduce confounding factors due to the intrinsic variability of the dataset; they correspond to transects in a defined latitudinal range and with small temperature variations. The first period extends from 4 to 17 February 2017 and includes measurements very close to the Antarctic continent with a temperature median and IQR of -0.8 $(-1.3\,;-0.3)$ °C. The second period lasts from 4 to 14 March

2017. It is more representative of Subantarctic conditions and was characterized by a temperature median and IQR of 1.1 (0.8; 1.4) °C. The number of MSA measurement points contained in these two periods is similar (80 and 89 hours of measurements, respectively) and corresponds in total to about 2/3 of the entire MSA dataset. The same plot of gaseous MSA as a function of RH for the full ACE dataset is reported in Figure S5.4. Both figure 5.8 and S5.4 show a clear increase of gaseous MSA with decreasing RH, most notably during night time. Focusing on Figure 5.8, in the first period the decrease is evident only for RH greater than 90% and 95% for day and night time, respectively. The second period, instead, is characterized by a more continuous decrease of MSA with increasing RH during night, whereas the trend in the day time data is less clear.

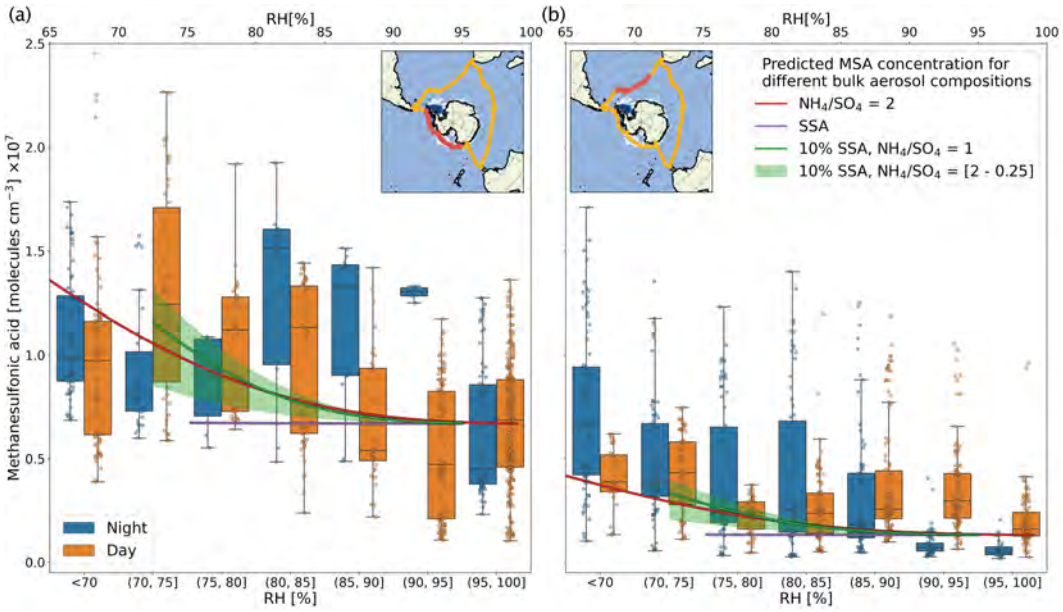

Figure 5.8: Gaseous MSA box and whiskers plot as a function of relative humidity (RH) during two different transects in **(a)** Leg 2 and **(b)** Leg 3. Data were separated between day and night and binned into different RH classes as indicated by the axis label. The original data are shown with the small semitransparent circles. The red line in the inset map illustrates the region over which data were collected. The box extends from the first quartile (Q1) to the third quartile (Q3) with a line indicating the median. The whiskers are set to 1.5×[Q3-Q1]. The solid lines in the plots are the predicted MSA gas phase concentrations by partitioning models for different simplified bulk aerosol compositions and as a function of RH (axis on the top). The red line refers to a fully neutralized aerosol system including only sulfate, ammonium and MSA. The purple line relates to a system containing also sea spray aerosol (SSA), in this case the chloride, sodium and sea spray sulfate median concentrations from ACE were used. The green line and shadowed region refer to a system with only 10% of the SSA concentration measured during ACE and varying ammonium concentrations to mimic different degrees of neutralization. The model used for the simulation cannot account for supersaturated solutions when including also sodium and chloride, therefore the two simulations with SSA stop at higher RH because of aerosol efflorescence.

We used E-AIM to investigate if MSA partitioning could explain the increased MSA gaseous concentration at lower RH. The model requires information on the aerosol chemical composition. For this purpose we used ion chromatography data of daily PM_{10} filters[140]. Non-sea-salt (nss) sulfate and ammonium in the PM_{10} filters were clearly affected by the ship exhaust, and therefore only a subset of the filters (23 over

a total of 91 filters) with minimum contamination was considered as explained in the SI. Figure S5.5 reports the concentrations of the major ions in the selected subset of filters. The mass concentration is dominated by sodium and chloride as expected given the large abundance of sea spray aerosols (SSA) during ACE[42]. The nss-sulfate to ammonium ratio points toward a large degree of neutralization (the molar ratio median and IQR are 0.57 and $0.40 - 0.63$, respectively). Previous studies in the Southern Ocean and coastal Antarctica have reported generally more acidic aerosols but there is a large range of variability with the nss-sulfate to ammonium ratio varying between 0.5 and 2 and in few cases even larger values[171,280–286]. It is also important to mention that we do not have any information about the aerosol mixing state but there is probably an external mixture with SSA being predominantly in the coarse mode and compounds of secondary origin (*i.e.* nss-sulfate, ammonium and MSA) in the accumulation mode[282,285,287,288]. We simulated three different systems: (I) a system composed only of nss-sulfate, MSA and different concentrations of ammonium, (II) a system dominated by SSA with the sodium and chloride concentration based on the daily PM_{10} filter values, (III) a mixed system composed of sulfate, MSA, ammonium and only 10% of the SSA concentration measured during ACE. Details on the E-AIM simulations are reported in the SI.

Based on the E-AIM results we estimated the MSA concentration that would partition to the gas phase as a function of RH. Figure 5.8 shows the results for the two transects presented before, where the reference value for the condensed phase concentration in each period was taken to be equal to the median concentration from the respective PM_{10} filter data. Additionally, we shifted the simulated gas phase concentration data by an amount equal to the measured gas phase MSA median concentration above 95% RH, based on the assumption that at this high RH there would be no repartitioning of MSA from the condensed phase as shown by all simulations. The first system composed of nss-sulfate, ammonium and MSA can reproduce the observed values only for a fully neutralized aerosol; a more acidic aerosol composition would lead to a much higher gas phase MSA concentration (as shown in Figure S5.6), which is not compatible with our observations. On the other hand, for the system with the full SSA aerosol concentration all MSA would stay in the condensed phase with negligible evaporation (in the case of a deliquesced aerosol). The third system produces results that are most in agreement with the observed trend. In this case the nss-sulfate to ammonium ratio has a much smaller influence on MSA partitioning compared to the first system. This result can be explained by the combination of three factors: (i) the overall aerosol acidity is reduced by the SSA components, (ii) SSA is more hygroscopic and takes up more water and (iii) the higher total aerosol mass retains more MSA in the condensed phase. The small effect of the nss-sulfate to ammonium ratio on MSA partitioning is consistent with our results considering that we observed a comparable increase of MSA at low RH in two very different regions of the Southern Ocean (panel a and b in Fig. 5.8). The first region being closer to the Antarctic coast and characterized by potentially higher ammonia emission compared to the second which was characterized by more open ocean conditions where aerosol particles are typically more acidic[281,284]. The same effect can be observed also in the gas to particle MSA ratio as shown in Figure 5.9. In fact, the gas to particle MSA ratio during the two transects is essentially equivalent despite the different MSA absolute values. The median and IQR gas to particle ratio in the first period are 0.0047 and $(0.0031\,;\,0.0085)$, while in the second period they are 0.0054 and $(0.0028\,;\,0.0084)$. An aspect that remains unclear is the concentration of gaseous MSA at high RH: for values larger than

about 90% the partitioning model would predict a gaseous MSA concentration more than one order of magnitude lower compared to the measurements. During the day this difference can be explained by gas phase production, which may be the dominant source of gaseous MSA at high RH, but there is no clear explanation for the night time values. A possible source of error is the choice of MSA thermodynamic properties in E-AIM, which suffers from a large degree of uncertainty, as explained in the SI. For example, a reduction in the Henry's law constant would directly affect MSA partitioning, producing higher concentrations in the gas phase. However, this change would affect the gas phase concentration across the entire RH range, leading to unrealistically high values at low RH. The simple approach adopted in this work to describe the aerosol chemical composition and mixing state also has an effect on the simulation results and probably contributes to this discrepancy. The SSA component, for example, was treated only as a neutral inorganic mixture based on the PM_{10} filter measurements but it is known that SSA is enriched in organics[204] and is generally characterized by a low pH, even when freshly emitted[289,290]. A more acidic aerosol would be characterized by a larger degree of MSA evaporation from the condensed phase.

Our model is clearly a simplification with no pretension to be exhaustive. However, it is based on fundamental thermodynamic calculations and provides support to the hypothesis of MSA evaporating from the condensed phase at low RH. To our knowledge, the only indications about MSA partitioning from the condensed phase are based on field observations and on thermodynamic modelling similar to those presented in this work, but dedicated experiments are missing. An accurate characterization of MSA equilibrium vapor pressure as a function of aerosol acidity would be highly valuable to improve our understanding of MSA partitioning in a realistic aerosol and its contribution to the total aerosol mass.

As described before and shown in Figure 5.9, we measured a low gas to particle MSA ratio during the entire campaign, around 0.5% on average. These low ratios are in line with previous measurements around coastal Antarctica[279] and tropical regions[263,291] and seem to support modelling studies predicting that MSA is predominantly formed via aqueous phase oxidation of DMS[48,173]. In order to investigate this hypothesis we calculated the time required to grow the particulate MSA concentration from gas phase condensation. This is only a qualitative calculation considering that daily averages were used and that MSA was treated as irreversibly condensing to the particles, which is not true as already described. However, our estimate is still valuable because it provides a lower time limit, as condensation cannot be faster than this. Figure S5.7 shows the result in terms of the number of hours that would be required to grow the observed particulate MSA concentration. Two different accommodation coefficients of 0.2 and 1 were used to reproduce the range of values reported in the literature[94,274]. Even in the fastest case, when an accommodation coefficient of one is assumed, the typical time required to reproduce the observed particulate MSA is about 3 days, which is equal or even longer than the typical lifetime of an aerosol in the marine BL (*e.g.* a previous study estimated a lifetime of 2 days for a 0.1 μm diameter particle over the Indian Ocean[292]).

In conclusion, measurements of gaseous MSA concentrations conducted during ACE show a lack of a diurnal cycle and an increase at low RH which can be explained by evaporation of MSA from the condensed phase and a low contribution from gas phase oxidation of DMS. Additionally, the low gas to particle MSA ratio consistently supports the hypothesis that MSA is predominantly produced in the aqueous phase as predicted by different modelling studies[48,173].

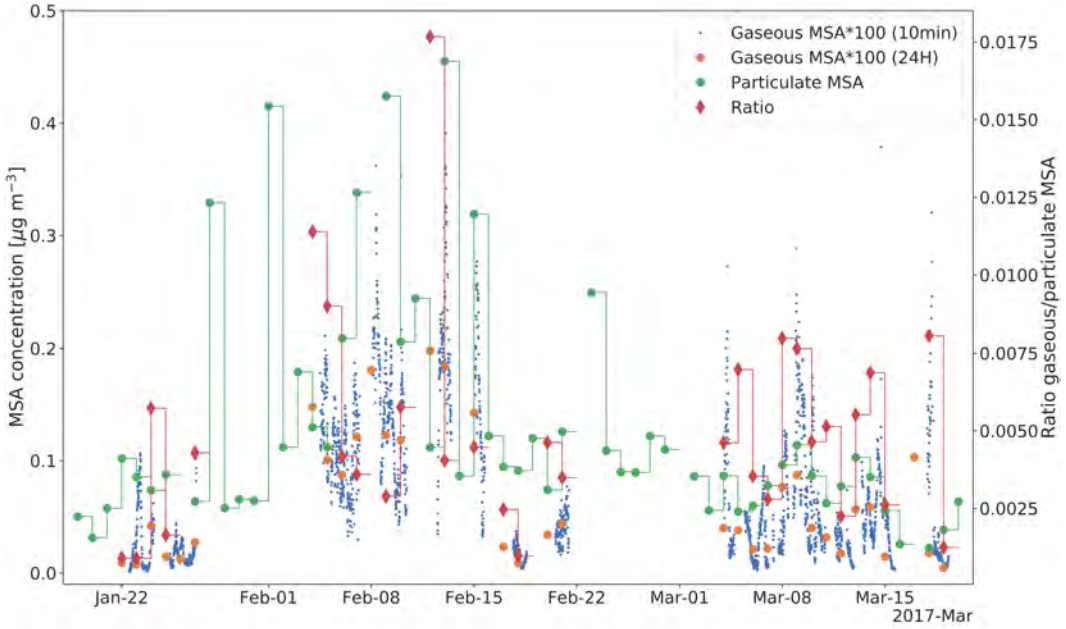

Figure 5.9: MSA concentrations in the gas and particulate phase, gaseous MSA was multiplied by a factor 100 so that the same scale as for particulate MSA could be used. The ratio between gaseous and particulate MSA is reported on the right axis.

5.4.3 New particle formation over the Southern Ocean

The frequency of NPF events observed during ACE was low with the events lasting only a few hours and newly formed particles not growing above 10 nm. The only exception are two events, which occurred on two consecutive days in the proximity of the Mertz glacier (67.1 °S, 145.0 °E). In this case newly formed particles grew above 10 nm, reaching 20 nm and forming a clear nucleation mode. All the other events were local bursts of newly formed particles, which disappeared shortly after the nucleation onset. Figure 5.10 illustrates the particle and negative ion size distributions corresponding to the 2 intense NPF events, solar irradiance and the number concentration of particles larger than 7 nm. A Roman numeral indicates the event number, in this and all the other figures. Unfortunately, for these events no information concerning the chemical composition of the nucleating vapor is available due to a malfunctioning of the mass spectrometer. Both events have a clear diurnal pattern, with particles being produced during the day and suggesting the involvement of sulfuric acid. However, the first and most intense NPF event starts very early in the morning which could also be compatible with the iodic acid diurnal profiles measured during the campaign (Fig. 5.6). Hence it is not possible to uniquely determine the NPF mechanism. The ion size distribution shows some peculiar bands between 2 and 4 nm, these are probably wind generated ions as similar features have been observed also at other snow-covered sites at high wind speeds[293,294], but it is not clear if they were involved in the NPF process. The effect of wind is shown in Figure S5.8, which reports both the negative and positive ion size distribution together with wind speed, relative wind direction and distance to land. It is evident that these ion bands are present only for wind speeds larger than about 10 ms^{-1} in close proximity to land, suggesting that blowing snow may be involved as reported by Chen *et al.*[294].

These two NPF events were interrpted by several short pollution periods. However, the natural origin of nucleation is ensured by the continuous growth of new particles

under persistently strong wind conditions with a prevalent wind direction from the clean sector (*i.e.* the bow of the ship as shown in Fig. S5.8).

Figure 5.11 shows two other NPF events, which are representative of the local NPF type detected during the expedition. Here, mass spectrometric measurements are available. These two events have again a diurnal evolution and the measurement of the neutral molecules and charged clusters suggest an involvement of sulfuric acid. It is known that, in this temperature range, sulfuric acid alone cannot lead to NPF at these low concentrations and a stabilizing compound is needed (*e.g.* ammonia or amines)[13,14]. However, the largest cluster that was detected during all NPF events was the sulfuric acid trimer only, without any additional molecule. The trimer alone is not indicative of the full nucleation mechanism and the stabilizing compound was not identified. Larger clusters were probably not measured because of the low concentrations of the nucleating vapors, which did not produce enough clusters (the sulfuric acid trimer was already close to the detection limit of the mass spectrometer).

Figures S5.9 and S5.10 show the remaining 3 NPF events, which are similar to those described above. The event in Figure S5.10 is slightly different because it occurred during sunset. However, the real onset of nucleation was not detected in this case (particles were already larger than 4 nm), indicating that the event started during day time and the newly formed particles were then advected to the ship location (or alternatively, the ship transited through the NPF location).

Figure 5.12 reports the locations of all the detected NPF events and the corresponding boundary layer 5-day airmass back trajectories calculated with the Lagrangian analysis tool LAGRANTO[185], for additional details the reader is referred to Thurnherr *et al.*[295]. Events are numbered according to Figures 5.10, 5.11, S5.9 and S5.10. All events are characterized by a marine influence with air masses usually coming from the more productive sea ice region around Antarctica. The only exception is event *VI*, which happened closer to South America and was not influenced by any sea ice region.

The two regional NPF events I and II were exceptional because of the environmental conditions encountered. In particular, the temperature and the condensation sink were low during these events with the median temperature being within the first 5 percentiles and the median condensation sink within the first 20 percentiles for both events. At the same time, solar irradiance was above the 75th percentile. Importantly, the combination of these 3 parameters was unique during the entire ACE expedition, which means that there were no other occurrences with similarly low temperature, condensation sink and high solar radiation at the same time. These three parameters are particularly important for NPF because they control the sulfuric acid concentration: more intense solar radiation enhances the OH production increasing the sulfuric acid concentration, while the condensation sink is the main sulfuric acid loss term. They also control the nucleation rates: temperature has a direct effect on the nucleating cluster stability[13]. The exceptional combination of these three parameters probably explains why these two events were different from the rest of the campaign and also helps understanding the difference between ACE and the NPF results reported from Aboa, an Antarctic research station located about 130 km inland from the Southern Ocean coast[15]. There, Jokinen *et al.*[15] reported the frequent occurrence of NPF when the air mass was coming from the surrounding oceanic or sea ice region. This region should be similar in terms of emissions to the area sampled during the most southerly part of the ACE track. However, the frequency and intensity of NPF events recorded in Aboa was much higher. NPF in Aboa is driven by sulfuric acid, which was fre-

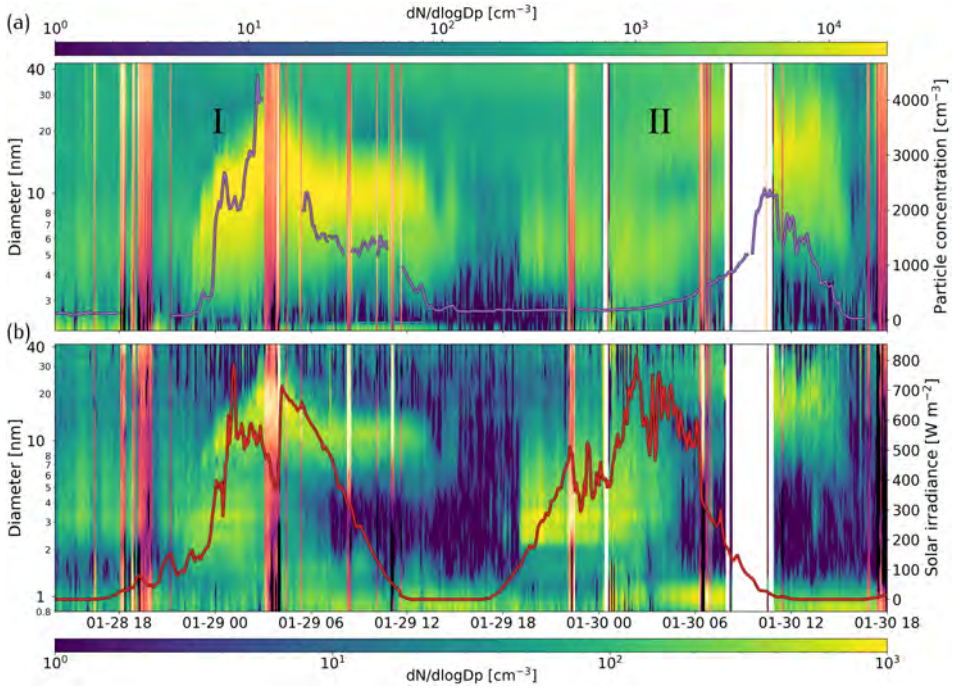

Figure 5.10: New particle formation events I and II, **(a)** total particle size distribution (2.5 - 42 nm) and number concentration of particles larger than 7 nm (right axis). **(b)** negatively charged ion size distribution (0.8 - 42 nm) and solar irradiance time series (right axis). Pollution spikes are highlighted with a different colour map (*magma*), in this case a less stringent pollution mask was used instead of the default from Schmale *et al.*[42] in order to clearly show the evolution of the NPF event.

quently higher than 10^7 molecules cm^{-3}, different from ACE where this threshold was almost never exceeded (Figure S5.11). However, this difference is unlikely driven by DMS emissions only, which are equal or higher along the ACE track than in the region of air mass origin for the Aboa NPF events[241,296]. Rather, the higher sulfuric acid reported at Aboa can probably be explained by the lower condensation sink, a factor two lower on average than during ACE (Figure S5.12), and the higher SIR. Additionally, the temperature measured in Aboa was 2 to 5 degrees lower than the minimum temperature recorded during ACE (with the exception of a single day), and this also enhances NPF. The different temperature and SIR values in Aboa are simply due to the meteorological conditions (the Antarctic continent is colder and less cloudy than the surrounding ocean[297]), whereas the lower condensation sink can be explained by the short lifetime of the coarse mode aerosol, which is responsible for a large fraction of the condensation sink over the ocean and would be removed by the time they have reached Aboa. Another important difference is the detection of ammonia, which was frequently measured by Jokinen *et al.*[15] in negative clusters with acids but never observed during ACE. A quantitative comparison of the ammonia concentration is not possible because this molecule was not measured directly during either campaign (ammonia was only detected as a cluster with sulfuric acid). It is possible that during the study of Jokinen *et al.*[15] the ammonia concentration was on average higher compared to ACE. However, during ACE a large variety of different locations were explored, including places in close proximity to penguin colonies which are known to be strong sources of ammonia[171,298]. Therefore, it is unlikely that ammonia was the only lim-

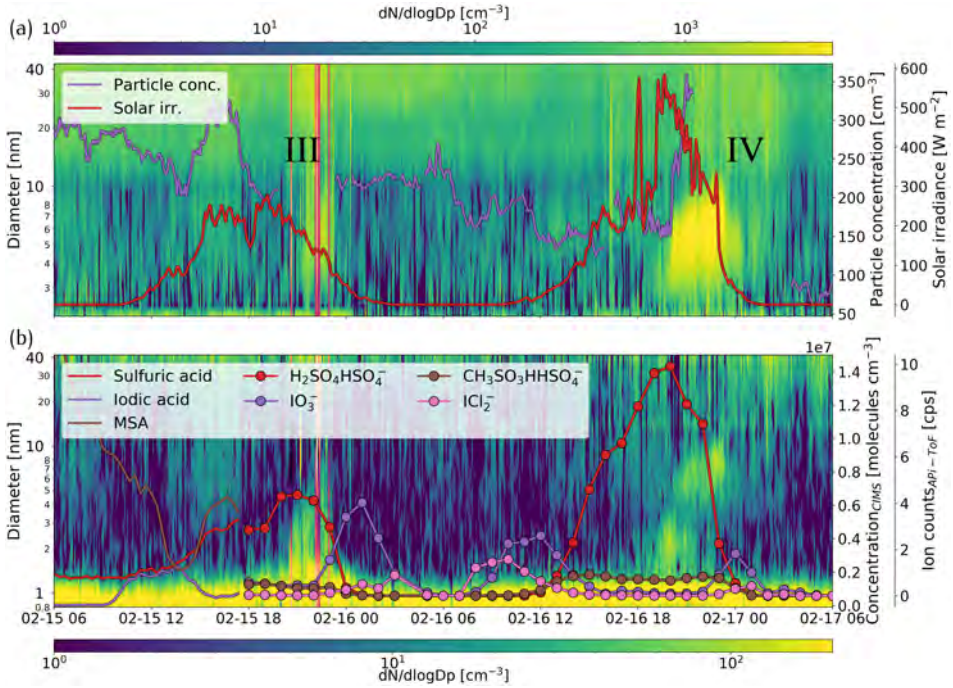

Figure 5.11: New particle formation events III and IV, **(a)** total particle size distribution (2.5 - 42 nm) and, on the right axis, number concentration of particles larger than 7 nm and solar irradiance time series. **(b)** negatively charged ion size distribution (0.8 - 42 nm), on the right axis the concentration of neutral molecules measured with the CI-APi-ToF (solid line) and the negative ions measured with the APi-ToF (round markers) are reported. Only the 4 ions with the largest signal are reported here, the sulfuric acid and MSA monomers are not present because of the instrument mass transmission, which was set to higher masses. Pollution spikes are highlighted with a different color map (*magma*), in this case a less stringent pollution mask was used instead of the default from Schmale *et al.*[42].

iting factor for NPF during ACE but it may have contributed together with the other factors described above (temperature, SIR and condensation sink).

Despite the rare occurrence of boundary layer NPF, an Aitken mode was frequently detected during ACE contributing to a large fraction of the total particle number concentration as reported in Figure S13. The origin of these Aitken mode particles remains unknown but it is compatible with the hypothesis from previous studies suggesting that NPF may be prevalently occurring in the free troposphere[47,56,58,250]. However, it is difficult to explain the growth of the freshly formed particles to the typical 30 to 50 nm Aitken mode diameter[42] considering the low concentration of condensable vapors. Investigating this topic in detail is beyond the scope of this work, but it clearly deserves more attention.

5.5 CONCLUSIONS

The Southern Ocean is one of the most pristine locations on Earth[41] and measurements in this region can be valuable to better understand the state of the atmosphere in preindustrial times and constrain the radiative forcing uncertainty in global climate models[31]. This work presents an overview of the spatial distribution of sulfuric acid, MSA and iodic acid across the Southern Ocean together with ultrafine particle and

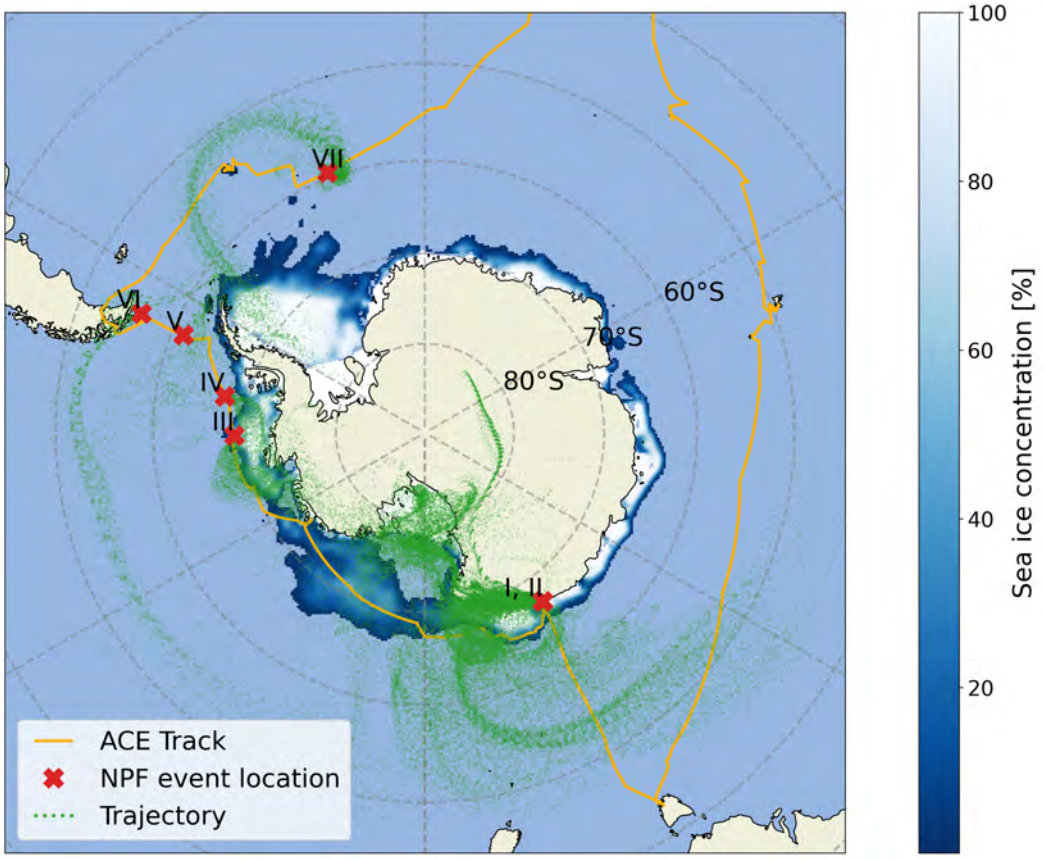

Figure 5.12: Map showing the ACE track, the location of NPF events and the 5-day boundary layer air mass back trajectories for each of the events. The back trajectories are shown using semi-transparent green dots, the density of dots in a specific region is proportional to the amount of trajectories passing over that region. The figure also shows the sea ice concentration (fraction of covered surface) retrieved for January 2017[77].

ion concentration as well as size distribution. These are all quantities that are relevant for new particle formation and growth. Obtaining a better understanding of the processes and the environmental conditions regulating their distribution can, therefore, be valuable to properly represent aerosol sources and properties in global climate models. There are studies which previously investigated trace gases (sulfuric acid and MSA)[59,279], new particle formation[47,52,53] or both[15] over the Southern Ocean and coastal Antarctica. However they were focused on single locations. The work presented here is the first comprehensive investigation of trace gases and new particle formation across the Southern Ocean providing a wide geographical coverage and a broader understanding of the processes involved.

Sulfuric acid vapor was characterized by a clear diurnal cycle with maxima at daytime consistent with photochemical production from SO_2. The concentration was lower compared to recent measurements from coastal Antartica[15], especially considering that only an upper limit was reported here. This had a direct effect on the occurrence of NPF events which were weak in terms of particle production and very sporadic. The lower sulfuric acid vapor concentration was attributed mainly to environmental reasons, such as the high condensation sink and rather low solar irradiance.

Iodic acid also exhibited a diurnal cycle with very low concentrations during night time, as expected from a molecule that is formed from the photochemically produced

iodine radical. However, the iodine concentration peaked at dawn and dusk with consistently lower concentration during the central part of the day when solar radiation was stronger. This observation, which has not been reported before, could be related with the photolysis of an iodic acid precursor molecule (*e.g.* IO or I_2O_3)[268,270]. This result is important because it indicates that iodic acid could eventually reach higher concentrations when solar radiation is lower, like in spring or in autumn, if the iodine flux were comparable. As a consequence, there may be periods of the year when iodic acid may be relevant for NPF also over the Southern Ocean. Additional measurements to investigate this possibility are needed.

Finally, the gaseous MSA concentration is too low to explain the required particulate MSA values via a condensation mechanism. This suggests that MSA may be predominantly produced in the aqueous phase, as indicated already by previous modelling studies[48,173]. Additionally, gaseous MSA does not show any diurnal cycle and tends to increase under dryer conditions, indicating that the gas phase MSA may be driven by evaporation from the particle phase. This is consistent with predictions from a thermodynamic model considering a mixture of sea spray, MSA ammonium and sulfate. Both the increase of MSA at lower RH and the absence of a diurnal cycle are in line with previous measurements of MSA in marine environments[259,263,265]. This suggests that a more accurate treatment of MSA production and partitioning in atmospheric chemistry models is needed to improve the representation of marine sulfur compounds in the atmosphere.

Schmale *et al.*[42] reported a large discrepancy in the CCN number concentration around the coast of Antarctica when comparing measurements with values modelled using the Global Model of Aerosol Processes (GLOMAP)[170]. This area corresponds also to the strongest MSA signal detected during the entire expedition (both in the gas and in the particle phase as shown in Figure 5.9). The area is also known to exhibit one of the largest DMS concentrations (both in the water and in the atmosphere) in the world during summer[241,296]. GLOMAP (as many other global climate models) only includes homogeneous production of MSA in the gas phase, whereas it does not consider condensation of this MSA nor heterogeneous production which could contribute to the underestimation of the CCN concentration around the coast of Antarctica. Future studies should focus on the MSA partitioning and aqueous phase production to understand its contribution to the concentration of CCN and their properties.

The results obtained during ACE clearly show that discernible NPF in the boundary layer is rare across the Southern Ocean in summer and only in exceptional cases it contributes to the aerosol Aitken mode population. Sulfuric acid was the main nucleating compound for the observed NPF events. A base, such as ammonia or amines, would also be required to stabilize the nucleating clusters given the low sulfuric acid concentration[13,14] but no stabilizing compound was identified. We also found that environmental conditions, mainly temperature and the condensation sink, are critical in determining the occurrence of NPF and are likely responsible for the different observations compared to previous studies between the open ocean and coastal Antarctica in terms of boundary layer NPF[15,53,239,248,251,252]. The low relevance of boundary layer NPF together with the frequent detection of Aitken mode aerosols is compatible with new particles being formed in the free troposphere and then transported downward as shown also by other studies[47,58,239,249]. This hypothesis cannot be confirmed with our dataset because we lack information concerning the vertical distribution of aerosol particles. Future expeditions in the region should specifically address this topic,

investigating aerosol sources both in the boundary layer and in the free troposphere while trying to understand their exchange processes.

5.6 SUPPORTING INFORMATION

5.6.1 Introduction

This supporting information contains a text section describing how the extended Aerosol Inorganic Model (E-AIM; http://www. aim.env.uea.ac.uk/aim/aim.php, last access: 22 April 2021)[277] was used to model the gas-particle partitioning of methanesulfonic acid (MSA) using an aerosol mixture representative of the Southern Ocean aerosol.

Figures S5.1 to S5.13 provide additional information to the results shown in the main text and are referenced therein. Figure S5.14 and Tables S5.1 and S5.2 are related to the SI Text and provide details regarding the E-AIM simulation.

5.6.2 E-AIM calculation

E-AIM was used to estimate MSA partitioning over the Southern Ocean aerosol. MSA is not included among the default species available in the E-AIM library and needs to be created by the user defining some of its fundamental thermodynamic properties. A part from the most basic properties, such as the molar mass and the molar volume, MSA thermodynamic properties are not readily available and model studies often use very different values. Table S5.1 reports all the values that were used in this study and the corresponding references, as a general criterion we decided to use values based on experimental results rather than modelling or ab initio calculation. By reporting all the information required to include MSA in E-AIM we hope to provide a useful reference for the community and to foster discussion, which thermodynamic properties are the most appropriate values for MSA. All the values in Table S5.1 were taken directly from the cited reference with minimal adaption (*e.g.* unit of measure), with the only exception of the surface tension parameters. In this case we had to recreate the surface tension data from Myhre *et al.*[299] and fit them with the function defined by Dutcher *et al.*[300] to obtain the parameters in the form required by E-AIM.

Concerning the specific details of the E-AIM simulations, we fixed the temperature to 273.15 K and varied relative humidity (RH) between 60% and 100%. These are representative values for the environmental conditions encountered during the two transects described in the main text. E-AIM model II was used for the simulations containing only sulfate, ammonium and MSA whereas E-AIM model IV was used when also sodium and chloride were included. Aerosol components were forced to stay in the liquid form as the efflorescence RH is below typical values encountered in the marine boundary layer. However, E-AIM model IV is unable to account for supersaturated solutions, for this reason only RH values above $\sim$ 75% could be considered when using this model.

The aerosol composition used for the E-AIM simulation was based on ion chromatography (IC) analysis of daily PM_{10} filters. These filters were collected using a high-volume sampler on the upper deck of the ship. The sampler had an automatic system to stop the sample flow when the wind was coming from the direction of the ship chimney. However, this system proved to be not sufficient to prevent sampling

of the exhaust plume as evident from the high elemental carbon (EC) concentrations measured on some of the filters (larger than 1 μg m^{-3}). We used EC as a proxy for contamination from the ship exhaust on the PM_{10} filters because ambient concentration of black carbon in the Southern Ocean is generally very low (less than 40 ng m^{-3})[42]. Figure S5.14 shows the ammonium and the non-sea-salt (nss) sulfate concentrations measured on the PM_{10} filters as a function of EC, there is an evident positive correlation indicating that both ammonium and nss-sulfate are probably affected by the ship exhaust. However, nss-sulfate and ammonium seem to become independent from the ship exhaust for EC values below about $0.6 - 0.7\,\mu$g m^{-3}. Under this condition, the concentration of these two compounds is dominated by natural sources and not by the ship exhaust. Hence, we decided to consider only the filters characterized by an EC concentration below $0.65\,\mu$g m^{-3} to minimize the influence of the ship exhaust. Additionally, we also excluded the filters with a total sampled volume below 240 m^3, which is one third of the maximum possible volume. Such a low sampling volume indicates that the samplers were often turned off because of the wind coming from the direction of the ship chimney. Figure S5 shows the concentration of the ions relevant for the E-AIM calculation from this filter selection.

In order to understand the effect of aerosol composition on MSA partitioning we run three different sets of simulations using E-AIM. For the first set of simulations we decided to fix the nss-sulfate concentration based on the median concentration measured during ACE and varied the ammonium concentration to obtain different ratios (2 : 1, 1 : 1 and 1 : 2). The MSA concentration was fixed based on the median MSA to nss-sulfate ratio (Fig.S5.5). Figure S5.6 shows the model predictions in terms of the MSA vapour pressure and the gas fraction due to partitioning from the condensed phase. The second set of simulations includes also sea spray, in the form of sodium, chloride and sea-salt (ss) sulfate. For the concentrations of ss-sulfate and chloride we used the median values from ACE, whereas the sodium concentration was increased to achieve neutrality of the SSA and account for the presence of other cations which cannot be included in E-AIM (*i.e.* magnesium and calcium). Finally, for the third set we considered only 10% of the sea spray concentration, together with nss-sulfate, MSA and different concentrations of ammonium spanning an ammonium to nss-sulfate ratio from 0.25 to 2. Results are shown in the main text. Table S2 shows the concentrations of aerosol constituents used for each model run.

The predicted MSA gas phase concentrations shown in the main text (Fig. 5.8) was calculated considering the estimated gas phase fraction from each E-AIM simulation multiplied by the average particulate MSA concentration measured during the two periods under analysis ($0.21\,\mu$g m^{-3} and $0.09\,\mu$g m^{-3} for the first and the second period, respectively).

5.6.3 Figures

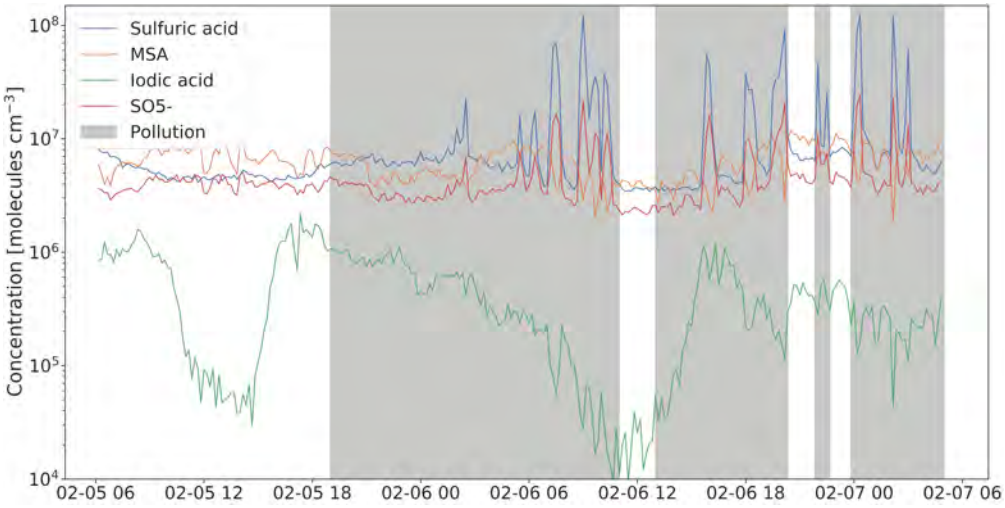

Figure S5.1: Time series showing the effect of pollution on the major compounds measured with the nitrate CI-APi-ToF, the polluted periods are highlighted with a gray shadow according to the pollution mask described in Schmale *et al.*[42]. SO_5^- is generated inside the inlet of the CI-APi-ToF and is a proxy for ambient SO_2.

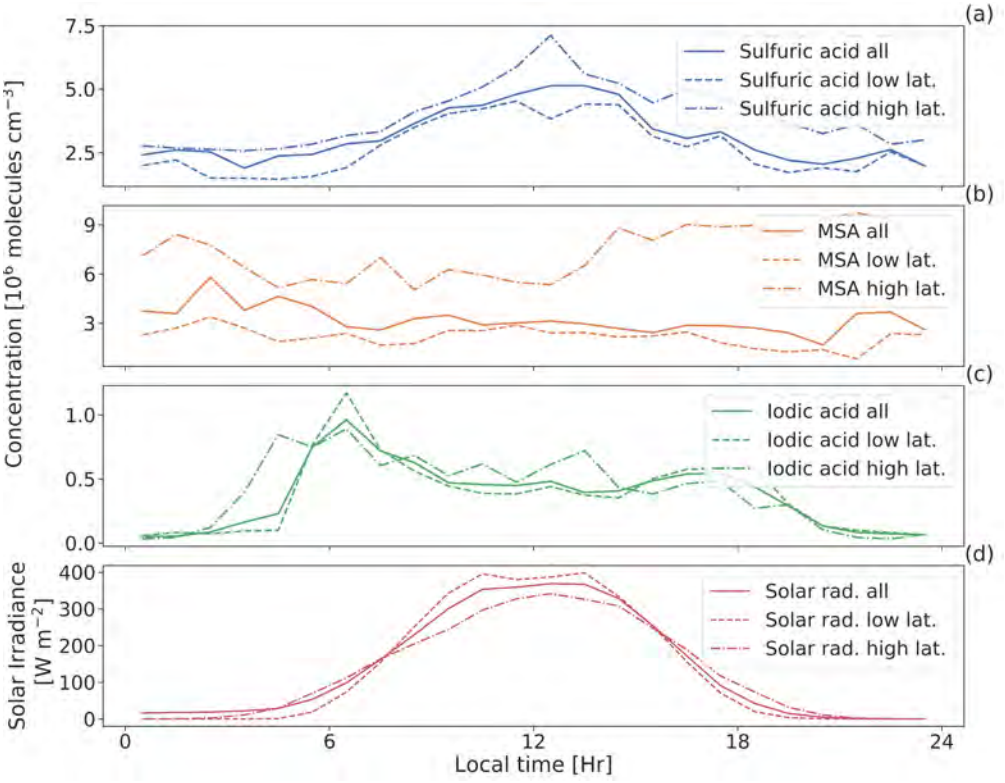

Figure S5.2: Diurnal profiles of **(a)** sulfuric acid, **(b)** MSA, **(c)** iodic acid and **(d)** solar irradiance for the entire campaign and separated by latitude. Here, high and low latitude indicates measurements above and below 60 °S, respectively.

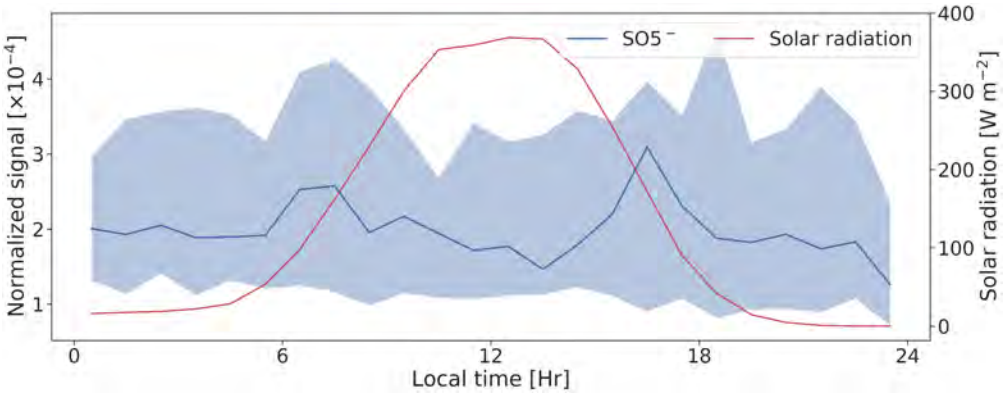

Figure S5.3: Diurnal cycle of SO_5^-. The thick line represents the median and the shaded area the interquartile range. The red line shows the solar irradiance median with values on the right axis.

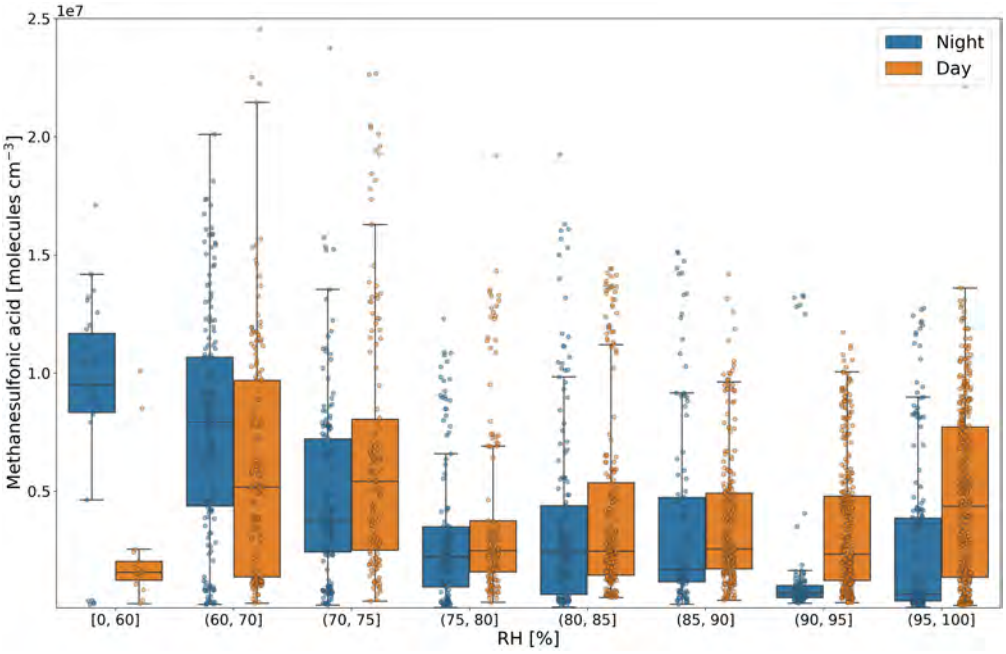

Figure S5.4: Gaseous MSA box and whiskers plot as a function of relative humidity (RH). Data were separated between day and night and binned into different RH classes as indicated by the axis label. The original data are shown with the small semi-transparent circles. The box extends from the first quartile (Q1) to the third quartile (Q3) with a line indicating the median. The whiskers are set to 1.5×[Q3-Q1].

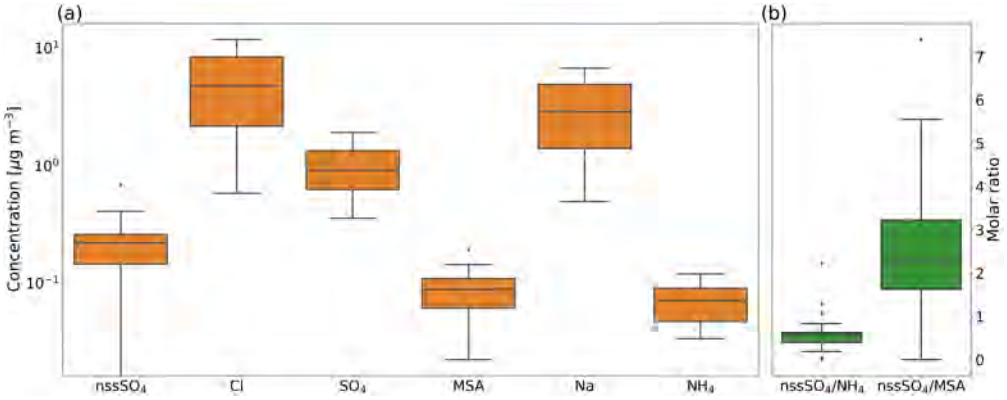

Figure S5.5: Box and whiskers plot of the ion chromatography data from PM_{10} daily aerosol filter. Only a subset of filters with minimum contamination from the ship exhaust was selected. (a) Concentration of the ions used for the thermodynamic modelling, (b) molar ratio of non-sea-salt (nss) sulfate to ammonium and nss-sulfate to MSA.

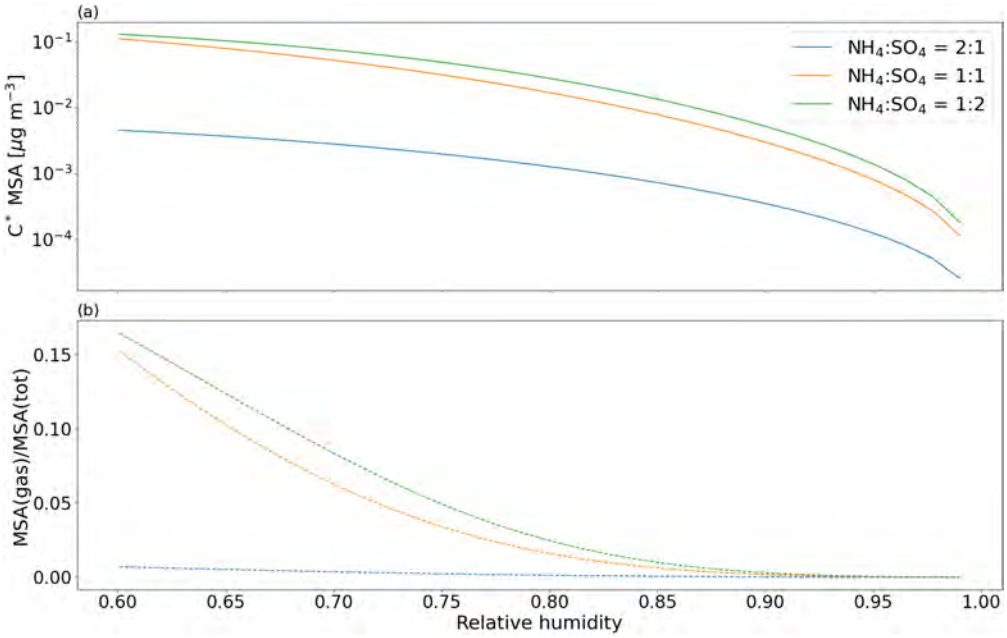

Figure S5.6: E-AIM results for MSA partitioning over an aerosol mixture composed of sulfate, MSA and ammonium as a function of relative humidity. **(a)** MSA equilibrium vapour pressure (C*), **(b)** fraction of MSA in the gas phase due to partitioning from the condensed phase. The sulfate, MSA and ammonium concentrations used for this simulation are reported in table S2 (run 1.1, 1.2 and 1.3).

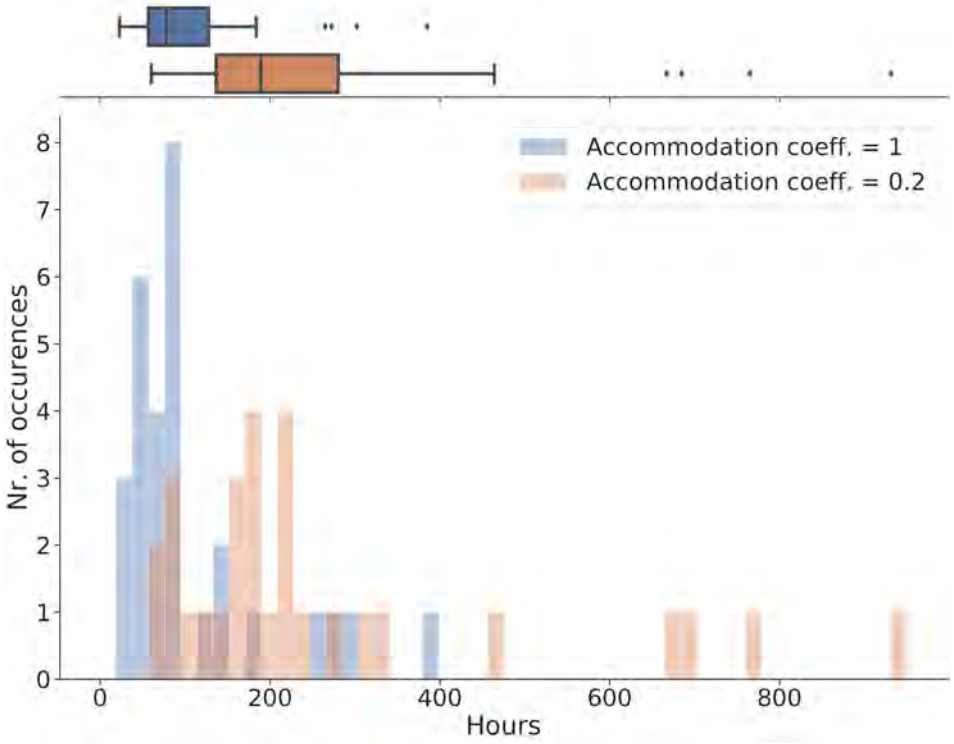

Figure S5.7: Number of hours required to reproduce the observed particulate MSA concentration assuming kinetic condensation of gaseous MSA with two different accommodation coefficients. This condensation time was calculated based on the daily average values and the figure shows the number of occurrences as a histogram and a box and whiskers plot on top. The box extends from the first quartile (Q1) to the third quartile (Q3) with a line indicating the median. The whiskers are set to 1.5×[Q3-Q1].

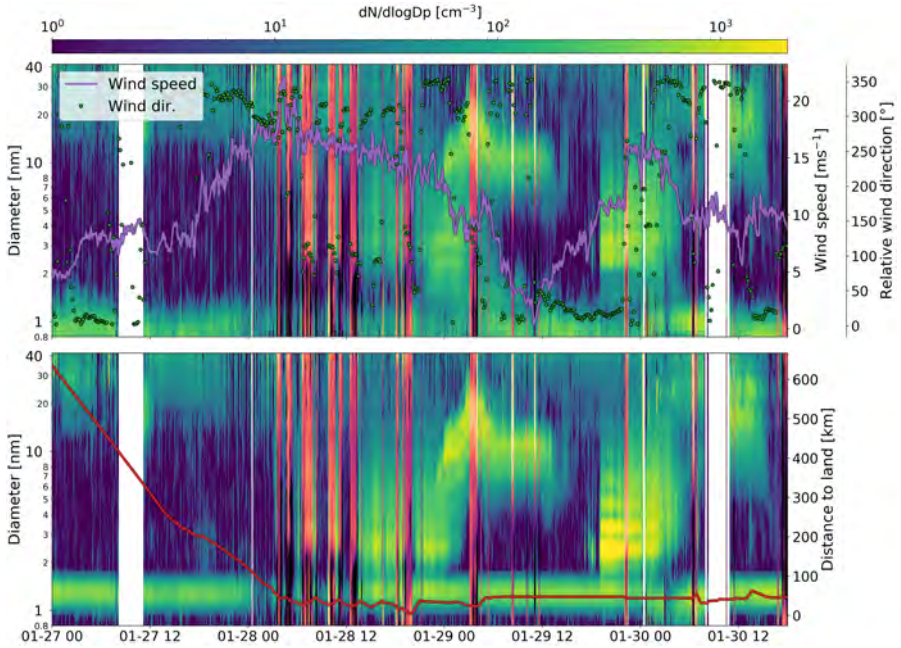

Figure S5.8: Wind induced ions, **(a)** negative ion size distribution and, on the right axis, wind speed and relative wind direction (the bow of the ship corresponds equivalently to 0° or 360°). **(b)** positive ion size distribution, on the right axis the distance to land is shown. Pollution periods are highlighted with a different color map (*magma*).

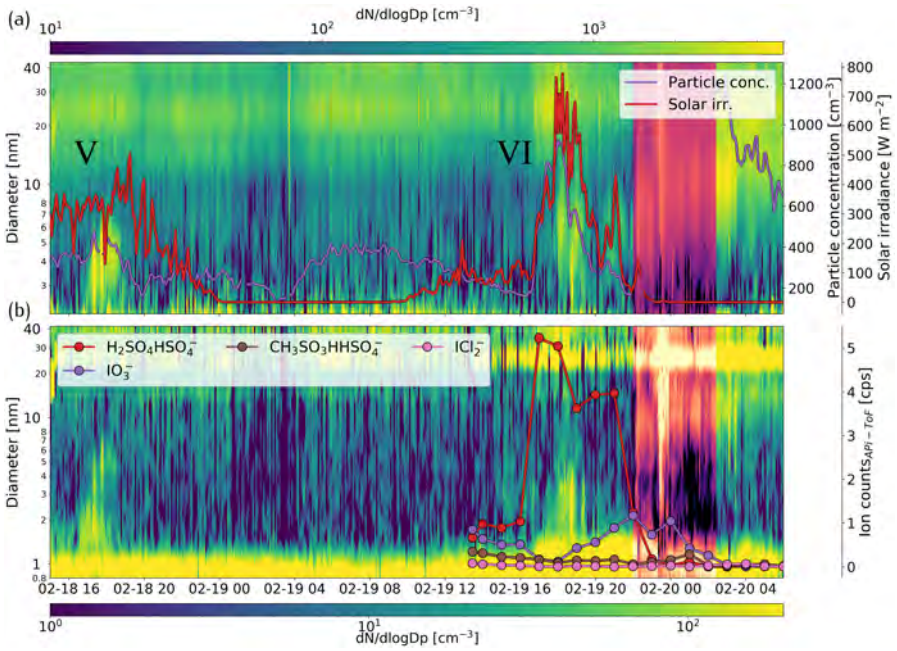

Figure S5.9: New particle formation event, **(a)** total particle size distribution and, on the right axis, number concentration of particles larger than 7 nm and solar irradiance time series. **(b)** negatively charged ion size distribution, on the right axis the concentration of negative ions measured with the APi-ToF (round markers) is reported. Only the 4 ions with the largest signal are reported here, the sulfuric acid and MSA monomers are not presented because of the instrument mass transmission, which was set to higher masses. Pollution spikes are highlighted with a different color map (*magma*).

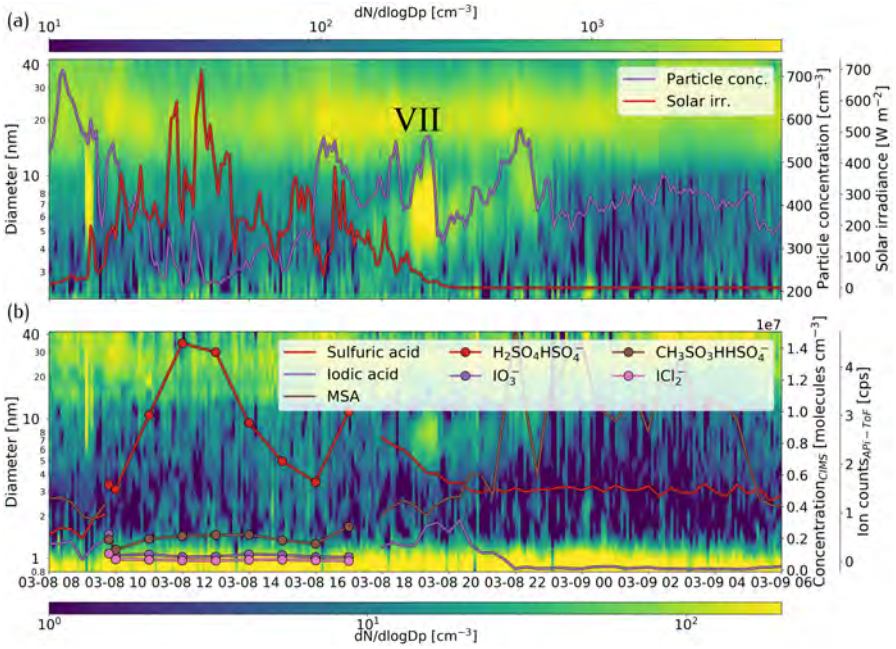

Figure S5.10: New particle formation event, **(a)** total particle size distribution and, on the right axis, number concentration of particles larger than 7 nm and solar irradiance time series. **(b)** negatively charged ion size distribution, on the right axis the concentration of neutral molecules measured with the CIMS (solid line) and the negative ions measured with the APi-ToF (round markers) are reported. Only the 4 ions with the largest signal are reported here, the sulfuric acid and MSA monomers are not presented because of the instrument mass transmission, which was set to higher masses.

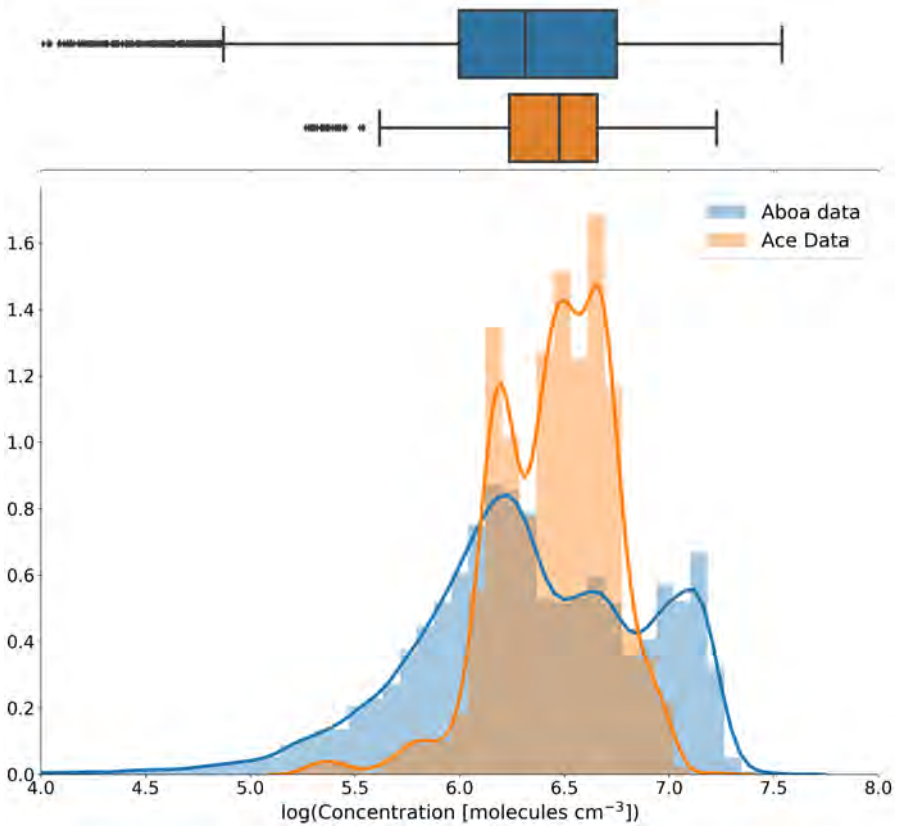

Figure S5.11: Comparison of the sulfuric acid measured during ACE and at Aboa. The figure shows a histogram reporting the frequency of the observation with a kernel density estimate (thick line) and box and whiskers plot on top. The box extends from the first quartile (Q1) to the third quartile (Q3) with a line indicating the median. The whiskers are set to 1.5×[Q3-Q1].

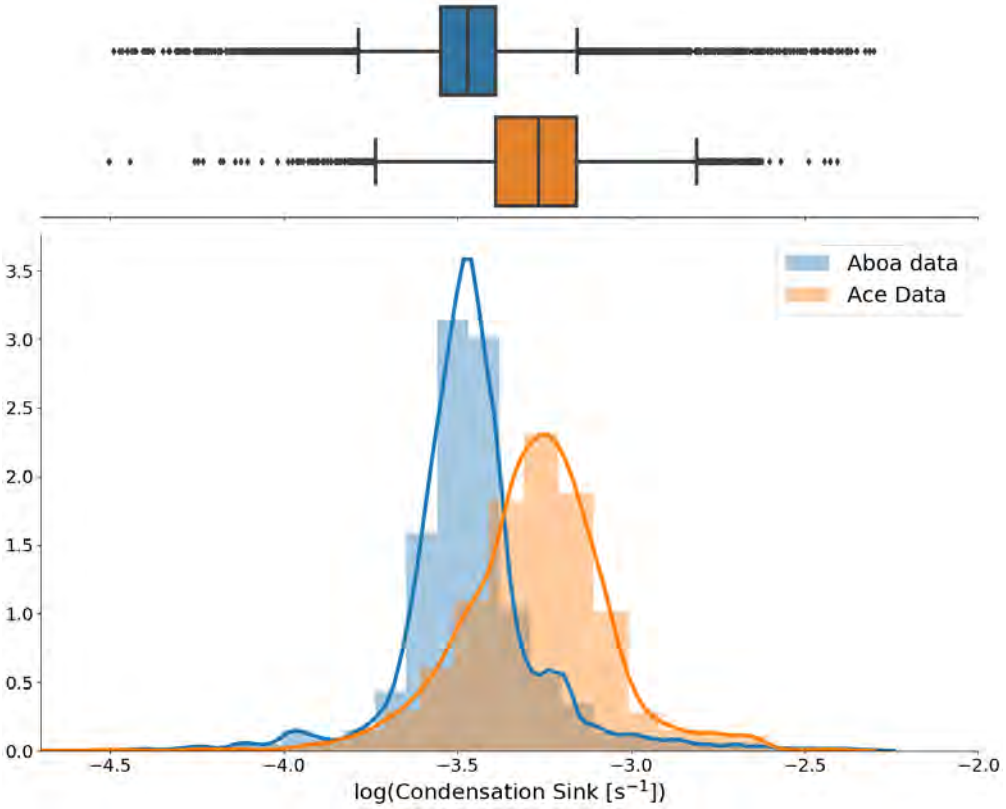

Figure S5.12: Comparison of the condensation sink measured during ACE and at Aboa. The figure shows a histogram reporting the frequency of the observation with a kernel density estimate (thick line) and box and whiskers plot on top. In this case the condensation sink from ACE was calculated using the same size range as at Aboa to improve the accuracy of the comparison (from 10 nm to 900 nm). The box extends from the first quartile (Q1) to the third quartile (Q3) with a line indicating the median. The whiskers are set to 1.5×[Q3-Q1].

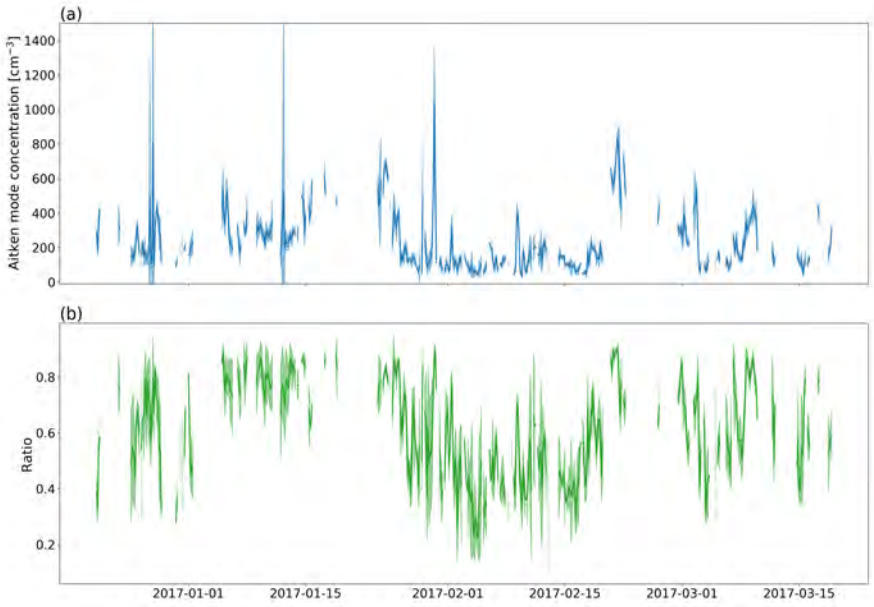

Figure S5.13: Aitken mode particles during ACE: **(a)** total Aitken mode particle number concentration from the fit of the SMPS size distribution and **(b)** ratio of the Aitken mode particle number to the total number particle concentration. The thick line is a 3 hours mean and the shadowed region indicates a 1 standard deviation interval.

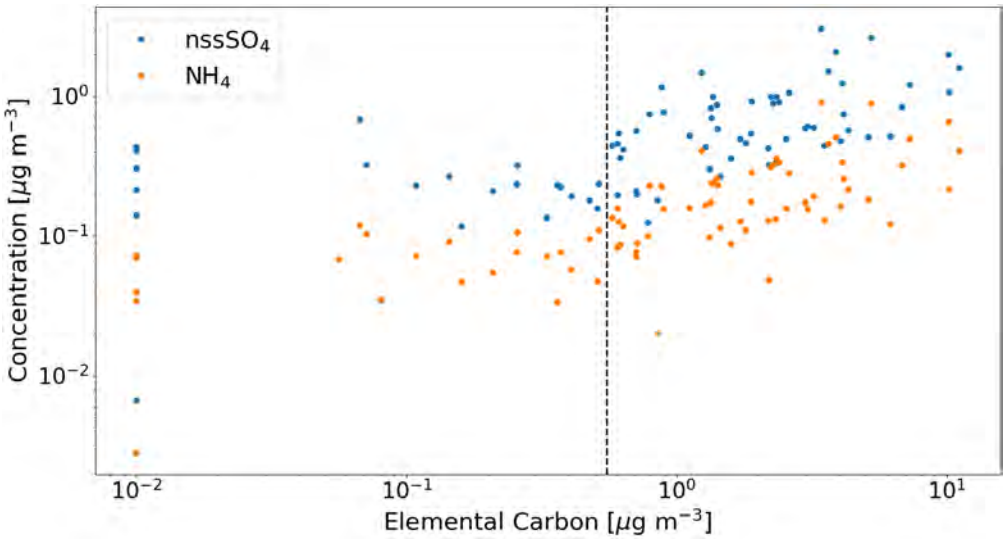

Figure S5.14: Concentration of nss-sulfate and ammonium as a function of elemental carbon. The vertical dashed line was drawn at 0.65 μg m^{-3} of carbon and indicates the concentration below which the effect of ship pollution is not evident anymore on nss-sulfate and ammonium. Elemental carbon measurements below detection limit were fixed to a value equal to 0.01 μg m^{-3}.

5.6.4 Tables

Table S5.1: MSA thermodynamic properties

Property	Unit of measure	Value	Reference
Molar mass	g mol^{-1}	96.1	Barnes *et al.*[267]
Molar Volume	cm^3 mol^{-1}	64.93	Barnes *et al.*[267]
First dissociation constant	mol kg^{-1}	73	Clarke *et al.*[301]
Enthalpy of dissociation	kJ mol^{-1}	0	Not determined
Henry's law constant	mol kg^{-1} atm^{-1}	8.9×10^{11}	Clegg *et al.*[302]
Henry's law enthalpy change	kJ mol^{-1}	14.644	De Bruyn *et al.*[274]
Surface tension: c_1	mN m^{-1}	138.23	Myhre *et al.*[299]
Surface tension: c_2	mN m^{-1} K^{-1}	−0.284	Myhre *et al.*[299]
Surface tension: a_{ws}	mN m^{-1}	147.86	Myhre *et al.*[299]
Surface tension: b_{ws}	mN m^{-1} K^{-1}	−0.275	Myhre *et al.*[299]
Surface tension: a_{sw}	mN m^{-1}	−167.117	Myhre *et al.*[299]
Surface tension: a_{sw}	mN m^{-1} K^{-1}	0.400	Myhre *et al.*[299]

Table S5.2: Concentration of aerosol constituents used for the E-AIM simulations

Run number	nss-sulfate nmol m^{-3}	Ammonium nmol m^{-3}	MSA nmol m^{-3}	ss sulfate nmol m^{-3}	Chloride nmol m^{-3}	Sodium nmol m^{-3}
1.1	2.3	4.6	1	0	0	0
1.2	2.3	2.3	1	0	0	0
1.3	2.3	1.15	1	0	0	0
2.1	2.3	3.9	1	7.2	134	148
3.1	2.3	4.6	1	0.7	13.4	14.8
3.2	2.3	2.3	1	0.7	13.4	14.8
3.3	2.3	1.15	1	0.7	13.4	14.8
3.4	2.3	0.58	1	0.7	13.4	14.8

6 FREQUENT NEW PARTICLE FORMATION OVER THE HIGH ARCTIC PACK ICE BY ENHANCED IODINE EMISSIONS

Andrea Baccarini[1], Linn Karlsson[2], Josef Dommen[1], Patrick Duplessis[3], Jutta Vüllers[4], Ian M. Brooks[4], Alfonso Saiz-Lopez[5], Matthew Salter[2], Michael Tjernström[6], Urs Baltensperger[1], Paul Zieger[2] and Julia Schmale[1,7].

[1] *Laboratory of Atmospheric Chemistry, Paul Scherrer Institute, Villigen, Switzerland*
[2] *Department of Environmental Science & Bolin Centre for Climate Research, Stockholm University, Stockholm, Sweden*
[3] *Department of Physics and Atmospheric Science, Dalhousie University, Halifax, Canada*
[4] *School of Earth and Environment, University of Leeds, Leeds, UK*
[5] *Department of Atmospheric Chemistry and Climate, Institute of Physical Chemistry Rocasolano, CSIC, Madrid, Spain*
[6] *Department of Meteorology & Bolin Centre for Climate Research, Stockholm University, Stockholm, Sweden*
[7] *School of Architecture, Civil and Environmental Engineering, École Polytechnique Fédérale de Lausanne, Switzerland*

Published in: **Nature Communications, DOI:10.1038/s41467-020-18551-0 (2020)**

6.1 ABSTRACT

In the central Arctic Ocean the formation of clouds and their properties are sensitive to the availability of cloud condensation nuclei (CCN). The vapours responsible for new particle formation (NPF), potentially leading to CCN, have remained unidentified since the first aerosol measurements in 1991. Here, we report that all the observed NPF events from the Arctic Ocean 2018 expedition are driven by iodic acid with little contribution from sulfuric acid. Iodic acid largely explains the growth of ultrafine particles (UFP) in most events. The iodic acid concentration increases significantly from summer towards autumn, possibly linked to the ocean freeze-up and a seasonal rise in ozone. This leads to a one order of magnitude higher UFP concentration in autumn. Measurements of cloud residuals suggest that particles smaller than 30 nm in diameter can activate as CCN. Therefore, iodine NPF has the potential to influence cloud properties over the Arctic Ocean.

6.2 INTRODUCTION

The Arctic is warming at least twice as fast as the global average (Arctic amplification)[24,303], particularly during autumn and winter[148]. Model studies have identified several local and remote drivers that contribute to the accelerated warming. State-of-the-art climate models are still unable to accurately represent local Arctic processes. This is particularly true for clouds and their radiative properties[64,148]. The presence or absence of a cloud over the pack ice makes a significant difference for the surface energy budget and is expected to impact the thickness and extent of sea ice[62]. Cloud formation in the central Arctic Ocean can be limited by the availability of cloud condensation nuclei (CCN)[65]. Under this CCN-limited cloud regime, a small increase in the CCN concentration can lead to a pronounced increase in surface warming due to the longwave cloud forcing. Hence, understanding the sources and evolution of particles in the central Arctic Ocean is crucial to modelling the CCN population and cloud formation correctly.

Previous measurements in the region have revealed a number of CCN sources, including secondary marine organic particles, primary marine emissions like sea salt and organic aerosol, long-range transported continental emissions and their down-mixing into the marine boundary layer from aloft[67,68,70,304]. Continental influence may make up about one-third of the non-refractory accumulation mode particles[67], highlighting the importance of regional and local Arctic sources which are not yet well constrained. This is particularly true for new particle formation (NPF) and Aitken mode particles since the online instrumentation capable of characterizing their chemical composition in situ has become available only recently[86,87]. A recent modelling work suggested that NPF may contribute to a large fraction of the high Arctic CCN number concentration[12]. However, no information was provided about the source region of these newly formed particles and none of the models currently includes iodine nucleation. Thus, the actual contribution of local NPF to the Arctic CCN budget remains highly uncertain. Nucleation mode particles have been observed over the pack ice since the first International Arctic Ocean Expedition in 1991[71,72,74], and are typically associated with prolonged air mass residence time over the pack ice, suggesting the influence of a source within the pack ice[69]. However, the source of these newly formed particles has not been identified[72,74]. Measurements around the Arctic marginal ice zone (MIZ)

have attributed NPF to sulfuric acid, ammonia, marine organics[305,306] and in a few cases to iodine[20,307,308]. While these studies provide valuable information about Arctic NPF they cannot be directly extrapolated to the central Arctic Ocean, which is characterized by a much lower concentration of gas precursors compared to the MIZ[309].

By deploying a real-time mass spectrometer[86,87] and various particle counters and sizers we have identified iodic acid (HIO_3) as the main driver for the frequent NPF events occurring over the central Arctic Ocean during August and September, the expedition period. Data were collected during the Microbiology–Ocean–Cloud-Coupling in the High Arctic (MOCCHA) campaign as part of the Arctic Ocean 2018 expedition on board the Swedish icebreaker (I/B) *Oden* (Fig. S6.1).

6.3 RESULTS AND DISCUSSION

6.3.1 Iodine drives NPF

A typical NPF event is illustrated in Figure 6.1. Iodic and sulfuric acid (H_2SO_4) increase before 10:00 (all times given in UTC) leading to the production of small particles as evident from the negative-ion number size distribution. During the passage of a small patch of fog, both the concentration of the acids and the newly formed particles are strongly reduced but increase again afterwards. On the regional scale particles have already grown to 3–7 nm size. While HIO_3 reaches a concentration of $> 8 \times 10^6$ molecule cm^{-3}, the sulfuric acid concentration remains six to ten times lower. The negatively charged clusters are composed of iodine oxides with a maximum of eight iodine atoms per cluster, whereas the largest pure sulfuric acid cluster detected is only the trimer (mass defect plot in Fig. 6.1c). Mixed clusters are also detected containing a maximum of two sulfur and up to eight iodine atoms. The chemical composition of the pure iodine clusters is typically $H_{0-4}O_xI_y$ with an oxygen to iodine ratio between 2.5 and 3. This closely resembles the first measurements of coastal HIO_3 nucleation performed in Mace Head (Ireland)[20], pointing towards a similar nucleation mechanism. The oxygen to iodine ratio is also in agreement with previous laboratory and modeling iodine NPF studies[310,311]; the full list of both neutral and charged iodine clusters is reported in Tables S6.1 and S6.2.

The sulfuric acid neutral monomer concentration is more than two orders of magnitude too low for binary NPF[13], while ternary sulfuric acid NPF with bases can be ruled out by the absence of clusters containing ammonia or amines in the negative-ion mass spectrum[13,14]. Furthermore, the continuous growth of the negative-ion size distribution from the ion cluster band (0.8–1.2 nm) is clear evidence that ultrafine particles (UFP) (defined here as particles with diameter D$<$ 15 nm) are produced by secondary particle formation. We did not find any evidence that UFP were produced by a primary mechanism as hypothesized previously[75].

During this campaign, we detected 11 major NPF events over the pack ice in total, all driven by HIO_3 with no important contribution from sulfuric acid or other compounds. All the events were characterized by a continuous growth of the negative ions from the cluster band into larger sizes, whereas no growth of the positive ions was observed. This indicates that ion-induced NPF is purely negative as expected for HIO_3 which has a very low proton affinity[20]. However, we were not able to quantify the importance of ion-induced compared to neutral NPF for our set of measurements. A list of the

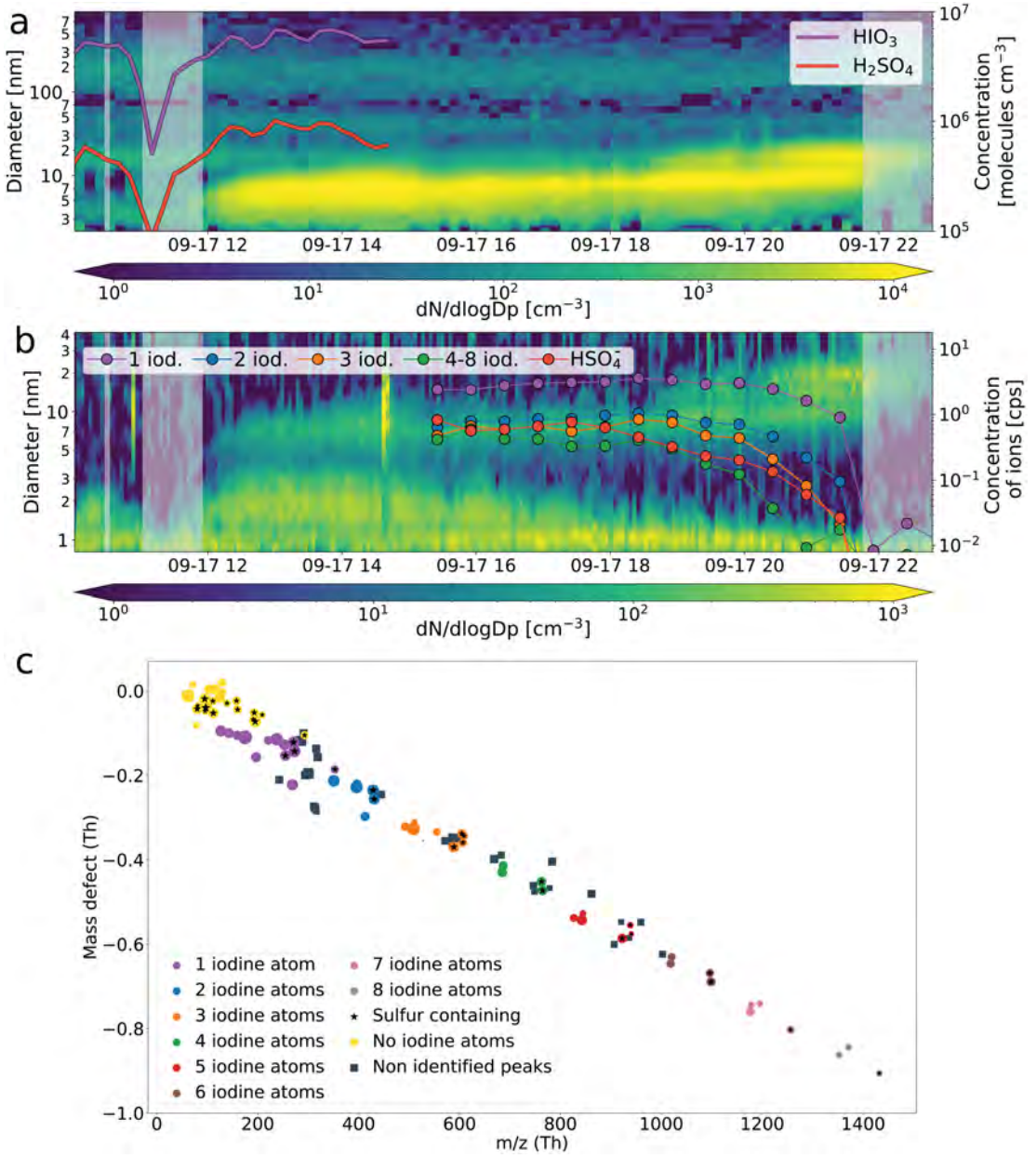

Figure 6.1: New particle formation mechanisms over the pack ice shown for 17 September 2018. **(a)** Evolution of particle size distribution; also shown are the iodic and sulfuric acid monomer concentration measured with a nitrate chemical ionization mass spectrometer. **(b)** Negative-ion size distribution from neutral cluster and air ion spectrometer measurements and naturally charged sulfuric acid and iodine clusters measured with the negative atmospheric pressure interface time of flight (APi-TOF) mass spectrometer. The legend indicates the number of iodine atoms per cluster where clusters with the same number of iodine atoms were summed up. The concentration is given in counts per second (cps). Grey shaded areas indicate periods with fog (here associated to a visibility below 2 km). **(c)** Mass defect plot of the negatively charged ions measured with the APi-TOF. The size of the markers is proportional to the logarithm of the concentration. The iodine clusters reported in the mass defect plot are the same as shown in the bottom panel of Fig. 1b. Squares indicate peaks for which it has not been possible to unambiguously identify their chemical composition, however their mass defect is compatible with iodine containing species.

events with the relative particle size distributions (PSD) and negative-ion spectra is reported in Methods section (Fig. S6.2).

6.3.2 Iodic acid sources, sinks, and variability

The 2-month time series of the HIO_3 concentration shows a clear and steady increase around the end of August (Fig. 6.2a), leading to an increase of the UFP concentration by more than one order of magnitude from summer (August) to autumn (September) (Fig. 6.2b). The covariation between HIO_3 and UFP (Fig. 6.2a) highlights the important role of HIO_3 and suggests that there were no other important sources of UFP over the pack ice during this period. The aggregated summer/autumn average comparison shows that sulfuric acid and methanesulfonic acid (MSA) are much less enhanced in autumn compared to HIO_3 (Fig. S6.3).

This clear regime change seems to be associated with a much weaker source of iodine during summer. Air mass back trajectories do not show a systematic difference in source region between summer and autumn (Fig. S6.4). The fact that high concentrations of HIO_3 were detected for several days continuously and over a large latitudinal range (from 89°N to 82°N approximately) points towards a pack ice-wide source rather than a local phenomenon. The transition from summer to autumn coincides with dropping temperatures and the start of the freeze-up period (sea ice formation). We identified the freeze onset as 28 August based on the running mean of the near-surface air temperature[312]. However, the freeze-up occurs over several days with multiple freezing and melting cycles. The near surface temperature dropped below zero around 13 August and then remained between -2 and 0°C for several days. This intermediate phase corresponds to a steady increase in the HIO_3 concentration. Between 27 and 28 August the near surface temperature shows a step decrease to below -2°C (Fig. 6.2b), which corresponds to the freeze-up onset and to the occurrence of the first NPF event. Previous studies have shown that iodine can be produced by microalgae below sea ice and transported via brine channels or cracks to the atmosphere[272,313]. Abiotic mechanisms can also release iodine from the snowpack and frozen saline surfaces via condensed phase reactions[314–318]. Concurrently with HIO_3 we also observed a marked increase of the ozone concentration (Fig. 6.2a), similar to measurements at Alert, in the Canadian Arctic[319]. A higher ozone concentration can enhance the emission of iodine from seawater and frozen saline surfaces[316,318,320], consistent with our observations. Therefore, we hypothesize that the increase in HIO_3 concentration and NPF frequency are linked to both, the formation of new sea ice and the increase in the ozone concentration. However, the individual contributions of these two processes cannot be disentangled with our set of measurements. Dedicated in situ measurements in the central Arctic Ocean are required to investigate these phenomena and precisely identify their contributions to the increased iodine emissions. Importantly, while at Arctic land-based observatories further south the occurrence of nucleation mode particles has generally been associated with biological activity in melting sea ice regions, primarily between May and August[307,321,322] NPF has so far never been associated with the freeze onset.

The HIO_3 concentration and the occurrence of NPF are regulated by local meteorology. In the central Arctic Ocean fogs and clouds are the dominant sink for these species since the low aerosol background concentration provides a very low condensation sink (CS) on the order of $10^{-5} - 10^{-4}$ s^{-1} (Fig. S6.5), more than one order of magnitude lower than most clean continental sites[92]. Because of the absence of any

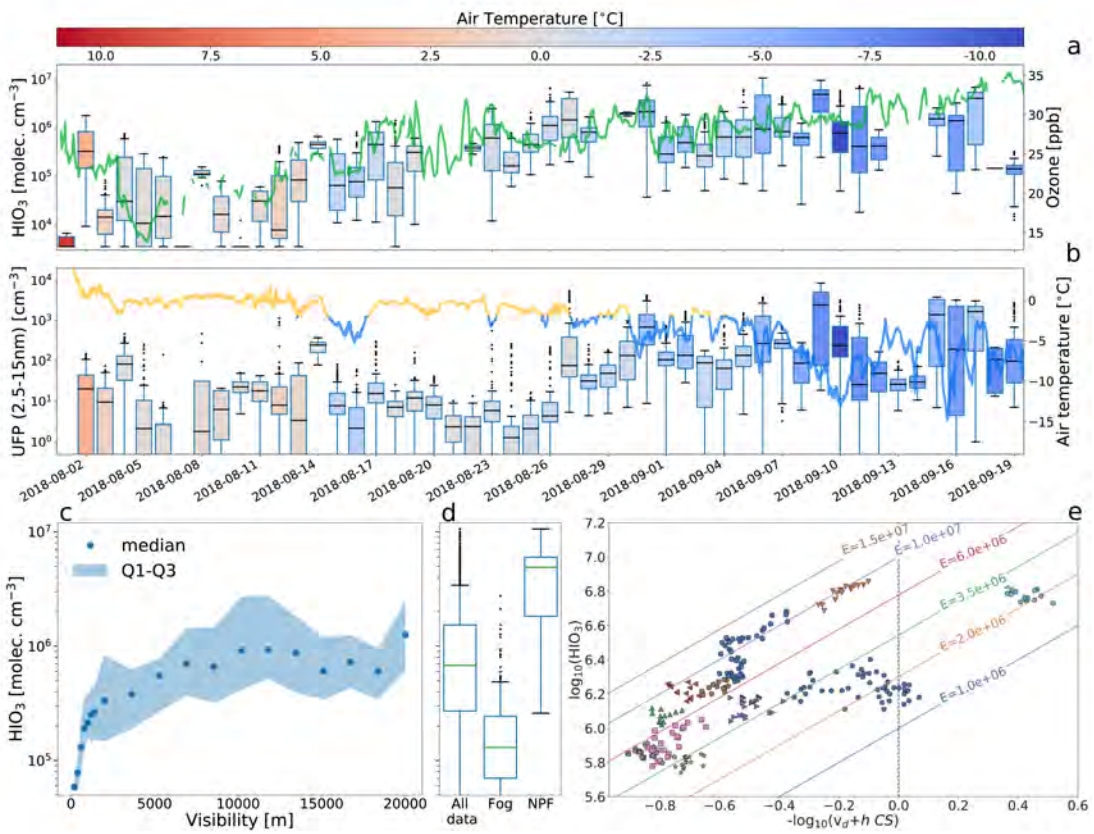

Figure 6.2: Factors controlling iodic acid concentration and NPF over the pack ice in the central Arctic Ocean. **(a)** Daily box and whiskers plot of iodic acid, where the box extends from the first quartile (Q1) to the third quartile (Q3) with a line indicating the median. The whiskers are set to $1.5 \cdot [Q3–Q1]$. The boxes are color-coded with the daily mean air temperature measured from the upper deck of the ship (roughly 25 m above sea level). The continuous green line shows the ozone concentration (axis on the right). **(b)** Daily box and whiskers plot of the ultrafine particle concentration (UFP), particles with a diameter between 2.5 and 15 nm. The continuous line shows the near-surface air temperature, with values lower than −2°C coloured in blue and above in yellow (axis on the right). **(c)** Iodic acid concentration during autumn as a function of visibility, dots indicate the median and the shaded area the interquartile range $[Q3–Q1]$. **(d)** Iodic acid concentration box and whiskers plot for different conditions during the autumn period. In particular, we report values for the entire autumn period, during fog (visibility below 2 km) and during NPF events. **(e)** Iodic acid data as a function of dry deposition velocity (v_d), boundary layer height (h) and condensation sink (CS). Iodic acid data correspond only to clear conditions (visibility > 4 km) and periods when steady-state conditions could be assumed. Eleven steady-state periods are given by differently coloured symbols. The coloured lines represent different emission rates (E) based on our model.

other important sink, a tenuous fog with visibility just below 4–5 km reduces HIO_3 enough to prevent NPF (Fig. 6.2c and d). During clear conditions the HIO_3 variability can be largely explained through the interplay of the surface mixed layer height (h), the CS and the dry deposition velocity of the gas (v_d). We have developed a simple model to combine these three factors and an emission rate (E in atoms $cm^{-2}s^{-1}$) of iodine that is assumed to be constant over the course of an event (details are given in

the Methods section). The concentration of HIO_3 at the steady-state can be described by

$$\log_{10}([HIO_3]) = \log_{10} E - \log_{10}(v_d + h \cdot CS). \tag{6.1}$$

The emission rate E is a net term that accounts for the emission of iodine from the surface and its conversion into HIO_3 which may occur via several intermediate reactions[20,268]. We have identified 11 periods satisfying a steady-state assumption. Figure 6.2e shows the dependence of HIO_3 on $(v_d + h \cdot CS)$ for each period with differently coloured symbols and expected linear trends by our model for different values of E. Data from each period was grouped around a given emission factor with some variability that probably reflects the simplicity of our model. Overall, the emission factor median and interquartile range (IQR) are equal to $5.0\ [3.2 - 7.6] \times 10^6$ iodine atoms $cm^{-2}s^{-1}$ with the full data distribution being shown in Figure S6.6.

In Figure S6.7, we show the fairly good agreement of a simulation of the HIO_3 concentration for a high and a low emission case scenario, corroborating our model and the underlying assumptions. Despite its simplicity, our model can explain a large fraction of the HIO_3 variability with emission rates ranging between 1.5 and 15.4×10^6 iodine atoms $cm^{-2}s^{-1}$ (two standard deviations of the mean).

This range is likely a lower limit estimate of the real emission rates as not all iodine atoms would be converted into HIO_3, however, it represents a valuable approach on which Earth system models could build to implement iodine NPF in the central Arctic Ocean.

6.3.3 Ultrafine particle growth and survival

This newly identified nucleation mechanism represents a massive source of aerosol particles for the central Arctic Ocean, which is usually characterized by extremely low aerosol concentrations[304,306]. For example, during this expedition, the median and IQR concentration of particles above 30 nm is 26 [10–48] cm^{-3} and the CCN concentration at 0.3% supersaturation (SS) is $17\ [6 - 33]\ cm^{-3}$ (Fig. S6.5). However, the relevance of NPF for the local cloud budget depends on the probability that newly formed particles grow to larger sizes where they can act as CCN.

The fate of newly formed particles is determined by their growth-to-loss rate ratio, with their growth being controlled by the concentration of condensable vapors and their loss by coagulation with other surfaces (*i.e.* pre-existing aerosol or fog droplets). Given the low particle concentration UFP are mainly lost through coagulation with fog droplets.

Typically, meteorological conditions are very variable as shown in Figure 6.3a. The measurement of the newly formed particles and their growth is rapidly interrupted, when the visibility drops below a few km. Fog in the central Arctic Ocean is characterized by a low number of droplets (usually below $30 - 50\ cm^{-3}$ during our campaign) due to CCN limitation. While the nucleating species with their high diffusivity rapidly disappear (Fig. 6.3b), UFP with a relatively long lifetime of $\simeq 2.5$ h for a 5 nm particle are not expected to disappear as fast as observed (Fig. S6.8). Our interpretation is that longer-lived patches of fog are advected to the observation point (the ship). Depending on the history of the foggy air mass, UFP may have been partially taken up by the fog droplets at the time of arrival or NPF was even inhibited because of the fast removal of HIO_3. This explanation is consistent with the fact that, after passage

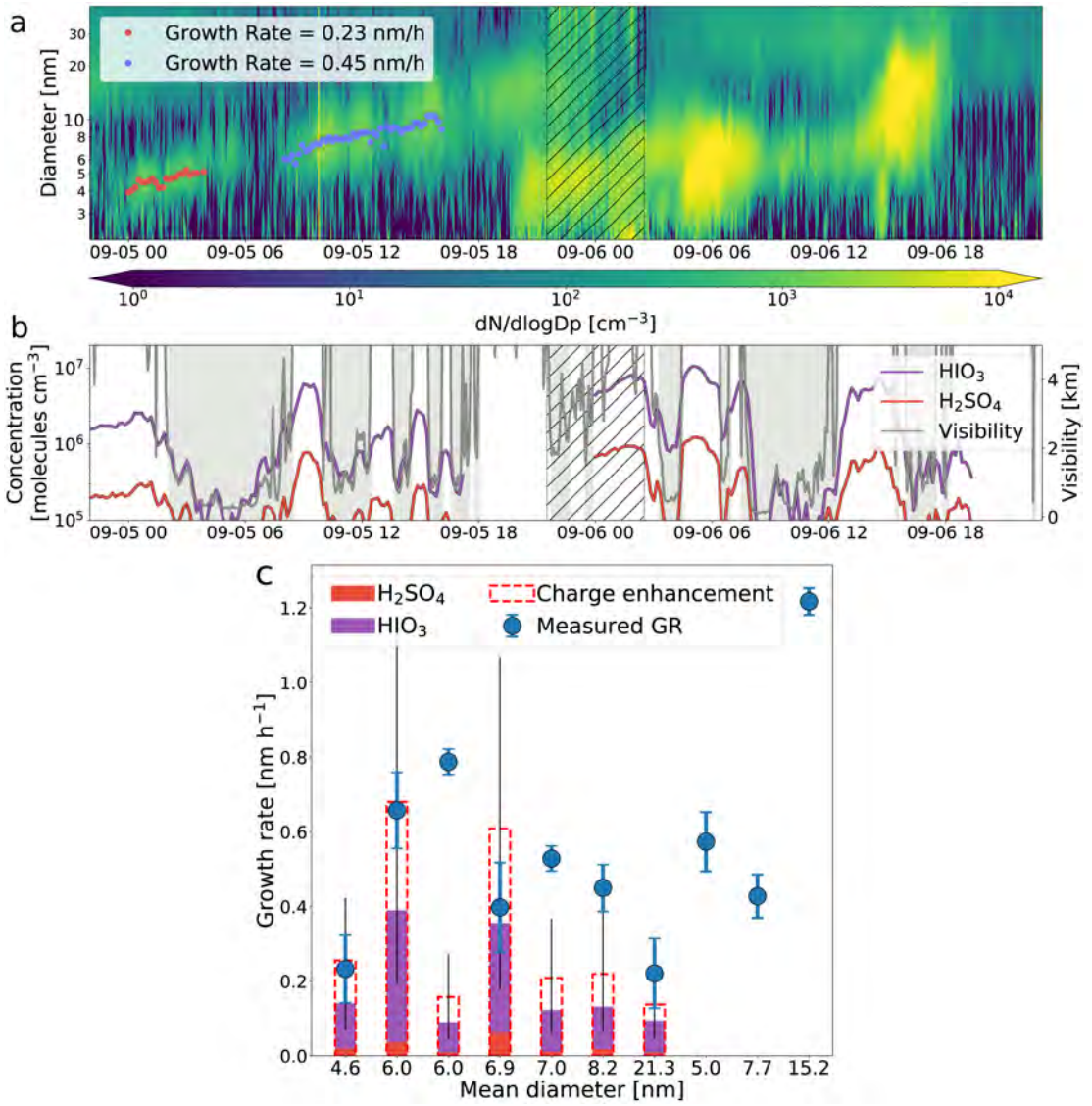

Figure 6.3: Ultrafine particle growth and losses. **(a)** Particle size distribution (PSD) measured with a neutral cluster and air ion spectrometer (NAIS) with the indication of the fitted mode diameter used for growth rate calculation. The black hatched region indicates a period influenced by pollution from the ship. **(b)** Concentrations of iodic and sulfuric acid together with visibility. Grey shaded areas indicate fog periods. **(c)** Growth rate (GR) measurements for the entire campaign as a function of the mean diameter mode during the event. The blue marker shows the measured growth rate obtained by fitting the mode diameter (the error bars represent the 95% confidence intervals from the fitted slope). The bar plot shows the estimated growth rate based on the mean mode diameter and the concentration of sulfuric and iodic acid[81]. The black lines are the error bars due to the uncertainty of sulfuric and iodic acid concentration. The red dashed bars show the predicted growth rate when considering also the charge enhancement factor (EF) derived from Stolzenburg *et al.*[60] Since for the last three events iodic and sulfuric acid measurements are not available, we report only the measured growth rates.

or dissipation of the fog, a UFP mode re-appeared, suggesting substantial continuity with the mode before the fog. This indicates that the fog is a spatially small-scale phenomenon, and that NPF was occurring on a larger scale with an estimated minimum air mass diameter of 160 km for this event (see Methods section). From the time trend of the PSD it is quite evident that the growing mode disappears and reappears at least

three times during this event as well as during the following event in association with fog patches.

Because of the long lifetime of UFP they can grow continuously for several hours reaching $15-20$ nm in size, despite the low growth rates that range between 0.2 and 1.2 nm h^{-1} with a median and IQR of $0.5\,[0.4-0.6]$ nm h^{-1} (Fig. 6.3c). Assuming kinetic condensation[81] we calculated the fraction of the growth attributable to iodic and sulfuric acid for all the events of the campaign with a clearly detectable growth (details in Methods section). In the majority of the cases more than 50% of the growth can be attributed to HIO_3 alone (Fig. 6.3c). Sub-10 nm aerosol growth can be enhanced by dipolar interactions[60,323] but the enhancement factor (EF) for HIO_3 is not known. By applying the sulfuric acid EF[60] most of the growth could be explained within uncertainty by HIO_3 alone (Fig. 6.3c). Moreover, we did not consider other iodine oxides that can partition into the particle phase[268] and contribute to the growth because we were not able to quantify their concentration. However, these compounds probably account for another fraction of the growth.

There are, however, two events (cases 3 and 5 in Fig. 6.2c) where only a small fraction of the growth could be explained. For these cases some other compounds must have contributed to the growth, most likely organics that were not oxygenated enough to be detectable with a nitrate CIMS[324]. While no gas phase measurement is available during the last event, the required HIO_3 concentration to explain such a large growth would be higher than any value measured during the campaign.

The more a newly formed particle grows the longer it survives (a 30 nm particle has a 10 times longer lifetime compared to a 10 nm particle) and the more likely it is that it can act as CCN. In summary, HIO_3 is not only vital for the formation of new particles above the pack ice but also for their growth and hence for their survival.

6.3.4 NPF contribution to the CCN budget

Since the growth rate of newly formed particles is generally below 1 nm h^{-1} it takes them several hours to days to reach a size where they can act as CCN (*e.g.* 30 nm at 1% SS[107]). However, the variability of fog occurrence and the frequent air mass and weather changes reduce the probability of observing the same aerosol population growing up to CCN size[325].

Low-level clouds in the Arctic are generally characterized by an SS of 0.3% which would not be sufficient to activate $20-40$ nm particles[66]. However, it has been indirectly shown that droplets often form on particles smaller than 50 nm[66,326]. We provide here direct evidence that particles in the $20-40$ nm size range activate as CCN in Arctic fog when the concentration of larger aerosols is low enough; this suggests that iodine NPF may be a relevant CCN source in the region.

One example is the activation of Aitken mode particles on 6 September (Fig. 6.4), the second part of the event described in Figure 6.3. We compare the properties of the dry PSD with measurements of cloud particle residuals obtained with a counter-flow virtual impactor (CVI) inlet. Figure 6.4a shows the PSD of the entire aerosol population with diameters D from 2 to 900 nm, overlaid with the particle concentrations in two different size ranges (37 <D< 70 nm and 70 <D< 900 nm), the concentration of cloud residuals, and the visibility. During the fog period from 08:00 to about 12:00, the accumulation mode particle concentration dropped below 1 cm^{-3} after 09:00. This is a clear indication that smaller particles act as CCN to sustain the fog. The residual number concentration matches the integrated aerosol concentration with diameters

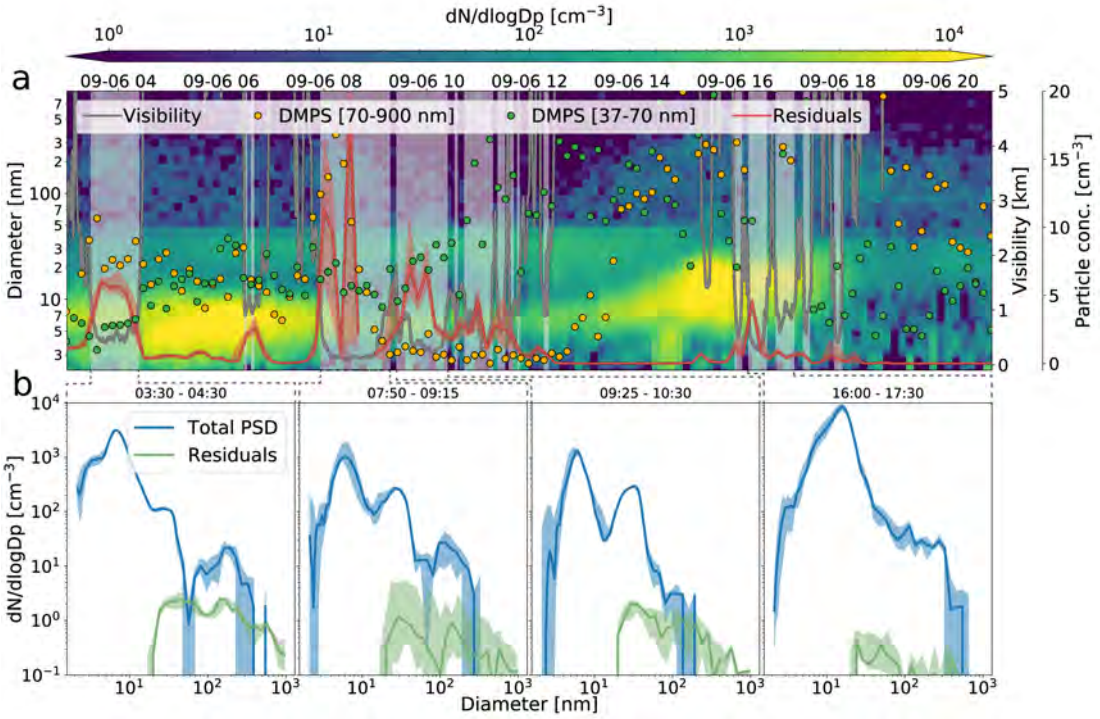

Figure 6.4: Activation of Aitken mode particles in fog. **(a)** Particle size distribution, visibility, particle concentrations in two different size ranges (37-70 and 70-900 nm, representing the larger tail of the Aitken mode and the accumulation mode, respectively) and the total droplet residual concentration (the solid line is the 10-min median and the shaded area the interquartile range, IQR). Grey shaded areas indicate fog periods. **(b)** Median (solid line) and IQR (shaded area) particle and residual size distribution for the four different fog periods during the event. The cloud residuals distribution is based on measurements with a differential mobility particle sizer (DMPS) behind a counter flow virtual impactor inlet.

above $37 - 44$ nm (the size of a diameter size bin), providing an upper limit estimate on the activation diameter. The real activation diameter is likely smaller given that this CVI only sampled droplets larger than 7.8 μm and a fraction of the droplets was persistently smaller than this threshold (Fig. S6.8). Based on the CCN and size distribution measurements for this event (Fig. S6.9) we estimate that an SS close to 1% is required to activate particles in this size range. It is conceivable that such high SS can occur due to the small total number of droplets such that excess water vapour is not depleted as quickly as in more accumulation mode-rich environments.

The activation of small Aitken mode particles is directly evident from the residual size distribution measured with a DMPS behind the CVI. Figure 6.4b shows the average residual size distributions for four different fog periods during the same day, and, as a reference, the corresponding average size distributions of the total aerosol population. In all four cases, there is a clear and consistent presence of Aitken mode particles in the cloud residuals smaller than 30 nm.

It is important to note that iodine NPF is not the only source contributing to the total Aitken mode aerosol population over the pack ice. Long-range transport of secondary particles formed in more biologically productive regions, such as the MIZ, may also be an important source[306]. As such, there is a clear need for dedicated studies on the sources of Aitken mode particles and their role for the Arctic CCN budget to quantitatively assess the importance of this newly identified NPF mechanism.

The source of NPF over the pack ice in the central Arctic Ocean has been elusive for almost 30 years. This study provides direct molecular evidence that iodine is the driver of NPF in August and September over the central Arctic Ocean while we find no evidence that UFP were produced by a primary mechanism as previously hypothesized[75]. We also show for the first time that the HIO_3 concentration over the pack ice increases steadily towards the end of August. We hypothesize that this trend is related to the formation of new sea ice and to the increase of boundary layer ozone. This is in line with observations at Alert, Canada, between 1980 and 2006, where, during autumn, higher ozone concentrations and a second peak of iodine in the aerosol was found (the first being in spring)[319,327]. Their seasonality of the iodine concentrations is remarkably similar to our HIO_3 trend indicating that our observations are not unique to the 2018 season (Fig. S6.10).

6.4 METHODS

TERMINOLOGY NOTE The beginning of the autumn season in the Arctic is generally associated with colder temperature and the formation of new sea ice, in contrast to the summer melt season[328]. For this reason and to be clear, in our work, we consistently refer to these two periods as summer and autumn. However, because our measurements cover August and September specifically, our findings are representative of the summer to autumn transition and cannot be directly extrapolated to the full Arctic summer and autumn seasons.

CAMPAIGN DESCRIPTION Data were collected during the MOCCHA campaign as part of the US-Swedish expedition Arctic Ocean 2018 on board the Swedish I/B *Oden* in August and September 2018 with more than 4 weeks of ice-drift operation at latitudes higher than 88°N (Fig. S6.1).

INSTRUMENTATION AND MEASUREMENTS Aerosol and cloud-related measurements were conducted on the 4th deck of I/B *Oden* inside two different containers. Three different inlets were used for this study, a NPF inlet designed to minimize diffusional losses with a short residence time, a whole air inlet sampling the entire aerosol population (interstitial and activated) and a CVI inlet sampling only cloud droplets and ice crystals larger than 7.8 μm (more details are provided below).

HIO_3, sulfuric acid, and MSA were measured using a nitrate chemical ionization mass spectrometer[125]. These molecules are detected both as deprotonated species and clustered with the nitrate monomer. The instrument was calibrated after the campaign for sulfuric acid as described in Kürten *et al.*[96], the same calibration constant was assumed also for HIO_3 and MSA. This assumption is motivated by the fact that these three molecules have a lower proton affinity compared to nitric acid and the ionization proceeds at the kinetic limit. Diffusion losses in the inlet were corrected using the diffusion constant of sulfuric acid[93]. The uncertainty in the determination of these compounds in well-controlled experiments is usually estimated to be $-30\%/+50\%$[60]. However, it is common to extend the uncertainty to $-30\%/+50\%$ for field measurements in order to account for the intrinsic variability of field conditions that cannot be quantified. We decided to use the larger uncertainty although it is likely to be an overestimation. Mass spectrometry data were integrated for 10 min, the corresponding lower limit of detection (LOD) based on three standard deviations of the background

noise was estimated to be lower than 5×10^3 molecule cm^{-3}; for the statistical analysis presented in Figure S6.2, values below the LOD were replaced by LOD/$\sqrt{2}$[329]. For a detailed description of the instrument, see Jokinen *et al.*[87], and for a detailed analysis of HIO_3 detection with a nitrate CIMS the reader is referred to Sipilä *et al.*[20]

The chemical composition of naturally charged negative ions was measured with an APi-TOF, this is the same mass spectrometer described before but without a chemical ionization unit. For a description of the instrument see Junninen *et al.*[86]. The absolute transmission of the APi-TOF was not characterized, therefore measurements are reported in counts per second (cps) and cannot be converted into atmospheric concentrations.

The size distribution of ions and particles below 40 nm was measured with a NAIS[126]. The aerosol size distribution was measured with a scanning mobility particle sizer, range $18 - 660$ nm, and with a differential mobility particle sizer (DMPS), range $10 - 959$ nm, both instruments were custom made[123,127]. A TSI condensation particle counter (CPC) 3776 and a particle size magnifier (PSM) were used to measure the total particle concentration above 2.5 nm. The PSM was not able to measure particles below 2.5 nm because of issues with the saturator flow but overall it compared very well with the UCPC[128]. The UFP time series in Figure S6.2b was obtained by combining measurements from both the CPC3776 and the PSM[131]. The particle size distribution shown in Figure S6.4a was obtained combining measurements from the NAIS and the DMPS[129]. A comparison of the NAIS with the DMPS and the UCPC data is reported in Supplementary note 6.7.

Cloud residuals were sampled using a ground-based counterflow virtual impactor (CVI) inlet. The working principles of the CVI inlet are described in detail in Shingler *et al.*[109]. The ground-based version uses a wind tunnel to accelerate air onto the tip of the inlet, where the counterflow prevents non-activated aerosol (particles with low inertia) from entering the sample flow but allows cloud droplets and ice crystals pass through. The droplet/crystal cut size depends on the flow rates in the inlet, and was around 7.8 μm (aerodynamic diameter) with our set-up. The geometry of the CVI inlet and the difference between the wind tunnel airspeed and the sample flow rate result in the sample volume being enriched in cloud particles compared to the ambient air. Concentrations measured behind the CVI inlet therefore have to be divided by an enrichment factor, which can be calculated from the aforementioned parameters (see Shingler *et al.*[109]). The enrichment factor was around 6.5 during the Arctic Ocean 2018 campaign. The cloud residual size distributions were not corrected for the droplet sampling efficiency of the CVI inlet, since the forward scattering spectrometer probe (FSSP) was not working for the event discussed in this paper. Cloud residual concentrations and number size distributions were measured with a TSI CPC3772 and a custom made DMPS in the size range $17 - 959$ nm.

CCN measurements were performed using a commercial DMT CCN counter scanning at five different SSs (0.1%, 0.2%, 0.3%, 0.5%, and 1.0%)[330].

All particle number measurements were corrected for diffusion and impaction losses using either the particle loss calculator[331] or user-made scripts based on the same equations.

Ozone measurements were performed using a model 205 ozone monitor from 2B Technologies[133]. The instrument was calibrated after the campaign and the data were corrected for a baseline drift based on zero measurements before and after the expedition. The overall accuracy of the instrument is estimated to be within 5% of the reading.

All gas and aerosol measurements were cleaned from ship pollution using an algorithm based on the derivative of the ultrafine particle concentration, the PSD, CO_2, black carbon measurements as well as wind direction[132].

The surface mixed layer height was estimated from the temperature profile measured from radiosondes which were launched every 6 h[121]. The surface inversion was calculated according to the algorithm from Tjernström *et al.*[332]. Data were linearly interpolated between each radiosonde. We adjusted the surface mixed layer height at noon on 17 September based on an inspection of the temperature profile that revealed a first inversion at 90 m. The algorithm did not identify this inversion because the temperature was not monotonically increasing.

The dry deposition velocity can be calculated as the inverse of the sum of the aerodynamic, the quasi-laminar and the canopy resistance[1]. We assumed a neutral boundary layer to calculate the aerodynamic resistance and used the sulfuric acid diffusion coefficient to calculate the quasi-laminar resistance. The canopy resistance over snow surfaces is generally assumed to be equal to zero[1]; hence, we did not consider it. Both the aerodynamic and the quasi-laminar resistance depends on the inverse of the friction velocity which can be calculated from wind speed[1]. Using the wind speed measurements from the ship, we have derived a dry deposition velocity time series whose median and IQR are 0.67 $[0.39 - 0.96]$ cm s^{-1}. These values are comparable to the nitric acid dry deposition velocity measured in Svalbard[333].

The 10-day backward trajectories were calculated by Heini Wernli (ETH Zürich, Switzerland) using the Lagrangian analysis tool LAGRANTO and wind fields from 3-hourly operational ECMWF analyses, interpolated to a regular grid with 0.5° horizontal resolution on the 137 model levels[185].

The meteorological data were collected from a weather station installed on the 7th deck of the I/B *Oden* at $\simeq$ 25 m above sea level[122].

The majority of the data were processed using Python and in particular Scipy, Pandas, and Numpy libraries[334–336] the raw mass spectrometer data were treated using Matlab and the TofTool library[86]. All the plots were produced using Matplotlib[337].

NPF EVENTS We identified 11 NPF events during our campaign, four of which were reported already in the main text (one event in Fig. 6.1a and three events in Fig. 6.3a). The remaining events are shown in Figure S6.2 by means of the corresponding particle and negative-ion size distribution. When available the sulfuric and HIO_3 concentration is also reported. Different events are marked with a Roman numeral. We excluded from this list two events that were heavily influenced by pollution (on 12 and 26 August) and another event that occurred at the beginning of the campaign while we were still in the marginal ice zone. We used a different color map (*i.e.* magma instead of viridis) to highlight periods that were potentially influenced by the ship pollution for more than 10 min. Shorter pollution periods were not included because these are spikes associated with short events (*e.g.* a helicopter flight) that do not affect the overall aerosol population.

SEASONAL VARIATION AND BACKGROUND AEROSOL CONCENTRATION We report seasonal variations of the three major acids, *i.e.* sulfuric acid, HIO_3, and MSA, detected with the nitrate CIMS in Figure S6.3 We used 27 August as the dividing date between summer and autumn based on the start of the freeze-up period as explained in the main text. All the three compounds show higher concentrations during autumn compared to summer, however, HIO_3 is characterized by the largest increase in both relat-

ive and absolute terms. The iodic acid median concentration is more than five times higher in autumn compared to summer, whereas sulfuric acid and MSA show less than a twofold increase. The same figure illustrates also the seasonal increase in the concentration of UFP particles, whose median concentration is 12 times higher in autumn compared to summer.

Although the sulfuric acid concentration is much lower compared to HIO_3 these two species are correlated on the short-term scale (see for example, Fig. 6.3b). This correlation is explained by the very short lifetime of these two acids whose concentration is largely controlled by changes in the sinks (*i.e.* fog or particle condensation as explained in the Iodic acid sources, sinks and variability section).

We have analysed back-trajectories to investigate whether the seasonal change could be related to a different air mass source regions. However, there is no evidence for a systematic shift in the air mass origin as shown in Figure S6.4. We considered only trajectories in the boundary layer for 5 days before arriving at the ship position.

The extremely low aerosol background concentration is shown in Figure S6.5 as a box and whiskers plot for concentrations of particles with a diameter larger than 30 nm, CCN concentrations at 0.3% SS and the sulfuric acid CS[130].

IODIC ACID MODEL We assume that HIO_3 is entirely produced by iodine that is emitted as I_2 to the atmosphere at a rate E^* [molecule $cm^{-2}s^{-1}$] and photolysed at a rate J [s^{-1}]:

$$\frac{dI_2}{dt} = \frac{E^*}{h} - J[I_2] = 0, \tag{6.2}$$

$$[I_2] = \frac{E^*/h}{J}, \tag{6.3}$$

with h being the height of the surface mixed layer. The HIO_3 concentration can be described by

$$\frac{d[HIO_3]}{dt} = 2J[I_2] - \frac{v_d}{h}[HIO_3] - CS[HIO_3] = \frac{E}{h} - \left(\frac{v_d}{h} - CS\right)[HIO_3], \tag{6.4}$$

with $E = 2E^*$ being the emission rate in terms of iodine atoms cm^{-2} s^{-1}. In a steady state, this equation reduces to:

$$[HIO_3] = \frac{E}{v_d + h \cdot CS} \rightarrow \log_{10}([HIO_3]) = \log_{10} E - \log_{10}(v_d + h \cdot CS) \tag{6.5}$$

From Eq.6.5 it follows that, for a given emission factor E, the logarithm of the HIO_3 concentration should vary linearly with the logarithm of $-(v_d + h \cdot CS)$ with a unity slope. Equation 6.5 can be used to infer the emission factor E for periods of data where the steady-state assumption holds. We identified periods of steady state by looking at the derivatives of both the HIO_3 and the $(v_d + h \cdot CS)$ signals over their respective time series and considered only those periods where the derivative to signal ratio was below 5% for both. An exception was made when only one or two data points were exceeding the 5% threshold. We only considered periods longer than 90 min in order to obtain enough data. Before calculating the derivative we smoothed the data with a one-hour running average and a hamming type window to reduce instrumental noise that would be amplified by the derivative calculation. With this approach, we

identified 11 steady-state periods as shown in Figure 6.2e. We estimated the emission factor of each individual data point[21] of these periods following Eq.6.5 and show the distribution of these values in Figure S6.6.

Another way to investigate the applicability of this model to our dataset is to integrate numerically Eq.6.4 and simulate the evolution of HIO_3. The model does not include losses of HIO_3 to cloud droplets and so HIO_3 could be simulated only for periods without fog. In Figure S6.7 we report the simulation results for two periods corresponding to two different emission rate scenarios. We have used a simple Euler integration method to simulate the HIO_3 evolution and initialized it with the mean HIO_3 concentration in the first hour. The simulation was run with three different emission factors to highlight the sensitivity of the result on the emission.

In the first simulation, the model is able to reproduce the measurements fairly well and starts deviating from its initialization only after about 14 h (around 12:00). As expected, it does not reproduce the rapid decrease of HIO_3 due to scavenging in fog after 13:00. In the second simulation, the model captures the overall trend but the discrepancy with the measurements is higher. There is, for example, a rapid change in the HIO_3 concentration after 06:00 which is not captured by the model. This is probably due to a sudden change in the air mass (see also the PSD of event V in Fig. S6.2).

The model incorporates the iodine emission and its conversion into HIO_3 into this E factor. Because the HIO_3 production pathways is still not fully understood[268], it is not possible to estimate a real iodine flux based on our measurements. Moreover, E represents a lower limit estimate of the real iodine flux given that only a fraction of the emitted iodine atoms would be converted to HIO_3. However, the E factor range (Fig. S6.6) provided in this study could be directly used by atmospheric models to simulate the HIO_3 concentration over the pack ice and estimate its role in terms of NPF.

FOG SCAVENGING Given the extremely low aerosol background the main sink for UFP over the central Arctic Ocean is scavenging by coagulation in fog and cloud droplets. In a mid-latitude non-precipitating cloud the lifetime of a 10-nm particle would be about 11 min[1]. However, Arctic clouds are typically characterized by a lower droplet number because of the CCN limitation and this has an effect on the UFP lifetime. Hence, we have calculated the aerosol lifetime starting from the average droplet size distribution measured using an FSSP during MOCCHA[124]. We included all data until 5 September as the instrument broke down afterwards. In Figure S6.8b we show the corresponding median and IQR droplet number size distribution. In Figure S6.8a we report the estimated lifetime of an interstitial aerosol particle as a function of its size (only losses due to coagulation into fog droplets are included). In this case the lifetime of a 10-nm particle would be about 10 h. The difference in lifetime for a representative Arctic and mid-latitude cloud is striking but consistent with the large difference in droplet number concentration (generally < 30 cm^{-3} in the central Arctic Ocean and about 1000 cm^{-3} in a mid-latitude cloud[1]. In the same figure, we highlight the lifetime of HIO_3, considered as a 0.5-nm particle, which is around 2 min. The diameter is calculated using HIO_3 bulk properties, i.e. density and mass. This value is consistent with the HIO_3 decay time in fog and is much lower compared to a situation where the lifetime was controlled by condensation on pre-existing aerosol only (Fig. S6.5).

SPATIAL EXTENT OF NPF EVENTS A simple estimate for the spatial extent of an NPF event can be calculated assuming a homogeneous air mass over the entire event duration:

$$L = W_s \Delta t, \tag{6.6}$$

with Δt being the duration of the event, W_s the mean wind speed during the event, and L the air mass diameter. This is a lower limit estimate because it is based on the assumption that the measurement location was sitting at the edge of the air mass at the beginning of the event. Applying such a calculation to the NPF event of 5 September leads to an areal diameter of about 160 km.

GROWTH RATE CALCULATION AND MODELLING We calculated the growth rate using the mode diameter fitting procedure. The data obtained from the NAIS were averaged to 10 min and the PSD was fitted with a multi-modal lognormal distribution. Other methods such as the appearance time-based calculation did not work reliably due to air mass inhomogeneity which produced fluctuations in the particle number concentration[338]. The growth rate was calculated only for those periods showing a continuous growth for at least 2 h excluding periods influenced by fog, clear air mass changes or the ship exhaust. For example we did not calculate a growth rate for the 6 September event (Fig. 6.3a) because a mix of pollution, fog, and air mass inhomogeneity impeded the identification of a clearly growing mode.

We used a hard-sphere model based on kinetic condensation to estimate the contributions by sulfuric and HIO_3 to the growth[81]. This model requires knowledge of the condensing vapor volumes which can be inferred from their bulk-phase densities. However, the molecular volume depends on the degree of hydration, which in principle is not known because it is not measured directly by the mass spectrometer. Considering that the median and [IQR] of the relative humidity during MOCCHA were 95.7% and $[90.8 - 98.4]$%, the degree of hydration is expected to be high and should not be neglected. Quantum chemical calculations for sulfuric acid predict each molecule to be prevalently bound to three water molecules at 80% RH, therefore we took this value as a lower limit estimate and calculated the sulfuric acid-water solution density accordingly[82,83]. Concerning HIO_3, there are no studies reporting the hydrate distribution at ambient relevant RH. Khanniche *et al.*[339] showed that HIO_3 forms stable hydrates with up to two water molecules but did not investigate larger hydrates. It has also been suggested that the iodate dimer ($HIO_3IO_3^-$) is hydrated with up to 5 water molecules at 65% RH[340]. Therefore, we assumed the HIO_3 monomer to be prevalently bound to three water molecules and estimated its volume based on bulk-phase density measurements[341]. This is in analogy with the sulfuric acid case and reasonable given the high RH values experienced during MOCCHA. Finally, the mass diameter was converted into a mobility diameter adding 0.3 nm as suggested by Larriba *et al.*[342]

The sulfuric acid growth rate EF was derived from Stolzenburg *et al.*[60] and applied also to the HIO_3 growth. This EF is based on a mechanism driven by van-der-Waals forces between UFP and neutral molecules and depends on the condensing species. HIO_3 will certainly have a different EF compared to sulfuric acid, however this value is not known and the two molecules share similar properties (*e.g.* dipole moment), therefore, we expect the final EF to be similar.

CRITICAL DIAMETER CALCULATIONS In Figure S6.9 we report critical diameter calculations at three different SSs (0.2%, 0.3%, and 1.0%) based on CCN measurements. The critical diameter is calculated assuming an internally mixed aerosol population and integrating the particle number concentration downward from the largest diameter of the aerosol number size distribution[107]. It is important to note the period from 09:00 until 12:00 which is characterized by fog without accumulation mode particles (see Fig. 6.4 in main text). The comparison between the cloud residual number concentration and the dry aerosol distribution suggests that particles with a diameter as small as 37 nm were activating. This value is consistent with the critical diameter at 1% SS.

COMPARISON WITH AEROSOL IODINE CONCENTRATION AT ALERT An increase in the concentration of iodine in autumn based on aerosol measurements was shown for the first time by Sirois *et al.*[327] more than 20 years ago. More recently, Sharma *et al.*[319] extended the analysis up to 2006 confirming the existence of an iodine autumn peak. Their data are based on instrumental neutron activation analysis (INAA) of aerosol filters collected at Alert, Canada (82.5°N 62.3°W) by the Canadian Aerosol Baseline Measurement (CABM) Network, Climate Research Division, Environment and Climate Change Canada from 1981 until 2006. In Figure S6.10 we compare weekly mean HIO_3 absolute concentrations in the gas phase from our measurements and iodine in the aerosol phase from Sharma *et al.*[319] The agreement between these two datasets is remarkable considering that they are from two locations about 900 km apart, from different decades and obtained with different measurement techniques. Besides the similar time trends only a few hours of condensation of the available HIO_3 on pre-existing particles is required to reach the observed concentrations of iodine in the aerosol at Alert. The key message is that our observations are not limited to a single year and specific location in the Arctic but have likely been observed over multiple decades and are representative for the high Arctic.

Sharma *et al.*[319] also showed that the aerosol iodine autumn concentration did not vary significantly from 1981 to 2006, indicating that the iodine emission rate has been relatively stable for the last few decades. This observation is different from recent results that reported almost a doubling of the atmospheric iodine concentration from 1980 to 2010 in the North Atlantic[343]. It is not the scope of this work to investigate the differences between these two previous studies, however, considering the similarities of our results with those reported in Sharma *et al.*[319] it seems likely that the autumn iodine emissions in the central Arctic Ocean did not change significantly during the past few decades.

6.5 DATA AVAILABILITY

All datasets used in this paper are referenced in the text[21,121–133] and publically available on the Bolin Centre database:

- Iodic acid, sulfuric acid and methanesulfonic acid collected during the Arctic Ocean 2018 expedition (DOI:10.17043/ao2018-aerosol-cims).

- Size distribution of neutral and charged particles smaller than 42 nm collected during the Arctic Ocean 2018 expedition (DOI:10.17043/ao2018-aerosol-nais).

- Size distribution of interstitial and total particles between 18 and 660 nm collected during the Arctic Ocean 2018 expedition (DOI:10.17043/ao2018-aerosol-smps).
- Aerosol particle number size distribution data collected during the Arctic Ocean 2018 expedition (DOI:10.17043/ao2018-aerosol-dmps).
- Concentration of particles larger than 2.5 nm collected during the Arctic Ocean 2018 expedition (DOI:10.17043/ao2018-aerosol-ucpc).
- Ultrafine particle concentration measured during the Arctic Ocean 2018 expedition (DOI:10.17043/ao2018-aerosol-ufp).
- Size distribution of aerosol particles between 2.5 and 920 nm measured during the Arctic Ocean 2018 expedition (DOI:10.17043/ao2018-aerosol-merged-psd).
- Ozone concentration measured during the Arctic Ocean 2018 expedition (DOI:10.17043/ao2018-aerosol-ozone).
- Mask to identify polluted periods during the Arctic Ocean 2018 expedition (DOI:10.17043/ao2018-aerosol-pollution-mask).
- Radiosonde data from the Arctic Ocean 2018 expedition (DOI:10.17043/ao2018-radiosonde-2).
- Weather data from MISU weather station during the Arctic Ocean 2018 expedition (DOI:10.17043/ao2018-misu-weather-2).
- Sulfuric acid condensation sink calculated for the Arctic Ocean 2018 expedition (DOI:10.17043/ao2018-aerosol-condensation-sink).
- Aerosol and droplet size distributions and concentrations measured during the Arctic Ocean 2018 expedition (DOI:10.17043/ao2018-aerosol-fssp).

The ancillary data required to reproduce some of the analysis and figures presented in this work (*e.g.* the iodic acid model) were also submitted as an individual dataset: Frequent new particle formation over the high Arctic pack ice by enhanced iodine emissions during Arctic Ocean 2018 expedition (DOI:10.17043/baccarini-2020-new-particle-formation).

6.6 CODE AVAILABILITY

The scripts used to analyze the data and produce the plots of the paper are available on GitHub.

6.7 SUPPLEMENTARY INFORMATION

Supplementary Figures

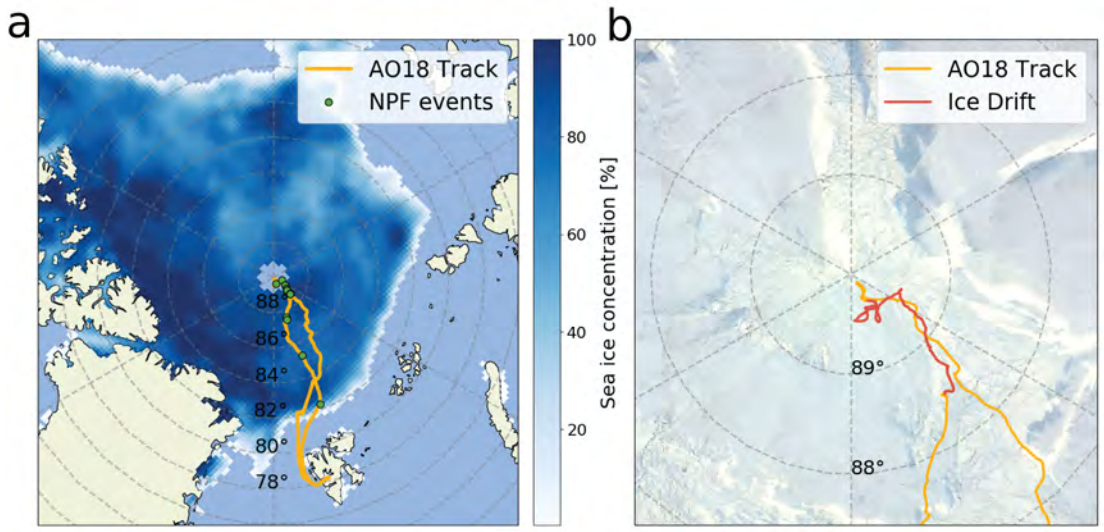

Figure S6.1: Map of the expedition track. **(a)** The track is shown in yellow, green markers indicate the position of new particle formation events. The underlying map is based on a Natural Earth map. We report in blue the sea ice concentration (fraction of covered surface)[77]. Sea ice data were retrieved for 15 September 2018. **(b)** Map enlargement showing the track during the ice drift period in red. The underlying image is a corrected reflectance image from MODIS Terra[344], retrieved for the 10 of September 2018.

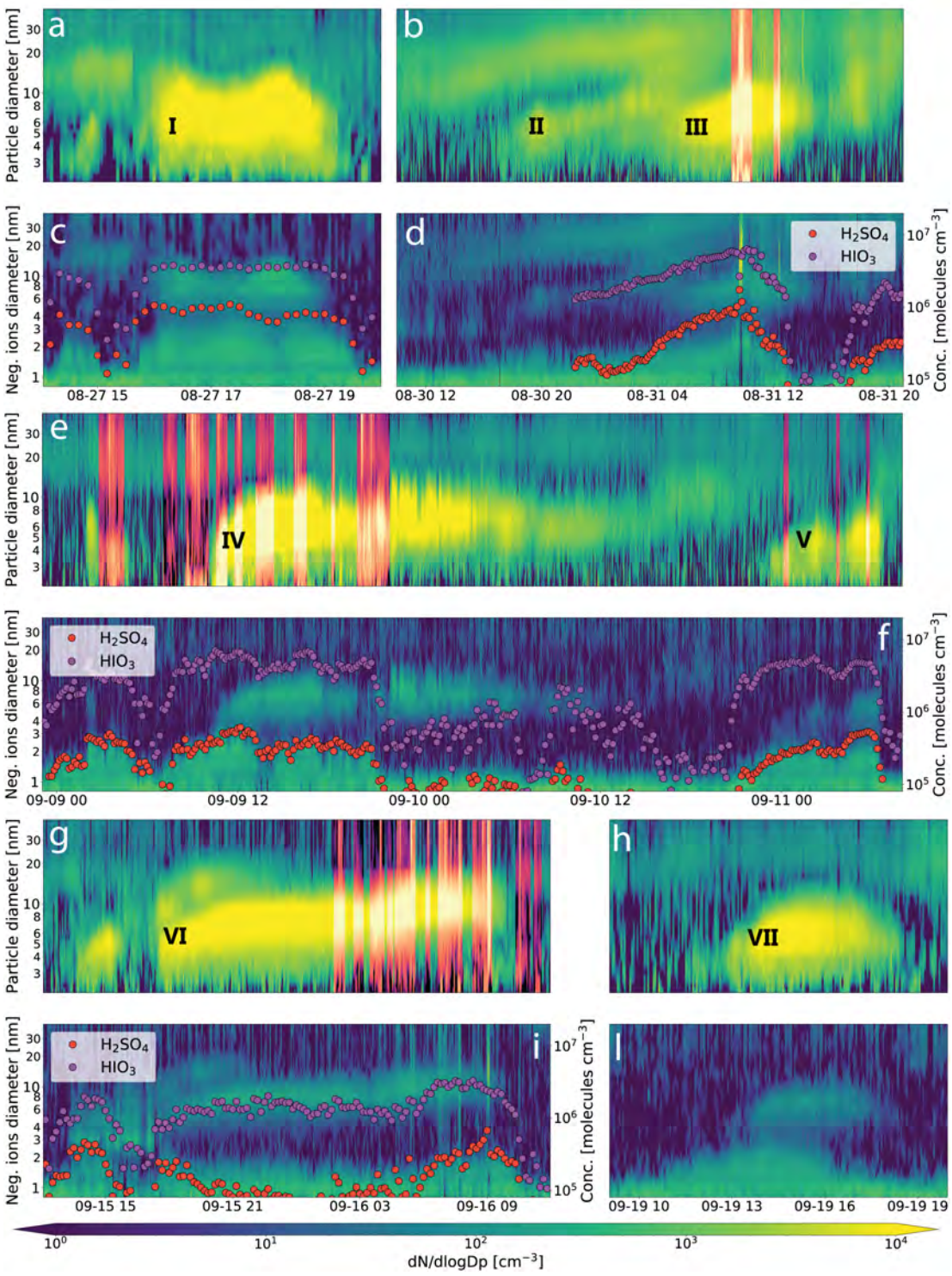

Figure S6.2: New particle formation events during the Arctic Ocean 2018 expedition. Neutral and negative ion size distribution are on odd and even rows, respectively. Different events are marked with a Roman numeral. The sulfuric and iodic acid concentrations are reported when available on the y-axis on the right side of the plot. Periods with suspected pollution are highlighted with a different colour map (magma instead of viridis) in the neutral PSD plots.

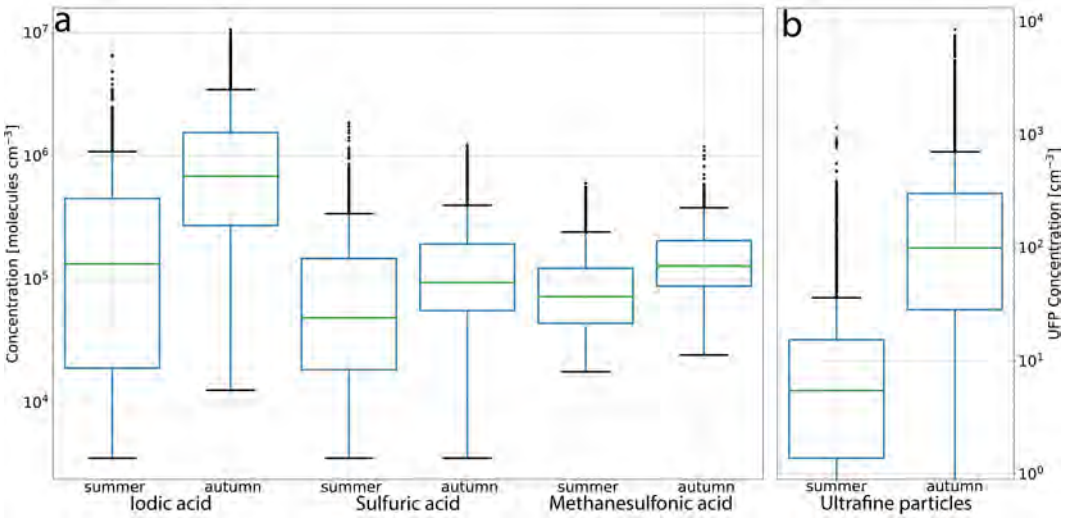

Figure S6.3: Summer to autumn transition. **a** Box and whiskers plot of iodic acid, sulfuric acid, methanesulfonic acid and **b** ultrafine particle concentration (UFP). All data were cleaned from ship exhaust influence. Iodic acid and UFP concentration data are the same as in the main text 6.2.

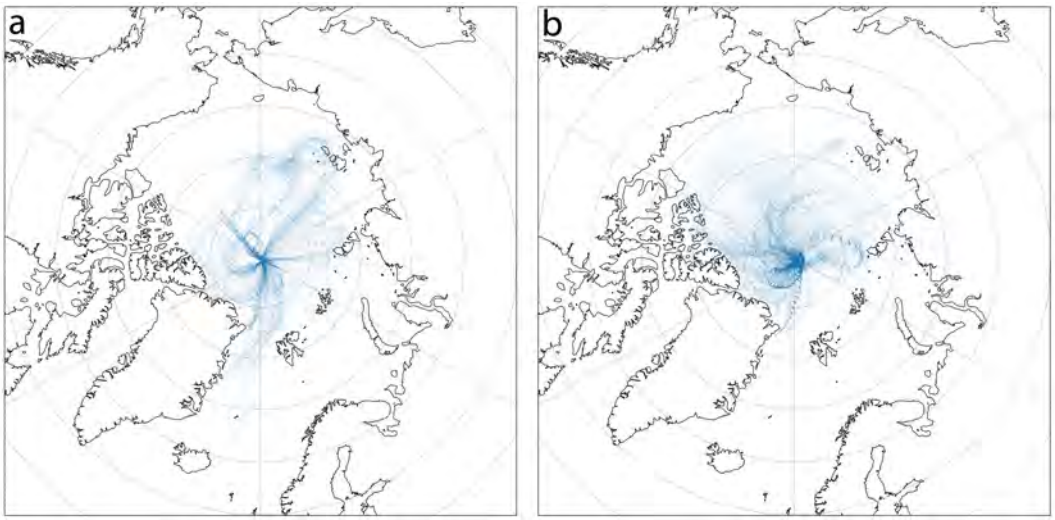

Figure S6.4: Air mass back trajectories. 5-day boundary layer back-trajectories released from the ship location for summer (panel a) and autumn (panel b). Only the ice drift period was included in this analysis. The darkness of points in the figures is proportional to the number of trajectories that passed over that area. The underlying map is based on a Natural Earth map

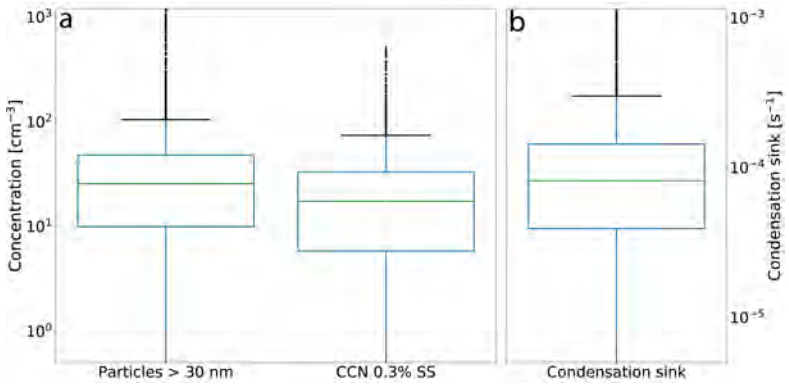

Figure S6.5: Background aerosol concentration. **a** Box and whiskers plot for the aerosol concentration above 30 nm (obtained from integration of the DMPS size distribution), the cloud condensation nuclei (CCN) concentration at 0.3% supersaturation (measured with a CCN counter) and **b**, the sulfuric acid condensation sink calculated from the particle size distribution measurement.

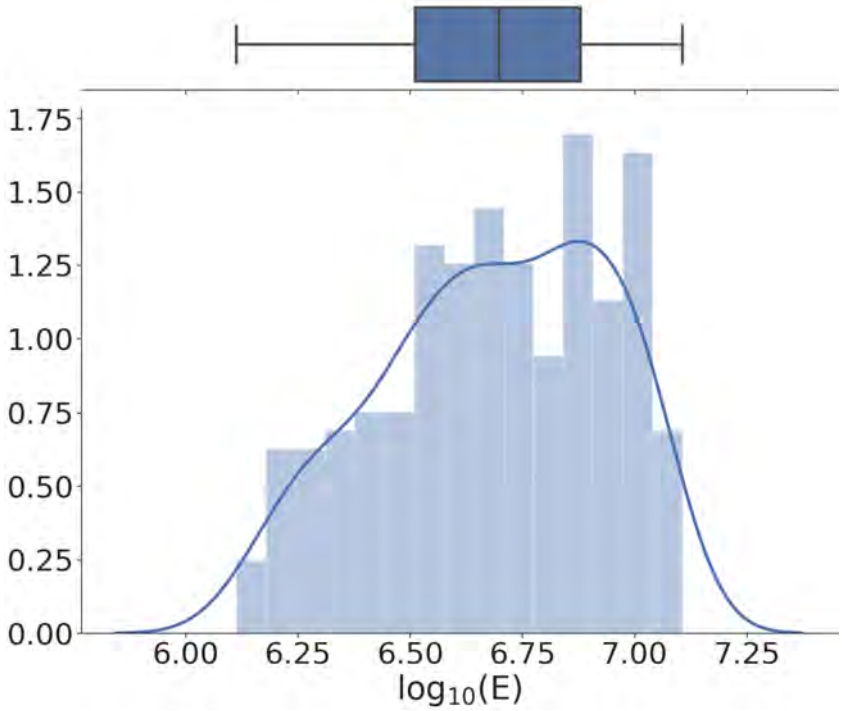

Figure S6.6: Iodine emission factor distribution. Box and whiskers plot and histogram of the inferred iodine emission factor distribution E [iodine atoms $cm^{-2}\,s^{-1}$], with an estimated probability density function (continuous line).

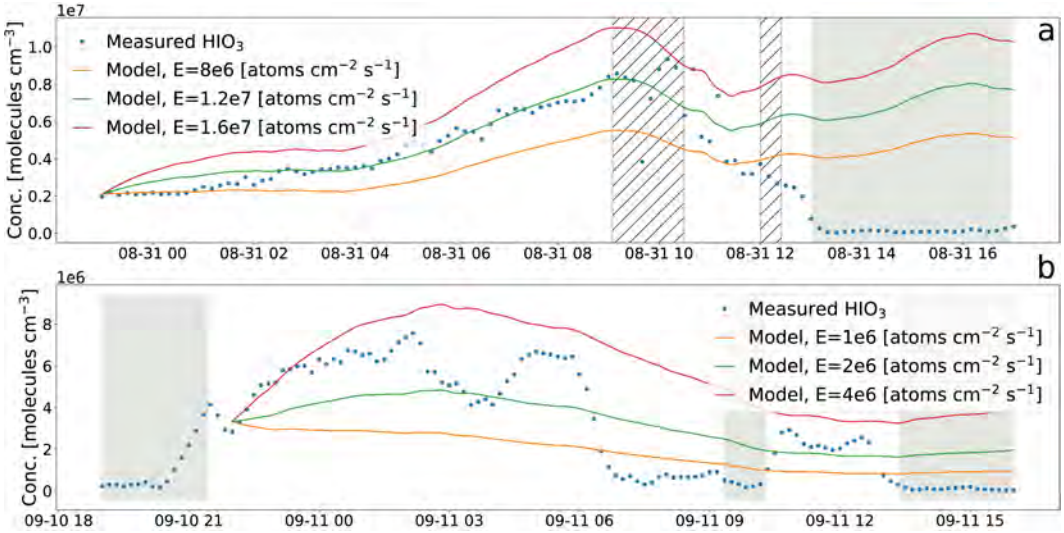

Figure S6.7: Iodic acid simulation. Simulation of iodic acid concentration for two periods characterized by a different emission rate E (higher and lower emission rate in panel **a** and **b**, respectively). The grey shaded areas indicate periods with fog (visibility < 2000 m), the hatching highlights periods influenced by ship pollution.

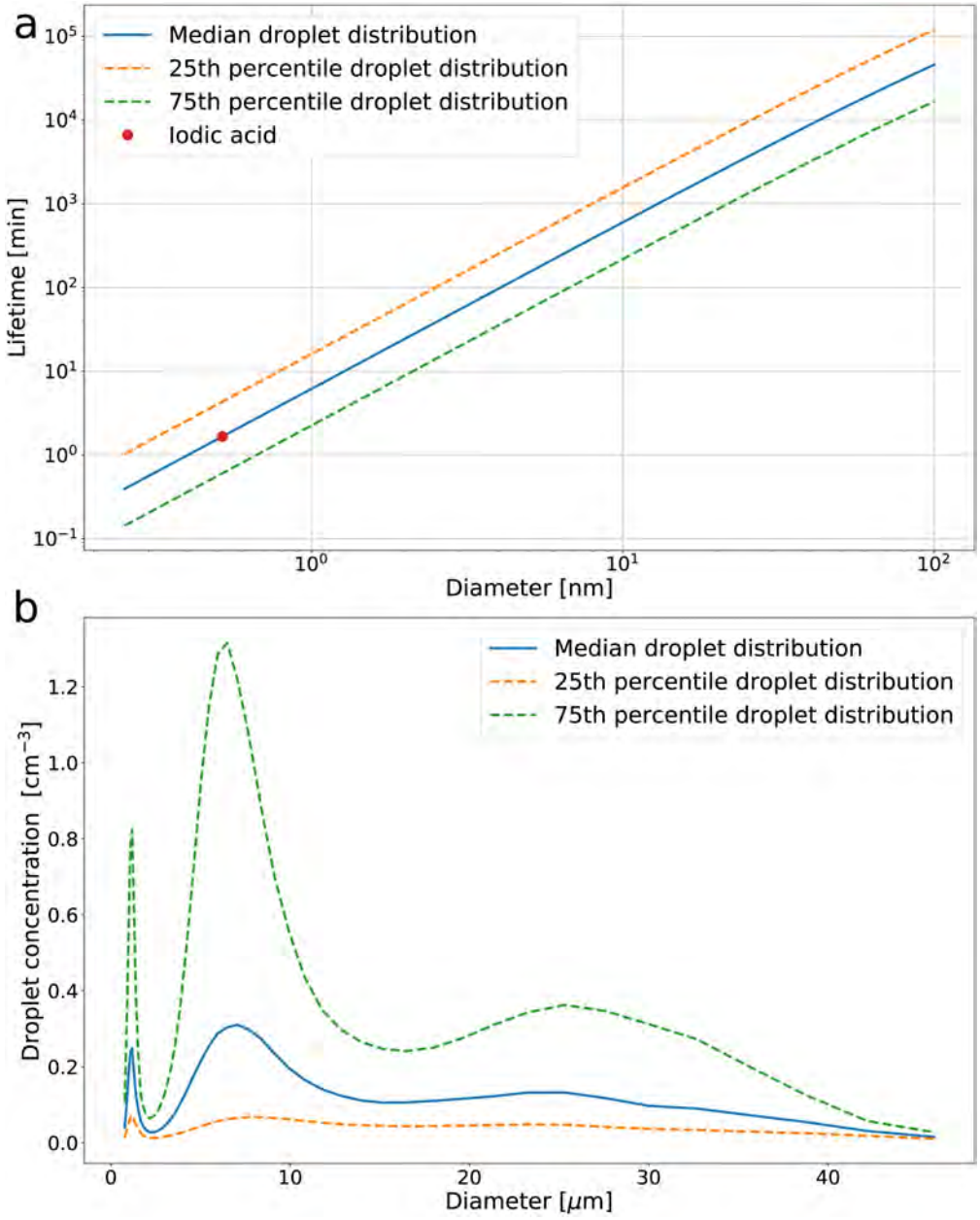

Figure S6.8: Aerosol lifetime in fog. **a** Interstitial aerosol lifetime in fog as a function of particle diameter, only losses due to coagulation with fog droplets were included. Calculations were performed using the average droplet size distribution for the entire Arctic Ocean 2018 expedition (reported in panel b). **b** Average droplet size distribution during the expedition measured with an FSSP, we only used data when visibility was below 2 km. The droplet size distribution shows the number of droplets [cm^{-3}] per size bin (it was produced multiplying a dN/dDp size distribution by the bin width).

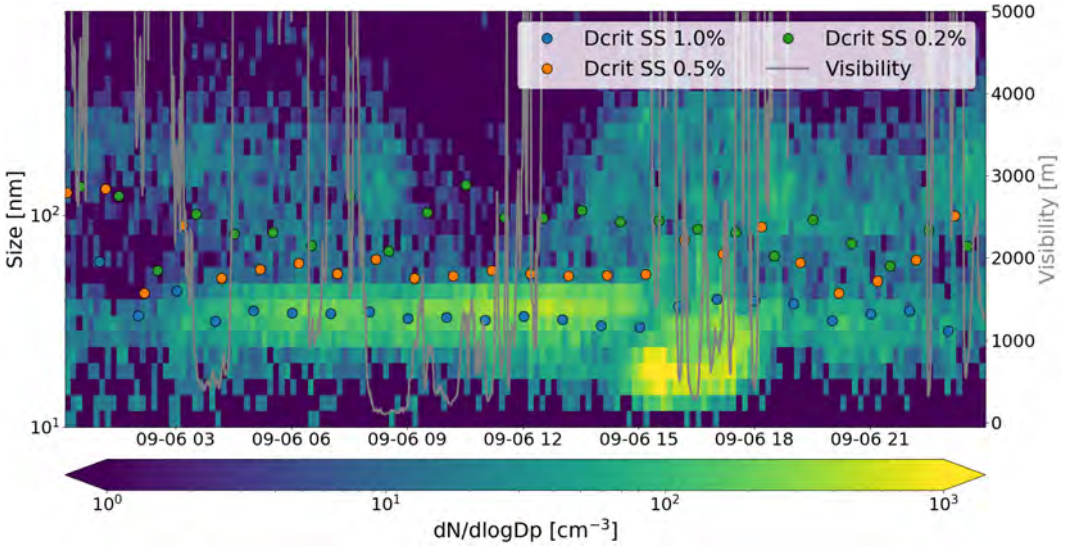

Figure S6.9: Critical diameter estimation. DMPS size distribution from 10 to 900 nm and critical diameter (D_{crit}) at three different supersaturations (SS). The visibility is indicated by the grey line on the right axis.

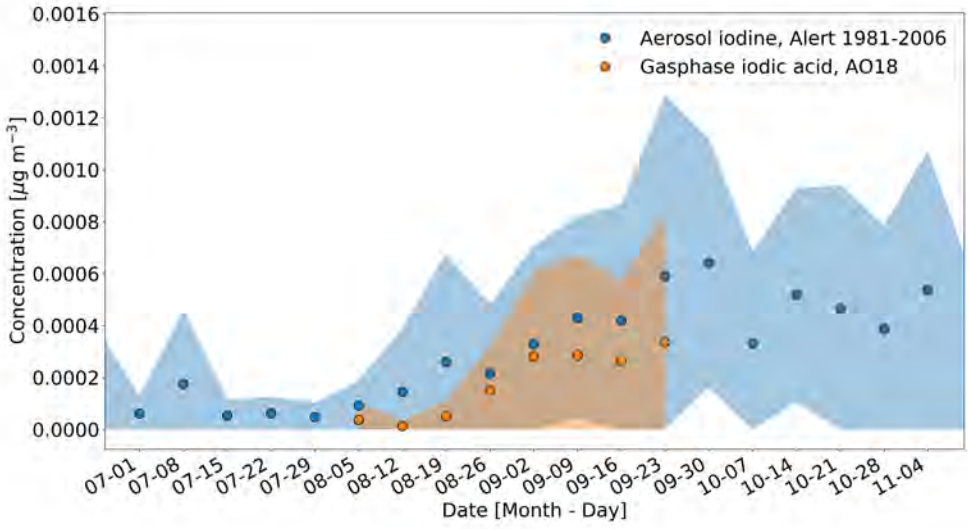

Figure S6.10: Increase of iodine concentration in autumn. Concentration of iodic acid during the Arctic Ocean 2018 expedition (AO18) compared against aerosol iodine concentration from filters collected at Alert between 1981 and 2006[319,327]. Markers represent weekly mean values and the shaded area plus or minus one standard deviation.

Supplementary note

We provide here an assessment of the NAIS measurement accuracy. In particular, we report in Figure S6.11 a comparison of the integrated particle number concentration of the NAIS and the DMPS PSDs between 20 nm and 40 nm for the entire campaign (each marker corresponds to a 30-minute average). The NAIS signal is higher compared to the DMPS, but this is expected and largely due to the NAIS background noise (coming from the electrometers and affecting only low number concentrations), the inversion algorithm and the fact that the NAIS is not a single particle instrument[103]. Moreover, the NAIS was sampling behind a much shorter inlet compared to the DMPS and the larger diffusion losses of the latter would also affect this comparison (as explained in the Method section we corrected for the inlet transmission but this is only based on theoretical calculations). As an indication of this effect, we also compared the NAIS concentration with the ultrafine CPC (UCPC) that was sampling behind the same inlet (Figure S6.12, also in this case data are 30-minute average for the entire campaign), the agreement is generally better between these two instruments. On average the NAIS concentration was between 1.5 and 2 times higher than the DMPS and the UCPC. These results are in line with previous studies[103,108], which also reported similarly higher concentrations from NAIS.

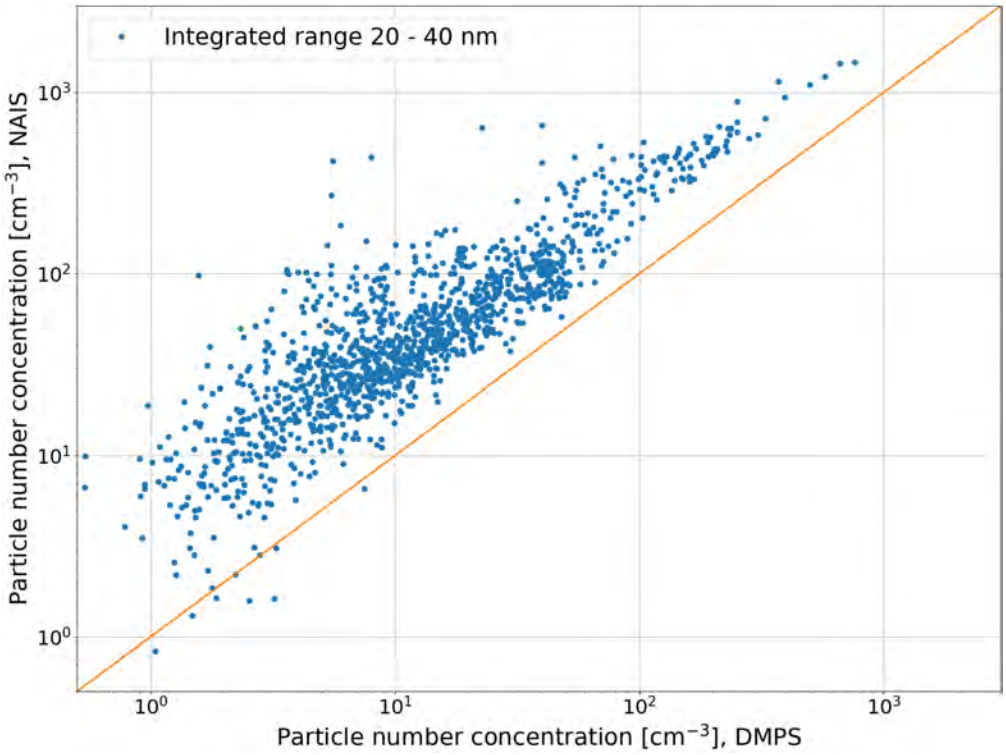

Figure S6.11: Comparison of NAIS and DMPS particle number concentration measurements. Integrated concentration of the NAIS and DMPS size distribution in the range between 20 and 40 nm.

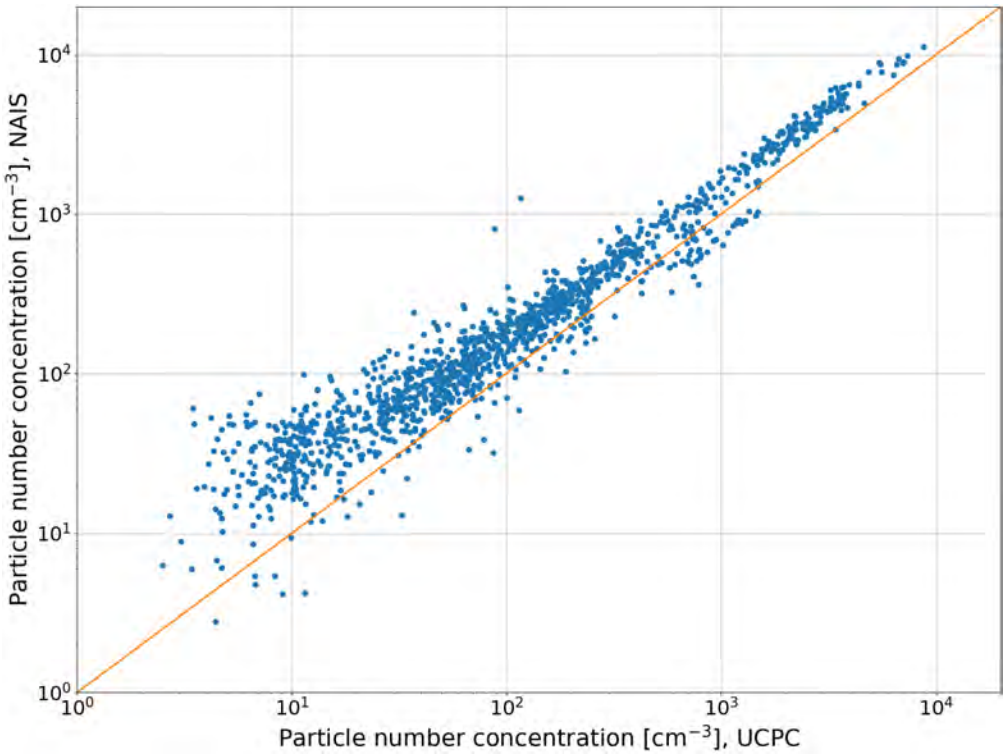

Figure S6.12: Comparison of NAIS and UCPC particle number concentration measurements. Integrated concentration of the NAIS size distribution above 3 nm compared against the UCPC. The UCPC has a nominal cut-off size of 2.5 and 3 nm at 50% and 100% detection efficiency respectively. Both instruments were sampling behind the same inlet.

Supplementary tables

Table S6.1: Identified neutral molecules and clusters during two selected NPF events. The molecular composition is provided for those peaks, where a reasonable identification was possible. The mass spectra were integrated for the duration of the event (4 and 3 hours for 17 September and 27 August respectively) and the signal corresponds to the integrated area in milli counts per second (mcps). We included only peaks above 4 mcps, that is our estimate of the lower limit of detection due to instrumental noise at three hours of averaging. We report only the peaks that are enhanced during the NPF event (three times higher than background conditions) in order to remove contaminants and background peaks (mainly due to contamination in the sheath air flow).

Mass	**PeakID**	**Signal (mcps)**		**Mass**	**PeakID**	**Signal (mcps)**	
		17-Sep	27-Aug			17-Sep	27-Aug
78.9189	Br^-	9.3		237.8854	$HIO_3NO_3^-$	17946.8	17375.1
79.9574	SO_3^-	996.0	852.2	241.8517		71.6	
94.9808	$CH_3SO_3^-$	4401.6	3535.0	250.8806	$O_6N_2I^-$	5460.2	6389.3
96.9601	HSO_4^-	7905.0	7689.4	266.8756	$O_7N_2I^-$	407.5	
110.9758	$CH_3SO_4^-$	24.4	21.1	272.8572	$H_2SO_4IO_3^-$	19.7	51.2
111.9472	SO_5^-	1306.6	1106.6	282.8705	$O_8N_2I^-$	1398.5	1296.8
126.905	I^-	1522.3	1440.4	284.8862	$HIO_2HNO_3NO_3^-$	115.8	
142.8999	IO^-	640.3	587.0	300.881	$HIO_3HNO_3NO_3^-$	120.2	208.8
157.9765	$CH_3SO_3HNO_3^-$	1441.6	1488.2	320.8126	$H_3O_4I_2^-$	120.1	
158.8948	IO_2^-	528.1	497.6	322.8283	$H_5O_5I_2^-$	71.0	
159.9558	$H_2SO_4NO_3^-$	1453.8	1958.7	357.0541			27.1
160.9105	H_2OIO^-	30.6	37.5	379.777	$I_2O_4NO_3^-$	155.0	71.1
174.8898	IO_3^-	48584.6	39807.1	395.7719	$I_2O_5NO_3^-$	26.6	44.8
186.8892		19.7	25.9	397.7875	$HIO_3HIO_2NO_3^-$	44.7	17.4
192.9003	$H_2OIO_3^-$	26.6	26.4	442.7726	$I_2O_4HNO_3NO_3^-$	24.0	12.3
194.9275	$H_2SO_4HSO_4^-$	14.7	29.1	508.6733	$I_2O_5IO_3^-$	8.4	5.3
212.8376	$IOCl_2^-$	64.8		608.6598		6.3	14.8
220.8827	$IO_2NO_3^-$	313.1		686.586	$(HIO_3)_2HIO_2IO_3^-$	6.7	8.6
220.9721	$CH_3SO_3HHNO_3NO_3^-$	26.6	44.8	723.6466		5.0	12.0
221.8905	$HIO_2NO_3^-$	30.5		783.5456	$H_4O_{15}I_4S^-$	9.7	14.0
223.8646	HSO_4I^-	61.3		881.5356			5.1

Table S6.2: Identified charged molecules and clusters during a selected NPF event. List of naturally charged negative ions and molecules measured during the new particle formation event on 17 September, the mass spectrum was integrated for 6 hours. The molecular composition is provided for those peaks, where a reasonable identification was possible. The nitrate ion signal could be partly due to contaminations in the inlet due to the switching between nitrate CIMS and negative APi-TOF mode.

Mass	Peak ID	Signal (mcps)
59.9853	CO_3^-	5.1
61.9884	NO_3^-	576.3
71.0139	$C_3H_3O_2^-$	5.3
78.9189	Br^-	4.9
79.9574	SO_3^-	63.7
80.9652	HSO_3^-	6.6
94.9808	$CH_3SO_3^-$	149.9
95.9523	SO_4^-	9.1
96.9601	HSO_4^-	642.7
103.0037	$C_3H_3O_4^-$	24.4
110.9758	$CH_3SO_4^-$	13.5
111.9472	SO_5^-	83.4
115.0037	$C_4H_3O_4^-$	49.7
124.984	$HNO_3NO_3^-$	47.5
126.905	I^-	110.1
129.0193	$C_5H_5O_4^-$	12.4
130.9986	$C_4H_3O_5^-$	3.9
138.9707	$(C_2H_2O)HSO_4^-$	9.6
142.8999	IO^-	39.2
157.9765	$CH_3SO_3HNO_3^-$	17.8
158.8949	IO_2^-	26.2
159.9558	$H_2SO_4NO_3^-$	21.1
174.8898	IO_3^-	1674.4
190.9326	$CH_3SO_3SO_4^-$	8.4
192.9482	$CH_3SO_3H_2SO_4^-$	26.7
194.9275	$H_2SO_4HSO_4^-$	270.5
196.8427	ICl_2^-	24.3
208.9431	$CH_4O_4SHSO_4^-$	7.3
220.8827	$IO_3NO_2^-$	20.5
237.8854	$HNO_3IO_3^-$	325.4
242.7893		5.8
252.8725	$IO_3NO_4^-$	86.8
254.8466	$IO_3SO_3^-$	100.5
266.7804	ICl_4^-	69.3
270.8779	$CH_3SO_3HIO_3^-$	201.1
272.8571	$HIO_3HSO_4^-$	366
282.8827		15.8
286.8807		29.4
290.8995		13.1
292.8949	$(H_2SO_4)_2HSO_4^-$	15.9
293.7999		9.2
295.8022		8.6
299.8061		26.2
301.8027		29.1
310.7273		5.7
312.7244		11.1
314.7199		7
314.8628		5.3
315.8629		12.3
316.7141		4.2
318.8429		15.8
350.7868	$HIO_3IO_3^-$	166.8
352.814	$HIO_3HSO_4SO_3^-$	18.3
395.7719	$I_2O_5NO_3^-$	303.7
396.7797	$HIO_2IO_3NO_3^-$	21
412.7024	$I_2O_5Br^-$	25.1
428.7644	$I_2O_5CH_3SO_3^-$	199.2
430.7436	$I_2O_5HSO_4^-$	117.3
444.7546		10.5
492.6784	$O_7I_3^-$	14.5
508.6733	$I_2O_5IO_3^-$	450.5
510.6889	$HIO_3HIO_2IO_3^-$	4.8
527.6447		1.6
554.6662	$O_{10}NI_3^-$	9
570.6454		6.9
572.6447		11.5
586.6519		20
588.6301	$I_2O_5IO_3SO_3^-$	93.1
602.6507		13.7
604.6614	$I_2O_5HIO_3CH_3SO_3^-$	23.8
606.6407	$I_2O_5HIO_3HSO_4^-$	16.6
608.6563	$HIO_3HIO_2IO_3H_2SO_4^-$	13.6
668.6018		16.2
682.6111		8.3
684.5703	$I_2O_5HIO_3IO_3^-$	38.5
686.586	$(HIO_3)_2HIO_2IO_3^-$	28.9
746.5384		6.8
748.5246		5.5
762.5479	$(I_2O_5)_2CH_3SO_3^-$	38.8
764.5271	$(I_2O_5)_2HSO_4^-$	50
778.5327		4.6
783.5955		16
826.4619	$(I_2O_5)_2IO_2^-$	10.4
842.4568	$(I_2O_5)_2IO_3^-$	57.5
844.4725	$(I_2O_5)_2H_2IO_3^-$	7
861.5192		11.8
906.3994		6.7
920.4524		4.4
922.4136	$(I_2O_5)_2IO_3SO_3^-$	43.8
936.4147		4.7
938.4449	$(I_2O_5)_2HIO_3CH_3SO_3^-$	6.4
940.4242	$(I_2O_5)_2HIO_3HSO_4^-$	4.2
959.4518		8.2
1002.376		7
1018.3539	$(I_2O_5)_2HIO_3IO_3^-$	15.5
1020.3695	$I_2O_5(HIO_3)_2HIO_2IO_3^-$	16.1
1096.3314	$(I_2O_5)_3CH_3SO_3^-$	14.2
1098.3107	$(I_2O_5)_3HSO_4^-$	28.8
1176.2403	$(I_2O_5)_3IO_3^-$	16.9
1178.256	$(I_2O_5)_2HIO_3HIO_2IO_3^-$	7.1
1195.2587	$I_6O_{16}H_3IO_3^-$	5.3
1256.1971	$(I_2O_5)_3IO_3SO_3^-$	14.5
1352.1374	$(I_2O_5)_3HIO_3IO_3^-$	5.7
1371.1558	$(I_2O_5)_3HIO_3H_3OIO_3^-$	7.3
1432.0942	$(I_2O_5)_4HSO_4^-$	6.1

7 CONCLUSION AND OUTLOOK

Natural aerosols in polar regions are a crucial aspect of cloud formation and the surface energy balance. A better knowledge of natural aerosol sources and processes in these regions would improve our understanding of the PI atmosphere and could be used to reduce the radiative forcing uncertainty. Additionally, this knowledge would also be helpful to understand how natural aerosols will change in a warming climate and make better predictions for the evolution of polar regions in the near future.

The objective of this Thesis was to characterize natural aerosols in polar regions, with a specific focus on secondary aerosol sources and processes. To investigate, in particular, the different possible nucleation and growth mechanisms, their drivers and the environmental conditions controlling the concentration of the relevant gaseous precursors. The ultimate goal was to understand the role of NPF for the CCN budget and contrast it with other sources of aerosol in these regions. These objectives were addressed by means of two measurements campaigns, in the Southern ocean (ACE) and in the central Arctic Ocean (AO18).

Aerosol sources and processes across the Southern Ocean were investigated during ACE (Chapters 4 and 5). In particular, a very low anthropogenic influence was confirmed especially south of 55°S, assuring the relevance of the measurements as a PI proxy. The contribution of sea spray aerosol to the CCN budget was found to be highly variable depending on the environmental conditions and location. The average contribution to the CCN number at 0.15% SS was about 35% for the entire campaign with higher values over the open ocean (reaching up to 100% in some extreme cases) and lower around the coast of Antarctica (on average 10%).

The remaining CCN fraction can be attributed to secondary processes, likely nucleation from DMS oxidation products. ACE measurements revealed that NPF in the boundary layer is mainly driven by sulfuric acid but is a very rare occurrence and does not contribute to the CCN budget. It was shown that the conditions over the Southern Ocean in summer are not favourable for boundary layer NPF. In particular, the sulfuric acid concentration was too low (lower than 10^7 molecules cm^{-3}) to support nucleation at the typical boundary layer temperatures which were encountered (95% of the time warmer than $-1.5\,°C$). Hence, the most likely hypothesis is that nucleation happens in the free troposphere where conditions are more favourable (temperature and condensation sink are lower and solar irradiance is higher) and particles are then entrained into the boundary layer from above.

Comparison of in situ CCN measurements with predicted values from a global climate model show that the model systematically underestimates the CCN concentration. This underestimation is particularly pronounced around the coast of Antarctica and it is consistent with a similar comparison of modelled droplet number concentration against satellite retrieved values[50]. This discrepancy indicates the presence of a structural deficiency in the model which could either be related to an aerosol source or a process (*e.g.* aerosol deposition or growth). The region around the coast of Antarctica was characterized by the lowest sea spray aerosol concentration but the highest MSA concentration, both in the particle and in the gas phase. This is consistent with DMS

emissions, which are expected to be higher in this region during summer compared to the rest of the Southern Ocean[241,296]. As a consequence, the structural model deficiency is more likely related to a secondary aerosol source or process, rather than sea spray emissions. Additionally, measurements of gaseous and particulate MSA suggest that most of the MSA may be produced via heterogeneous oxidation of DMS, consistent with previous studies[48,294]. This process grows the mass of aerosol particles that are activated in clouds, lowering the critical SS required to re-activate these particles after dissipation of the clouds. The presence of a clear Hoppel minimum and the larger accumulation mode measured in the PSD around the coast Antarctica indicate that cloud processing is a critical process which shapes the aerosol properties. If multiple cycles of cloud formation and dissipation occur, then the number of CCNs at a fixed supersaturation would increase. This process could explain at least part of the discrepancy between the observations and the model (the model does not include heterogeneous oxidation of DMS).

The main limitation of the ACE study is the absence of vertical information about aerosol properties and trace gases. There are several indications supporting the hypothesis that free tropospheric NPF may be an important source of CCN over the Southern Ocean, both from this and previous studies, but there are only a handful of direct observations[47,58]. Dedicated studies to investigate nucleation in the free troposphere and characterize exchange processes between the free troposphere and the boundary layer are key to better constrain CCN sources over the Southern Ocean. Another important aspect that was not investigated in this study is the growth of newly formed particles, which have to become larger before acting as a CCN. Based on Hoppel minimum considerations, the critical activation diameter during ACE varied between 44 nm and 82 nm roughly. Several days would be required to grow a few nanometre particle into this size range with the typical boundary layer sulfuric acid and MSA concentrations. It is not clear if there were other compounds contributing to the particle growth and if this process is also prevalently occurring in the free troposphere or not. Future studies should also focus on investigating the chemical composition of Aitken mode particles and their vertical distribution to be able to link NPF with the CCN population.

On the other side of the globe, the central Arctic Ocean is characterized by substantially different processes and environmental conditions compared toF the Southern Ocean (Chapter 6). In particular, the large extent of sea ice almost completely prevents sea spray formation leading to a strong reduction of both accumulation and coarse mode aerosol concentration in the summer. Additionally, also DMS fluxes are smaller and the concentrations of both sulfuric acid and MSA are much lower (one to two orders of magnitude). Therefore, both primary and secondary sources of aerosols are weaker resulting in a lower condensation sink and smaller CCN number concentration (about one order of magnitude in both cases).

On the contrary, NPF is an important source of aerosols in this case, it was found to regularly occur inside the boundary layer and to be driven by iodic acid. In particular, iodic acid was characterized by a seasonal cycle with a marked increase towards the end of summer. This increase had a direct effect on the NPF occurence and concentration of UFP, which was about one order of magnitude higher in autumn compared to summer. The iodic acid transition coincided with the freeze-up onset and an increase in the ozone concentration. Both factors are potentially relevant for atmospheric iodine, which can be released by heterogeneous reactions on the snowpack or on frozen saline surfaces[314–317] but also via phytoplankton biogenic production[272,313]. The con-

centration of iodic acid in the atmosphere was found to be largely regulated by an interplay of different meteorological factors, such as the boundary layer height, deposition velocity, condensation sink and fog. These factors were included into a simple model by means of which it was possible to infer an iodine emission factor range.

Iodic acid was also vital for the growth of the newly formed particles, which was explained by iodic acid alone in most of the cases. There were also few exceptions where the condensing material growing the particles could not be identified. Overall, the growth rates were slow (on average 0.5 nm h^{-1}) but the coagulation sink for newly formed particles was also small and particles were often able to reach $15 - 20$ nm in size. A relatively high supersaturation (larger than 1%) would be required to activate a 20 nm size particle as a CCN. Such high supersaturation values are not typical for low level clouds or fog in a marine environment. However, the summertime Arctic is a special case because of the low aerosol concentration, which limits the number of cloud droplets. Hence, the excess water vapour inside the cloud is not depleted as quickly as in a typical mid-latitude cloud and higher supersaturation values can be reached. A single case study was shown in this work, where fog was forming despite the extremely low concentration of accumulation mode particles (less than 1 cm^{-3}). An analysis of cloud residuals has shown that particles smaller than 30 nm activated in clouds, revealing that NPF can impact cloud formation when the concentration of accumulation mode particles is sufficiently small.

The activation of small Aitken mode particles inside clouds was shown only for an individual case study. This is a very valuable observation, however, it does not provide any quantitative information about the relevance of NPF for the CCN budget over the Arctic pack ice. This is one of the questions that the study presented here was not able to address and represents one of its main limitation. A similarly important question would be to understand the contribution of iodine NPF to the Aitken mode particle concentration compared to other sources, like long-range transport of secondary particles formed in the marginal ice zone (a more biologically productive region). Both research questions deserve dedicated experimental studies to identify and constrain the contribution of the different sources of Aitken mode particles and CCN. A complementary approach to understand the relevance of iodine NPF over the Arctic pack ice would be to implement this mechanism into regional or global climate models. Generally, the implementation of a new nucleation mechanism into models is not a trivial task, especially in this case where so little is known about the formation and sources of iodic acid. The iodic acid emission rate proposed in this work is currently being tested in a global climate model by collaborators from the University of Leeds. First results show that the model produces a reasonable iodic acid concentration over the Arctic pack ice, which is promising. However, the iodic acid nucleation mechanism, which is the most critical part, has not been implemented yet.

In conclusion, the results presented in this Thesis represent an advancement in the understanding of secondary aerosol sources in polar regions, both in the Southern and in the Northern hemisphere. Information about the occurrence of NPF, the underlying mechanisms and the environmental factors controlling the nucleating vapours concentration was provided. These results can be used to improve the representation of natural sources of aerosols in global climate models and constrain the PI aerosol baseline. Ideally, the findings of this Thesis should be integrated with measurements from other locations and different periods or years to fully understand their relevance. For example, in Chapter 6 the iodic acid data have been compared with multi-year iodine aerosol measurements from Alert, in the Canadian Arctic. The agreement between

these two datasets is remarkably good and indicates that the autumn iodine emission increase is an Arctic pack ice wide phenomenon, which has been occurring for several decades already. It is not known, however, if this process will change in the future because of the projected Arctic temperature increase and reduced sea ice coverage. Understanding changes of natural aerosol processes in a warming climate is critical for two reasons: (1) to improve the accuracy of future climate predictions and (2) to correctly interpret present day observations of natural processes as a proxy for the PI atmosphere. Short-term expeditions can be very valuable for process-based studies but their findings need to be complemented by long-term observations in order to assess the evolution and changes of natural processes. The findings of this Thesis add several new pieces to the natural aerosol puzzle contributing to the better understanding of the bigger picture.

A APPENDIX: SULFURIC ACID BACKGROUND IN THE API-TOF

During ACE, the nitrate CI-APi-ToF was affected by a sulfuric acid background issue, which was probably related to the low nitric acid concentration in the inlet sheath flow. This problem was identified only after the ACE campaign, during experiments at the PSI smog chamber (SC). In particular, the nitrate CI-APi-ToF measured an HSO_4^- signal also when lights inside the chamber were turned off and no sulfuric acid production was occurring. Additionally, an SO_5^- signal was also measured when SO_2 was present in the chamber. Figure A.1 shows a smog chamber experiment illustrating this issue: after injection of SO_2 both HSO_4^- and SO_5^- increase even if lights are turned off. Afterwards, when lights are turned on, sulfuric acid is produced inside the chamber and the HSO_4^- signal increases further as expected. In contrast, SO_5^- decreases slightly when lights are on. This effect is still not understood but it is probably related with the temperature increase produced by the lights in the chamber.

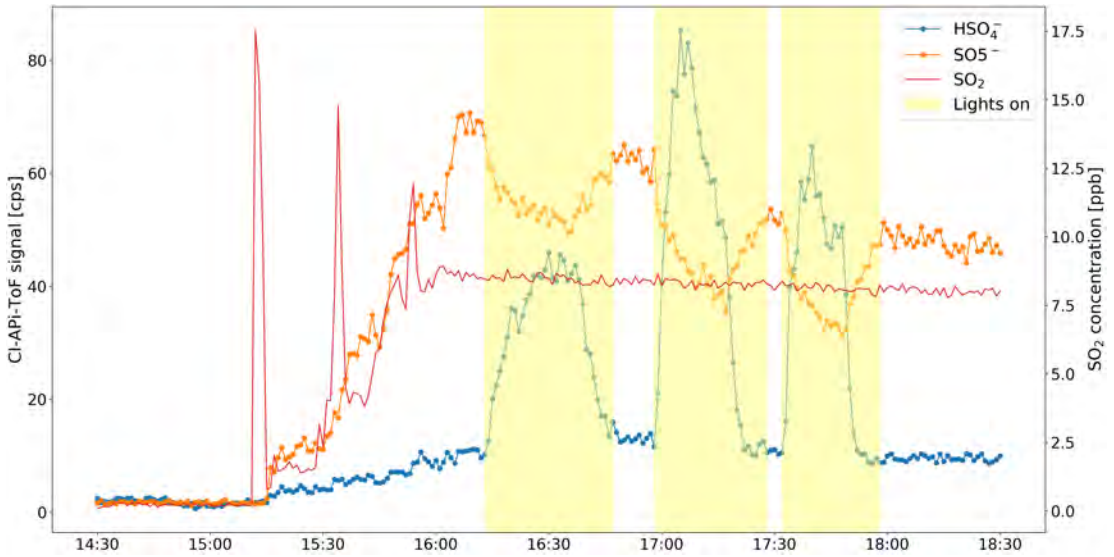

Figure A.1: Example of an experiment showing the sulfuric acid background issue. The left y-axis is relative to the nitrate CI-APi-ToF HSO_4^- and SO_5^- signal, whereas the right y-axis shows the SO_2 concentration inside the chamber.

HSO_4^- and SO_5^- are probably produced inside the nitrate CI-APi-ToF inlet from a reaction with SO_2. Since the inlet was operated with a low nitric acid concentration, it is possible that other ions where produced (*e.g.* O_2^- and O_3^-) and reacted with trace gases in the sample flow in addition to the nitrate ion. The reaction leading to the SO_5^- signal was probably[345]:

$$O_3^- + SO_2 \longrightarrow SO_3^- \tag{RA.1}$$

$$SO_3^- + O_2 \longrightarrow SO_5^-. \tag{RA.2}$$

The reaction leading to HSO_4^- is less clear. Bork *et al.*[346] proposed a charge transfer reaction between SO_3^- and O_3:

$$SO_3^- + O_3 \longrightarrow SO_3 + O_3^-. \tag{RA.3}$$

SO_3 would then quickly react with water forming sulfuric acid (Reaction R3.5). Another possibility is the reaction suggested by Tsona *et al.*[347]:

$$SO_3^- + O_2 + H_2O \longrightarrow HSO_4^- + HO_2. \tag{RA.4}$$

However, there are no measurements showing that this reaction can actually occur. It would also contradict an older study, which only measured SO_5^- as the outcome of reaction RA.4[348].

In order to identify the exact reaction leading to sulfuric acid formation inside the inlet a dedicated study would be required, which is out of the scope of this work. With the present knowledge, reaction RA.3 is the most plausible pathway.

A.1 BACKGROUND CORRECTION

The experiments performed at the PSI smog chamber together with measurements collected at the CERN CLOUD chamber were used to derive a correction factor for the sulfuric acid background. During both campaigns the instrument was operated under similar conditions and with a low nitric acid concentration in the sheath flow. However, the results were largely different. For this reason it has not been possible to reliably correct the sulfuric acid data from ACE. Nevertheless, it is instructive to describe the analysis performed on the background sulfuric acid production to provide a better characterization of this problem.

Figure A.2a shows the HSO_4^- signal as a function of SO_2 for both CLOUD and the SC experiments. To remove periods characterized by an active production of sulfuric acid only data collected when lights were turned off are reported here. Different colours are used to indicate different settings of the nitrate CI-APi-ToF inlet (mainly the voltage applied to the inlet), which were used during the ACE expedition and replicated during the chamber experiments. The box and whiskers plot on the right-hand side of the figure indicates the ACE measurements range. The HSO_4^- signal is clearly related to SO_2 but it shows a saturation effect above about 2×10^{10} molecules cm^{-3}. Additionally, there are strong differences between the different CI settings. Figure A.2b shows the same data with HSO_4^- being multiplied by the water vapour concentration inside the chamber. This multiplicative factor was found to be important only based on an empirical analysis of the data. With the inclusion of water vapour as a multiplicative factor, a more uniform relation between HSO_4^- and SO_2 emerges, however, differences between different CI settings persist. Water vapour is probably involved in the stabilization of the charged cluster inside the nitrate CI-APi-ToF inlet but a clear mechanistic understanding is missing.

Ideally, one could use the SO_2 concentration to estimate the sulfuric acid background and correct the data. Unfortunately SO_2 was not measured during ACE. An alternative approach is to use the SO_5^- signal as a proxy for SO_2, given their good correlation as shown in Figure A.3. This approach can be applied to field data only if there are no atmospheric molecules which would also be detected as SO_5^- by the nitrate CI-APi-

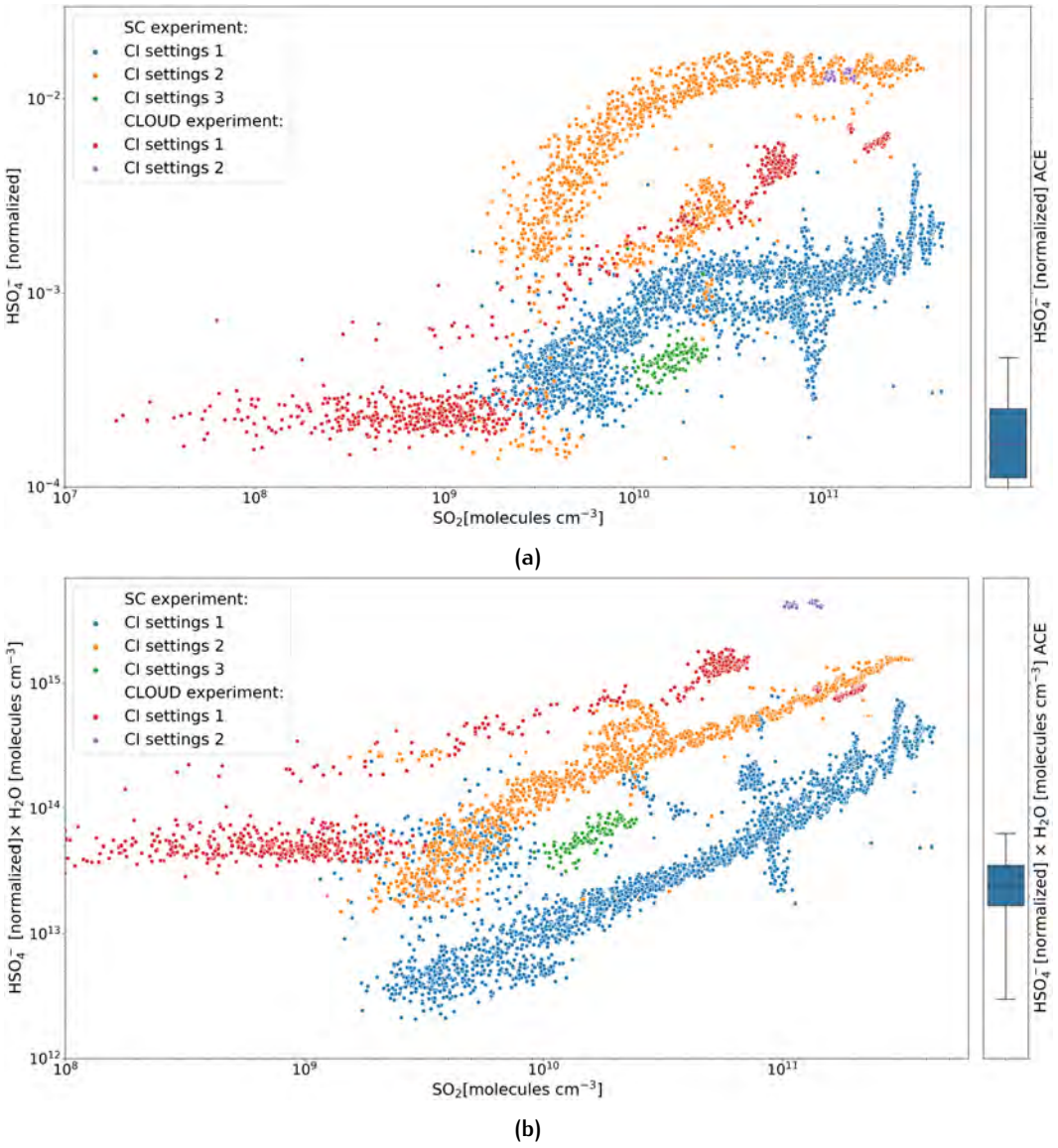

Figure A.2: Sulfuric acid production inside the nitrate CI-APi-ToF inlet as a function of the SO_2 concentration. Panel **(a)** shows the HSO_4^- signal and panel **(b)** HSO_4^- times the water concentration. The box and whiskers plot on the right-hand side shows the range of data measured during ACE.

ToF, namely HSO_5. HSO_5 is an intermediate radical produced during the oxidation of SO_2 by OH[349]. However, according to quantum chemical calculations HSO_5 is not stable and quickly decomposes into SO_3 and HO_2[350,351]. Therefore, the concentration of HSO_5 in the atmosphere is probably negligible and the main source of SO_5^- in the nitrate CI-APi-ToF remains the reaction with SO_2 via RA.1-RA.2.

Figure A.4 shows the SO_5^- signal plotted against HSO_4^- times H_2O for the same experiments described before. In this case, the data were not normalized by the CI-APi-ToF primary ion concentration because the normalization factor is the same for both HSO_4^- and SO_5^- and it would not affect their relation. Also in this case, there is a strong discrepancy between different CI settings and experiments (*i.e.* CLOUD and SC). However, the SC *CI settings 2* and the CLOUD *CI settings 1* are characterized by a very similar slope (excluding the saturation effect for the larger SO_5^- data), which is an indication of the same process being involved.

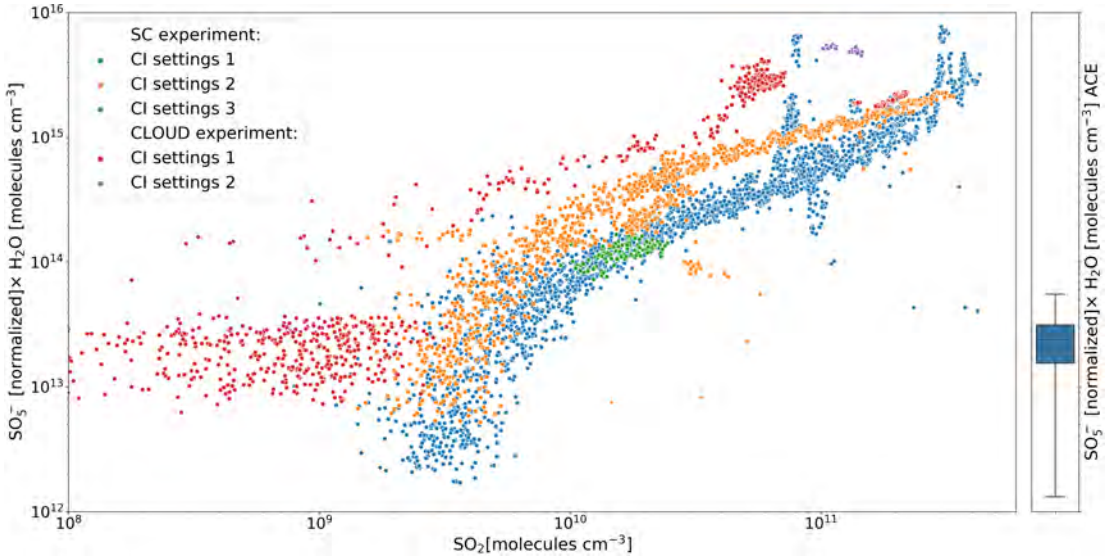

Figure A.3: SO_5^- production inside the nitrate CI-APi-ToF inlet as a function of the SO_2 concentration. The box and whiskers plot on the right-hand side shows the range of data measured during ACE.

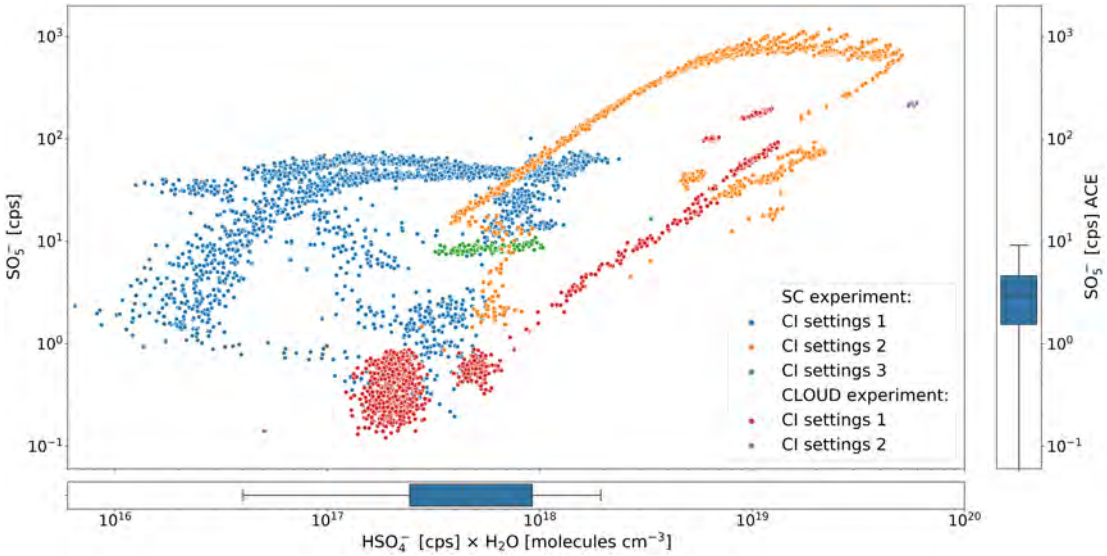

Figure A.4: Relation between the production of SO_5^- and HSO_4^- times water concentration. The box and whiskers plots on the right-hand side and on the bottom of the figure show the corresponding SO_5^- and $HSO_4^- \times H_2O$ range of data measured during ACE.

Additionally, most of the ACE data points falls between the SC *CI settings 2* and the CLOUD *CI settings 1* branches as highlighted by the two box and whiskers plot on the side of the figure. These two branches were fitted with a simple power law and the results were used to identify a correction function for the sulfuric acid background. Figure A.5a shows the data selected for the power law fit and the corresponding results. Figure A.5b shows the night time data from ACE, which fall between the two branches. A new power law function created by averaging the parameters of the two power law fits is also shown, this is the function that was tentatively used to correct the ACE data. The two original power law fits were used to estimate an uncertainty range on the background correction.

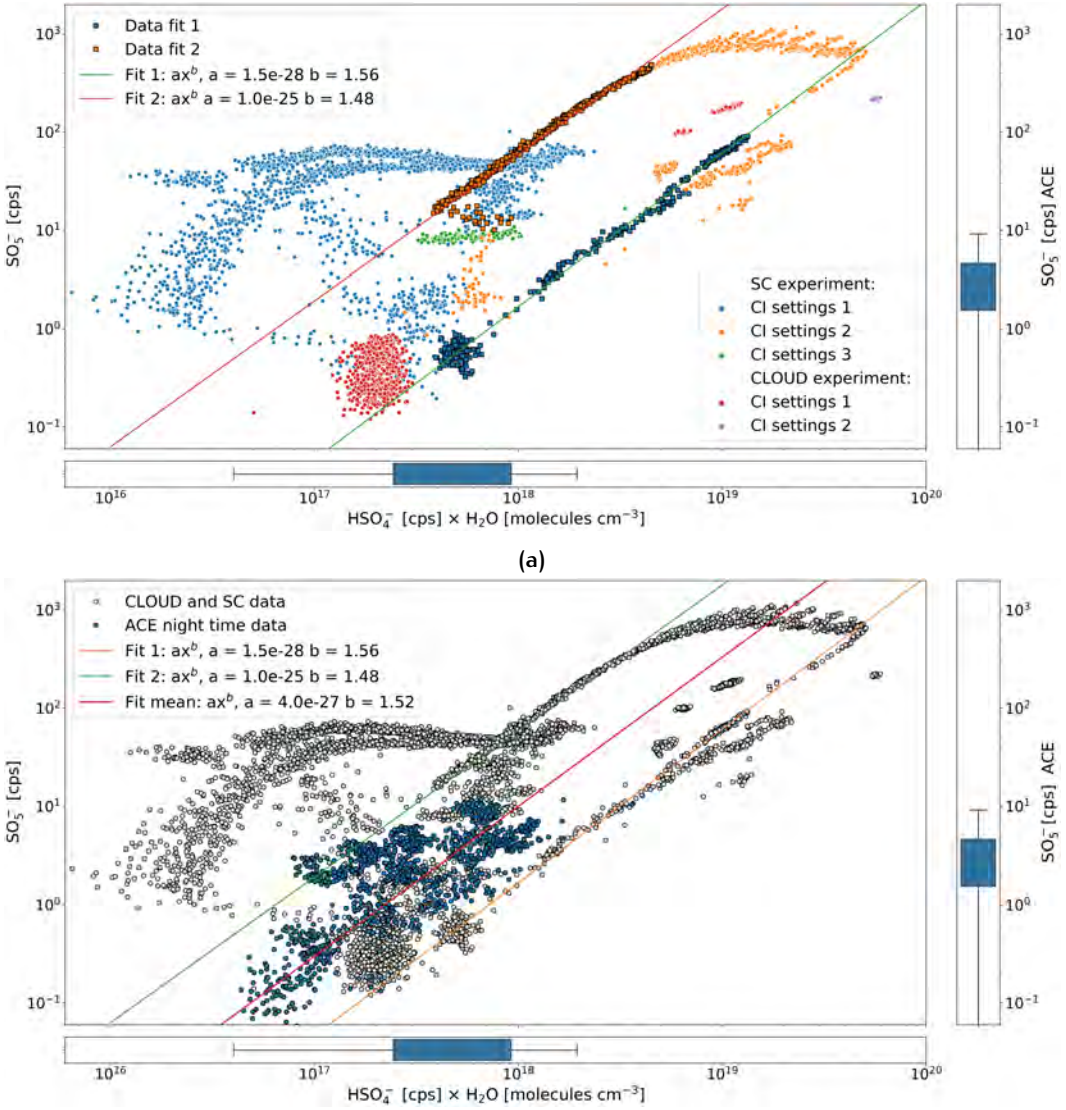

Figure A.5: Sulfuric acid background correction function. Panel **(a)** shows the power law fit of the two branches of data, which were chosen for the correction function. Panel **(b)** shows the mean power law correction function and the night time data from ACE. In both panels, the box and whiskers plots on the right-hand side and on the bottom of the figure show the corresponding SO_5^- and $HSO_4^- \times H_2O$ range of data measured during ACE.

Figure A.6 shows the original sulfuric acid time series from ACE and the estimated background sulfuric acid with uncertainty range. The estimated background is comparable to the measured sulfuric acid signal and often larger, while the estimated uncertainty is extremely large. Therefore, this correction method does not provide meaningful results in this case. Considering that the sulfuric acid data from ACE were in a reasonable range and showed a diurnal cycle, which is typical of ambient data (as described in Chapter 5), the background correction factor is very likely overestimated. The reason for this overestimation is probably related with the different conditions between the chamber experiments and the field data (*e.g.* different CO_2 and O_3 concentration) but remains largely unclear.

In conclusion, it has not been possible to properly remove the sulfuric acid background from the ACE data. Therefore, it was decided to report sulfuric acid concentration as an upper limit estimate.

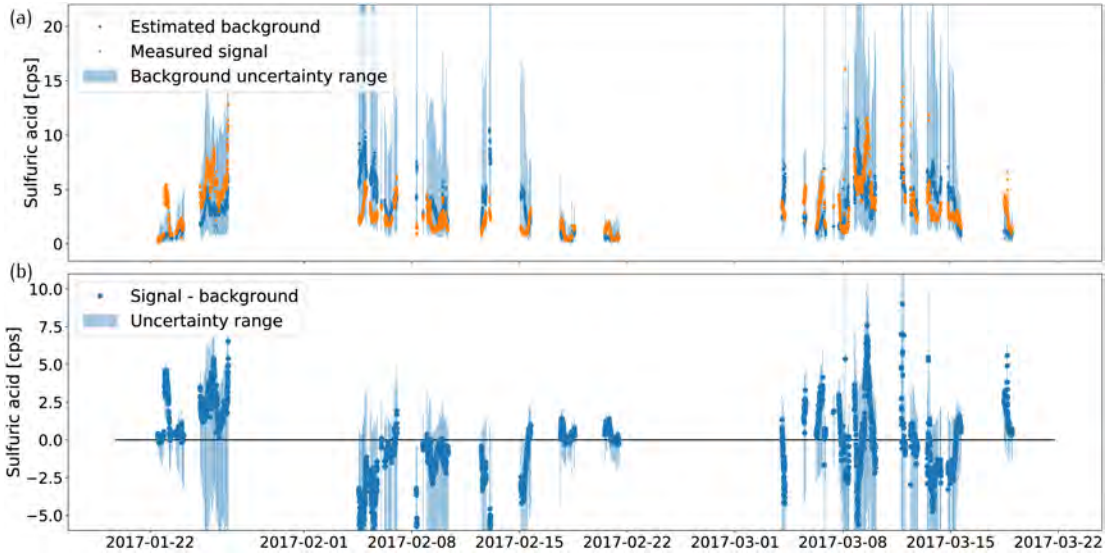

Figure A.6: Sulfuric acid background correction. **(a)** original sulfuric acid data from ACE and estimated background. **(b)** sulfuric acid data corrected for the background.

BIBLIOGRAPHY

1. Seinfeld, J. H. & Pandis, S. N. *Atmospheric Chemistry and Physics: from Air Pollution to Climate Change* ISBN: 978-1-118-94740-1 (John Wiley & Sons, 2016).
2. Ramanathan, V., Crutzen, P. J., Kiehl, J. T. & Rosenfeld, D. Aerosols, Climate, and the Hydrological Cycle. *Science* **294,** 2119–2124. ISSN: 00368075. doi:10.1126/science.1064034 (2001).
3. Xu, J., Hu, W., Liang, D. & Gao, P. Photochemical impacts on the toxicity of $PM_{2.5}$. *Critical Reviews in Environmental Science and Technology*, 1–27. ISSN: 1064-3389. doi:10.1080/10643389.2020.1816126 (2020).
4. Milton, D. K. A Rosetta Stone for understanding infectious drops and aerosols. *Journal of the Pediatric Infectious Diseases Society*, 1–3. ISSN: 2048-7207. doi:10.1093/jpids/piaa079 (2020).
5. Sorensen, C. M., Flagan, R. C., Baltensperger, U. & Pui, D. Y. H. Grand challenges for aerosol science and technology. *Aerosol Science and Technology* **53,** 731–734. ISSN: 0278-6826. doi:10.1080/02786826.2019.1611333 (2019).
6. Fröhlich-Nowoisky, J. *et al.* Bioaerosols in the Earth system: Climate, health, and ecosystem interactions. *Atmospheric Research* **182,** 346–376. ISSN: 01698095. doi:10.1016/j.atmosres.2016.07.018 (2016).
7. Frey, M. M. *et al.* First direct observation of sea salt aerosol production from blowing snow above sea ice. *Atmospheric Chemistry and Physics* **20,** 2549–2578. ISSN: 16807324. doi:10.5194/acp-20-2549-2020 (2020).
8. Faber, P., Drewnick, F. & Borrmann, S. Aerosol particle and trace gas emissions from earthworks, road construction, and asphalt paving in Germany: Emission factors and influence on local air quality. *Atmospheric Environment* **122,** 662–671. ISSN: 13522310. doi:10.1016/j.atmosenv.2015.10.036 (2015).
9. Thorpe, A. & Harrison, R. M. Sources and properties of non-exhaust particulate matter from road traffic: A review. *Science of The Total Environment* **400,** 270–282. ISSN: 00489697. doi:10.1016/j.scitotenv.2008.06.007 (2008).
10. Jimenez, J. L. *et al.* Evolution of organic aerosols in the atmosphere. *Science* **326,** 1525–1529. ISSN: 0036-8075. doi:10.1126/science.1180353 (2009).
11. Dunne, E. M. *et al.* Global atmospheric particle formation from CERN CLOUD measurements. *Science* **354,** 1119–1124. ISSN: 10959203. doi:10.1126/science.aaf2649 (2016).
12. Gordon, H. *et al.* Causes and importance of new particle formation in the present-day and preindustrial atmospheres. *Journal of Geophysical Research: Atmospheres* **122,** 8739–8760. ISSN: 21698996. doi:10.1002/2017JD026844 (2017).
13. Kirkby, J. *et al.* Role of sulphuric acid, ammonia and galactic cosmic rays in atmospheric aerosol nucleation. *Nature* **476,** 429–435. ISSN: 00280836. doi:10.1038/nature10343 (2011).

14. Almeida, J. *et al.* Molecular understanding of sulphuric acid–amine particle nucleation in the atmosphere. *Nature* **502,** 359–363. ISSN: 0028-0836. doi:10.1038/nature12663 (2013).

15. Jokinen, T. *et al.* Ion-induced sulfuric acid – ammonia nucleation drives particle formation in coastal Antarctica. *Science Advances* **4,** eaat9744. ISSN: 2375-2548. doi:10.1126/sciadv.aat9744 (2018).

16. Yao, L. *et al.* Atmospheric new particle formation from sulfuric acid and amines in a Chinese megacity. *Science* **361,** 278–281. ISSN: 10959203. doi:10.1126/science.aao4839 (2018).

17. Lee, S. H. *et al.* New particle formation in the atmosphere: from molecular clusters to global climate. *Journal of Geophysical Research: Atmospheres* **124,** 7098–7146. ISSN: 21698996. doi:10.1029/2018JD029356 (2019).

18. Bianchi, F. *et al.* New particle formation in the free troposphere: A question of chemistry and timing. *Science* **352,** 1109–1112. ISSN: 0036-8075. doi:10.1126/science.aad5456 (2016).

19. Kirkby, J. *et al.* Ion-induced nucleation of pure biogenic particles. *Nature* **533,** 521–526. ISSN: 14764687. doi:10.1038/nature17953 (2016).

20. Sipilä, M. *et al.* Molecular-scale evidence of aerosol particle formation via sequential addition of HIO_3. *Nature* **537,** 532–534. ISSN: 14764687. doi:10.1038/nature19314 (2016).

21. Baccarini, A. *et al.* Frequent new particle formation over the high Arctic pack ice by enhanced iodine emissions. *Nature Communications* **11,** 4924. ISSN: 2041-1723. doi:10.1038/s41467-020-18551-0 (2020).

22. Hoppel, W. A., Fitzgerald, J. W. & Larson, R. E. Aerosol size distributions in air masses advecting off the east coast of the United States. *Journal of Geophysical Research* **90,** 2365. ISSN: 0148-0227. doi:10.1029/JD090iD01p02365 (1985).

23. Hudson, J. G., Noble, S. & Tabor, S. Cloud supersaturations from CCN spectra Hoppel minima. *Journal of Geophysical Research: Atmospheres* **120,** 3436–3452. ISSN: 2169-897X. doi:10.1002/2014JD022669 (2015).

24. Masson-Delmotte, V. *et al.* IPCC, 2018: Global Warming of 1.5°C. An IPCC Special Report on the impacts of global warming of 1.5°C above pre-industrial levels and related global greenhouse gas emission pathways, in the context of strengthening the global response to the threat of climate change, sustainable development, and efforts to eradicate poverty. *Intergovernmental Panel on Climate Change (IPCC)* (2018).

25. Pörtner, H.-O. *et al.* IPCC special report on the ocean and cryosphere in a changing climate. *IPCC Intergovernmental Panel on Climate Change (IPCC)* (2019).

26. Stocker, T. F. *et al.* Climate Change 2013: The physical science basis. contribution of working group I to the fifth assessment report of IPCC the intergovernmental panel on climate change (2014).

27. Boucher, O. & Haywood, J. On summing the components of radiative forcing of climate change. *Climate Dynamics* **18,** 297–302. ISSN: 0930-7575. doi:10.1007/s003820100185 (2001).

28. Solomon, S. *et al.* Contribution of Working Group I to the Fourth Assessment Report of the Intergovernmental Panel on Climate Change, 2007 (2007).

29. Carslaw, K. S. *et al.* Large contribution of natural aerosols to uncertainty in indirect forcing. *Nature* **503,** 67–71. ISSN: 00280836. doi:10.1038/nature12674 (2013).

30. Carslaw, K. S. *et al.* Aerosols in the Pre-industrial Atmosphere. *Current Climate Change Reports* **3,** 1–15. ISSN: 21986061. doi:10.1007/s40641-017-0061-2 (2017).

31. Regayre, L. A. *et al.* The value of remote marine aerosol measurements for constraining radiative forcing uncertainty. *Atmospheric Chemistry and Physics* **20,** 10063–10072. ISSN: 1680-7324. doi:10.5194/acp-20-10063-2020 (2020).

32. Serreze, M. C. & Francis, J. A. The Arctic Amplification Debate. *Climatic Change* **76,** 241–264. ISSN: 0165-0009. doi:10.1007/s10584-005-9017-y (2006).

33. Cohen, J. *et al.* Recent Arctic amplification and extreme mid-latitude weather. *Nature Geoscience* **7,** 627–637. ISSN: 17520908. doi:10.1038/ngeo2234 (2014).

34. Seneviratne, S. I., Donat, M. G., Pitman, A. J., Knutti, R. & Wilby, R. L. Allowable CO_2 emissions based on regional and impact-related climate targets. *Nature* **529,** 477–483. ISSN: 14764687. doi:10.1038/nature16542 (2016).

35. Richter-Menge, J. *et al.* The Arctic [in "State of the Climate in 2019"]. *Bulletin of the American Meteorological Society* **101** (eds Richter-Menge, J. & Druckenmiller, M. L.) S239–S286. ISSN: 0003-0007. doi:10.1175/BAMS-D-20-0086.1 (2020).

36. Polyak, L. *et al.* History of sea ice in the Arctic. *Quaternary Science Reviews* **29,** 1757–1778. ISSN: 02773791. doi:10.1016/j.quascirev.2010.02.010 (2010).

37. Pithan, F. & Mauritsen, T. Arctic amplification dominated by temperature feedbacks in contemporary climate models. *Nature Geoscience* **7,** 181–184. ISSN: 17520908. doi:10.1038/ngeo2071 (2014).

38. Lique, C., Holland, M. M., Dibike, Y. B., Lawrence, D. M. & Screen, J. A. Modeling the Arctic freshwater system and its integration in the global system: Lessons learned and future challenges. *Journal of Geophysical Research G: Biogeosciences* **121,** 540–566. ISSN: 21698961. doi:10.1002/2015JG003120 (2016).

39. Collins, M. *et al.* in *Climate Change 2013-The Physical Science Basis: Contribution of Working Group I to the Fifth Assessment Report of the Intergovernmental Panel on Climate Change* 1029–1136 (Cambridge University Press, 2013).

40. Korhonen, H. *et al.* Aerosol climate feedback due to decadal increases in Southern Hemisphere wind speeds. *Geophysical Research Letters* **37,** 1–6. ISSN: 00948276. doi:10.1029/2009GL041320 (2010).

41. Hamilton, D. S. *et al.* Occurrence of pristine aerosol environments on a polluted planet. *Proceedings of the National Academy of Sciences* **111,** 18466–18471. ISSN: 0027-8424. doi:10.1073/pnas.1415440111 (2014).

42. Schmale, J. *et al.* Overview of the antarctic circumnavigation expedition: Study of preindustrial-like aerosols and their climate effects (ACE-SPACE). *Bulletin of the American Meteorological Society* **100,** 2260–2283. ISSN: 00030007. doi:10.1175/BAMS-D-18-0187.1 (2019).

43. Uetake, J. *et al.* Airborne bacteria confirm the pristine nature of the Southern Ocean boundary layer. *Proceedings of the National Academy of Sciences* **117,** 13275–13282. ISSN: 0027-8424. doi:10.1073/pnas.2000134117 (2020).

44. Quinn, P. K., Coffman, D. J., Johnson, J. E., Upchurch, L. M. & Bates, T. S. Small fraction of marine cloud condensation nuclei made up of sea spray aerosol. *Nature Geoscience* **10,** 674–679. ISSN: 17520908. doi:10.1038/ngeo3003 (2017).

45. Fossum, K. N. *et al.* Summertime primary and secondary contributions to Southern Ocean cloud condensation nuclei. *Scientific Reports* **8,** 13844. ISSN: 2045-2322. doi:10.1038/s41598-018-32047-4 (2018).

46. Kreidenweis, S. M., McInnes, L. M. & Brechtel, F. J. Observations of aerosol volatility and elemental composition at Macquarie Island during the First Aerosol Characterization Experiment (ACE 1). *Journal of Geophysical Research: Atmospheres* **103,** 16511–16524. ISSN: 01480227. doi:10.1029/98JD00800 (1998).

47. Weber, R. J. *et al.* A study of new particle formation and growth involving biogenic and trace gas species measured during ACE 1. *Journal of Geophysical Research Atmospheres* **103,** 16385–16396. ISSN: 01480227. doi:10.1029/97JD02465 (1998).

48. Hoffmann, E. H. *et al.* An advanced modeling study on the impacts and atmospheric implications of multiphase dimethyl sulfide chemistry. *Proceedings of the National Academy of Sciences of the United States of America* **113,** 11776–11781. ISSN: 10916490. doi:10.1073/pnas.1606320113 (2016).

49. McCoy, D. T. *et al.* Natural aerosols explain seasonal and spatial patterns of Southern Ocean cloud albedo. *Science Advances* **1,** e1500157. ISSN: 2375-2548. doi:10.1126/sciadv.1500157 (2015).

50. McCoy, I. L. *et al.* The hemispheric contrast in cloud microphysical properties constrains aerosol forcing. *Proceedings of the National Academy of Sciences of the United States of America* **117,** 18998–19006. ISSN: 10916490. doi:10.1073/pnas.1922502117 (2020).

51. Humphries, R. S. *et al.* Boundary layer new particle formation over East Antarctic sea ice – possible Hg-driven nucleation? *Atmospheric Chemistry and Physics* **15,** 13339–13364. ISSN: 1680-7324. doi:10.5194/acp-15-13339-2015 (2015).

52. Dall'Osto, M. *et al.* Antarctic sea ice region as a source of biogenic organic nitrogen in aerosols. *Scientific Reports* **7,** 6047. ISSN: 20452322. doi:10.1038/s41598-017-06188-x (2017).

53. Weller, R., Schmidt, K., Teinilä, K. & Hillamo, R. Natural new particle formation at the coastal Antarctic site Neumayer. *Atmospheric Chemistry and Physics Discussions* **15,** 15655–15681. ISSN: 16807375. doi:10.5194/acpd-15-15655-2015 (2015).

54. Jang, E. *et al.* New particle formation events observed at the King Sejong Station, Antarctic Peninsula – Part 2: Link with the oceanic biological activities. *Atmospheric Chemistry and Physics* **19,** 7595–7608. ISSN: 1680-7324. doi:10.5194/acp-19-7595-2019 (2019).

55. Lachlan-Cope, T. *et al.* On the annual variability of Antarctic aerosol size distributions at Halley Research Station. *Atmospheric Chemistry and Physics* **20,** 4461–4476. ISSN: 1680-7324. doi:10.5194/acp-20-4461-2020 (2020).

56. Korhonen, H., Carslaw, K. S., Spracklen, D. V., Riley, D. A. & Ström, J. A global model study of processes controlling aerosol size distributions in the Arctic spring and summer. *Journal of Geophysical Research Atmospheres* **113,** 1–20. ISSN: 01480227. doi:https://doi.org/10.1029/2007JD009114 (2008).

57. Revell, L. E. *et al.* The sensitivity of Southern Ocean aerosols and cloud microphysics to sea spray and sulfate aerosol production in the HadGEM3-GA7.1 chemistry–climate model. *Atmospheric Chemistry and Physics* **19,** 15447–15466. ISSN: 1680-7324. doi:10.5194/acp-19-15447-2019 (2019).

58. Sanchez, K. J. *et al.* Measurement report: Cloud processes and the transport of biological emissions affect southern ocean particle and cloud condensation nuclei concentrations. *Atmospheric Chemistry and Physics* **21,** 3427–3446. doi:10.5194/acp-21-3427-2021 (2021).

59. Jefferson, A., Tanner, D. J., Eisele, F. L. & Berresheim, H. Sources and sinks of H_2SO_4 in the remote Antarctic marine boundary layer. *Journal of Geophysical Research: Atmospheres* **103,** 1639–1645. ISSN: 01480227. doi:10.1029/97JD01212 (1998).

60. Stolzenburg, D. *et al.* Enhanced growth rate of atmospheric particles from sulfuric acid. *Atmospheric Chemistry and Physics* **20,** 7359–7372. ISSN: 1680-7324. doi:10.5194/acp-20-7359-2020 (2020).

61. Intrieri, J. M. An annual cycle of Arctic surface cloud forcing at SHEBA. *Journal of Geophysical Research* **107,** 8039. ISSN: 0148-0227. doi:10.1029/2000JC000439 (2002).

62. Kapsch, M. L., Graversen, R. G., Tjernström, M. & Bintanja, R. The effect of downwelling longwave and shortwave radiation on Arctic summer sea ice. *Journal of Climate* **29,** 1143–1159. ISSN: 08948755. doi:10.1175/JCLI-D-15-0238.1 (2016).

63. Tjernström, M., Sedlar, J. & Shupe, M. D. How well do regional climate models reproduce radiation and clouds in the arctic? An evaluation of ARCMIP simulations. *Journal of Applied Meteorology and Climatology* **47,** 2405–2422. ISSN: 15588424. doi:10.1175/2008JAMC1845.1 (2008).

64. Stevens, R. G. *et al.* A model intercomparison of CCN-limited tenuous clouds in the high Arctic. *Atmospheric Chemistry and Physics* **18,** 11041–11071. ISSN: 16807324. doi:10.5194/acp-18-11041-2018 (2018).

65. Mauritsen, T. *et al.* An Arctic CCN-limited cloud-aerosol regime. *Atmospheric Chemistry and Physics* **11,** 165–173. ISSN: 16807316. doi:10.5194/acp-11-165-2011 (2011).

66. Leaitch, W. R. *et al.* Effects of 20 – 100 nm particles on liquid clouds in the clean summertime Arctic, 11107–11124. doi:10.5194/acp-16-11107-2016 (2016).

67. Chang, R. Y. *et al.* Aerosol composition and sources in the central Arctic Ocean during ASCOS. *Atmospheric Chemistry and Physics* **11,** 10619–10636. ISSN: 16807316. doi:10.5194/acp-11-10619-2011 (2011).

68. Sierau, B., Chang, R. Y., Leck, C., Paatero, J. & Lohmann, U. Single-particle characterization of the high-Arctic summertime aerosol. *Atmospheric Chemistry and Physics* **14,** 7409–7430. ISSN: 16807324. doi:10.5194/acp-14-7409-2014 (2014).

69. Heintzenberg, J., Leck, C. & Tunved, P. Potential source regions and processes of aerosol in the summer Arctic. *Atmospheric Chemistry and Physics* **15,** 6487–6502. ISSN: 1680-7324. doi:10.5194/acp-15-6487-2015 (2015).

70. Hamacher-Barth, E., Leck, C. & Jansson, K. Size-resolved morphological properties of the high Arctic summer aerosol during ASCOS-2008. *Atmospheric Chemistry and Physics* **16,** 6577–6593. ISSN: 16807324. doi:10.5194/acp-16-6577-2016 (2016).

71. Covert, D. S. *et al.* Aerosol number size distributions from 3 to 500 nm diameter in the arctic marine boundary layer during summer and autumn. *Tellus, Series B: Chemical and Physical Meteorology* **48,** 197–212. ISSN: 02806509. doi:10.3402/tellusb.v48i2.15886 (1996).

72. Wiedensohler, A. *et al.* Occurrence of an ultrafine particle mode less than 20 nm in diameter in the marine boundary layer during Arctic summer and autumn. *Tellus, Series B: Chemical and Physical Meteorology* **48,** 213–222. ISSN: 02806509. doi:10.3402/tellusb.v48i2.15887 (1996).

73. Kerminen, V.-M. & Leck, C. Sulfur chemistry over the central Arctic Ocean during the summer: Gas-to-particle transformation. *Journal of Geophysical Research: Atmospheres* **106,** 32087–32099. ISSN: 01480227. doi:10.1029/2000JD900604 (2001).

74. Karl, M., Leck, C., Gross, A. & Pirjola, L. A study of new particle formation in the marine boundary layer over the central Arctic Ocean using a flexible multicomponent aerosol dynamic model. *Tellus B: Chemical and Physical Meteorology* **64,** 17158. ISSN: 1600-0889. doi:10.3402/tellusb.v64i0.17158 (2012).

75. Karl, M., Leck, C., Coz, E. & Heintzenberg, J. Marine nanogels as a source of atmospheric nanoparticles in the high Arctic. *Geophysical Research Letters* **40,** 3738–3743. ISSN: 00948276. doi:10.1002/grl.50661 (2013).

76. Browse, J. *et al.* The complex response of Arctic aerosol to sea-ice retreat. *Atmospheric Chemistry and Physics* **14,** 7543–7557. ISSN: 16807324. doi:10.5194/acp-14-7543-2014 (2014).

77. Maslanik, J. & Stroeve, J. *Near-Real-Time DMSP SSMIS Daily Polar Gridded Sea Ice Concentrations, Version 1* Boulder, Colorado USA, 1999. doi:https://doi.org/10.5067/U8C09DWVX9LM.

78. Blundell, S. J. & Blundell, K. M. *Concepts in thermal physics* (Oxford University Press, 2010).

79. Kürten, A. *et al.* Neutral molecular cluster formation of sulfuric acid–dimethylamine observed in real time under atmospheric conditions. *Proceedings of the National Academy of Sciences* **111,** 15019–15024. ISSN: 0027-8424. doi:10.1073/pnas.1404853111 (2014).

80. Ehrhart, S. *et al.* Comparison of the SAWNUC model with CLOUD measurements of sulphuric acid-water nucleation. *Journal of Geophysical Research: Atmospheres* **121,** 12, 401–12, 414. ISSN: 2169-897X. doi:10.1002/2015JD023723 (2016).

81. Nieminen, T., Lehtinen, K. E. & Kulmala, M. Sub-10 nm particle growth by vapor condensation-effects of vapor molecule size and particle thermal speed. *Atmospheric Chemistry and Physics* **10,** 9773–9779. ISSN: 16807316. doi:10.5194/acp-10-9773-2010 (2010).

82. Kurtén, T., Noppel, M., Vehkamäki, H., Salonen, M. & Kulmala, M. Quantum chemical studies of hydrate formation of H_2SO_4 and HSO_4^-. *Boreal Environment Research* **12,** 431–453. ISSN: 12396095 (2007).

83. Myhre, C. E., Nielsen, C. J. & Saastad, O. W. Density and surface tension of aqueous H_2SO_4 at low temperature. *Journal of Chemical and Engineering Data* **43,** 617–622. ISSN: 00219568. doi:10.1021/je980013g (1998).

84. Sceats, M. G. Brownian coagulation in aerosols—the role of long range forces. *Journal of Colloid and Interface Science* **129,** 105–112. ISSN: 00219797. doi:10.1016/0021-9797(89)90419-0 (1989).

85. Gettelman, A., Fetzer, E. J., Eldering, A. & Irion, F. W. The global distribution of supersaturation in the upper troposphere from the Atmospheric Infrared Sounder. *Journal of Climate* **19,** 6089–6103. ISSN: 1520-0442. doi:10.1175/JCLI3955.1 (2006).

86. Junninen, H. *et al.* A high-resolution mass spectrometer to measure atmospheric ion composition. *Atmospheric Measurement Techniques* **3,** 1039–1053. ISSN: 18671381. doi:10.5194/amt-3-1039-2010 (2010).

87. Jokinen, T. *et al.* Atmospheric sulphuric acid and neutral cluster measurements using CI-APi-TOF. *Atmospheric Chemistry and Physics* **12,** 4117–4125. ISSN: 16807316. doi:10.5194/acp-12-4117-2012 (2012).

88. Riva, M. *et al.* Evaluating the performance of five different chemical ionization techniques for detecting gaseous oxygenated organic species. *Atmospheric Measurement Techniques Discussions*, 1–39. doi:10.5194/amt-2018-407 (2018).

89. Eisele, F. L. & Tanner, D. J. Measurement of the gas phase concentration of H_2SO_4 and methane sulfonic acid and estimates of H_2SO_4 production and loss in the atmosphere. *Journal of Geophysical Research* **98,** 9001–9010. ISSN: 01480227. doi:10.1029/93JD00031 (1993).

90. Wine, P. H. *et al.* Kinetics of the reaction OH + SO_2 + M $\longrightarrow$ $HOSO_2$ + M. Temperature and pressure dependence in the fall-off region. *The Journal of Physical Chemistry* **88,** 2095–2104. ISSN: 0022-3654. doi:10.1021/j150654a031 (1984).

91. Paulsen, D. *et al.* Secondary Organic Aerosol Formation by Irradiation of 1,3,5-Trimethylbenzene - NOx - H_2O in a New Reaction Chamber for Atmospheric Chemistry and Physics. *Environmental Science & Technology* **39,** 2668–2678. ISSN: 0013-936X. doi:10.1021/es0489137 (2005).

92. Dal Maso, M. *et al.* Condensation and coagulation sinks and formation of nucleation mode particles in coastal and boreal forest boundary layers. *Journal of Geophysical Research* **107,** 8097. ISSN: 0148-0227. doi:10.1029/2001JD001053 (2002).

93. Hanson, D. R. & Eisele, F. Diffusion of H2SO4 in humidified nitrogen: hydrated H2SO4. *The Journal of Physical Chemistry A* **104,** 1715–1719. ISSN: 1089-5639. doi:10.1021/jp993622j (2000).

94. Hanson, D. R. Mass Accommodation of H_2SO_4 and CH_3SO_3H on Water-Sulfuric Acid Solutions from 6% to 97% RH. *The Journal of Physical Chemistry A* **109,** 6919–6927. ISSN: 1089-5639. doi:10.1021/jp0510443 (2005).

95. Kramp, F. & Paulson, S. E. On the uncertainties in the rate coefficients for OH reactions with hydrocarbons, and the rate coefficients of the 1,3,5-trimethylbenzene and m-xylene reactions with OH radicals in the gas phase. *Journal of Physical Chemistry A* **102,** 2685–2690. ISSN: 10895639. doi:10.1021/jp973289o (1998).

96. Kürten, A., Rondo, L., Ehrhart, S. & Curtius, J. Calibration of a chemical ionization mass spectrometer for the measurement of gaseous sulfuric acid. *Journal of Physical Chemistry A* **116,** 6375–6386. ISSN: 10895639. doi:10.1021/jp212123n (2012).

97. Stolzenburg, M. R. & McMurry, P. H. An ultrafine aerosol condensation nucleus counter. *Aerosol Science and Technology* **14,** 48–65. ISSN: 15217388. doi:10.1080/02786829108959470 (1991).

98. McMurry, P. H. The History of Condensation Nucleus Counters. *Aerosol Science and Technology* **33,** 297–322. ISSN: 0278-6826. doi:10.1080/02786820050121512 (2000).

99. Kangasluoma, J. & Attoui, M. Review of sub-3 nm condensation particle counters, calibrations, and cluster generation methods. *Aerosol Science and Technology* **53,** 1277–1310. ISSN: 0278-6826. doi:10.1080/02786826.2019.1654084 (2019).

100. Fissan, H. J., Helsper, C. & Thielen, H. J. Determination of particle size distributions by neans of an electrostatic classifier. *Journal of Aerosol Science* **14,** 354–357. ISSN: 00218502. doi:10.1016/0021-8502(83)90133-7 (1983).

101. Wang, S. C. & Flagan, R. C. Scanning electrical mobility spectrometer. *Aerosol Science and Technology* **13,** 230–240. ISSN: 15217388. doi:10.1080/02786829008959441 (1990).

102. Wiedensohler, A. *et al.* Mobility particle size spectrometers: harmonization of technical standards and data structure to facilitate high quality long-term observations of atmospheric particle number size distributions. *Atmospheric Measurement Techniques* **5,** 657–685. ISSN: 1867-8548. doi:10.5194/amt-5-657-2012 (2012).

103. Mirme, S. & Mirme, A. The mathematical principles and design of the NAIS - A spectrometer for the measurement of cluster ion and nanometer aerosol size distributions. *Atmospheric Measurement Techniques* **6,** 1061–1071. ISSN: 18671381. doi:10.5194/amt-6-1061-2013 (2013).

104. Manninen, H. E., Mirme, S., Mirme, A., Petäjä, T. & Kulmala, M. How to reliably detect molecular clusters and nucleation mode particles with Neutral cluster and Air Ion Spectrometer (NAIS). *Atmospheric Measurement Techniques* **9,** 3577–3605. ISSN: 18678548. doi:10.5194/amt-9-3577-2016 (2016).

105. Wagner, R. *et al.* On the accuracy of ion measurements using a Neutral cluster and Air Ion Spectrometer. *Boreal Environment Research* **21,** 230–241. ISSN: 12396095 (2016).

106. Roberts, G. C. & Nenes, A. A continuous-flow streamwise thermal-gradient CCN chamber for atmospheric measurements. *Aerosol Science and Technology* **39,** 206–221. ISSN: 02786826. doi:10.1080/027868290913988 (2005).

107. Schmale, J. *et al.* Long-term cloud condensation nuclei number concentration, particle number size distribution and chemical composition measurements at regionally representative observatories. *Atmospheric Chemistry and Physics* **18,** 2853–2881. ISSN: 16807324. doi:10.5194/acp-18-2853-2018 (2018).

108. Manninen, H. E. *et al.* Long-term field measurements of charged and neutral clusters using Neutral cluster and Air Ion Spectrometer (NAIS). *Boreal Environment Research* **14,** 591–605. ISSN: 12396095 (2009).

109. Shingler, T. *et al.* Characterisation and airborne deployment of a new counterflow virtual impactor inlet. *Atmospheric Measurement Techniques* **5,** 1259–1269. ISSN: 18671381. doi:10.5194/amt-5-1259-2012 (2012).

110. Hinds, W. C. *Aerosol Technology: Properties, Behavior, and Measurement of Airborne Particles* (John Wiley & Sons, 1999).

111. Corbin, J. C. *et al.* Brown and black carbon emitted by a marine engine operated on heavy fuel oil and distillate fuels: optical properties, size distributions, and emission factors. *Journal of Geophysical Research: Atmospheres* **123,** 6175–6195. ISSN: 21698996. doi:10.1029/2017JD027818 (2018).

112. Celik, S. *et al.* Influence of vessel characteristics and atmospheric processes on the gas and particle phase of ship emission plumes: In situ measurements in the Mediterranean Sea and around the Arabian Peninsula. *Atmospheric Chemistry and Physics* **20,** 4713–4734. ISSN: 16807324. doi:10.5194/acp-20-4713-2020 (2020).

113. Leck, C. *et al.* Overview of the atmospheric research program during the International Arctic Ocean Expedition of 1991 (IAOE-91) and its scientific results. *Tellus, Series B: Chemical and Physical Meteorology* **48,** 136–155. ISSN: 02806509. doi:10.3402/tellusb.v48i2.15833 (1996).

114. Tjernström, M. *et al.* The Arctic Summer Cloud Ocean Study (ASCOS): Overview and experimental design. *Atmospheric Chemistry and Physics* **14,** 2823–2869. ISSN: 16807316. doi:10.5194/acp-14-2823-2014 (2014).

115. Humphries, R. S. *et al.* Identification of platform exhaust on the RV Investigator. *Atmospheric Measurement Techniques Discussions*, 1–25. doi:10.5194/amt-2018-214 (2018).

116. Baker, M. 1,500 scientists lift the lid on reproducibility. *Nature* **533,** 452–454. ISSN: 0028-0836. doi:10.1038/533452a (2016).

117. Munafò, M. R. *et al.* A manifesto for reproducible science. *Nature Human Behaviour* **1,** 0021. ISSN: 2397-3374. doi:10.1038/s41562-016-0021 (2017).

118. Showstack, R. New Arctic science cooperation agreement comes into force. *Eos* **99.** doi:https://doi.org/10.1029/2018EO099941 (2018).

119. Schmidt, B., Gemeinholzer, B. & Treloar, A. Open Data in Global Environmental Research: The Belmont Forum's Open Data Survey. *PLOS ONE* **11** (ed Guralnick, R.) e0146695. ISSN: 1932-6203. doi:10.1371/journal.pone.0146695 (2016).

120. Stuart, D. *et al.* Practical challenges for researchers in data sharing. *Whitepaper.* doi:https://doi.org/10.6084/m9.figshare.5971387 (2018).

121. Prytherch, J. *et al. Radiosonde data from the Arctic Ocean 2018 expedition* 2019. doi:https://doi.org/10.17043/ao2018-radiosonde-2.

122. Prytherch, J. *Weather data from MISU weather station during the Arctic Ocean 2018 expedition* 2020. doi:10.17043/ao2018-misu-weather-2.

123. Karlsson, L. & Zieger, P. *Aerosol particle number size distribution data collected during the Arctic Ocean 2018 expedition* 2020. doi:https://doi.org/10.17043/ao2018-aerosol-dmps.

124. Brooks, I., Brooks, B. & Achtert, P. *Aerosol and droplet size distributions and concentrations measured during the Arctic Ocean 2018 expedition* 2020. doi:https://doi.org/10.17043/ao2018-aerosol-fssp.

125. Baccarini, A., Schmale, J. & Dommen, J. *Iodic acid, sulfuric acid and methanesulfonic acid collected during the Arctic Ocean 2018 expedition.* 2020. doi:https://doi.org/10.17043/ao2018-aerosol-cims.

126. Baccarini, A., Schmale, J. & Dommen, J. *Size distribution of neutral and charged particles smaller than 42 nm collected during the Arctic Ocean 2018 expedition.* 2020. doi:https://doi.org/10.17043/ao2018-aerosol-nais.

127. Baccarini, A., Schmale, J. & Gysel-Beer, M. *Size distribution of interstitial and total particles between 18 and 660 nm collected during the Arctic Ocean 2018 expedition.* 2020. doi:https://doi.org/10.17043/ao2018-aerosol-smps.

128. Baccarini, A., Schmale, J. & Dommen, J. *Concentration of particles larger than 2.5 nm collected during the Arctic Ocean 2018 expedition.* 2020. doi:https://doi.org/10.17043/ao2018-aerosol-ucpc.

129. Baccarini, A., Schmale, J., Dommen, J., Karlsson, L. & Zieger, P. *Size distribution of aerosol particles between 2.5 and 920 nm measured during the Arctic Ocean 2018 expedition* 2020. doi:https://doi.org/10.17043/ao2018-aerosol-merged-psd.

130. Baccarini, A., Schmale, J. & Dommen, J. *Sulfuric acid condensation sink calculated for the Arctic Ocean 2018 expedition* (Bolin Centre Database, 2020). doi:https://doi.org/10.17043/ao2018-aerosol-condensation-sink.

131. Baccarini, A., Schmale, J. & Dommen, J. *Ultrafine particle concentration measured during the Arctic Ocean 2018 expedition* (Bolin Centre Database, 2020). doi:https://doi.org/10.17043/ao2018-aerosol-ufp.

132. Baccarini, A., Schmale, J. & Dommen, J. *Mask to identify polluted periods during the Arctic Ocean 2018 expedition* (Bolin Centre Database, 2020). doi:https://doi.org/10.17043/ao2018-aerosol-pollution-mask.

133. Baccarini, A., Schmale, J. & Dommen, J. *Ozone concentration measured during the Arctic Ocean 2018 expedition* 2020. doi:https://doi.org/10.17043/ao2018-aerosol-ozone.

134. Baccarini, A. *et al. Concentration of gaseous methanesulfonic acid measured over the Southern Ocean in the austral summer of 2016/2017, during the Antarctic Circumnavigation Expedition (ACE).* 2019. doi:10.5281/ZENODO.2636771.

135. Baccarini, A. *et al. Concentration of gaseous sulfuric acid measured over the Southern Ocean in the austral summer of 2016/2017, during the Antarctic Circumnavigation Expedition (ACE).* 2019. doi:10.5281/ZENODO.3265832.

136. Schmale, J. *et al. Trace gas mixing ratios measured over the Southern Ocean in the austral summer of 2016/2017, during the Antarctic Circumnavigation Expedition.* 2020. doi:10.5281/ZENODO.4028749.

137. Tatzelt, C. *et al. Cloud Condensation Nuclei number concentrations over the Southern Ocean during the austral summer of 2016/2017.* 2019. doi:10.5281/ZENODO.2636765.

138. Tatzelt, C. *et al. Ice Nucleating Particle number concentration over the Southern Ocean during the austral summer of 2016/2017 on board the Antarctic Circumnavigation Expedition (ACE).* 2019. doi:10.5281/ZENODO.2636777.

139. Schmale, J. *et al. Aerosol particle number concentration measured over the Southern Ocean in the austral summer of 2016/2017, during the Antarctic Circumnavigation Expedition.* 2019. doi:10.5281/ZENODO.2636690.

140. Tatzelt, C. *et al. Ionic composition of particulate matter (PM_{10}) from high-volume sampling over the Southern Ocean during the austral summer of 2016/2017 on board the Antarctic Circumnavigation Expedition (ACE).* 2020. doi:10.5281/ZENODO.3922147.

141. Schmale, J. *et al. Sub-micron aerosol particle size distribution collected in the Southern Ocean in the austral summer of 2016/2017, during the Antarctic Circumnavigation Expedition.* 2019. doi:10.5281/ZENODO.2636700.

142. Schmale, J. *et al. Coarse mode aerosol particle size distribution collected in the Southern Ocean in the austral summer of 2016/2017, during the Antarctic Circumnavigation Expedition.* 2019. doi:10.5281/ZENODO.2636709.

143. Schmale, J. *et al. Equivalent black carbon aerosol measured over the Southern Ocean in the austral summer of 2016/2017, during the Antarctic Circumnavigation Expedition.* 2019. doi:10.5281/ZENODO.2636763.

144. Bony, S. & Stevens, B. *Clouds, circulation and climate sensitivity: How the interactions between clouds, greenhouse gases and aerosols affect temperature and precipitation in a changing climate* tech. rep. (2012), 7.

145. Flato, G. *et al.* Climate change 2013: the physical science basis. Contribution of Working Group I to the Fifth Assessment Report of the Intergovernmental Panel on Climate Change. *Evaluation of Climate Models, eds TF Stocker, D. Qin, G.-K. Plattner, M. Tignor, SK Allen, J. Boschung, et al.(Cambridge: Cambridge University Press)* (2013).

146. Ceppi, P., Hwang, Y.-T., Frierson, D. M. W. & Hartmann, D. L. Southern Hemisphere jet latitude biases in CMIP5 models linked to shortwave cloud forcing. *Geophysical Research Letters* **39,** n/a–n/a. ISSN: 00948276. doi:10.1029/2012GL053115 (2012).

147. Hwang, Y.-T. & Frierson, D. M. W. Link between the double-Intertropical Convergence Zone problem and cloud biases over the Southern Ocean. *Proceedings of the National Academy of Sciences* **110,** 4935–4940. ISSN: 0027-8424. doi:10.1073/pnas.1213302110 (2013).

148. Kay, J. E. *et al.* Global climate impacts of fixing the Southern Ocean shortwave radiation bias in the Community Earth System Model (CESM). *Journal of Climate* **29,** 4617–4636. ISSN: 0894-8755. doi:10.1175/JCLI-D-15-0358.1 (2016).

149. Bodas-Salcedo, A. *et al.* Origins of the solar radiation biases over the Southern Ocean in CFMIP2 models. *Journal of Climate* **27,** 41–56. ISSN: 08948755. doi:10.1175/JCLI-D-13-00169.1 (2014).

150. Trenberth, K. E. & Fasullo, J. T. Simulation of Present-Day and Twenty-First-Century Energy Budgets of the Southern Oceans. *Journal of Climate* **23,** 440–454. ISSN: 1520-0442. doi:10.1175/2009JCLI3152.1 (2010).

151. Huang, Y. *et al.* Evaluation of boundary-layer cloud forecasts over the Southern Ocean in a limited-area numerical weather prediction system using in situ , space-borne and ground-based observations. *Quarterly Journal of the Royal Meteorological Society* **141,** 2259–2276. ISSN: 00359009. doi:10.1002/qj.2519 (2015).

152. Vergara-Temprado, J. *et al.* Strong control of Southern Ocean cloud reflectivity by ice-nucleating particles. *Proceedings of the National Academy of Sciences* **115,** 2687–2692. ISSN: 0027-8424. doi:10.1073/pnas.1721627115 (2018).

153. Hanley, K. E., Belcher, S. E. & Sullivan, P. P. A global climatology of wind–wave interaction. *Journal of Physical Oceanography* **40,** 1263–1282. ISSN: 1520-0485. doi:10.1175/2010JPO4377.1 (2010).

154. Reutter, P. *et al.* Aerosol- and updraft-limited regimes of cloud droplet formation: influence of particle number, size and hygroscopicity on the activation of cloud condensation nuclei (CCN). *Atmospheric Chemistry and Physics* **9,** 7067–7080. ISSN: 1680-7324. doi:10.5194/acp-9-7067-2009 (2009).

155. Ayers, G. P., Cainey, J. M., Gillett, R. W. & Ivey, J. P. Atmospheric sulphur and cloud condensation nuclei in marine air in the Southern Hemisphere. *Philosophical Transactions of the Royal Society of London. Series B: Biological Sciences* **352** (eds Cox, R. A. *et al.*) 203–211. ISSN: 0962-8436. doi:10.1098/rstb.1997.0015 (1997).

156. O'Dowd, C. D. *et al.* Biogenic sulphur emissions and inferred non-sea-salt-sulphate cloud condensation nuclei in and around Antarctica. *Journal of Geophysical Research: Atmospheres* **102,** 12839–12854. ISSN: 01480227. doi:10.1029/96JD02749 (1997).

157. Bates, T. S. & Quinn, P. K. Dimethylsulfide (DMS) in the equatorial Pacific Ocean (1982 to 1996): Evidence of a climate feedback? *Geophysical Research Letters* **24,** 861–864. ISSN: 00948276. doi:10.1029/97GL00784 (1997).

158. Boers, R., Jensen, J. B., Krummel, P. B. & Gerber, H. Microphysical and short-wave radiative structure of wintertime stratocumulus clouds over the Southern Ocean. *Quarterly Journal of the Royal Meteorological Society* **122,** 1307–1339. ISSN: 00359009. doi:10.1256/smsqj.53404 (1996).

159. Boers, R., Jensen, J. B. & Krummel, P. B. Microphysical and short-wave radiative structure of stratocumulus clouds over the Southern Ocean: Summer results and seasonal differences. *Quarterly Journal of the Royal Meteorological Society* **124,** 151–168. ISSN: 00359009. doi:10.1002/qj.49712454507 (1998).

160. Bates, T. S., Huebert, B. J., Gras, J. L., Griffiths, F. B. & Durkee, P. A. International Global Atmospheric Chemistry (IGAC) project's first Aerosol Characterization Experiment (ACE 1): overview. *Journal of Geophysical Research: Atmospheres* **103,** 16297–16318. ISSN: 01480227. doi:10.1029/97JD03741 (1998).

161. Vana, M. *et al.* Air ion measurements during a cruise from Europe to Antarctica. *Nucleation and Atmospheric Aerosols: 17th International Conference, Galway, Ireland, 2007,* 368 (2007).

162. Wofsy, S. C. HIAPER Pole-to-Pole Observations (HIPPO): fine-grained, global-scale measurements of climatically important atmospheric gases and aerosols. *Philosophical Transactions of the Royal Society A: Mathematical, Physical and Engineering Sciences* **369,** 2073–2086. ISSN: 1364-503X. doi:10.1098/rsta.2010.0313 (2011).

163. Law, C. S. *et al.* Overview and preliminary results of the Surface Ocean Aerosol Production (SOAP) campaign. *Atmospheric Chemistry and Physics* **17,** 13645–13667. ISSN: 1680-7324. doi:10.5194/acp-17-13645-2017 (2017).

164. Humphries, R. S. *et al.* Unexpectedly high ultrafine aerosol concentrations above East Antarctic sea ice. *Atmospheric Chemistry and Physics* **16,** 2185–2206. ISSN: 1680-7324. doi:10.5194/acp-16-2185-2016 (2016).

165. Kohout, A. L., Williams, M. J. M., Dean, S. M. & Meylan, M. H. Storm-induced sea-ice breakup and the implications for ice extent. *Nature* **509,** 604–607. ISSN: 0028-0836. doi:10.1038/nature13262 (2014).

166. O'Shea, S. J. *et al.* In situ measurements of cloud microphysics and aerosol over coastal Antarctica during the MAC campaign. *Atmospheric Chemistry and Physics* **17,** 13049–13070. ISSN: 1680-7324. doi:10.5194/acp-17-13049-2017 (2017).

167. Stephens, B. B. *et al.* The O_2/N_2 ratio and CO_2 airborne Southern Ocean study. *Bulletin of the American Meteorological Society* **99,** 381–402. ISSN: 00030007. doi:10.1175/BAMS-D-16-0206.1 (2018).

168. Protat, A. *et al.* Shipborne observations of the radiative effect of Southern Ocean clouds. *Journal of Geophysical Research: Atmospheres* **122,** 318–328. ISSN: 2169897X. doi:10.1002/2016JD026061 (2017).

169. Mace, G. G. & Protat, A. Clouds over the Southern Ocean as observed from the R/V investigator during CAPRICORN. Part I: Cloud occurrence and phase partitioning. *Journal of Applied Meteorology and Climatology* **57,** 1783–1803. ISSN: 15588432. doi:10.1175/JAMC-D-17-0194.1 (2018).

170. Mann, G. W. *et al.* Description and evaluation of GLOMAP-mode: a modal global aerosol microphysics model for the UKCA composition-climate model. *Geoscientific Model Development* **3,** 519–551. ISSN: 1991-9603. doi:10.5194/gmd-3-519-2010 (2010).

171. Schmale, J. *et al.* Sub-Antarctic marine aerosol: Dominant contributions from biogenic sources. *Atmospheric Chemistry and Physics* **13,** 8669–8694. ISSN: 16807316. doi:10.5194/acp-13-8669-2013 (2013).

172. Schmidt, A. *et al.* Importance of tropospheric volcanic aerosol for indirect radiative forcing of climate. *Atmospheric Chemistry and Physics* **12,** 7321–7339. ISSN: 1680-7324. doi:10.5194/acp-12-7321-2012 (2012).

173. Chen, Q., Sherwen, T., Evans, M. & Alexander, B. DMS oxidation and sulfur aerosol formation in the marine troposphere: a focus on reactive halogen and multiphase chemistry. *Atmospheric Chemistry and Physics* **18,** 13617–13637. ISSN: 1680-7324. doi:10.5194/acp-18-13617-2018 (2018).

174. Hodshire, A. L. *et al.* The potential role of methanesulfonic acid (MSA) in aerosol formation and growth and the associated radiative forcings. *Atmospheric Chemistry and Physics* **19,** 3137–3160. ISSN: 1680-7324. doi:10.5194/acp-19-3137-2019 (2019).

175. Twomey, S. The influence of pollution on the shortwave albedo of clouds. *Journal of the Atmospheric Sciences* **34,** 1149–1152. ISSN: 0022-4928. doi:10.1175/1520-0469(1977)034⟨1149:TIOPOT⟩2.0.CO;2 (1977).

176. Freud, E. & Rosenfeld, D. Linear relation between convective cloud drop number concentration and depth for rain initiation. *Journal of Geophysical Research: Atmospheres* **117,** 1–13. ISSN: 01480227. doi:10.1029/2011JD016457 (2012).

177. Albrecht, B. A. Aerosols, cloud microphysics, and fractional cloudiness. *Science* **245,** 1227–1230. ISSN: 0036-8075. doi:10.1126/science.245.4923.1227 (1989).

178. Rosenfeld, D., Kaufman, Y. J. & Koren, I. Switching cloud cover and dynamical regimes from open to closed Benard cells in response to the suppression of precipitation by aerosols. *Atmospheric Chemistry and Physics* **6,** 2503–2511. ISSN: 1680-7324. doi:10.5194/acp-6-2503-2006 (2006).

179. Goren, T. & Rosenfeld, D. Satellite observations of ship emission induced transitions from broken to closed cell marine stratocumulus over large areas. *Journal of Geophysical Research: Atmospheres* **117,** n/a–n/a. ISSN: 01480227. doi:10.1029/2012JD017981 (2012).

180. Rosenfeld, D. *et al.* Aerosol-driven droplet concentrations dominate coverage and water of oceanic low-level clouds. *Science* **363,** 1–17. ISSN: 10959203. doi:10.1126/science.aav0566 (2019).

181. Twomey, S. The nuclei of natural cloud formation part II: The supersaturation in natural clouds and the variation of cloud droplet concentration. *Geofisica Pura e Applicata* **43,** 243–249. ISSN: 0033-4553. doi:10.1007/BF01993560 (1959).

182. Regayre, L. A. *et al.* Aerosol and physical atmosphere model parameters are both important sources of uncertainty in aerosol ERF. *Atmospheric Chemistry and Physics* **18,** 9975–10006. ISSN: 1680-7324. doi:10.5194/acp-18-9975-2018 (2018).

183. Regayre, L. A. *et al.* Uncertainty in the magnitude of aerosol-cloud radiative forcing over recent decades. *Geophysical Research Letters* **41,** 9040–9049. ISSN: 00948276. doi:10.1002/2014GL062029 (2014).

184. Wernli, H. & Davies, H. C. A Lagrangian-based analysis of extratropical cyclones. I: The method and some applications. *Quarterly Journal of the Royal Meteorological Society* **123,** 467–489. ISSN: 1477870X. doi:10.1256/smsqj.53810 (1997).

185. Sprenger, M. & Wernli, H. The LAGRANTO Lagrangian analysis tool - Version 2.0. *Geoscientific Model Development* **8,** 2569–2586. ISSN: 19919603. doi:10.5194/gmd-8-2569-2015 (2015).

186. O'Connor, F. M. *et al.* Evaluation of the new UKCA climate-composition model – Part 2: The Troposphere. *Geoscientific Model Development* **7,** 41–91. ISSN: 1991-9603. doi:10.5194/gmd-7-41-2014 (2014).

187. Yoshioka, M. *et al.* Ensembles of global climate model variants designed for the quantification and constraint of uncertainty in aerosols and their radiative forcing. *Journal of Advances in Modeling Earth Systems* **11,** 3728–3754. ISSN: 19422466. doi:10.1029/2019MS001628 (2019).

188. Dee, D. P. *et al.* The ERA-Interim reanalysis: configuration and performance of the data assimilation system. *Quarterly Journal of the Royal Meteorological Society* **137,** 553–597. ISSN: 00359009. doi:10.1002/qj.828 (2011).

189. Papritz, L. *et al.* The Role of Extratropical Cyclones and Fronts for Southern Ocean Freshwater Fluxes. *Journal of Climate* **27,** 6205–6224. ISSN: 0894-8755. doi:10.1175/JCLI-D-13-00409.1 (2014).

190. Turner, J. *et al.* Unprecedented springtime retreat of Antarctic sea ice in 2016. *Geophysical Research Letters* **44,** 6868–6875. ISSN: 00948276. doi:10.1002/2017GL073656 (2017).

191. Schlosser, E., Haumann, F. A. & Raphael, M. N. Atmospheric influences on the anomalous 2016 Antarctic sea ice decay. *The Cryosphere* **12,** 1103–1119. ISSN: 1994-0424. doi:10.5194/tc-12-1103-2018 (2018).

192. Young, I. An intercomparison of GEOSAT, TOPEX and ERS1 measurements of wind speed and wave height. *Ocean Engineering* **26,** 67–81. ISSN: 00298018. doi:10.1016/S0029-8018(97)10016-6 (1998).

193. Monahan, E. C., Spiel, D. E. & Davidson, K. L. *A Model of Marine Aerosol Generation Via Whitecaps and Wave Disruption* Oceanic Wh (eds Monahan, E. C. & Niocaill, G. M.) ISBN: 978-94-009-4668-2. doi:https://doi.org/10.1007/978-94-009-4668-2_16 (Springer, 1986).

194. Johnson, R., Strutton, P. G., Wright, S. W., McMinn, A. & Meiners, K. M. Three improved satellite chlorophyll algorithms for the Southern Ocean. *Journal of Geophysical Research: Oceans* **118,** 3694–3703. ISSN: 21699275. doi:10.1002/jgrc.20270 (2013).

195. Cozic, J. *et al.* Scavenging of black carbon in mixed phase clouds at the high alpine site Jungfraujoch. *Atmospheric Chemistry and Physics* **7,** 1797–1807. ISSN: 1680-7324. doi:10.5194/acp-7-1797-2007 (2007).

196. Wang, Z. B. *et al.* Long-term measurements of particle number size distributions and the relationships with air mass history and source apportionment in the summer of Beijing. *Atmospheric Chemistry and Physics* **13,** 10159–10170. ISSN: 1680-7324. doi:10.5194/acp-13-10159-2013 (2013).

197. Pikridas, M. *et al.* In situ formation and spatial variability of particle number concentration in a European megacity. *Atmospheric Chemistry and Physics* **15,** 10219–10237. ISSN: 1680-7324. doi:10.5194/acp-15-10219-2015 (2015).

198. McCluskey, C. S. *et al.* Marine and terrestrial organic ice-nucleating particles in pristine marine to continentally influenced northeast atlantic air masses. *Journal of Geophysical Research: Atmospheres* **123,** 6196–6212. ISSN: 2169897X. doi:10.1029/2017JD028033 (2018).

199. Bigg, E. K. Ice Nucleus Concentrations in Remote Areas. *Journal of the Atmospheric Sciences* **30,** 1153–1157. ISSN: 0022-4928. doi:10.1175/1520-0469(1973)030⟨1153:INCIRA⟩2.0.CO;2 (1973).

200. McCluskey, C. S. *et al.* Observations of ice nucleating particles over Southern Ocean Waters. *Geophysical Research Letters* **45,** 11, 989–11, 997. ISSN: 00948276. doi:10.1029/2018GL079981 (2018).

201. Hoppel, W. & Frick, G. Submicron aerosol size distributions measured over the tropical and South Pacific. *Atmospheric Environment. Part A. General Topics* **24,** 645–659. ISSN: 09601686. doi:10.1016/0960-1686(90)90020-N (1990).

202. Clarke, A. D. *et al.* Particle nucleation in the tropical boundary sulfur sources. *Science* **282,** 89–92 (1998).

203. Gras, J. L., Jimi, S. I., Siems, S. T. & Krummel, P. B. Postfrontal nanoparticles at Cape Grim: Observations. *Environmental Chemistry* **6,** 508–514. ISSN: 14482517. doi:10.1071/EN09075 (2009).

204. Quinn, P. K. *et al.* Contribution of sea surface carbon pool to organic matter enrichment in sea spray aerosol. *Nature Geoscience* **7,** 228–232. ISSN: 1752-0894. doi:10.1038/ngeo2092 (2014).

205. Modini, R. L. *et al.* Primary marine aerosol-cloud interactions off the coast of California. *Journal of Geophysical Research: Atmospheres* **120,** 4282–4303. ISSN: 2169897X. doi:10.1002/2014JD022963 (2015).

206. Prather, K. A. *et al.* Bringing the ocean into the laboratory to probe the chemical complexity of sea spray aerosol. *Proceedings of the National Academy of Sciences* **110,** 7550–7555. ISSN: 0027-8424. doi:10.1073/pnas.1300262110 (2013).

207. Grazioli, J. *et al.* Katabatic winds diminish precipitation contribution to the Antarctic ice mass balance. *Proceedings of the National Academy of Sciences* **114,** 10858–10863. ISSN: 0027-8424. doi:10.1073/pnas.1707633114 (2017).

208. Saxena, V. K. Bursts of cloud condensation nuclei (CCN) by dissipating clouds at Palmer Station, Antarctica. *Geophysical Research Letters* **23,** 69–72. ISSN: 00948276. doi:10.1029/95GL03588 (1996).

209. Petters, M. D. & Kreidenweis, S. M. A single parameter representation of hygroscopic growth and cloud condensation nucleus activity. *Atmospheric Chemistry and Physics* **7,** 1961–1971. ISSN: 1680-7324. doi:10.5194/acp-7-1961-2007 (2007).

210. Johnson, G., Ristovski, Z. & Morawska, L. Method for measuring the hygroscopic behaviour of lower volatility fractions in an internally mixed aerosol. *Journal of Aerosol Science* **35,** 443–455. ISSN: 00218502. doi:10.1016/j.jaerosci.2003.10.008 (2004).

211. Zieger, P. *et al.* Revising the hygroscopicity of inorganic sea salt particles. *Nature Communications* **8,** 15883. ISSN: 2041-1723. doi:10.1038/ncomms15883 (2017).

212. Asmi, E. *et al.* Hygroscopicity and chemical composition of antarctic sub-micrometre aerosol particles and observations of new particle formation. *Atmospheric Chemistry and Physics* **10,** 4253–4271. ISSN: 16807316. doi:10.5194/acp-10-4253-2010 (2010).

213. O'Dowd, C. D. *et al.* Biogenically driven organic contribution to marine aerosol. *Nature* **431,** 676–680. ISSN: 0028-0836. doi:10.1038/nature02959 (2004).

214. Ovadnevaite, J. *et al.* Surface tension prevails over solute effect in organic-influenced cloud droplet activation. *Nature* **546,** 637–641. ISSN: 0028-0836. doi:10.1038/nature22806 (2017).

215. Rosenfeld, D. *et al.* Satellite retrieval of cloud condensation nuclei concentrations by using clouds as CCN chambers. *Proceedings of the National Academy of Sciences* **113,** 5828–5834. ISSN: 0027-8424. doi:10.1073/pnas.1514044113 (2016).

216. Johnson, J. S. *et al.* The importance of comprehensive parameter sampling and multiple observations for robust constraint of aerosol radiative forcing. *Atmospheric Chemistry and Physics* **18,** 13031–13053. ISSN: 1680-7324. doi:10.5194/acp-18-13031-2018 (2018).

217. Schutgens, N. *et al.* On the spatio-temporal representativeness of observations. *Atmospheric Chemistry and Physics* **17,** 9761–9780. ISSN: 1680-7324. doi:10.5194/acp-17-9761-2017 (2017).

218. Weingartner, E., Nyeki, S. & Baltensperger, U. Seasonal and diurnal variation of aerosol size distributions ($10 < D < 750$ nm) at a high-alpine site (Jungfraujoch 3580 m asl). *Journal of Geophysical Research: Atmospheres* **104,** 26809–26820. ISSN: 01480227. doi:10.1029/1999JD900170 (1999).

219. Ng, N. L. *et al.* An Aerosol Chemical Speciation Monitor (ACSM) for Routine Monitoring of the Composition and Mass Concentrations of Ambient Aerosol. *Aerosol Science and Technology* **45,** 780–794. ISSN: 0278-6826. doi:10.1080/02786826.2011.560211 (2011).

220. Fröhlich, R. *et al.* The ToF-ACSM: a portable aerosol chemical speciation monitor with TOFMS detection. *Atmospheric Measurement Techniques* **6,** 3225–3241. ISSN: 1867-8548. doi:10.5194/amt-6-3225-2013 (2013).

221. Conen, F., Henne, S., Morris, C. E. & Alewell, C. Atmospheric ice nucleators active > -12°C can be quantified on PM_{10} filter. *Atmospheric Measurement Techniques* **5,** 321–327. ISSN: 1867-8548. doi:10.5194/amt-5-321-2012 (2012).

222. Budke, C. & Koop, T. BINARY: an optical freezing array for assessing temperature and time dependence of heterogeneous ice nucleation. *Atmospheric Measurement Techniques* **8,** 689–703. ISSN: 1867-8548. doi:10.5194/amt-8-689-2015 (2015).

223. Visakorpi, K. *et al.* Small-scale indirect plant responses to insect herbivory could have major impacts on canopy photosynthesis and isoprene emission. *New Phytologist* **220,** 799–810. ISSN: 0028646X. doi:10.1111/nph.15338 (2018).

224. Szczodrak, M., Austin, P. H. & Krummel, P. B. Variability of optical depth and effective radius in marine stratocumulus clouds. *Journal of the Atmospheric Sciences* **58,** 2912–2926. ISSN: 0022-4928. doi:10.1175/1520-0469(2001)058⟨2912:VOODAE⟩2.0.CO;2 (2001).

225. Zhu, Y., Rosenfeld, D. & Li, Z. Under what conditions can we trust retrieved cloud drop concentrations in broken marine stratocumulus? *Journal of Geophysical Research: Atmospheres* **123,** 8754–8767. ISSN: 2169897X. doi:10.1029/2017JD028083 (2018).

226. Zheng, Y., Rosenfeld, D. & Li, Z. Quantifying cloud base updraft speeds of marine stratocumulus from cloud top radiative cooling. *Geophysical Research Letters* **43,** 11, 407–11, 413. ISSN: 00948276. doi:10.1002/2016GL071185 (2016).

227. Pinsky, M., Khain, A., Mazin, I. & Korolev, A. Analytical estimation of droplet concentration at cloud base. *Journal of Geophysical Research: Atmospheres* **117.** ISSN: 01480227. doi:10.1029/2012JD017753 (2012).

228. Edson, J. B. *et al.* On the exchange of momentum over the open ocean. *Journal of Physical Oceanography* **43,** 1589–1610. ISSN: 0022-3670. doi:10.1175/JPO-D-12-0173.1 (2013).

229. Fairall, C. W., Bradley, E. F., Hare, J. E., Grachev, A. A. & Edson, J. B. Bulk parameterization of air–sea fluxes: updates and verification for the COARE algorithm. *Journal of Climate* **16,** 571–591. ISSN: 0894-8755. doi:10.1175/1520-0442(2003)016⟨0571:BPOASF⟩2.0.CO;2 (2003).

230. Schmidt, K. M., Swart, S., Reason, C. & Nicholson, S.-A. Evaluation of satellite and reanalysis wind products with In situ wave glider wind observations in the Southern Ocean. *Journal of Atmospheric and Oceanic Technology* **34,** 2551–2568. ISSN: 0739-0572. doi:10.1175/JTECH-D-17-0079.1 (2017).

231. Vehkamäki, H. An improved parameterization for sulfuric acid–water nucleation rates for tropospheric and stratospheric conditions. *Journal of Geophysical Research* **107,** 4622. ISSN: 0148-0227. doi:10.1029/2002JD002184 (2002).

232. Metzger, A. *et al.* Evidence for the role of organics in aerosol particle formation under atmospheric conditions. *Proceedings of the National Academy of Sciences* **107,** 6646–6651. ISSN: 0027-8424. doi:10.1073/pnas.0911330107 (2010).

233. Kipling, Z. *et al.* Constraints on aerosol processes in climate models from vertically-resolved aircraft observations of black carbon. *Atmospheric Chemistry and Physics* **13,** 5969–5986. ISSN: 1680-7324. doi:10.5194/acp-13-5969-2013 (2013).

234. West, R. E. L. *et al.* The importance of vertical velocity variability for estimates of the indirect aerosol effects. *Atmospheric Chemistry and Physics* **14,** 6369–6393. ISSN: 1680-7324. doi:10.5194/acp-14-6369-2014 (2014).

235. Edwards, J. & Slingo, A. Studies with a flexible new radiation code. I: Choosing a configuration for a large-scale model. *Quarterly Journal of the Royal Meteorological Society* **122,** 689–719. ISSN: 1477870X. doi:10.1256/smsqj.53106 (1996).

236. Gong, S. L. A parameterization of sea-salt aerosol source function for sub- and super-micron particles. *Global Biogeochemical Cycles* **17,** n/a–n/a. ISSN: 08866236. doi:10.1029/2003GB002079 (2003).

237. Kettle, A. J. & Andreae, M. O. Flux of dimethylsulfide from the oceans: A comparison of updated data sets and flux models. *Journal of Geophysical Research: Atmospheres* **105,** 26793–26808. ISSN: 01480227. doi:10.1029/2000JD900252 (2000).

238. Nightingale, P. D., Liss, P. S. & Schlosser, P. Measurements of air-sea gas transfer during an open ocean algal bloom. *Geophysical Research Letters* **27,** 2117–2120. ISSN: 00948276. doi:10.1029/2000GL011541 (2000).

239. Clarke, A. D. *et al.* Particle production in the remote marine atmosphere: Cloud outflow and subsidence during ACE 1. *Journal of Geophysical Research: Atmospheres* **103,** 16397–16409. ISSN: 01480227. doi:10.1029/97JD02987 (1998).

240. Yoon, Y. J. & Brimblecombe, P. Modelling the contribution of sea salt and dimethyl sulfide derived aerosol to marine CCN. *Atmospheric Chemistry and Physics* **2,** 17–30. ISSN: 1680-7324. doi:10.5194/acp-2-17-2002 (2002).

241. Lana, A. *et al.* An updated climatology of surface dimethlysulfide concentrations and emission fluxes in the global ocean. *Global Biogeochemical Cycles* **25,** 1–17. ISSN: 08866236. doi:10.1029/2010GB003850 (2011).

242. Riddick, S. *et al.* The global distribution of ammonia emissions from seabird colonies. *Atmospheric Environment* **55,** 319–327. ISSN: 13522310. doi:10.1016/j.atmosenv.2012.02.052 (2012).

243. Riddick, S. *et al.* Measurement of ammonia emissions from temperate and subpolar seabird colonies. *Atmospheric Environment* **134,** 40–50. ISSN: 13522310. doi:10.1016/j.atmosenv.2016.03.016 (2016).

244. He, X.-c. *et al.* Role of iodine oxoacids in atmospheric aerosol nucleation. *Science* **371,** 589–595. ISSN: 0036-8075. doi:10.1126/science.abe0298 (2021).

245. Saiz-Lopez, A. *et al.* Boundary layer halogens in coastal Antarctica. *Science* **317,** 348–351. ISSN: 00368075. doi:10.1126/science.1141408 (2007).

246. Schönhardt, A. *et al.* Observations of iodine monoxide columns from satellite. *Atmospheric Chemistry and Physics* **8,** 637–653. ISSN: 1680-7324. doi:10.5194/acp-8-637-2008 (2008).

247. Järvinen, E. *et al.* Seasonal cycle and modal structure of particle number size distribution at Dome C, Antarctica. *Atmospheric Chemistry and Physics* **13,** 7473–7487. ISSN: 16807324. doi:10.5194/acp-13-7473-2013 (2013).

248. Heintzenberg, J., Birmili, W., Wiedensohler, A., Nowak, A. & Tuch, T. Structure, variability and persistence of the submicrometre marine aerosol. *Tellus B: Chemical and Physical Meteorology* **56,** 357–367. ISSN: 1600-0889. doi:10.3402/tellusb.v56i4.16450 (2004).

249. Clarke, A. D. & Kapustin, V. N. A Pacific Aerosol Survey. Part I: A Decade of Data on Particle Production, Transport, Evolution, and Mixing in the Troposphere. *Journal of the Atmospheric Sciences* **59,** 363–382. ISSN: 0022-4928. doi:10.1175/1520-0469(2002)059⟨0363:APASPI⟩2.0.CO;2 (2002).

250. McCoy, I. L. *et al.* Influences of Recent Particle Formation on Southern Ocean Aerosol Variability and Low Cloud Properties. *Journal of Geophysical Research: Atmospheres* **126,** 1–39. ISSN: 2169-897X. doi:10.1029/2020jd033529 (2021).

251. Jimi, S. I., Siems, S. T., McGregor, J. L., Gras, J. L. & Katzfey, J. J. An investigation into the origin of aerosol nucleation events observed in the Southern Ocean boundary layer. *Australian Meteorological Magazine* **57,** 85–93. ISSN: 00049743 (2008).

252. Gras, J. L., Jimi, S. I., Siems, S. T. & Krummel, P. B. Postfrontal nanoparticles at Cape Grim: observations. *Environmental Chemistry* **6,** 508. ISSN: 1448-2517. doi:10.1071/EN09075 (2009).

253. Katoshevski, D., Nenes, A. & Seinfeld, J. H. A study of processes that govern the maintenance of aerosols in the marine boundary layer. *Journal of Aerosol Science* **30,** 503–532. ISSN: 00218502. doi:10.1016/S0021-8502(98)00740-X (1999).

254. Pirjola, L., O'Dowd, C. D., Brooks, I. M. & Kulmala, M. Can new particle formation occur in the clean marine boundary layer? *Journal of Geophysical Research: Atmospheres* **105,** 26531–26546. ISSN: 01480227. doi:10.1029/2000JD900310 (2000).

255. Chambers, S. D. *et al.* Characterizing Atmospheric transport pathways to Antarctica and the remote Southern Ocean using Radon-222. *Frontiers in Earth Science* **6,** 1–28. ISSN: 2296-6463. doi:10.3389/feart.2018.00190 (2018).

256. MÅrtensson, M., Tunved, P., Korhonen, H. & Nilsson, D. The role of sea-salt emissions in controlling the marine Aitken and accumulation mode aerosol: a model study. *Tellus B: Chemical and Physical Meteorology* **62,** 259–279. ISSN: 1600-0889. doi:10.1111/j.1600-0889.2010.00465.x (2010).

257. Spracklen, D. V. *et al.* Evaluation of a global aerosol microphysics model against size-resolved particle statistics in the marine atmosphere. *Atmospheric Chemistry and Physics* **7,** 2073–2090. ISSN: 16807324. doi:10.5194/acp-7-2073-2007 (2007).

258. Preunkert, S. *et al.* Interannual variability of dimethylsulfide in air and seawater and its atmospheric oxidation by-products (methanesulfonate and sulfate) at Dumont d'Urville, coastal Antarctica (1999-2003). *Journal of Geophysical Research Atmospheres* **112,** 1–13. ISSN: 01480227. doi:10.1029/2006JD007585 (2007).

259. Yan, J. *et al.* Significant underestimation of gaseous methanesulfonic acid (MSA) over Southern Ocean. *Environmental Science and Technology* **53,** 13064–13070. ISSN: 15205851. doi:10.1021/acs.est.9b05362 (2019).

260. Walton, D. W. H. & Thomas, J. *Cruise Report - Antarctic Circumnavigation Expedition (ACE) 20th December 2016 - 19th March 2017* tech. rep. (Swiss Polar Institute, 2018). doi:https://doi.org/10.5281/zenodo.1443510.

261. Hintze, J. L. & Nelson, R. D. Violin plots: a box plot-density trace synergism. *The American Statistician* **52,** 181–184. ISSN: 0003-1305. doi:10.1080/00031305.1998.10480559 (1998).

262. Nowlin, W. D. & Klinck, J. M. The physics of the Antarctic Circumpolar Current. *Reviews of Geophysics* **24,** 469–491. ISSN: 87551209. doi:10.1029/RG024i003p00469 (1986).

263. Mauldin, R. L., Tanner, D. J., Heath, J. A., Huebert, B. J. & Eisele, F. L. Observations of H_2SO_4 and MSA during PEM-Tropics-A. *Journal of Geophysical Research Atmospheres* **104,** 5801–5816. ISSN: 01480227. doi:10.1029/98JD02612 (1999).

264. Lucas, D. D. Mechanistic studies of dimethylsulfide oxidation products using an observationally constrained model. *Journal of Geophysical Research* **107,** 4201. ISSN: 0148-0227. doi:10.1029/2001JD000843 (2002).

265. Berresheim, H. *et al.* Gas-aerosol relationships of H_2SO_4 , MSA, and OH: Observations in the coastal marine boundary layer at Mace Head, Ireland. *Journal of Geophysical Research* **107,** 8100. ISSN: 0148-0227. doi:10.1029/2000JD000229 (2002).

266. Mauldin, R. L. *et al.* Highlights of OH, H_2SO_4, and methane sulfonic acid measurements made aboard the NASA P-3B during Transport and Chemical Evolution over the Pacific. *Journal of Geophysical Research D: Atmospheres* **108,** 1–13. ISSN: 01480227. doi:10.1029/2003jd003410 (2003).

267. Barnes, I., Hjorth, J. & Mihalapoulos, N. Dimethyl sulfide and dimethyl sulfoxide and their oxidation in the atmosphere. *Chemical Reviews* **106,** 940–975. ISSN: 00092665. doi:https://doi.org/10.1021/cr020529+ (2006).

268. Saiz-Lopez, A. *et al.* Atmospheric Chemistry of Iodine. *Chemical Reviews* **112,** 1773–1804. ISSN: 0009-2665. doi:10.1021/cr200029u (2012).

269. Gómez Martín, J. C. *et al.* A gas-to-particle conversion mechanism helps to explain atmospheric particle formation through clustering of iodine oxides. *Nature Communications* **11,** 4521. ISSN: 2041-1723. doi:10.1038/s41467-020-18252-8 (2020).

270. Lewis, T. R. *et al.* Determination of the absorption cross sections of higher-order iodine oxides at 355 and 532 nm. *Atmospheric Chemistry and Physics* **20,** 10865–10887. ISSN: 1680-7324. doi:10.5194/acp-20-10865-2020 (2020).

271. Saiz-Lopez, A. *et al.* Iodine chemistry in the troposphere and its effect on ozone. *Atmospheric Chemistry and Physics* **14,** 13119–13143. ISSN: 16807324. doi:10.5194/acp-14-13119-2014 (2014).

272. Saiz-Lopez, A., Blaszczak-Boxe, C. S. & Carpenter, L. J. A mechanism for biologically induced iodine emissions from sea ice. *Atmospheric Chemistry and Physics* **15,** 9731–9746. ISSN: 16807324. doi:10.5194/acp-15-9731-2015 (2015).

273. Beck, L. J. *et al.* Differing Mechanisms of New Particle Formation at Two Arctic Sites. *Geophysical Research Letters* **48,** 1–11. ISSN: 0094-8276. doi:10.1029/2020GL091334 (2021).

274. De Bruyn, W. J. *et al.* Uptake of gas phase sulfur species methanesulfonic acid, dimethylsulfoxide, and dimethyl sulfone by aqueous surfaces. *Journal of Geophysical Research* **99,** 16927. ISSN: 0148-0227. doi:10.1029/94JD00684 (1994).

275. Ammann, M. *et al.* Evaluated kinetic and photochemical data for atmospheric chemistry: Volume VI – heterogeneous reactions with liquid substrates. *Atmospheric Chemistry and Physics* **13,** 8045–8228. ISSN: 1680-7324. doi:10.5194/acp-13-8045-2013 (2013).

276. Berresheim, H. *et al.* Missing SO_2 oxidant in the coastal atmosphere? - Observations from high-resolution measurements of OH and atmospheric sulfur compounds. *Atmospheric Chemistry and Physics* **14,** 12209–12223. ISSN: 16807324. doi:10.5194/acp-14-12209-2014 (2014).

277. Clegg, S. L. & Seinfeld, J. H. Thermodynamic Models of Aqueous Solutions Containing Inorganic Electrolytes and Dicarboxylic Acids at 298.15 K. 1. The Acids as Nondissociating Components. *The Journal of Physical Chemistry A* **110,** 5692–5717. ISSN: 1089-5639. doi:10.1021/jp056149k (2006).

278. Davis, D. *et al.* DMS oxidation in the Antarctic marine boundary layer: Comparison of model simulations and held observations of DMS, DMSO, $DMSO_2$, H_2SO_4 (g), MSA(g), and MSA(p). *Journal of Geophysical Research: Atmospheres* **103,** 1657–1678. ISSN: 01480227. doi:10.1029/97JD03452 (1998).

279. Jefferson, A. *et al.* OH photochemistry and methane sulfonic acid formation in the coastal Antarctic boundary layer. *Journal of Geophysical Research: Atmospheres* **103,** 1647–1656. ISSN: 01480227. doi:10.1029/97JD02376 (1998).

280. Savoie, D. L. *et al.* Nitrogen and sulfur species in Antarctic aerosols at Mawson, Palmer Station, and Marsh (King George Island). *Journal of Atmospheric Chemistry* **17,** 95–122. ISSN: 0167-7764. doi:10.1007/BF00702821 (1993).

281. Legrand, M., Ducroz, F., Wagenbach, D., Mulvaney, R. & Hall, J. Ammonium in coastal Antarctic aerosol and snow: Role of polar ocean and penguin emissions. *Journal of Geophysical Research: Atmospheres* **103,** 11043–11056. ISSN: 01480227. doi:10.1029/97JD01976 (1998).

282. Quinn, P. K., Coffman, D. J., Kapustin, V. N., Bates, T. S. & Covert, D. S. Aerosol optical properties in the marine boundary layer during the First Aerosol Characterization Experiment (ACE 1) and the underlying chemical and physical aerosol properties. *Journal of Geophysical Research: Atmospheres* **103,** 16547–16563. ISSN: 01480227. doi:10.1029/97JD02345 (1998).

283. Teinilä, K., Kerminen, V. M. & Hillamo, R. A study of size-segregated aerosol chemistry in the Antarctic atmosphere. *Journal of Geophysical Research Atmospheres* **105,** 3893–3904. ISSN: 01480227. doi:10.1029/1999JD901033 (2000).

284. Zorn, S. R., Drewnick, F., Schott, M., Hoffmann, T. & Borrmann, S. Characterization of the South Atlantic marine boundary layer aerosol using an aerodyne aerosol mass spectrometer. *Atmospheric Chemistry and Physics* **8,** 4711–4728. ISSN: 16807324. doi:10.5194/acp-8-4711-2008 (2008).

285. Xu, G., Gao, Y., Lin, Q., Li, W. & Chen, L. Characteristics of water-soluble inorganic and organic ions in aerosols over the Southern Ocean and coastal East Antarctica during austral summer. *Journal of Geophysical Research: Atmospheres* **118,** 13, 303–13, 318. ISSN: 2169897X. doi:10.1002/2013JD019496 (2013).

286. Barbaro, E. *et al.* Particle size distribution of inorganic and organic ions in coastal and inland Antarctic aerosol. *Environmental Science and Pollution Research* **24,** 2724–2733. ISSN: 16147499. doi:10.1007/s11356-016-8042-x (2017).

287. Berg, O. H., Swietlicki, E. & Krejci, R. Hygroscopic growth of aerosol particles in the marine boundary layer over the Pacific and Southern Oceans during the First Aerosol Characterization Experiment (ACE 1). *Journal of Geophysical Research: Atmospheres* **103,** 16535–16545. ISSN: 01480227. doi:10.1029/97JD02851 (1998).

288. Jourdain, B. & Legrand, M. Year-round records of bulk and size-segregated aerosol composition and HCl and HNO_3 levels in the Dumont d'Urville (coastal Antarctica) atmosphere: Implications for sea-salt aerosol fractionation in the winter and summer. *Journal of Geophysical Research Atmospheres* **107,** 1–13. ISSN: 01480227. doi:10.1029/2002JD002471 (2002).

289. Fridlind, A. M. & Jacobson, M. Z. A study of gas-aerosol equilibrium and aerosol pH in the remote marine boundary layer during the First Aerosol Characterization Experiment (ACE 1). *Journal of Geophysical Research: Atmospheres* **105,** 17325–17340. ISSN: 01480227. doi:10.1029/2000JD900209 (2000).

290. Angle, K. J. *et al.* Acidity across the interface from the ocean surface to sea spray aerosol. *Proceedings of the National Academy of Sciences* **118,** e2018397118. ISSN: 0027-8424. doi:10.1073/pnas.2018397118 (2021).

291. Davis, D. *et al.* Dimethyl sulfide oxidation in the equatorial Pacific: Comparison of model simulations with field observations for DMS, SO_2 , H_2SO_4 (g), MSA(g), MS and NSS. *Journal of Geophysical Research: Atmospheres* **104,** 5765–5784. ISSN: 01480227. doi:10.1029/1998JD100002 (1999).

292. Williams, J., de Reus, M., Krejci, R., Fischer, H. & Ström, J. Application of the variability-size relationship to atmospheric aerosol studies: estimating aerosol lifetimes and ages. *Atmospheric Chemistry and Physics* **2,** 133–145. ISSN: 1680-7324. doi:10.5194/acp-2-133-2002 (2002).

293. Manninen, H. E. *et al.* EUCAARI ion spectrometer measurements at 12 European sites-analysis of new particle formation events. *Atmospheric Chemistry and Physics* **10,** 7907–7927. ISSN: 16807316. doi:10.5194/acp-10-7907-2010 (2010).

294. Chen, X. *et al.* Features in air ions measured by an air ion spectrometer (AIS) at Dome C. *Atmospheric Chemistry and Physics* **17,** 13783–13800. ISSN: 1680-7324. doi:10.5194/acp-17-13783-2017 (2017).

295. Thurnherr, I., Wernli, H. & Aemisegger, F. *10-day backward trajectories from ECMWF analysis data along the ship track of the Antarctic Circumnavigation Expedition in austral summer 2016/2017* 2020. doi:https://doi.org/10.5281/zenodo.4031704.

296. Mahajan, A. S. *et al.* Quantifying the impacts of an updated global dimethyl sulfide climatology on cloud microphysics and aerosol radiative forcing. *Journal of Geophysical Research: Atmospheres* **120,** 2524–2536. ISSN: 2169897X. doi:10.1002/2014JD022687 (2015).

297. King, J. C. & Turner, J. *Antarctic Meteorology and Climatology* (Cambridge University Press, 1997).

298. Croft, B. *et al.* Contribution of Arctic seabird-colony ammonia to atmospheric particles and cloud-albedo radiative effect. *Nature Communications* **7,** 1–10. ISSN: 20411723. doi:10.1038/ncomms13444 (2016).

299. Myhre, C. E. L., D'Anna, B., Nicolaisen, F. M. & Nielsen, C. J. Properties of aqueous methanesulfonic acid: complex index of refraction and surface tension. *Applied Optics* **43,** 2500. ISSN: 0003-6935. doi:10.1364/AO.43.002500 (2004).

300. Dutcher, C. S., Wexler, A. S. & Clegg, S. L. Surface Tensions of Inorganic Multicomponent Aqueous Electrolyte Solutions and Melts. *The Journal of Physical Chemistry A* **114,** 12216–12230. ISSN: 1089-5639. doi:10.1021/jp105191z (2010).

301. Clarke, J. H. R. & Woodward, L. A. Raman spectrophotometric determination of the degrees of dissociation of methanesulphonic acid in aqueous solution at 25°C. *Trans. Faraday Soc.* **62,** 2226–2233. ISSN: 0014-7672. doi:10.1039/TF9666202226 (1966).

302. Clegg, S. & Brimblecombe, P. The solubility of methanesulphonic acid and its implications for atmospheric chemistry. *Environmental Technology Letters* **6,** 269–278. ISSN: 0143-2060. doi:10.1080/09593338509384344 (1985).

303. Manabe, S. & Wetherald, R. T. *The Effects of Doubling the CO2 Concentration on the climate of a General Circulation Model* 1975. doi:10.1175/1520-0469(1975)0322.0.CO;2.

304. Heintzenberg, J. *et al.* Aerosol number-size distributions during clear and fog periods in the summer high Arctic: 1991, 1996 and 2001. *Tellus, Series B: Chemical and Physical Meteorology* **58,** 41–50. ISSN: 02806509. doi:10.1111/j.1600-0889.2005.00171.x (2006).

305. Abbatt, J. P. D. *et al.* Overview paper: New insights into aerosol and climate in the Arctic. *Atmospheric Chemistry and Physics* **19,** 2527–2560. ISSN: 1680-7324. doi:10.5194/acp-19-2527-2019 (2019).

306. Willis, M. D., Leaitch, W. R. & Abbatt, J. P. Processes controlling the composition and abundance of Arctic aerosol. *Reviews of Geophysics* **56,** 621–671. ISSN: 87551209. doi:10.1029/2018RG000602 (2018).

307. Dall´Osto, M. *et al.* Abiotic and biotic sources influencing spring new particle formation in North East Greenland. *Atmospheric Environment* **190,** 126–134. ISSN: 13522310. doi:10.1016/j.atmosenv.2018.07.019 (2018).

308. Allan, J. D. *et al.* Iodine observed in new particle formation events in the Arctic atmosphere during ACCACIA. *Atmospheric Chemistry and Physics* **15,** 5599–5609. ISSN: 16807324. doi:10.5194/acp-15-5599-2015 (2015).

309. Lunden, J. *et al.* The vertical distribution of atmospheric DMS in the high Arctic summer. *Tellus, Series B: Chemical and Physical Meteorology* **62,** 160–171. ISSN: 16000889. doi:10.1111/j.1600-0889.2010.00458.x (2010).

310. Saunders, R. W. & Plane, J. M. Formation pathways and composition of iodine oxide ultra-fine particles. *Environmental Chemistry* **2,** 299–303. ISSN: 14482517. doi:10.1071/EN05079 (2005).

311. Kumar, M., Saiz-Lopez, A. & Francisco, J. S. Single-molecule catalysis revealed: elucidating the mechanistic framework for the formation and growth of atmospheric iodine oxide aerosols in gas-phase and aqueous surface environments. *Journal of the American Chemical Society* **140,** 14704–14716. ISSN: 15205126. doi:10.1021/jacs.8b07441 (2018).

312. Tjernström, M. *et al.* Meteorological conditions in the central Arctic summer during the Arctic Summer Cloud Ocean Study (ASCOS). *Atmospheric Chemistry and Physics* **12,** 6863–6889. ISSN: 16807316. doi:10.5194/acp-12-6863-2012 (2012).

313. Hill, V. L. & Manley, S. L. Release of reactive bromine and iodine from diatoms and its possible role in halogen transfer in polar and tropical oceans. *Limnology and Oceanography* **54,** 812–822. ISSN: 00243590. doi:10.4319/lo.2009.54.3.0812 (2009).

314. Gálvez, Ó., Teresa Baeza-Romero, M., Sanz, M. & Saiz-Lopez, A. Photolysis of frozen iodate salts as a source of active iodine in the polar environment. *Atmospheric Chemistry and Physics* **16,** 12703–12713. ISSN: 16807324. doi:10.5194/acp-16-12703-2016 (2016).

315. Raso, A. R. W. *et al.* Active molecular iodine photochemistry in the Arctic. *Proceedings of the National Academy of Sciences* **114,** 10053–10058. ISSN: 0027-8424. doi:10.1073/pnas.1702803114 (2017).

316. Halfacre, J. W., Shepson, P. B. & Pratt, K. A. PH-dependent production of molecular chlorine, bromine, and iodine from frozen saline surfaces. *Atmospheric Chemistry and Physics* **19,** 4917–4931. ISSN: 16807324. doi:10.5194/acp-19-4917-2019 (2019).

317. Kim, K. *et al.* Production of molecular iodine and tri-iodide in the frozen solution of iodide: implication for polar atmosphere. *Environmental Science and Technology* **50,** 1280–1287. ISSN: 15205851. doi:10.1021/acs.est.5b05148 (2016).

318. Abbatt, J. P. *et al.* Halogen activation via interactions with environmental ice and snow in the polar lower troposphere and other regions. *Atmospheric Chemistry and Physics* **12,** 6237–6271. ISSN: 16807316. doi:10.5194/acp-12-6237-2012 (2012).

319. Sharma, S. *et al.* A factor and trends analysis of multidecadal lower tropospheric observations of Arctic aerosol composition, black carbon, ozone, and mercury at Alert, Canada. *Journal of Geophysical Research: Atmospheres* **124,** 14133–14161. ISSN: 2169-897X. doi:10.1029/2019JD030844 (2019).

320. Carpenter, L. J. *et al.* Atmospheric iodine levels influenced by sea surface emissions of inorganic iodine. *Nature Geoscience* **6,** 108–111. ISSN: 17520894. doi:10.1038/ngeo1687 (2013).

321. Dall'Osto, M. *et al.* Arctic sea ice melt leads to atmospheric new particle formation. *Scientific Reports* **7,** 1–10. ISSN: 20452322. doi:10.1038/s41598-017-03328-1 (2017).

322. Freud, E. *et al.* Pan-Arctic aerosol number size distributions: seasonality and transport patterns. *Atmospheric Chemistry and Physics* **17,** 8101–8128. ISSN: 1680-7324. doi:10.5194/acp-17-8101-2017 (2017).

323. Ouyang, H., Gopalakrishnan, R. & Hogan, C. J. Nanoparticle collisions in the gas phase in the presence of singular contact potentials. *The Journal of Chemical Physics* **137,** 064316. ISSN: 0021-9606. doi:10.1063/1.4742064 (2012).

324. Stolzenburg, D. *et al.* Rapid growth of organic aerosol nanoparticles over a wide tropospheric temperature range. *Proceedings of the National Academy of Sciences of the United States of America* **115,** 9122–9127. ISSN: 10916490. doi:10.1073/pnas.1807604115 (2018).

325. Pithan, F. *et al.* Role of air-mass transformations in exchange between the Arctic and mid-latitudes. *Nature Geoscience* **11,** 805–812. ISSN: 17520908. doi:10.1038/s41561-018-0234-1 (2018).

326. Koike, M. *et al.* Year-round in situ measurements of Arctic low-level clouds: microphysical properties and their relationships with aerosols. *Journal of Geophysical Research: Atmospheres* **124,** 1798–1822. ISSN: 2169897X. doi:10.1029/2018JD029802 (2019).

327. Sirois, A. & Barrie, L. A. Arctic lower tropospheric aerosol trends and composition at Alert, Canada: 1980-1995. *Journal of Geophysical Research Atmospheres* **104,** 11599–11618. ISSN: 01480227. doi:10.1029/1999JD900077 (1999).

328. Rigor, I. G., Colony, R. L. & Martin, S. Variations in surface air temperature observations in the Arctic, 1979-97. *Journal of Climate* **13,** 896–914. ISSN: 08948755. doi:10.1175/1520-0442(2000)013⟨0896:VISATO⟩2.0.CO;2 (2000).

329. Glass, D. C. & Gray, C. N. Estimating mean exposures from censored data: Exposure to benzene in the Australian petroleum industry. *Annals of Occupational Hygiene* **45,** 275–282. ISSN: 00034878. doi:10.1016/S0003-4878(01)00022-9 (2001).

330. Lance, S., Medina, J., Smith, J. & Nenes, A. Mapping the operation of the DMT continuous flow CCN counter. *Aerosol Science and Technology* **40,** 242–254. ISSN: 02786826. doi:10.1080/02786820500543290 (2006).

331. Von der Weiden, S.-L., Drewnick, F. & Borrmann, S. Particle Loss Calculator – a new software tool for the assessment of the performance of aerosol inlet systems. *Atmospheric Measurement Techniques* **2,** 479–494. ISSN: 1867-8548. doi:10.5194/amt-2-479-2009 (2009).

332. Tjernström, M. & Graversen, R. G. The vertical structure of the lower Arctic troposphere analysed from observations and the ERA-40 reanalysis. *Quarterly Journal of the Royal Meteorological Society* **135,** 431–443. ISSN: 00359009. doi:10.1002/qj.380 (2009).

333. Björkman, M. *et al.* Nitrate dry deposition in Svalbard. *Tellus B: Chemical and Physical Meteorology* **65,** 19071. ISSN: 1600-0889. doi:10.3402/tellusb.v65i0.19071 (2013).

334. Virtanen, P. *et al.* SciPy 1.0: fundamental algorithms for scientific computing in Python. *Nature methods*, 1–12. ISSN: 1548-7105. doi:10.1038/s41592-019-0686-2 (2020).

335. McKinney, W. *Data Structures for Statistical Computing in Python* tech. rep. (2010), 51.

336. Van der Walt, S., Colbert, S. C. & Varoquaux, G. The NumPy Array: A Structure for Efficient Numerical Computation. *Computing in Science & Engineering* **13,** 22–30. ISSN: 1521-9615. doi:10.1109/MCSE.2011.37 (2011).

337. Hunter, J. D. Matplotlib: A 2D graphics environment. *Computing in Science and Engineering* **9,** 99–104. ISSN: 15219615. doi:10.1109/MCSE.2007.55 (2007).

338. Kulmala, M. *et al.* Direct observations of atmospheric aerosol nucleation. *Science* **339,** 943–946. ISSN: 10959203. doi:10.1126/science.1227385 (2013).

339. Khanniche, S., Louis, F., Cantrel, L. & Černušák, I. A theoretical study of the microhydration of iodic acid ($HOIO_2$). *Computational and Theoretical Chemistry* **1094,** 98–107. ISSN: 2210271X. doi:10.1016/j.comptc.2016.09.010 (2016).

340. Ahonen, L. *et al.* Ion mobility-mass spectrometry of iodine pentoxide-iodic acid hybrid cluster anions in dry and humidified atmospheres. *Journal of Physical Chemistry Letters* **10,** 1935–1941. ISSN: 19487185. doi:10.1021/acs.jpclett.9b00453 (2019).

341. Kumar, R., Saunders, R. W., Mahajan, A. S., Plane, J. M. & Murray, B. J. Physical properties of iodate solutions and the deliquescence of crystalline I_2O_5 and HIO_3. *Atmospheric Chemistry and Physics* **10,** 12251–12260. ISSN: 16807316. doi:10.5194/acp-10-12251-2010 (2010).

342. Larriba, C. *et al.* The mobility-volume relationship below 3.0 nm examined by tandem mobility-mass measurement. *Aerosol Science and Technology* **45,** 453–467. ISSN: 02786826. doi:10.1080/02786826.2010.546820 (2011).

343. Cuevas, C. A. *et al.* Rapid increase in atmospheric iodine levels in the North Atlantic since the mid-20th century. *Nature Communications* **9,** 1–6. ISSN: 20411723. doi:10.1038/s41467-018-03756-1 (2018).

344. Vermot, E. *MOD09A1 MODIS Surface Reflectance 8-Day L3 Global 500m SIN Grid V006. NASA EOSDIS Land Processes DAAC* 2015. doi:http://doi.org/10.5067/MODIS/MOD09A1.006.

345. Fehsenfeld, F. C. & Ferguson, E. E. Laboratory studies of negative ion reactions with atmospheric trace constituents. *The Journal of Chemical Physics* **61,** 3181–3193. ISSN: 00219606. doi:10.1063/1.1682474 (1974).

346. Bork, N., Kurtén, T. & Vehkamäki, H. Exploring the atmospheric chemistry of $O_2SO_3^-$ and assessing the maximum turnover number of ion-catalysed H_2SO_4 formation. *Atmospheric Chemistry and Physics* **13,** 3695–3703. ISSN: 1680-7324. doi:10.5194/acp-13-3695-2013 (2013).

347. Tsona, N. T. & Du, L. A potential source of atmospheric sulfate from O_2^--induced SO_2 oxidation by ozone. *Atmospheric Chemistry and Physics* **19,** 649–661. ISSN: 1680-7324. doi:10.5194/acp-19-649-2019 (2019).

348. Möhler, O., Reiner, T. & Arnold, F. The formation of SO_5^- by gas phase ion-molecule reactions. *The Journal of Chemical Physics* **97,** 8233–8239. ISSN: 00219606. doi:10.1063/1.463394 (1992).

349. Davis, D. D., Ravishankara, A. R. & Fischer, S. SO_2 oxidation via the hydroxyl radical: Atmospheric fate of HSOx radicals. *Geophysical Research Letters* **6,** 113–116. ISSN: 00948276. doi:10.1029/GL006i002p00113 (1979).

350. González-García, N. & Olzmann, M. Kinetics of the chemically activated HSO_5 radical under atmospheric conditions – a master-equation study. *Physical Chemistry Chemical Physics* **12,** 12290. ISSN: 1463-9076. doi:10.1039/c0cp00284d (2010).

351. Kurtén, T., Berndt, T. & Stratmann, F. Hydration increases the lifetime of HSO_5 and enhances its ability to act as a nucleation precursor – a computational study. *Atmospheric Chemistry and Physics* **9,** 3357–3369. ISSN: 1680-7324. doi:10.5194/acp-9-3357-2009 (2009).

ACKNOWLEDGEMENTS

I remember very well the day of my PhD interview at PSI and the sensation after receiving the PhD offer from Urs and Josef. I felt honoured and excited for the opportunity, yet I was very debated because I was not too convinced by the research topic at the time. Looking back now I realize that accepting that offer is one of the best decisions of my life: this PhD has been an incredible experience and I have truly enjoyed it. Of course I also had my fair share of struggle and stress but I could always find someone supporting and advising me during the most critical periods. This is one of the reasons why it is so great to be part of the LAC, no matter the situation you can always find someone to help you.

I would like to start thanking Prof. Dr. Ruth Signorell and Prof. Dr. Hans-Christen Hansson for accepting to be my co-referee and to review my thesis.

I would like to thank Prof. Dr. Urs Baltensperger for your fantastic support during my PhD and your scientific vision, which was always a source of inspiration for me.

I am very grateful to Prof. Dr. Julia Schmale, you have been the driving force behind the two expeditions that were the core of my PhD, without you none of this would have happened. We shared a lot of time together in the field, you were always there whenever I need it and I learned a lot by working and discussing with you. I truly admire your commitment, your passion for science and your ability to efficiently work on thousands of different projects at the same time.

My sincere thanks go to Dr. Josef Dommen, it is difficult to describe how valuable your continuous and unconditional support was in every situation. I have always been amazed by your patience and the nearly infinite amount of time that you dedicated not just to me but to every person in the lab, working together or discussing about science for hours. This is the reason why the Smog Chamber group was such a nice working environment. I am also grateful because you made me appreciate chemistry and the value of simple calculations and models to support observations and hypotheses.

A special thank you also to the former smog chamber, now MCPP, group, it was great to share the last four years working with you. I am particularly grateful to the *cafeteria lunch sub-group*, Imad, Mao, Houssni, Ping and Ruby. It was always fun to discuss with you the most diverse and crazy topics and to spend time together!

I want to thank all PhD students, scientists and technicians of the LAC for the help in different occasions, the scientific discussions and the time spent together outside of PSI. I am also very grateful for all the amazing people that I met during ACE, MOCCHA and the various CLOUD campaigns, I learned a lot by sharing these experiences with you!

My deepest thanks to my sisters Anna, Arianna and Chiara and to my parents Massimo and Franca, you have always been there with patience and enthusiasm believing in my choices. If I am who I am today the merit is yours.

Barbara, you are the last but as the saying goes certainly not the least. There are no words to express my gratitude for having you on my side for so long, continuously helping me and supporting my decisions even when these were bringing me away for several months. Life is just so much better when it is shared with you.

ETH zürich

PAUL SCHERRER INSTITUT

PSI